Project[1] **Number:** [709607]

Project Acronym: [TIANOBAIN]

Project title: [Towards industrial applicability of (medium C) nanostructured bainitic steels]

Final Technical Report

Part B

Carlos Garcia-Mateo, Adriana Eres-Castellanos, Francisca G. Caballero

National Center for Metallurgical Research (CENIM-CSIC), Madrid, Spain

Andreas Latz, Sebastian Schreiber

ThyssenKrupp Steel Europe AG (tkSE), Duisburg, GERMANY

Arunim Ray, Lieven Bracke

Onderzoekscentrum Voor Aanwending Van Staal NV (OCAS), Zelzate, Belgium

Mahesh Somani, Pentti Kaikkonen, Aarne Pohjonen, David A. Porter

OULUN YLIOPISTO (OULU), Oulu, Finland

Period covered by the report: from [01/10/2016] to [31/03/2020]

Final report: *[August 2020]*

[1] The term 'project' used in this template equates to an 'action' in certain other Horizon 2020 documentation

Table of Contents

1 Final Summary.

1.1 Objectives of the Project

The project aimed at exploring the industrial feasibility of new super-high strength steels (SHSS) made using innovative processing methods and based on medium carbon nanostructured bainitic microstructures. It was envisaged that the steels could be applied in engineering applications in the transport industry and wear-resistant applications for example in the mining industry.

The microstructural concept that was exploited, with the purpose of attaining UTS > 1600MPa, is the ausformed bainite in medium carbon steels (0.4-0.5 wt.%). In this process, austenite is deformed and during subsequent cooling and holding at lower temperatures (than that in regular practice) the unrecrystallized austenite transforms to refined bainite with enhanced strength and toughness properties.

The industrialization of this new steel design concept, involving innovative process development and novel design of relatively inexpensive compositions, is accompanied by new manufacturing risks and uncertainties in terms of achieving advanced mechanical and in-use properties (tensile, impact toughness, wear, bendability, etc.). Therefore, this project intended to gather information in terms of chemical composition design, alternative TMCP routes, microstructural evolution, mechanical properties and in-use performance to assess the potential of novel bainitic steel grades in order to develop recommendations for viable industrial processes.

Within the partnership three concepts were selected as the most promising, see Figure 1:

- Ausforming at somewhat high temperature (T), hereinafter termed as HT-TMCP. Where, the finish rolling T (FRT) should be lower than the RST (recrystallization stop temperature) but above the Ar3.
- Ausforming at Medium T, from now on MT-TMCP. Where austenite is deformed in the bay between F/P and bainite.
- Ausforming at Low T, from now LT-TMCP. Where austenite is deformed close to, or at, the intended bainitic transformation temperature.

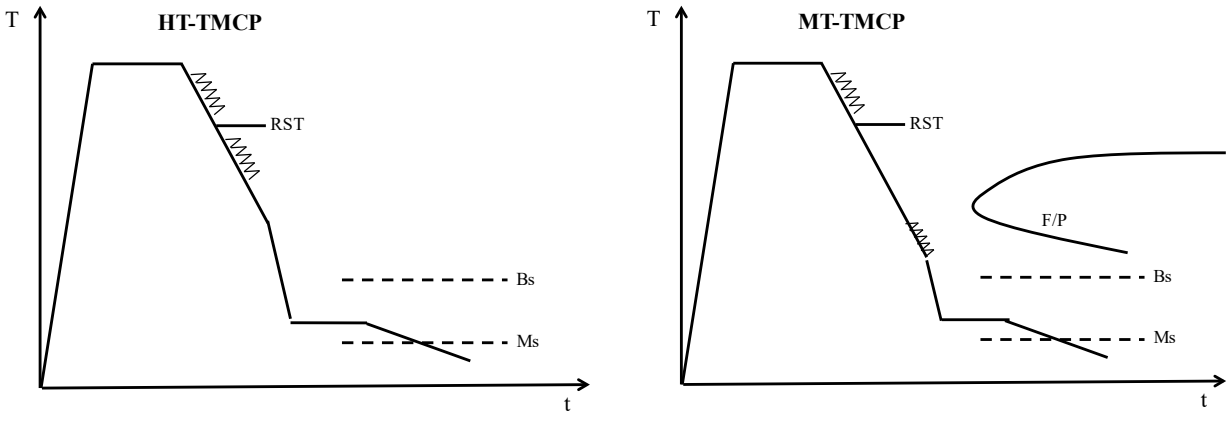

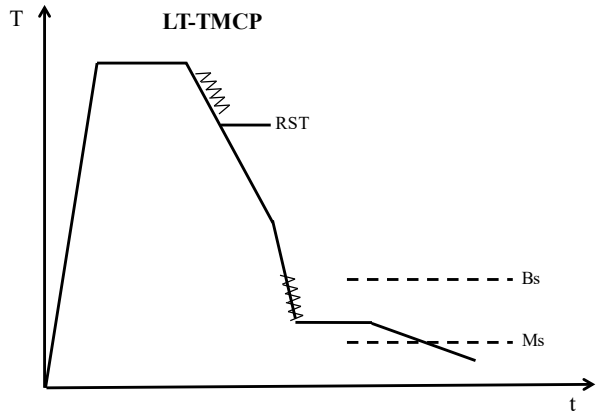

Figure 1. Scheme of the different TMCP concepts pursued in the project.

The main objectives of the project were:

1. Design of medium carbon compositions which would be suitable for ausforming and transformation to high-strength, tough nanostructured bainitic-austenitic microstructures.
2. The assessment of different TMCP (HT,MT and LT) schedules on the microstructures and mechanical properties.
3. Identification of relevant microstructural constituents, evolution, and their relationships with the measured properties.
4. Selection of appropriate compositions with processing parameters viable for industrial full-scale production.

1.2 Project structure

The project was designed with the work package (WP) structure shown in Figure 2, and divided into three clear Stages. In a first Stage an approach at laboratory scale is made, where the chemical compositions and processing parameter for the different TMCP are proposed and tested. WP1, WP2 and WP4 composed this Stage 1.

In Stage 2, the ausforming concept is scaled up to the level of a pilot plant or rolling laboratory simulator, where, after the application of TMCPs selected conditions, the properties are tested and the microstructure is characterised, allowing to establish criteria for the next level of scaling (WP6-Stage 3). In this Stage 2, a final product thickness of 12 mm was targeted representing plate material, and additional strips with a thickness of 3 mm were also produced representing a target thickness suitable for automotive applications. WP3, WP4 and WP5 composed this Stage 1

In the last Stage 3, solely composed of WP6, data produced through the project is used with two aims, i) to establish the mentioned criteria for the next level of production and ii) generation of relevant models.

This technical report will follow the described Stage structure.

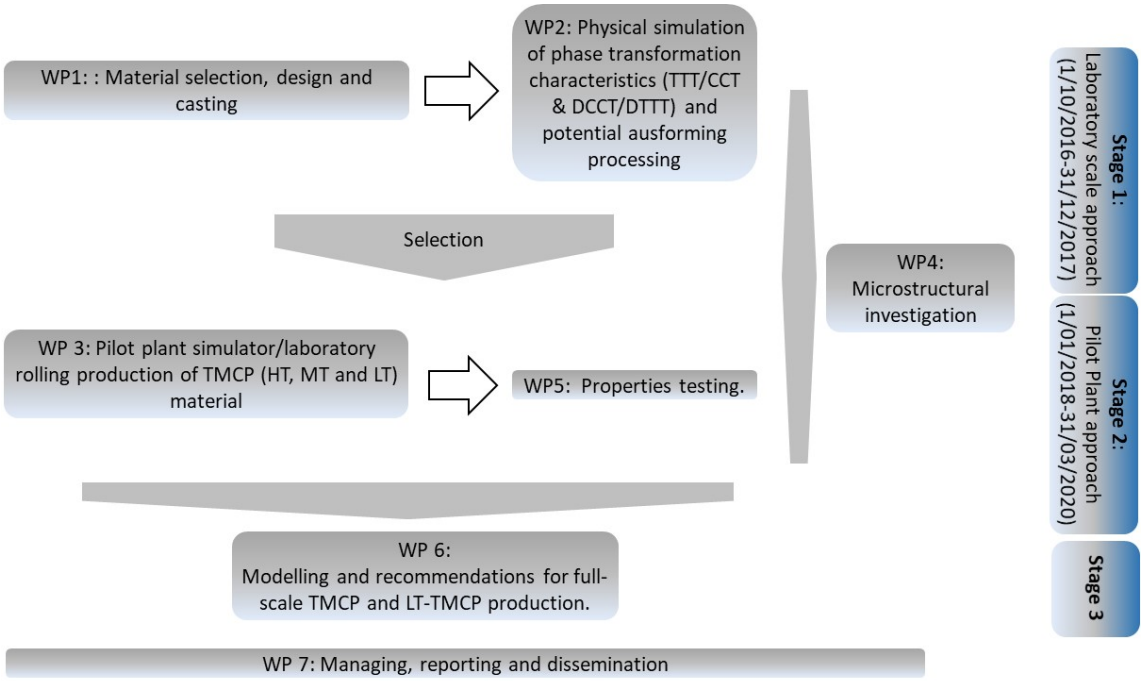

Figure 2. Project structure.

1.2.1 Stage 1. Laboratory Scale approach.

1.2.1.i Work Package 1. Material selection, design and casting

The achieved objectives for this WP were:

- Definition of the chemical compositions to be investigated.
- Theoretical design of alloy compositions based on thermodynamics modelling using advanced software such as Thermo-calc/ MTDATA, and suitable controlled processing for the development of potentially successful nanostructured TMCP and LT-TMCP bainitic steels.
- Recommendation and selection of chemical grades for casting.
- Laboratory castings of experimental heats with controls on impurity/trace (S,P, etc.) and gaseous (N, O and H) elements.
- Provision of the material to the consortium for different WPs and studies.

1.2.1.ii Work Package 2. Physical simulation of phase transformation characteristics (TTT/CCT & DCCT/DTTT) and potential ausforming processing.

The achieved objectives for this WP were:

- Hot strength of the alloys to estimate feasibility of the TMCP and LT-TMCP procedures.
- Determination of the recrystallization stop temperature (RST) temperature.
- Constructions of TTT and CCT diagrams, with and without prior deformation in austenite.
- Study on the microstructural evolution after different heat and thermomechanical treatments.

1.2.1.iii Work Package 4. Microstructural investigation.

For Stage 1 the achieved objectives of this WP were:

- Preliminary microstructure characterisation for the identification of phases (polygonal ferrite, pearlite, bainite/martensite and retained austenite) using light optical microscopy (LOM).
- Detailed characterisation of selected microstructures by means of SEM and TEM to determine size and distribution of the different constituents of the bainitic microstructures.
- Quantitative measurements of residual austenite content and average carbon content of the austenite by X-ray diffraction in bainitic microstructures.
- Dissolution technique in combination with TEM to determine the possible occurrence of precipitation and its identification in microstructures.

1.2.1.iv Stage 1. Main achievements

For stage 1 of this project, based on thermodynamic and kinetic calculations, 15 preliminary potential compositions of (0.3-0.5)C-(1.0-2.0)Mn-(0.8-1.5)Si-(0-1.0)Al-(0.7-1.5)Cr-(0-0.3)Mo-(0-0.02)Nb-(0-0.1)V in wt.%, were designed. Following casting and hot rolling in laboratory, dilatometer specimens were prepared for subsequent phase transformation and precipitation studies. Detailed inclusion analysis showed the presence of aluminium oxides, manganese sulphides, aluminium nitrides and Al2O3-MnO-Spinel. But the volume fraction and number density of such inclusions were not significant and was not expected to affect the subsequent phase transformation studies.

Study of austenite strength at different temperatures (T=900-300°C) showed increasing mean flow stress at decreasing deformation temperature. There might be some phase transformation (bainite) induced by deformation at 300-400°C. Al has a significant effect on the flow stress at relatively low temperature while Nb has a more moderate effect and Mo, V have a relatively lower effect. The no-recrystallisation temperature (T_{NR}) for the alloys were approximatelly ~900°C and for subsequent phase transformation studies, finish deformation temperature was kept ~850°C which was sufficiently lower than the approximated T_{NR}.

Detailed CCT diagrams both with and without deformation for all the 15 preliminary compositions were constructed. The Ms was around 220-227°C for high C (0.5 wt% C) alloys while for low carbon (0.3 wt% C) alloys, Ms was around 312-325°C. A cooling rate of over 10ºC/s was found to be sufficient to avoid the ferrite-pearlite bay both with and without deformation. In terms of isothermal TTT study, bainite fraction increased with decreasing transformation temperature indicating incomplete transformation phenomena at higher temperatures. The microstructure became finer and the hardness increased as the transformation temperature decreased. In terms of deformation-TTT (D-TTT), the onset of transformation tends to be accelerated compared to the isothermal transformation without deformation, but relatively more austenite remains untransformed at the end due to mechanical stabilization of the already deformed austenite. Degree of austenite stabilization increases with decreasing finish deformation temperature.

1.2.2 Stage 2. Pilot Plant/Rolling Simulators approach.

Base on the results of Stage 1 the next Phase was developed following the WP structure shown below. In this Stage 2, a final product thickness of 12 mm was targeted representing plate material, and additional strips with a thickness of 3 mm were also produced representing a target thickness suitable for automotive applications.

1.2.2.i Work Package 3. Pilot Plant Simulators/ Lab rolling production of TMCP (HT,MT and LT)

The achieved objectives of this WP were:

- Determination of processing parameters adapted to the different equipment capabilities and alloys for the development of nanostructured bainite by means of TMCP.
- Castings of optimized chemical composition heats with controls on impurity/trace (S,P, etc.) and gaseous (N, O and H) elements. Provision of material for pilot plant trials and laboratory investigations.
- Grain growth and recrystallization kinetics studies.
- Provide material for metallographic and properties characterization.

1.2.2.ii Work Package 4. Microstructural investigation.

For Stage 2 the achieved objectives of this WP were:

- Preliminary microstructure characterisation for the identification of phases (polygonal ferrite, pearlite, bainite/martensite and retained austenite) using light optical microscopy (LOM).
- Detailed characterisation of selected microstructures by means of SEM, EBSD and TEM.
- Quantitative measurements of residual austenite by X-ray diffraction in selected microstructures.
- Dissolution technique in combination with TEM to determine the possible occurrence of precipitation and its identification in selected conditions.
- Austenite grain size reconstruction by EBSD in selected conditions.

1.2.2.iii Work Package 5. Properties testing.

Microstructures obtained after TMCP processes in WP3, with final product thickness of 3 and 12 mm, were tested in this WP to determine their properties. The achieved objectives of this WP were

- To determine strength, ductility and work-hardening (tensile tests) of all the studied steels.
- To evaluate the toughness on selected conditions.
- To assess the wear resistance of selected grades with specific processing parameters.
- To study in-use properties by bending and hole expansion tests with specific processing parameters.
- Identification of relevant microstructural parameters.

1.2.2.iv Stage 2. Main achievements

In stage 2, based on the results obtained in WP2, CCT/DCCT and TTT/DTT diagrams, 5 final compositions were selected for pilot scale production and rolling simulations.

Following casting and rough rolling of the pilot scale plates, the static recrystallisation kinetics (SRX) characteristics of selected steels were evaluated by stress-relaxation tests on dilatometry specimens and the kinetics were modelled using a fractional softening approach to determine the time for 50 % recrystallization as a function of strain, strain rate, grain size and temperature during hot-deformation. The apparent activation energy for static recrystallisation during hot deformation for different steels was calculated to be around 225-268 kJ/mol. The t50 equations were used to estimate the interpass time during the final hot-rolling schedule and the recrystallised grain size after each pass was also estimated.

The rough rolled plates for different compositions were reheated and final hot-rolled at different finish rolling temperatures e.g. at ~1050°C (Isothermal TMCP), ~850°C (HT-TMCP), ~550°C(MT-TMCP) and ~400°C (LT-TMCP) down to 12mm plates followed by isothermal holding and simulated coiling at 350°C. Some plates were hot-rolled down to 3mm sheets with 850°C finish rolling temperature and similarly followed by isothermal holding and simulated coiling at 350°C and 325°C. MT-TMCP and LT-TMCP for 3mm final thicknesses were carried out via plane-strain compression testing. The major challenges that were faced during such pilot scale rolling trials could be summarized as:

- Difficult control of the water cooling after the finish rolling pass and before the coiling at temperatures <400°C due to Leidenfrost effect, particularly for the 12mm final thicknesses. This resulted into variable cooling stop temperature and variable transformation start temperatures among the plates.
- Variable isothermal holding time among the plates before the start of coiling furnace simulation.
- High rolling loads during MT-TMCP and LT-TMCP rolling of 12mm thicknesses at low temperatures.
- Water cooling before the last LT-TMCP pass at low temperature (~400C) was not possible to avoid roll damage due to hard martensite formation at plate surfaces if plates were cooled by water.
- Free-air cooling rate (0.7-1.0°C/s) before last LT-TMCP pass at low temperature (~400°C) risks possible ferrite formation before coiling.
- During LT-TMCP, temperature of the plates increased during rolling passes at low temperatures due to intense rolling pressure.
- Low coiling temperatures <325°C may lead to martensite formation at coil surfaces before the bainite transformation could finish during coiling.

In terms of detailed microstructural investigation for final TMCP rolled plates, reconstructed prior austenite (PA) grains via EBSD showed recrystallised prior austenite grains for isothermal-TMCP rolled plates while unrecrystallised pancaked prior austenite grains for HT, MT and LT -TMCP rolled plates. Degree of pancaking increased with decreasing finish rolling temperature. The final microstructures are predominantly bainitic with retained austenite as well as comprised of negligible to varying degree of martensite fractions. TEM investigations showed presence of 100-400nm thick bainite laths with cementite precipitates within as well as 15-100nm thick interlath films of retained austenite. Bulk hardness ranging from 350HV to 600HV were obtained on the final 12mm plates or 3mm sheets, depending on different TMCP. Hardness increased and retained austenite fraction decreased with decreasing isothermal holding temperature or, coiling temperature as well as increasing isothermal holding time for the 3mm sheets. HT-TMCP and MT-TMCP plates have comparable hardness (420-550HV) at 350°C coiling temperature. The 12mm LT-TMCP plates have the lowest hardness (350-450HV) and high retained austenite fraction (24-36%) mainly due to mechanical stabilization of austenite at low temperatures as well as due to a slow free-air cooling before the last hot-rolling pass.

In terms of microalloyed precipitation analysis by inductively coupled plasma-optical emission spectrometer, approximately half of the total Nb is precipitated in the final TMCP plates while V precipitation is negligible.

In terms of detailed mechanical property characterisation, ultimate tensile strength varied from 1.3GPa to 2.0GPa with total elongation ranging around 27% to 4% respectively. Tensile properties of HT and MT-TMCP plates are comparable. The 12mm LT-TMCP plates have relatively low UTS ~1.3-1.5GPa but the total elongation is quite high ~20-30% compared to other TMCP rolled plates of similar strength. This is mainly related to an increased retained austenite fraction (24-36%) in LT-TMCP plates due to mechanical stabilisation of austenite. For each type of TMCP, Nb-V microalloyed compositions result into best strength-ductility combinations. In terms of Charpy impact toughness, approximately all the 12mm plates that were tested had average impact energies less than 27J at -20C while some Nb-V microalloyed HT and LT-TMCP rolled plates had average impact energies more than 27J at -20C. Although the tests have been performed at several temperatures, the brittle-ductile transition temperature cannot be estimated, as more Charpy tests at higher and lower temperatures would be required. When comparing with the charpy energies corresponding to the isothermal TMCP samples, it can be observed that only the MT-TMCP, characterized by having larger fractions of martensite (and lower retained austenite) than the rest of the samples, only exceeds 27 J (typical material testing standard) at 100ºC, whereas the HT and LT-TMCP have superior behaviour, in ascending order.

In terms of wear resistance of these type of bainitic microstructures, dry pot wear test and ASTM G65 abrasion test results show decreasing mass loss and increasing wear resistance with increasing hardness. But results also indicate that the initial hardness may not be the only contributor describing the abrasive wear resistance, but also the fraction, location and the morphology of retained austenite too had a significant effect on the wear performance. A higher fraction of retained austenite with a high HV seems to be the optimal combination for lower wear rates. In most cases, the Al alloyed plates show the worst wear rate and Nb-V microalloyed higher carbon compositions show relatively good wear performance.

Cold bending of these kinds of steel were possible. The measured critical bending ratios of approximately 2 to 4 are at par or even better than the bending recommendations for 90° bending of commercial steels of similar hardness. The presence of a significant amount of retained austenite in bainitic microstructures provides a better bendability of these steels compared to a fully martensitic microstructure based steel.

Hole-expansion ratio (HER) was negligible (~0%) on punched holes on 3mm sheets. When tests were done with wire-eroded holes, the pre-existing damage at the edge is much smaller compared to that of the punched holes, leading to much higher hole-expansion values for example a maximum value of 75% HER was obtained on the 3mm sheets. HER is generally larger with the lower coiling temperature of 325°C compared to 350°C. The comparative HER behaviour among different composition was directly related to their tensile stress-strain behaviour.

1.2.3 Stage 3. Work Package 6. Modelling and recommendations for full-scale TMCP production.

This Stage 3 (WP6) is a final wrap up of the whole project with two distinctive objectives:

- Recommendations for full scale TMCP.
- Modelling of the thermomechanical process and the subsequent bainitic transformation.

1.2.3.i Stage 3. Main achievements

A thorough set of recommendations and considerations is provided for each one of the relevant steps involved in the TMCP proposed in this project. Thus, from slab reheating to the coiling procedures, each one of the steps are carefully revised with the final aim to safely facilitate further industrial implementation.

Using the data generated in the frame of this project in conjunction with other specific experiments different models have been generated. Thus, a coupled heat transfer, conduction and phase transformation model allowed for a realistically simulation of the austenite to bainite transformation in the steels through the plate thickness during cooling. After careful calibration of the models involved, it was possible to simulate the evolution of the fraction of generated bainite at different isothermal temperatures.

A more theoretical approach was also undertaken, in order to develop an improved bainite transformation model that allowed for estimations of industrially observed bainite transformation kinetics. The model is a step forward to existing models as it takes into account the evolution of the developing microstructure and the effect that it has on relevant thermodynamic magnitudes controlling bainitic transformation.

Taking advantage of the huge amount of data produced in the frame of the project, and also in-house provided by some of the partners, a model for the yield strength of austenite that considers not only the composition but also the effect of strain and strain rate has been created. The model has demonstrated to be robust, and applicable to a wide range of composition and temperatures, providing improvement at predicting yield strength with respect to previous models.

Finally, given the detected possibility that bainitic transformation might start during deformation, a new theoretical approach, thermodynamic based, to calculate all critical temperatures describing the temperature ranges in which stress and strain-free, stress-induced and strain induced bainitic or martensitic phase transformation can occur have been developed.

2 State of The Art Review (SoA) (WP1, ALL)

A through bibliographic search in the matter of ausforming in steels was performed for the preparation and at the beginning of this project. The results of such bibliographic study were published in an open access journal [1], which abstract reads as follows:

The major strengthening mechanisms in bainitic steels arise from the bainitic ferrite plate thickness rather than the length, which primarily determines the mean free slip distance. Both the strength of the austenite from where the bainite grows and the driving force of the transformation, are the two factors controlling the final scale of the bainitic microstructure. Usually, those two parameters can be tailored by means of selection of chemical composition and transformation temperature. However, there is also the possibility of introducing plastic deformation on austenite and prior to the bainitic transformation as a way to enhance both the austenite strength and the driving force for the transformation; the latter by introducing a mechanical component to the free energy change. This process, known as ausforming, has awoken a great deal of interest and it is the object of ongoing research with two clear aims. First, an acceleration of the sluggish bainitic transformation observed typically in high C steels (0.7–1 wt. %) transformed at relatively low temperatures. Second, to extend the concept of nanostructured bainite from those of high C steels to much lower C contents, 0.4–0.5 wt. %, keeping a wider range of applications in view.

The paper “Transferring nanoscale bainite concept to lower C contents: A perspective” [1], is an open access publication available at https://www.mdpi.com/2075-4701/7/5/159

3 Stage 1. Laboratory Scale approach.

3.1 Work Package 1. Material selection, design and casting (All)

3.1.1 Task 1.2: Chemistry design of bainitic steels (All).

A set of 15 alloys were discussed and proposed during the preparation of the proposal, see Table 1 the following “constraints” were used to narrow the range of chemical compositions:

- Apart from carbon (0.3-0.5 wt.%) Al and/or Si were used to delay cementite precipitation during bainite transformation [2].
- Microalloying with Nb and/or V not only facilitates grain size refinement, but also raises the RST appreciably to enable a large processing window for controlled rolling/deformation prior to continuous cooling down to the bainite transformation temperature. Alloying with Nb and V might also induce some strain induced precipitation.
- Mn (<2 wt.%) and Cr (<1wt.%) was used to increase the hardenability, while keeping in mind segregation related problems at higher concentrations.
- To avoid the formation of carbonitrides in the steels, the desired nitrogen content would be as low as 10ppm. However, sufficiently low N content cannot be achieved industrially without extra effort, so the formation of the carbonitrides should be minimized with optimization of the rolling practice.
- Lean, inexpensive steel chemistry with a rational use of raw materials, not only for sustainable development but also for cost reasons.

Table 1. Initial proposal of chemical compositions based on initial reflections, all in wt.%.

No		ID	C	Si	Mn	Mo	Cr	V	Al	Nb
1	R-C	1	0.3	1.3	2	0	0.7	0	0	0
2	R	2	0.4	1.3	2	0	0.7	0	0	0
3	R+C	3	0.5	1.3	2	0	0.7	0	0	0
4	R-Si+Al	4	0.4	0.8	2	0	0.7	0	1	0
5	R+Al	5	0.4	1.3	2	0	0.7	0	1	0
6	R+Si+Al	6	0.4	1.5	2	0	0.7	0	1	0
7	R+Mo	7	0.4	1.3	2	0.3	0.7	0	0	0
8	R+Mo+Nb	8	0.4	1.3	2	0.3	0.7	0	0	0.05
9	R+C+Mo+Nb	9	0.5	1.3	2	0.3	0.7	0	0	0.1
10	R-Mn	10	0.4	1.3	1	0	0.7	0	0	0
11	R+Si	11	0.4	1.5	2	0	0.7	0	0	0
12	R+Cr	12	0.4	1.3	2	0	1.5	0	0	0
13	R+V	13	0.4	1.3	2	0	0.7	0.1	0	0
14	R+Nb+V	14	0.4	1.3	2	0	0.7	0.1	0	0.05
15	R+C+Nb+V	15	0.5	1.3	2	0	0.7	0.1	0	0.05

3.1.2 Task 1.3: Theoretical Calculations. (CSIC, tkSE, OULU).

The consortium carried out different types of calculations of great value to anticipate difficulties for the aim of the project.

Thermodynamics calculations of the incomplete reaction phenomena or T_0 line [2] were performed to estimate the fraction and C content of retained austenite after bainitic transformation. Kinetics models based on phase transformation theory were used to obtain CCT and TTT diagrams [2–5]. Among other parameters, estimated by different means (empirical formulae, thermodynamic calculations [6,7], commercial software packages....) relevant temperatures as the Ac3 [8], Ms [4,8], Bs [4][9] and T_{NR} [10], were also calculated. Some examples of the results obtained by means of the described calculations are shown in Table 2 and Figure 3.

Of special relevance were the calculations performed by Oulu in terms of the segregation of the different alloying elements during casting. OULU applied IDS (Inter-Dendritic Segregation) model [11], which predicts interdendritic segregation taking into account alloy element partitioning between ferrite, austenite and liquid phases during solidification and back diffusion in the solid phases during slab or ingot cooling. Solidification theory becomes necessary as the C contents intended, 0.4-0.5 wt.%, enhances interdendritic segregation by increasing the fraction that solidifies to austenite.

After discussion of the results, some considerations were made:

- The alloys with Al, 4 to 6, present very high Ae3 temperatures, and it is expected that the rolling forces are also high. There is also the possibility of the formation of ferrite during rolling. It was reminded that when Si is not present in sufficient quantities, the addition of Al was necessary to avoid cementite precipitation during bainitic transformation. It was agreed to take the opportunity to evaluate the influence of Al [2].
- The calculated T_{NR} temperatures were disregarded as unusually low temperatures for some of the steels were obtained, it was decided that decisions won't be made on the basis of such

calculations, as most of the T_{NR} expressions found in literature are very specific or to a particular set of chemicals compositions, and very different to the ones used in this project.

- From the discussion on TTT and CCT [4,5] diagrams it was clear that in some cases, mainly those with low C and low Mn, faster cooling rates were necessary to avoid the ferrite/pearlite nose, though technically doable within the installations to be used.
- In most of the steels there is a region around 500ºC, between the two C-curves of ferrite and bainite phase fields, where it is possible to carry out the desired MT-TMCP.

As it is not a regular industrial practise to homogenize the steels in order to minimize the chemical composition related segregation during casting and solidification, calculations were performed that could anticipate this type of problems, using the IDS software from Aalto University [11].

According to such calculations, examples of which are shown in Figure 4 (OULU, tkSE) :

- -Given the high C content of the alloys it is expected that, during solidification, a high fraction of austenite forms. Thus, and given the different solubility and diffusion coefficients of the phases involved, viz., austenite, delta ferrite and liquid, it is anticipated that Mn, Mo and Cr will remain heterogeneously distributed after casting, which will lead to regions with very different hardenabilities.
- -The most important concern was about the Nb solubility. It was shown (OULU) and later confirmed (tkSE) that of the two levels of Nb levels originally selected of 0.1 & 0.05 (alloys 8,9,14 & 15) and 0.1 (alloy 9), most of that Nb will precipitate in the interdendritic regions during solidification forming particles that will impair toughness.

Table 2. Specific values of some of the calculations performed according to the references provided in the main body of the text.

	ID	Bs (ºC)	Ms (ºC)	Tdiff (s)	tBs (s)	To at 400ºC	Austenite YS at 350ºC (MPa)	Ae1 (ºC)	Ae3 (ºC)	T_{NR} (ºC)
R-C	1	430	320	67	13	0.023	109.3	751.3	789.2	562
REF (R)	2	365	275	170	36	0.023	128.4	751.3	772.0	608
R+C	3	310	230	350	180	0.023	147.5	751.3	756.9	654
R-Si+Al	4	480	310	11	93	0.0273	123.0	736.7	1149.7	1150
R+Al	5	480	310	8.9	94	0.0273	128.4	751.3	1172.0	971
R+Si+Al	6	480	310	7.9	95	0.0273	130.6	757.1	1181.0	900
R+Mo	7	355	270	190	48	0.0225	130.8	751.3	781.5	608
R+Mo+Nb	8	355	270	190	48	0.0225	130.8	751.3	781.5	786
R+C+Mo +Nb	9	300	225	410	260	0.0225	149.9	751.3	766.3	1095
R-Mn	10	495	325	11	4.9	0.0286	128.4	762.0	802.0	608
R+Si	11	365	275	150	36	0.023	130.6	757.1	781.0	537
R+Cr	12	310	255	530	220	0.0207	130.0	764.8	763.2	608
R+V	13	350	270	200	54	0.0224	128.4	751.3	782.4	609
R+Nb+V	14	350	270	200	54	0.0224	128.4	751.3	782.4	787
R+C+Nb +V	15	300	225	430	260	0.0224	147.5	751.3	767.3	833

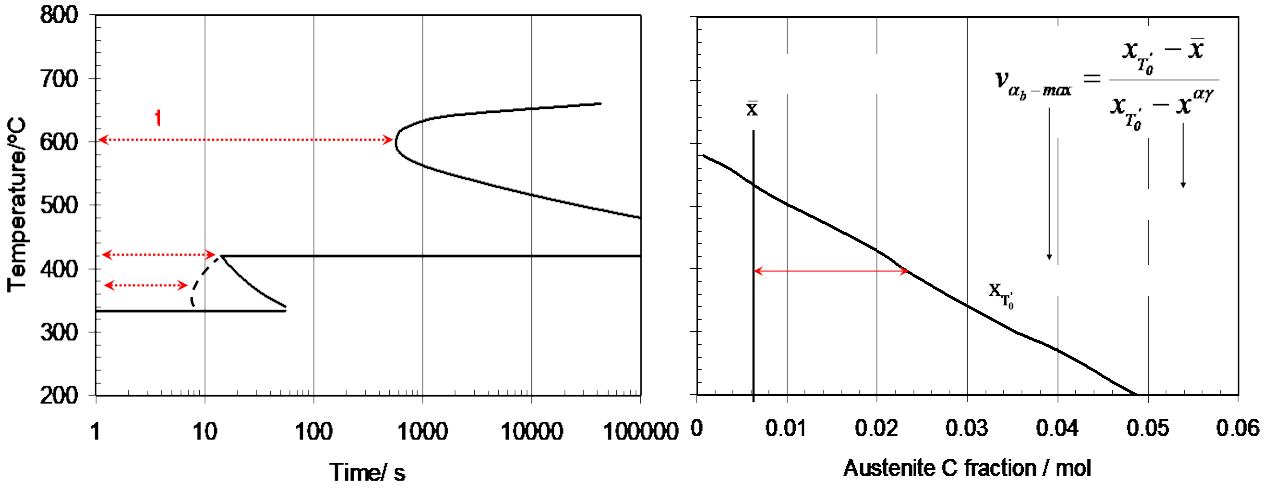

Figure 3. Examples of the type of theoretical calculations, mainly related with bainitic transformation, and the parameters used in decision-making, Task 1.3 & Task 1.4.

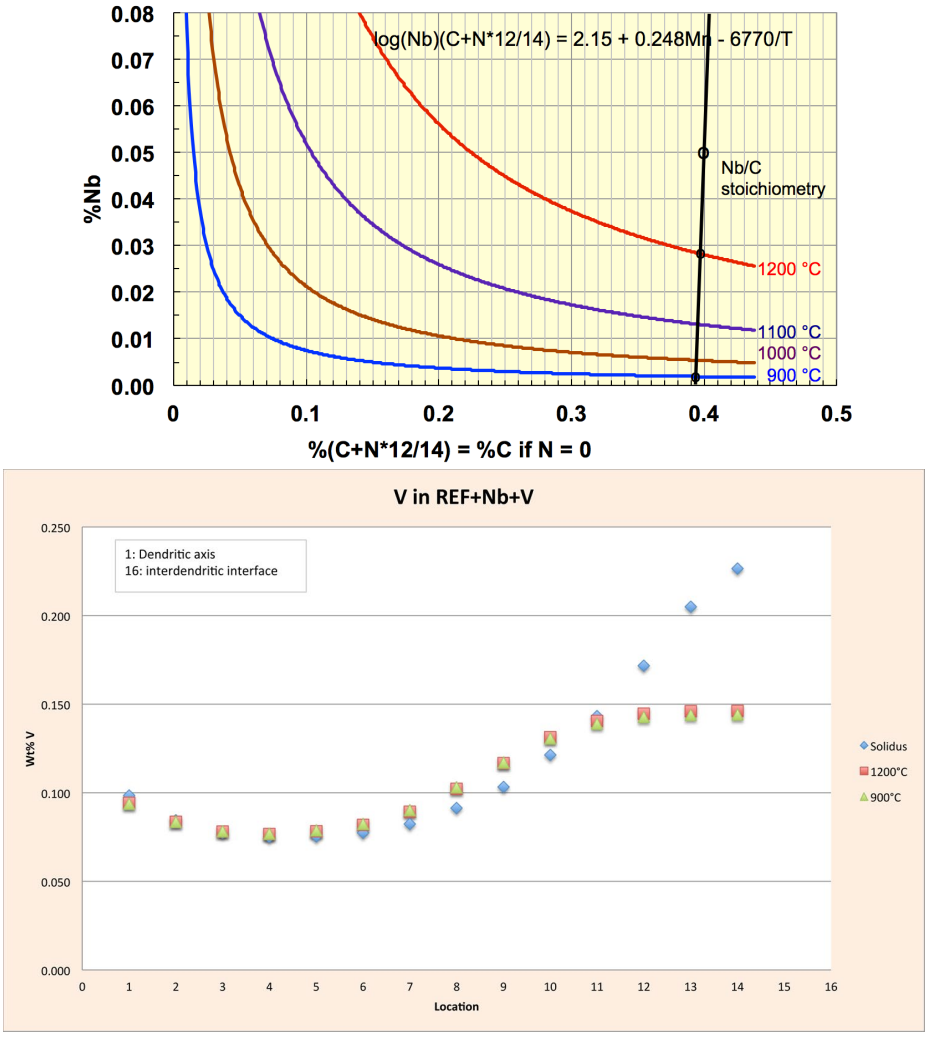

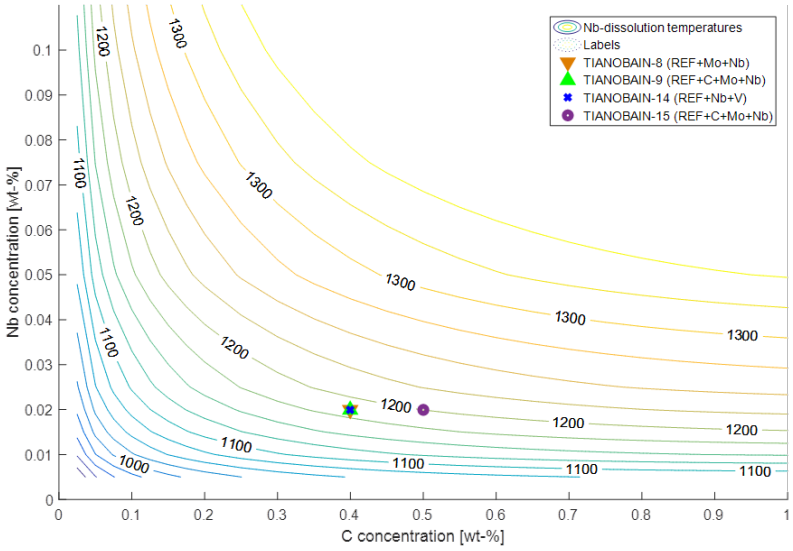

Figure 4. Examples of the type of theoretical calculations, related with segregation and dissolution during solidification and afterwards used for decision-making in Task 1.3 & Task 1.4.

3.1.3 Task 1.4: Selection of Grades. (ALL).

On the basis of the reported information, it was decided to reduce the Nb content down to 0.02 wt.% to avoid the above mentioned problems and still to have an acceptable processing window for controlled rolling/deformation prior to continuous cooling down to the bainite transformation temperature. The final selection of chemical compositions is shown in Table 3.

Table 3. Final proposal of chemical compositions to be casted, all in wt.%.

No		ID	C	Si	Mn	Mo	Cr	V	Al	Nb
1	R-C	1	0.3	1.3	2	0	0.7	0	0	0
2	R	2	0.4	1.3	2	0	0.7	0	0	0
3	R+C	3	0.5	1.3	2	0	0.7	0	0	0
4	R-Si+Al	4	0.4	0.8	2	0	0.7	0	1	0
5	R+Al	5	0.4	1.3	2	0	0.7	0	1	0
6	R+Si+Al	6	0.4	1.5	2	0	0.7	0	1	0
7	R+Mo	7	0.4	1.3	2	0.3	0.7	0	0	0
8	R+Mo+Nb	8	0.4	1.3	2	0.3	0.7	0	0	0.02
9	R+C+Mo+Nb	9	0.5	1.3	2	0.3	0.7	0	0	0.02
10	R-Mn	10	0.4	1.3	1	0	0.7	0	0	0
11	R+Si	11	0.4	1.5	2	0	0.7	0	0	0
12	R+Cr	12	0.4	1.3	2	0	1.5	0	0	0
13	R+V	13	0.4	1.3	2	0	0.7	0.1	0	0
14	R+Nb+V	14	0.4	1.3	2	0	0.7	0.1	0	0.02
15	R+C+Nb+V	15	0.5	1.3	2	0	0.7	0.1	0	0.02

3.1.4 Task 1.5: Production of Material. (OCAS).

The 15 steels in Table 3 were casted in a laboratory induction casting furnace under N_2 atmosphere, in a series of 3 consecutive cast ingots with a weight of about 30kg for each ingot (135mm x 135mm x 200mm). After removal of the 'head' of the ingots (which contained shrinkage holes), approximately 20kg of material for each incremental cast, remained available for rolling. Where chemical compositions did not allowed for incremental casting, full casts of about 100kg (250mm x 250mm x 200mm) where prepared. After removal of the 'head' which contained shrinkage holes, approximately 60kg of material for each full casts remained available for rolling. P and S level was in all cases < 0.005 and < 0.002 wt.% respectively.

Given the high levels of C and Mn, a significant segregation of those elements was expected during solidification of the ingots. Therefore, all blocks were annealed at 1250°C under N_2 atmosphere for 24 h to promote elemental diffusion and reduce the segregation, Figure 5.

Then, blocks with a thickness of 45mm were cut from the cast ingots to be lab rolled into plates of about 12mm thickness. These plates serve as feed-stock for the production of dilatometry and also hot compression samples for WP2.

Prior to rolling, the blocks have been reheated to 1250°C. Hot rolling down to a thickness of 12mm was done in 5 passes to break up the as-cast structure and refine the grain size. After rolling, the blocks were quenched in water to avoid grain growth during cooling. For the Nb (and V) containing alloys, the blocks were rolled to a thickness of 18mm, and reheated to 1250°C before applying the final rolling pass, Figure 5. This was done to re-dissolve any strain induced precipitation of Nb and V. As such, no additional precipitation dissolution reheating is needed prior to the dilatometer tests and the starting austenite grain size will be smaller than in the case such a treatment would have been applied.

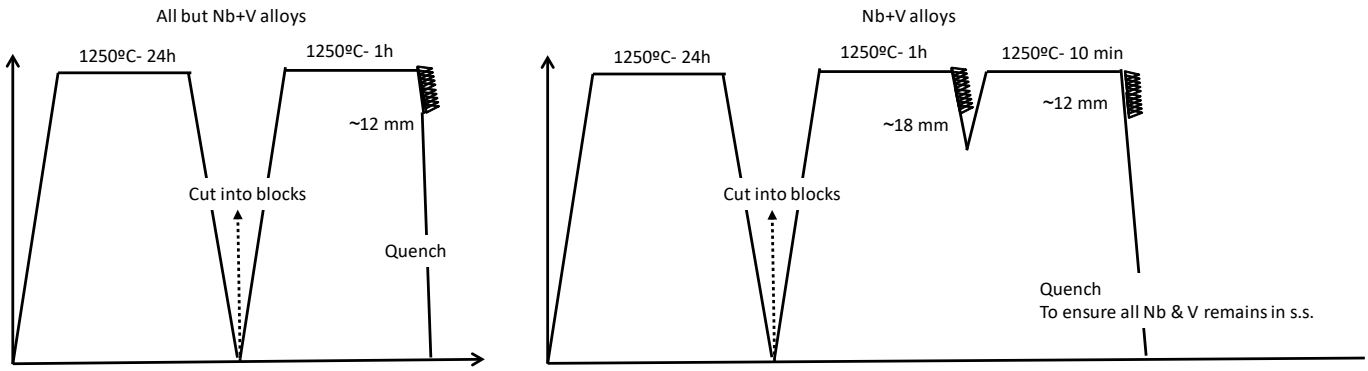

Figure 5. Scheme of the applied homogenisation and rolling procedures.

Inclusion analysis was performed in selected alloys with the purpose of ruling out anomalies that might interfere with results later. The study was performed in the R+Cr, R-C & R+C and R-Si+Al & R+Si+Al alloys, Table 3. Al bearing alloys were also selected, as they might be more prone to Al oxide formation.

A non-metallic inclusions analysis was performed using a PSEM (Personal Scanning Electron Microscope) manufactured by R. J. Lee, USA. In addition to a conventional SEM the PSEM is also equipped with an EDX analyzer, which allows a detailed information about the inclusion composition. Using a self-developed software (tkSE) that it offers the possibility of a fully automatic search and analysis of the inclusions, an overview of the number density and the volume fraction of the relevant inclusion types as well as an overview of the size distribution of the inclusions can be created. A surface section of approximately 50 mm^2 was investigated.

The inclusions analysis was within normal values and therefore it hasn't got an influence on the studies performed in the following WP.

The number density and volume fraction of the identified inclusions in the five investigated steels are shown in Table 4. The lower limit of the detected inclusion diameter was 1 µm. All steels contained aluminium oxides, manganese sulfides and Al_2O_3-MnO-Spinel. With the addition of Al in the steels R(±Si)+Al, aluminum nitrides too were found, leading to a significant increase of the total number density and volume fraction of inclusions. However, the amount of aluminium oxides did not increase with the addition of Al. Due to the casting on a laboratory scale no inclusions from basic slag could be found (e.g. very few calcium and magnesium oxides were found).

The steels R-C and R+C were part of an incremental cast as well as R-Si+Al and R+Si+Al. Only the amount of aluminium oxides decreased from the first (R-C, R-Si+Al) to the last part of the incremental cast (R+C, R+Si+Al). Thus, the influence of the incremental casting on the inclusion composition is weak. The single cast R+Cr did not differ significantly from the incremental casts, apart from higher amounts of aluminium oxides of the order of the R(±Si)+Al steels.

Using the PSEM, the size distribution of the inclusion density was also determined, and it showed that the inclusion density rapidly decreased with increasing inclusion size, and almost no inclusions larger than 5 µm were found. Taking into account the volume fraction and the size distribution of the inclusion, no influence of the inclusions on the results of task 2 was expected.

Table 4. Number density and volume fraction of inclusions in the steels R-C, R+C, R-Si+Al, R+Si+Al and R+Cr. The results were obtained with a PSEM.

Steel:	R-C		R+C		R-Si+Al		R+Si+Al		R+Cr	
Inclusion	n/cm²	V	n/cm²	V	n/cm²	V	n/cm²	V	n/cm²	V
> 80% Al_2O_3	846,9	17,84	443,3	11,67	613,4	30,76	154,6	6,98	1435,9	30,75
Al_2O_3 with MnS	368,8	11,19	241,7	5,35	155,6	7,72	140,1	6,01	395,3	9,28
Al_2O_3 with TiN	12,5	0,18	16,7	0,46			6,2	0,23	6,3	0,18
MgO-Al_2O_3-Spinel			1,7	0,03					14,1	0,19
MgO-Al_2O_3-Spinel with MnS									3,1	0,07
Calcium aluminates 20-40% CaO	3,1	0,12								
Al_2O_3-MnO-Spinel	795,3	10,91	565,0	8,65	194,1	3,87	92,7	2,17	968,8	12,77
Manganese sulfid	1040,6	43,52	1345,0	37,28	831,3	30,19	638,9	16,93	1065,6	44,72
Titanium nitrides	3,1	0,06	13,3	0,25					12,5	0,36
Alumnium nitrides					10519,9	263,60	10223,8	240,95		
Alumnium nitrides with MnS					831,3	26,47	3219,0	93,78		
Alumnium- + Titanium nitrides							6,2	0,15		
Al and Ti nitrides + Mn sulfides					1,8	0,02				
Mn sulfid + Ti nitrid	9,4	0,18	1,7	0,03					4,7	0,17
total	3079,7	84,00	2628,4	63,72	13147,4	362,63	14481,5	367,20	3906,3	98,49
Measuring area in mm²:	64,0		60,0		54,6		48,5		64,0	

n = number
V = Volume fraction in ppm

3.2 Work Package 2. Physical simulation and potential ausforming processing

3.2.1 Task 2.1: Evolution of austenite strength with temperature (OULU).

The aim of this task is to determine the evolution of austenite strength with temperature. This knowledge is essential for studying the feasibility of the ausforming process. While HT-TMCP uses more traditional controlled rolling in the no-recrystallization regime above A_{r3} temperature and cooling prior to bainite transformation. In the case of LT/MT-TMCP there might be a limiting factor could be the excesive increase in flow stress with decreasing temperature, which can cause the rolling loads to rise too high.

Four compositions, based on Oulu previous experiences, were selected to determine the austenite strength in the controlled rolling /ausforming regime. Steel R was selected, as it is the reference steel. Aluminium is known to affect flow stress of austenite at lower temperatures, therefore R+Al was selected. The effect of Nb is studied by selecting the R+Mo+Nb and R+C+Nb+V. Mo and V might have a minor effect.

The strength of austenite was studied via single-hit compression tests using a Gleeble 3800 thermo-mechanical simulator, on cilindrical samples of ø8x10mm . The compression tests were performed in the temperature range 900 -300°C in steps of 100°C. The effect of strain rate was taken into account by using three different strain rates: 10, 1 and 0.1s^{-1}. A total strain of 0.6 was aimed for. Austenitization temperatures were selected as 1100°C for the microalloyed (R+Mo+Nb and R+C+Nb+V) and 1000°C for the non-microalloyed (R and R+Al) steels. The selection of higher temperature for the R+Mo+Nb and R+C+Nb+V steels is related to the need for Nb to be in solution. The remaining parameters are shown in Figure 6.

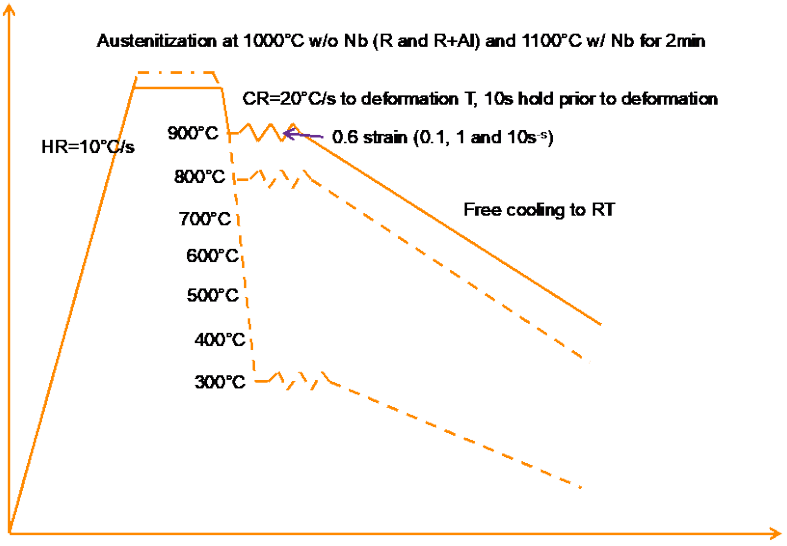

Figure 6. The Gleeble-program used for the austenite strength tests.

Mean flow stress (MFS) is the most important material parameter corresponding to the strength of the material, when calculating the rolling loads. It can be calculated from the area under a given stress-strain curve for a selected strain interval as given in Eq. 1.

$$MFS = \frac{1}{\varepsilon_1 - \varepsilon_0} \int_{\varepsilon_0}^{\varepsilon_1} \sigma \, d\varepsilon \qquad \text{Eq. 1}$$

where ε_0 is strain at the start and ε_1 strain at the end of the selected interval and σ is the stress. Mean flow stress can be approximately estimated as shown in Eq. 2.

$$MFS \approx \frac{1}{\varepsilon_1 - \varepsilon_0} \times \sum_{\varepsilon_0}^{\varepsilon_1} (\varepsilon_b - \varepsilon_a) \times \frac{(\sigma_a + \sigma_b)}{2} \qquad \text{Eq. 2}$$

where ε_a is strain at the start and ε_b strain at the end of each increment, σ_a and σ_b are the corresponding stresses. This estimation was used in this research, to simplify the effort and the calculation tools used.

3.2.1.i Temperature during strain

The Gleeble is programmed to keep the specimen temperature constant during the compression by constantly supplying requisite electric current (power) through the resistance-heated sample to balance the loss of heat by conduction to the water cooled anvils and radiation to the surrounding vacuum; however, rapid internal heat generation can cause the specimen temperature to deviate from the aimed control value.

A significant rise in temperature during straining was observed at temperatures below 600°C with strain rates 1 and 10 s^{-1}. An example of the variation of temperature with strain at different deformation temperatures in the range 900-300°C for R+Al steel is shown in Figure 7. The magnitude of the temperature rise is very high at the lower straining temperatures, the highest being an increase from 300°C to 380°C at 0.6 strain.

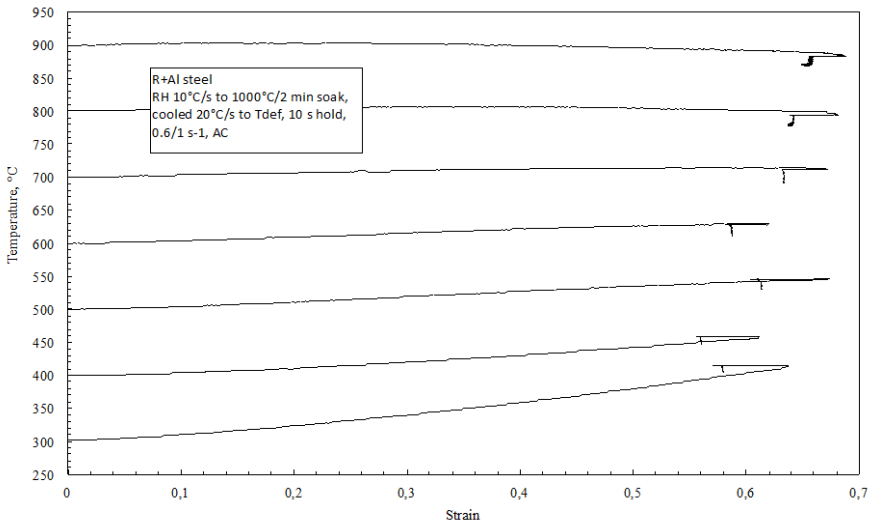

Figure 7. An example of the temperature rise during strain at $1s^{-1}$.

The rise in temperature is believed to be mainly due to latent heat released during phase transformation occurring during the straining, even though adiabatic heating due to the work of deformation may also make a contribution to the increase in temperature at 10 s^{-1}. Calculations based on literature data for latent heat of transformation and specific heat [12,13] indicate that large increases in temperature due to phase transformation during straining are feasible.

Following discussion held to ascertain the cause of the temperature rise during straining at low temperatures (300–400°C), quenching experiments (Figure 8) were planned and conducted to study the microstructure after deformation at different temperatures (700°C, 600°C, 500°C and 400°C). Materials selected for the tests were steels R and R+Mo+Nb. Deformation to 0.6 strain at strain rate of $1s^{-1}$ was followed by immediate quenching in water to room temperature. Microstructures were then revealed by etching with 2% Nital

etchant for 5–10 seconds. Phase transformation from austenite to martensite was expected to occur during quenching, but microstructural characterization was done to reveal possible formation of ferrite or bainite.

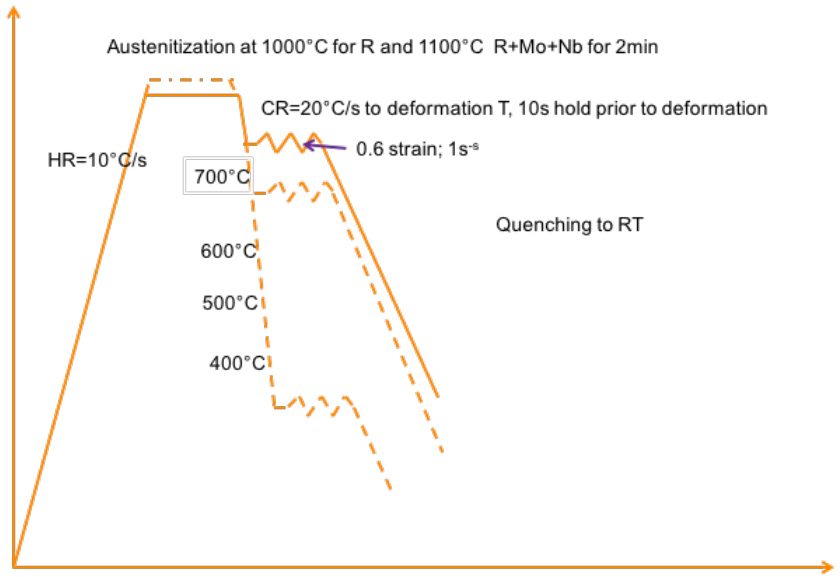

Figure 8. Construction of the quenching test designed to study the microstructure after deformation.

Examples of the microstructures obtained in both steels after deformation at 400ºC followed by quenching to room T, are shown in Figure 9. It is evident that some bainitic sheaves are visible in an essentially martensitic matrix, a similar situation is reproduced after deformation at 500ºC but with smaller amount of bainite. In neither case was ferrite observed in the microstructure.

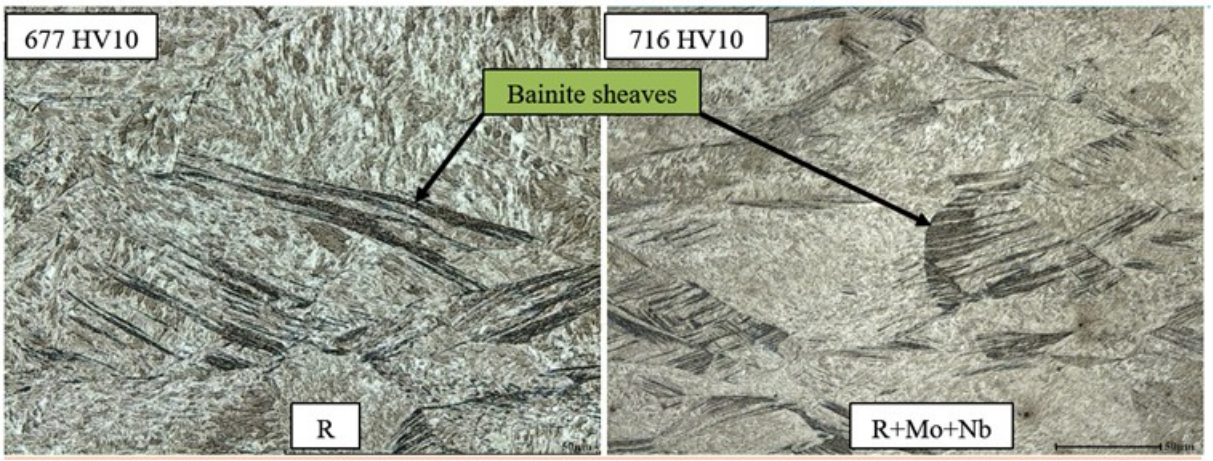

Figure 9. Quenched microstructures after deformation at 400°C.

Microstructures of quenched samples following deformation at 700°C are shown in Figure 10. Unlike in the case of samples deformed at 400°C, no clear traces of either bainite or ferrite were found in the microstructures of samples deformed at 600°C or 700°C. Hardness of the samples did not significantly vary from each other regardless of the deformation temperature.

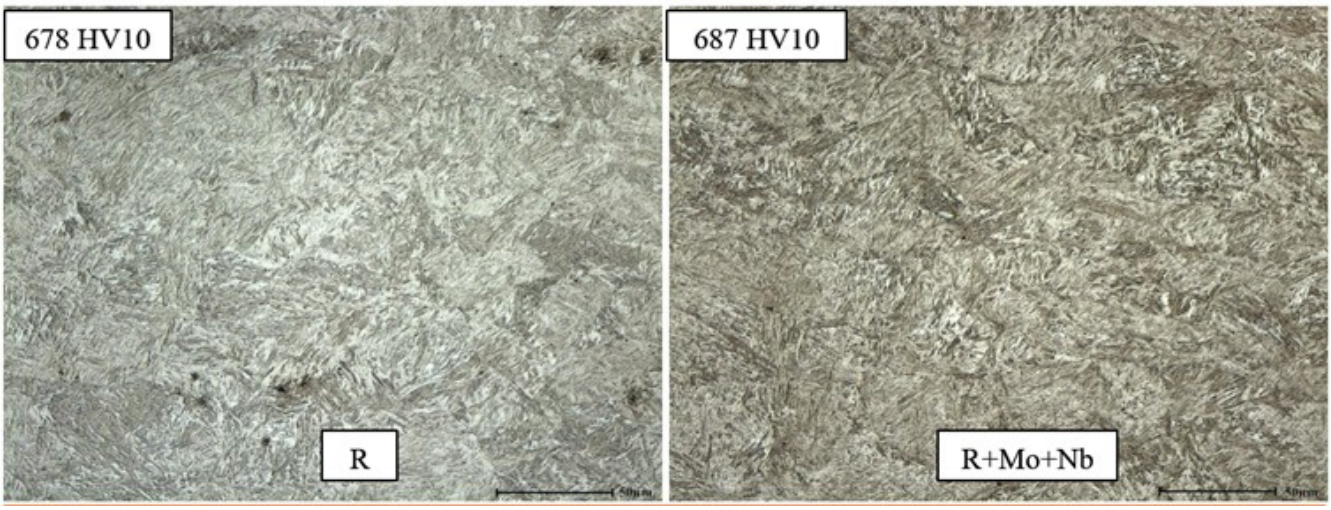

Figure 10. Quenched microstructures after deformation at 700°C.

3.2.1.ii True stress - true strain

An example of the typical true stress-true strain curves plotted from the Gleeble data are presented in Figure 11 for the R alloy. The Figure is divided into three individual graphs (a-c) depicting flow stress behaviour at the three different strain rates.

From Figure 11 it can be seen that with strain rates $1s^{-1}$ and $10s^{-1}$ the stress levels increase quite linearly with decreasing temperature, as expected, and the shape of the curves remains by and large the same. With a strain rate of 0.1 s^{-1}, the shape of the curves at temperatures 300°C and 400°C differs from the rest. Approximately at 0.25 to 0.3 strain, the stress levels start to increase more rapidly, marked by inflexion in the curves. This is a clear indication of phase transformation taking place during straining. The austenite is transforming to a stronger phase (bainite), which causes an additional increase in flow stress required for a certain strain.

The same can be said about the flow stress behaviour of R+Al, but for the Nb-bearing steels the effect is not that significant at 400°C. Note that Nb may have an influence on the bainitic transformation, but the effect may not be as pronounced as that of C, Mo and Mn, therefore the influence of Nb may not be discernible in presence of other elements with a strong influence.

This suggests that for the steels R+Mo+Nb and R+C+Nb+V the bainite transformation is slower at 400°C, presumably as a consequence of the strong effect of Mo and C in delaying bainitic transformation [2].

To understand the effect of temperature on the flow stress behaviour in these materials, stress-strain curves at different strain rates were plotted at various temperatures. An example of these plots is presented in Figure 12 for R+C+Nb+V steel showing plots at 800, 600 and 400°C. As expected, the sensitivity to strain rate change increases with increasing temperature, so that higher strain rate results in higher flow stress. At 300°C and 400°C the test materials seem to be least sensitive to strain rate. Note that at the strain rate of 0.1 s^{-1} the stress at high strain is affected by phase transformation

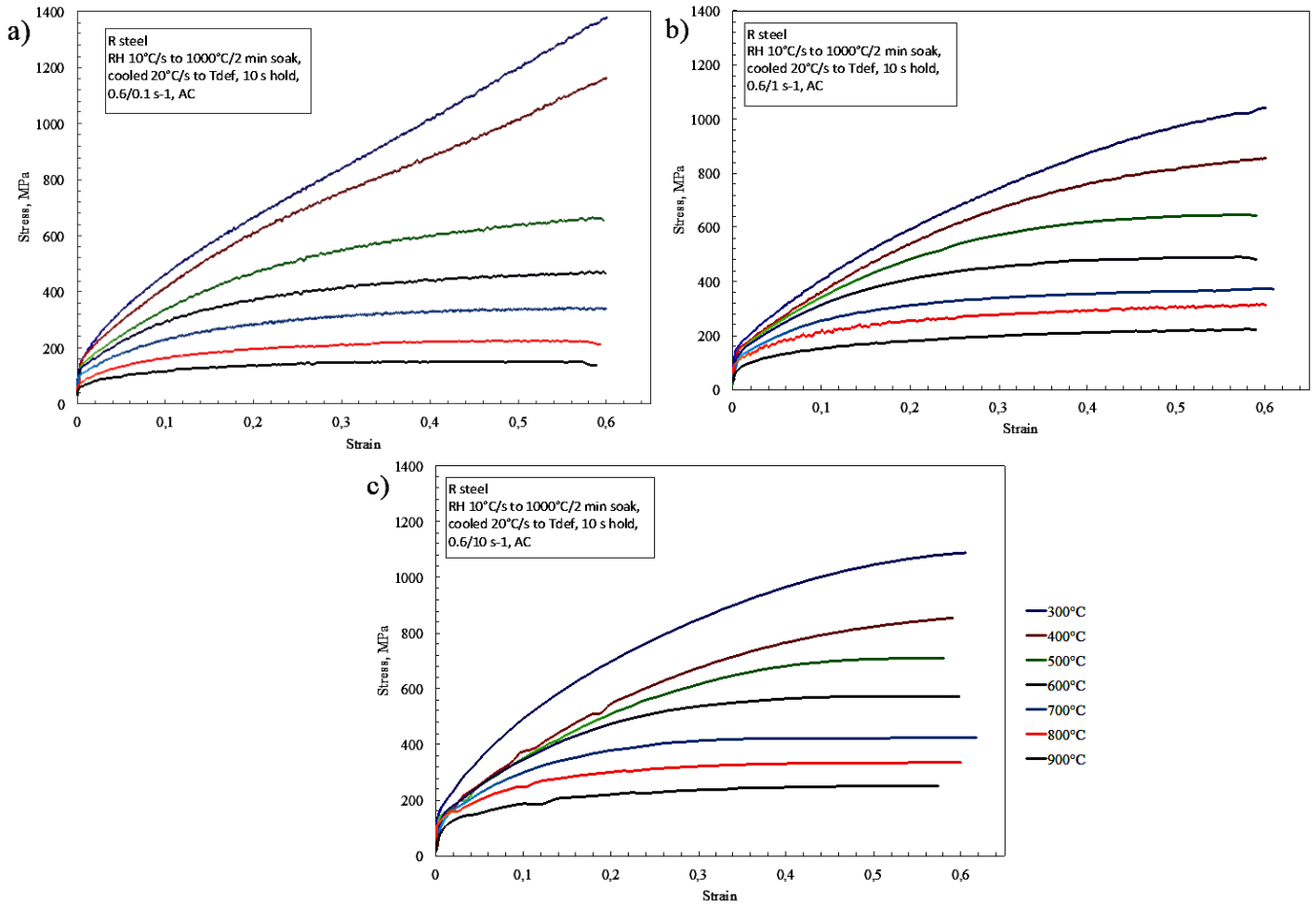

Figure 11. True stress - true strain curves with strain rates a) $0.1s^{-1}$, b) $1s^{-1}$ and c) $10s^{-1}$ for steel R.

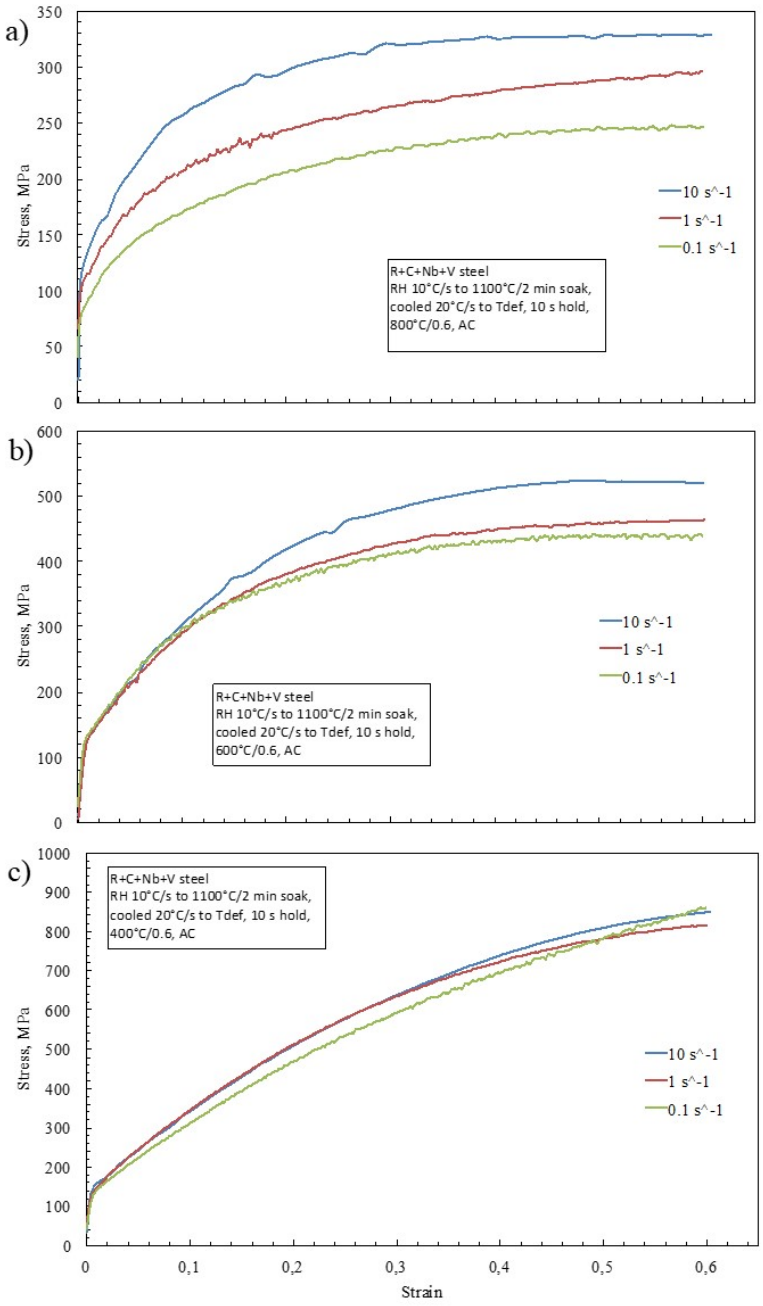

Figure 12. Effect of strain rate at a) 800°C, b) 600°C and c) 400°C for steel R+C+Nb+V.

3.2.1.iii Strain hardening rate

To highlight the effect of temperature with 0.1 s^{-1} strain rate on the work hardening, the work hardening rates (WHR) and strain hardening exponents (n) were calculated and plotted for steel R+Al.

WHR and n can be derived from the Hollomon's equation [14]:

$$\sigma = K\varepsilon^n \qquad \text{Eq. 3}$$

where K is a constant, σ is stress and ε is total strain. n can be derived as a function of stress and strain:

$$n = \frac{d\ log(\varepsilon)}{d\ log(\sigma)} = \frac{\varepsilon}{\sigma}\frac{d\sigma}{d\varepsilon} \qquad \text{Eq. 4}$$

WHR $d\sigma/d\varepsilon$ can then be written:

$$\frac{d\sigma}{d\varepsilon} = n\frac{\sigma}{\varepsilon} \qquad \text{Eq. 5}$$

The plotted WHR vs. true strain curves at temperatures 300°C and 400°C differ from the rest (Figure 13). At higher temperatures WHR keeps decreasing or reaches a plateau with increasing strain up to 0.6. At 300°C and 400°C there is a slight increase after approximately 0.25 to 0.3 strain and the WHR remains at a higher level compared to the rest of the curves at higher temperatures. The same rise can be seen in the plotted n-exponents in Figure 14. This phenomenon again implies occurrence of phase transformation during straining.

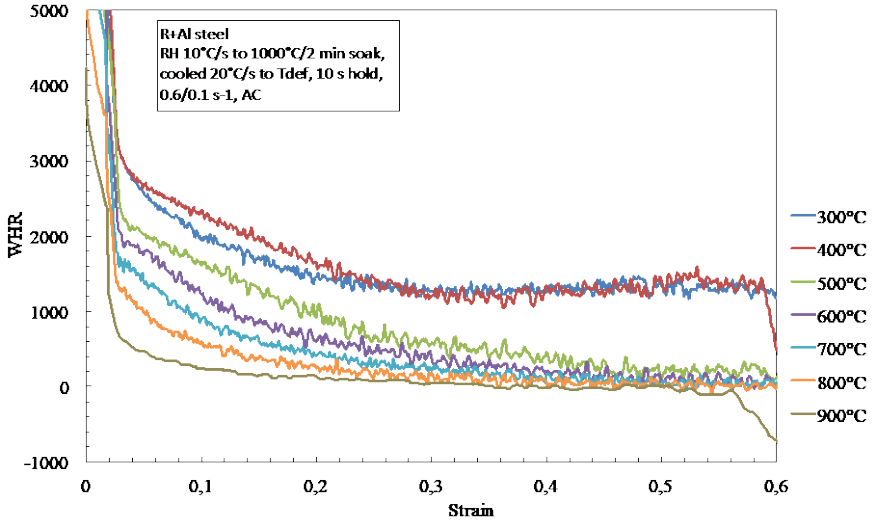

Figure 13. WHR-curves at different temperatures with $0.1s^{-1}$ for steel R+Al.

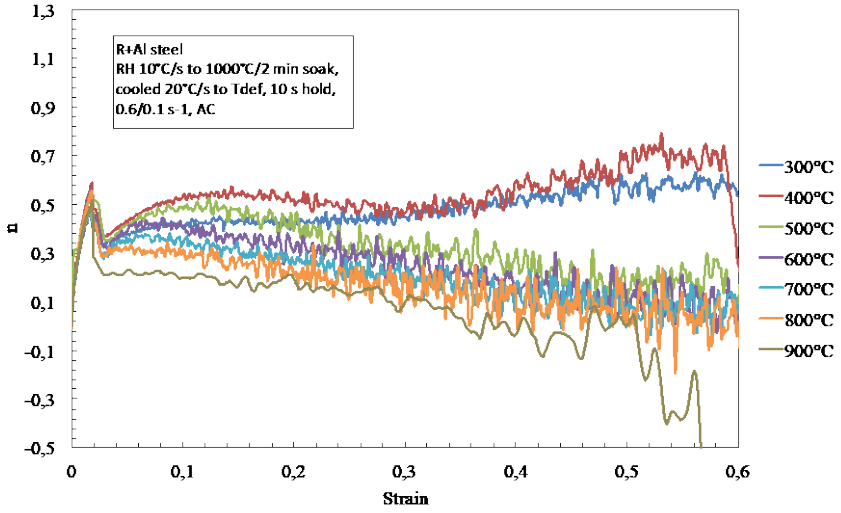

Figure 14. Work hardening exponent -curves at different temperatures with $0.1s^{-1}$ for steel R+Al.

3.2.1.iv Mean flow stress

An example of the evolution of MFS with inverse absolute temperature at different strains is presented in Figure 15 for R+Mo+Nb steel tested at different strain rates. The rise in temperature at strain rates 10 s^{-1}

and 1 s^{-1} during straining is taken into account by plotting the MFS against the real measured temperature. The plots are only up to 0.5 strains, due to problems in keeping the strain rate constant till the end of the compression.

Figure 16 was plotted to highlight the fact that even though the bainitic transformation would occur at a certain strain with lower strain rates, the MFS can still be at the same level or slightly lower with a higher strain rate. This means that the average stress needed for a certain strain is not necessarily higher when phase transformation is occurring at the end part of the strain.

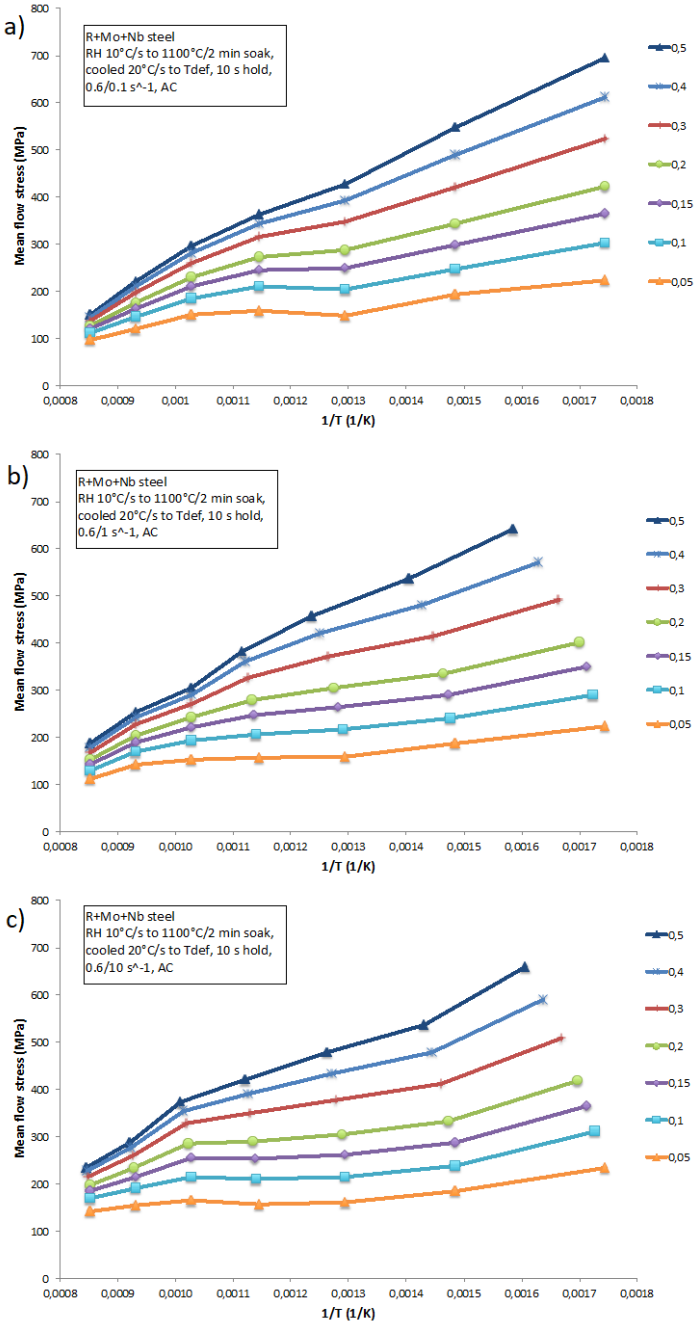

Figure 15. Plotted MFS - 1/T curves for different strains with strain rates a) 0.1s-1, b) 1s-1 and c) 10s-1 steel R+Mo+Nb.

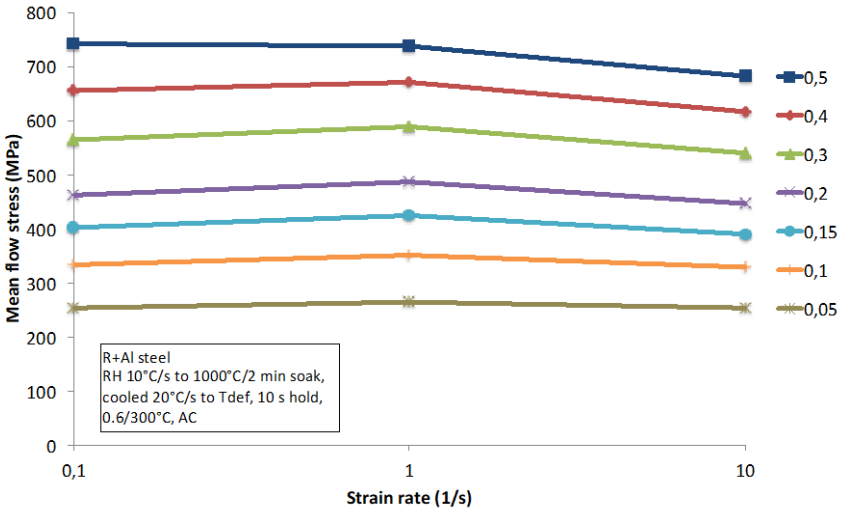

Figure 16. The effect of strain rate on MFS at 300°C on steel R+Al.

In Figure 17 all of the steels are plotted in the same diagrams to show the differences in mean flow stress behaviour at strains 0.2 and 0.4. However, no clear picture of how composition affects the flow stress behaviour is apparent. The original idea was to compare the austenite flow stress and the compositions were selected based on that assumption. The onset phase transformation restrict the comparison of austenite strength to temperatures from 500°C to 900°C. In that temperature range, Al raises the MFS slightly. At lower temperatures, the comparison is hard, as there is no real record of the microstructure produced and the amount of different phases can vary between compositions.

Generally speaking, it can be concluded from this study that:

- There might be some phase transformation (bainite) induced by deformation at T in the range 300-400ºC.
- Al has a significant effect on the flow stress at relatively low T.
- Nb has a more moderate effect
- Mo and V have a relatively lower effect.

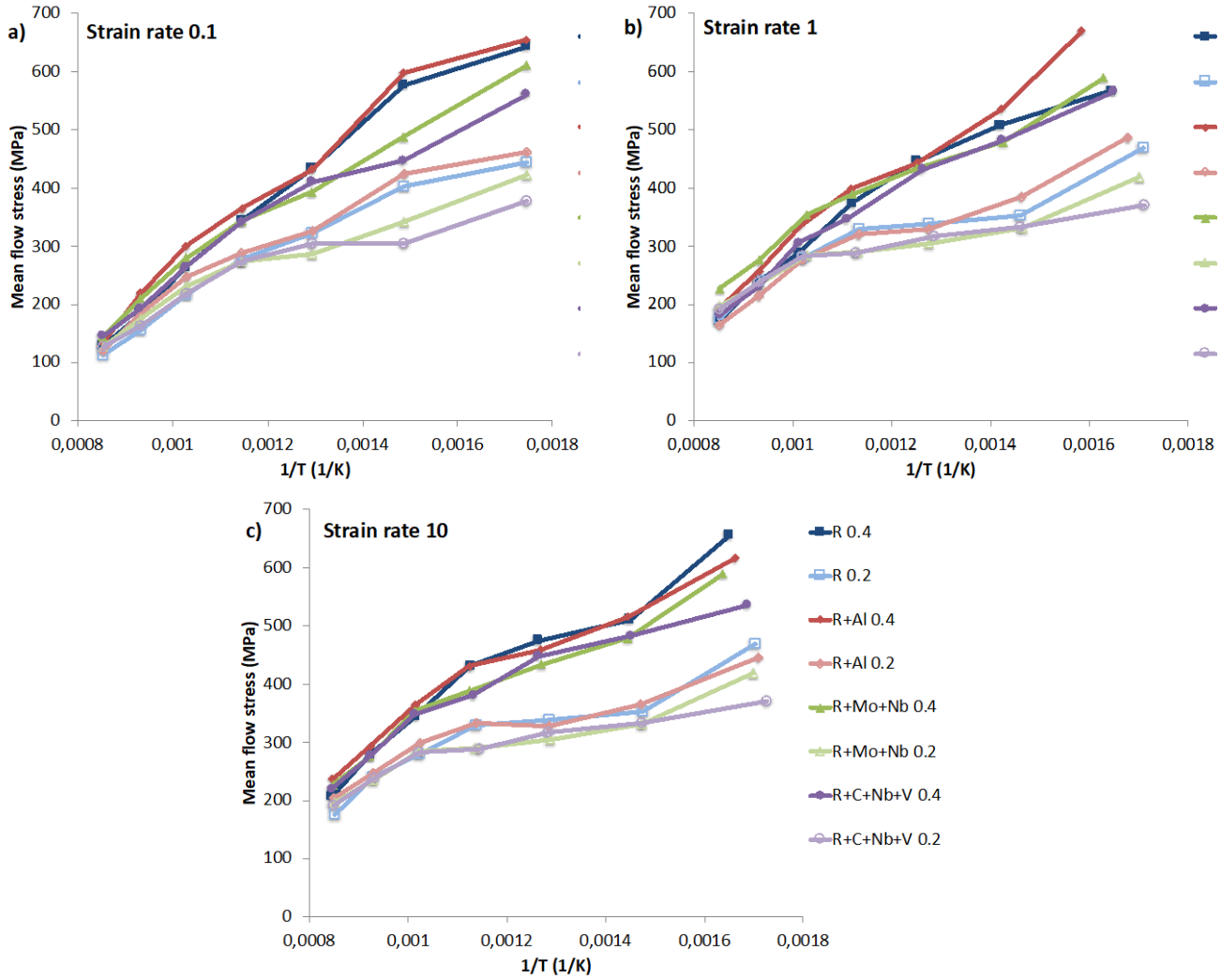

Figure 17. Differences in MFS at 0.2 and 0.4 strain with strain rates a) $0.1s^{-1}$, b) $1s^{-1}$ and c) $10s^{-1}$ between the steels.

3.2.2 Task 2.2: Austenite T_{NR} temperatures (OCAS).

The objective of this task is to determine the temperature at which the deformation needs to be applied in the D-CCTs and D-TTTs to ensure that the transformations are starting from deformed austenite. As such, an approximation of Thermo-Mechanically Controlled Processing (TMCP) can be obtained.

The initial objective was to determine the T_{NR} by multihit torsion testing but due to an unexpected failure of the torsion set-up at OCAS, the recrystallization behaviour of the alloys were studied in a Bahr 805 dilatometer in deformation mode. Cylindrical specimens of 9mm length and a diameter of 4mm have been used for this purpose. The set-up of the multiple-hit deformation dilatometry experiment is shown in Figure 18 (a). 6 consecutive deformation steps of 0.1 with a strain rate of 0.5/s have been applied with temperature of steps of 20°C, with a 5s interpass time. This has been done in the temperature intervals 1000-900°C and 900-800°C for all alloys, and additionally in the interval 960-860°C for the R, R+Mo and R+Mo+Nb alloys. Typical flow curves obtained for the R alloy are shown in Figure 18 (b)

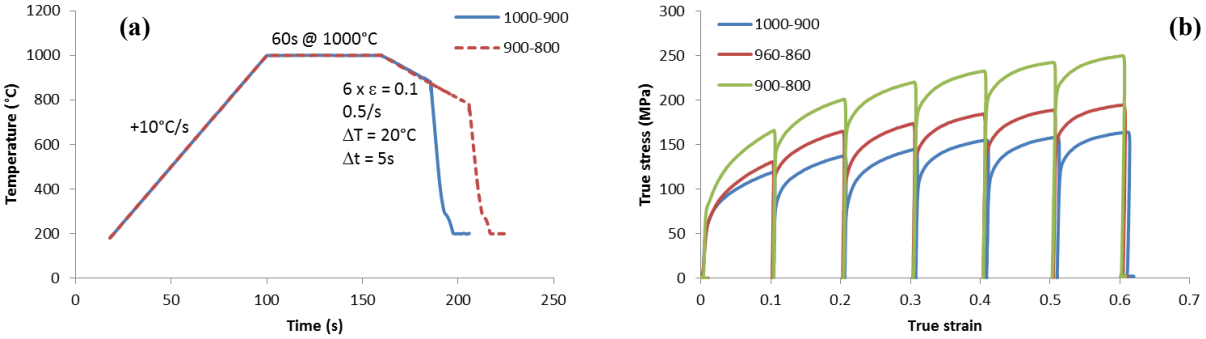

Figure 18. (a) Schematic of the thermal cycle and deformation in the dilatometer to address recrystallization behaviour, (b) Typical flow curves obtained for the R alloy

Figure 19 shows the peak stresses measured in the 900-800°C for the R, R-C and R+C alloys. Contrary to expectations, the slope of the curve becomes lower at lower temperatures, indicating some kind of softening. Note that transformation to ferrite is not expected for these alloys under these conditions. In any case, it proved impossible to determine a temperature of non-recrystallization (T_{NR}) from these data.

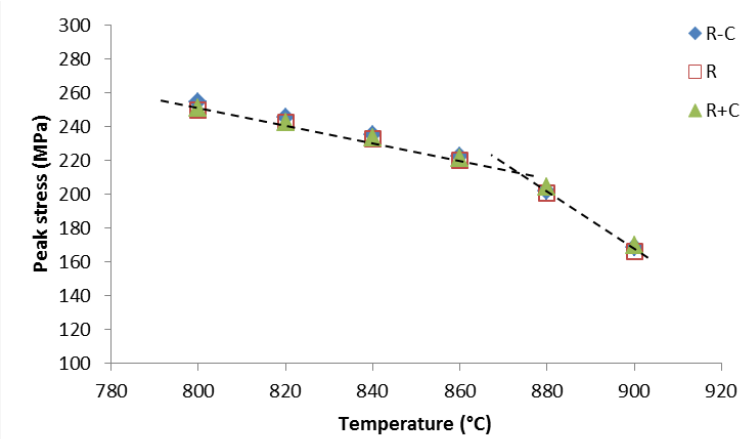

Figure 19. Example of peak stresses measured at different consecutive deformation steps, for the R, R-C and R+C alloys in the temperature interval 900-800°C

To have an indication of the difference in recrystallization behaviour of the alloys, the peak stress at 900°C in the different deformation sequences has been compared, as illustrated in Figure 20 for the R, R+Mo and R+Mo+Nb alloys.

The difference in peak stress at 900°C for the R alloy is negligible, indicating that the conditions at the end of the 1000-900°C and the beginning of the 900-800°C sequence are similar, i.e. the austenite is recrystallized.

In the case of the R+Mo and R+Mo+Nb alloys, there is a significant difference, indicating these materials are not recrystallized at the end of the 1000-900°C sequence. This suggests that the T_{NR} for these alloys is above 900°C and as such that Mo and Nb increase the T_{NR}. This is in line with expectations.

As shown in Figure 21, the addition of Si, Al, Mo and Nb increase the T_{NR} to above 900°C, whereas C, Mn, Cr and V seem to have a very limited effect.

The main conclusion therefore was that, for the alloys containing Al, Si, Mo and Mo+Nb the $T_{NR} > 900$ºC, while the remaining alloys have a $T_{NR} < 900$ºC.

Based on these results and the fact that typical TMCP finish rolling temperatures are around 850°C in strip mill processing, it was decided to fix the deformation temperature for the D-CCTs at 850°C.

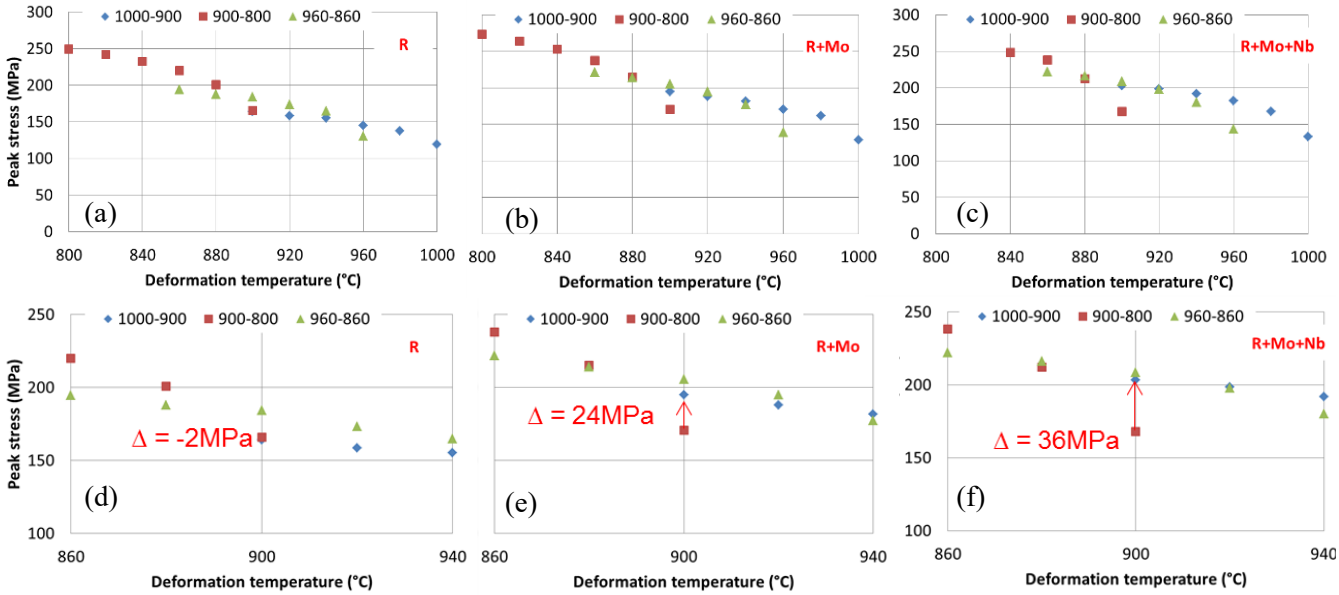

Figure 20. Peak stresses measured at different temperatures comparing 1000-900°C, 960-860°C and 900-800°C for (a), (d) R alloy, (b), (e) R+Mo alloy, (c), (f) R+Mo+Nb alloy.

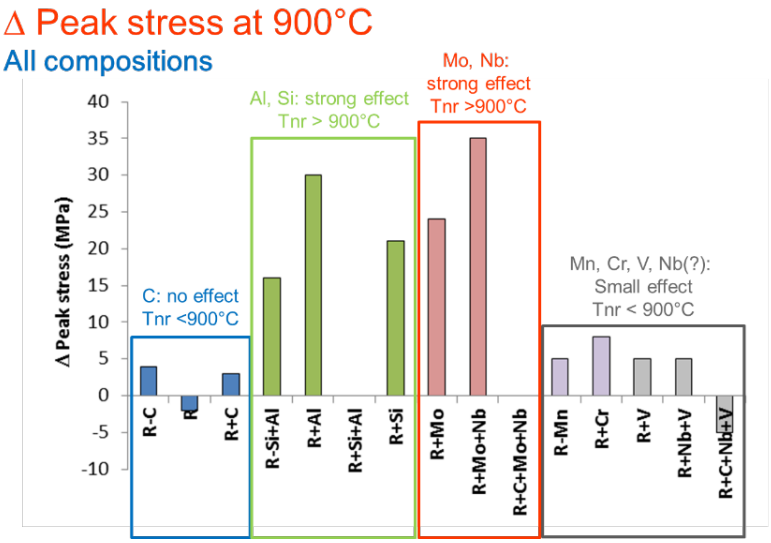

Figure 21. Difference between the peak stress measured at 900°C, measured at the end of the 1000-900°C sequence and at the beginning of the 900-800°C sequence.

3.2.3 Task 2.3: Phase transformation studies (ALL).

The aim of this task is to gather the necessary information to finally define the best parameters for the simulation of the TMCP at pilot scale on WP3. With this aim, CCT, TTT and D-CCT and D-TTT diagrams where obtained as explained in the following paragraphs. For this task, different equipment were used, according to Table 5.

Table 5. Equipment, sample size and direction for microstructural characterisation and dimension change measurement, used per type of experiment and partner.

Experiment	Partner	Equipment	Cylinder(Ø x l)/mm	Micros.charac. direction	Measurement of dimension change
CCT	CSIC	Bahr	4x9	Radial	Longitudinal
	OCAS	Bahr	4x9	Radial	Longitudinal
	tkSE	Bahr	4x9	Longitudinal	Longitudinal
TTT	CSIC	Bahr	4x9	Radial	Longitudinal
	OCAS	Bahr	4x9	Radial	Longitudinal
	tkSE	Bahr	4x9	Longitudinal	Longitudinal
D-CCT	CSIC	Bahr	4x9	Radial	Longitudinal
	OCAS	Bahr	4x9	Radial	Longitudinal
	tkSE	Bahr	4x9	Longitudinal	Longitudinal
LT-TTT	tkSE	Bahr	3.2x7.2	Longitudinal	Longitudinal
	OULU	Gleeble	5x7.5	Longitudinal	Radial
MT-TTT	OULU	Gleeble	6x9	Longitudinal	Radial
HT-TTT	OCAS	Bahr	4x9	Radial	Radial

Considering the results regarding the A_{c1}-A_{c3} and T_{NR} (OCAS), and in order to conceal the fact that samples has to be fully austenitic when deformation is applied, it was decided use the cycle shown in Figure 22.

3.2.3.i CCT diagrams

The construction of the CCT was used to estimate the Ms temperatures of all alloys and to estimate the necessary CR to be applied to avoid the F/P transformation. The same austenitisation T, 1000ºC, was agreed for all alloys with a stop at 850ºC for 15 s (the holding at 850°C for 15s is to keep the analogy with the D-CCT's in Figure 25), see Figure 22.

The Ms temperature was estimated at a cooling rate of 25ºC/s for all alloys, and after proving that this cooling rate was enough to avoid F/P transformation.

Some examples of the CCT diagrams and the obtained microstructure are presented in Figure 23 and Figure 24 respectively. A summary of the most relevant results extracted from these diagrams are summarised from Table 6 to Table 8. The main results of this part are as follows:

- No transformation was detected in the first cooling from 1000ºC down to 850ºC.
- Ms Temperatures for all the alloys range between 227ºC for the higher C alloys and 325ºC for the lowest C.
- Designed alloys have a high hardenability as a cooling rate over 10ºC/s is sufficient to ensure that, in all alloys, the microstructure is martensitic with no intermediate transformations.
- -Hardness of the martensite is commonly over 600HV and between 700-820 HV for the alloys containing higher C.

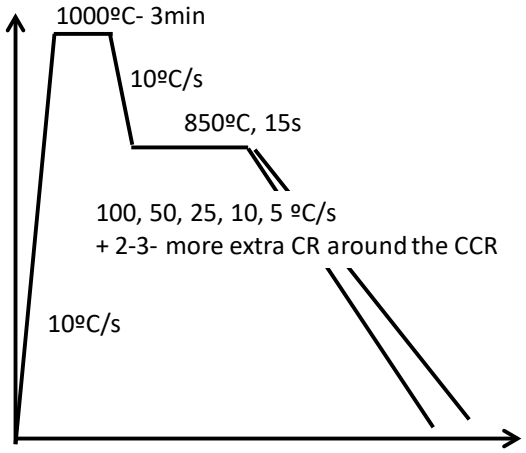

Figure 22. General overview of the parameters to be used on the construction of the CCT diagrams.

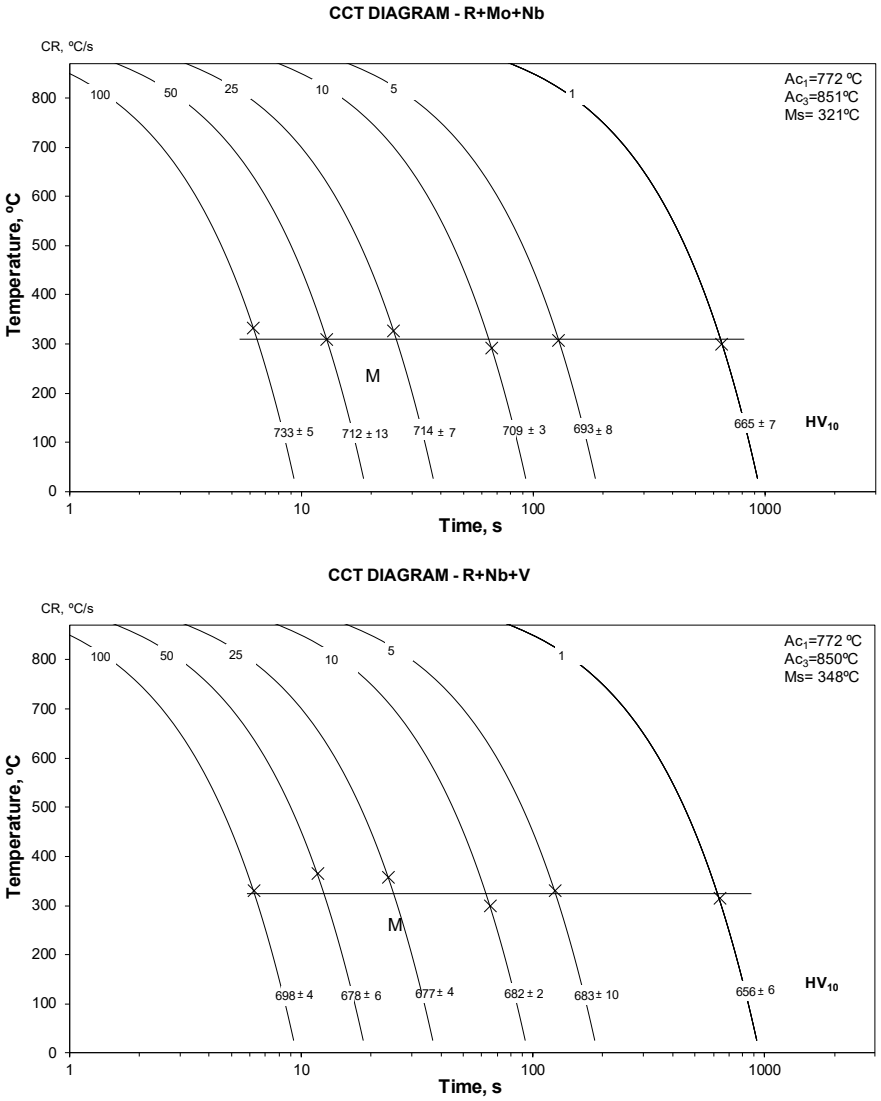

Figure 23. Example of CCT diagrams for two selected alloys.

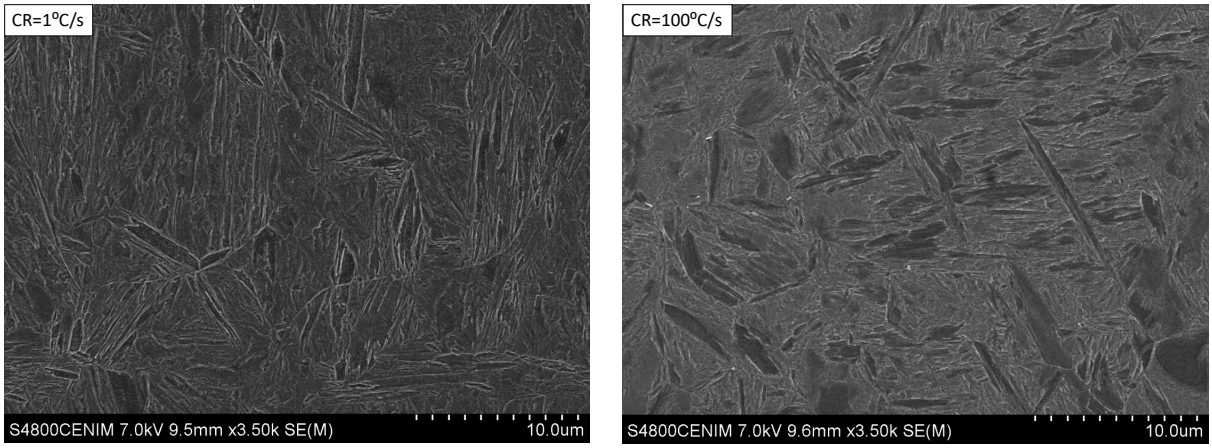

Figure 24. For R+Mo+Nb steel, high magnification detail of the (almost fully) martensitic microstructure obtained after cooling at 1 and 100ºC/s.

Table 6. Summary of the main results obtained from the CCT diagrams. F/P stands for Ferrite/Perlite, B for bainite, M for martensite, Ms is the martensite start T at 25ºC/s, HV is the Vickers hardness, Vγ and Cγ the volume fraction and C content of austenite respectively measured by XRD.

C effect

	Partner	CR (ºC/s)	F/P?	B?	M?	Ms(ºC)	HV10	Vγ /%	Cγ /%
R-C	OCAS	0.1	YES	X	X	X	268±12	-	-
	OCAS	0.5	YES	YES	YES	275	434±38	-	-
	OCAS	1	YES	YES	YES	294	470±30	-	-
	OCAS	2	X	YES	YES	303	512±20	-	-
	OCAS	5	X	TRACE	YES	321	532±8	-	-
	OCAS	10	X	X	YES	325	538±8	-	-
	OCAS	25	X	X	YES	322	538±9	-	-
R	OCAS	0.1	YES	X	X	X	295±10	-	-
	OCAS	0.5	YES	YES	YES	263	571±36	-	-
	OCAS	1	YES	TRACE	YES	271	639±14	-	-
	OCAS	2	X	X	YES	279	632±6	-	-
	OCAS	5	X	X	YES	281	656±11	-	-
	OCAS	10	X	X	YES	287	655±11	-	-
	OCAS	25	X	X	YES	293	601±27	-	-
R+C	OCAS	0.1	YES	X	X	X	413±11	-	-
	OCAS	0.5	YES	X	YES	247	467±56	-	-
	OCAS	1	YES	X	YES	246	713±9	-	-
	OCAS	2	X	X	YES	241	719±7	-	-
	OCAS	5	X	X	YES	250	709±17	-	-
	OCAS	10	X	X	YES	244	730±13	-	-
	OCAS	25	X	X	YES	246	717±17	-	-

Si effect

	Partner	CR (ºC/s)	F/P?	B?	M?	Ms(ºC)	HV5	Vγ /%	Cγ /%
R-Si+Al	tkSE	5	No	No	Yes	297.9	615±2	4	-
	tkSE	10	No	No	Yes	295.9	626±3	4	-
	tkSE	25	No	No	Yes	292.5	637±1	3	-
	tkSE	50	No	No	Yes	292.6	647±1	3	-
	tkSE	100	No	No	Yes	304.2	631±2	2.5	-
R+Al	**tkSE**	5	No	No	Yes	295.5	625±4	3.5	-
	tkSE	10	No	No	Yes	298.3	630±4	2.5	-
	tkSE	25	No	No	Yes	298.4	634±1	2	-
	tkSE	50	No	No	Yes	305.3	645±1	2	-
	tkSE	100	No	No	Yes	280.4	635±2	2	-
R+Si+Al	tkSE	5	No	No	Yes	290.8	648±2	3.5	-
	tkSE	10	No	No	Yes	285.1	579±1	7.5	-
	tkSE	25	No	No	Yes	288.6	646±2	3	-
	tkSE	50	No	No	Yes	289	631±3	3	-
	tkSE	100	No	No	Yes	258	637±4	3	-

Table 7. Summary of the main results obtained from the CCT diagrams. F/P stands for Ferrite/Perlite, B for bainite, M for martensite, Ms is the martensite start T at 25ºC/s, HV is the Vickers hardness, Vγ and Cγ the volume fraction and C content of austenite respectively measured by XRD.

Nb & C effect

	Partner	CR (ºC/s)	F/P?	B?	M?	Ms(ºC)	HV10	Vγ /%	Cγ /%
R+Mo	CENIM	1	No	No	Yes	282.79	661±4	-	-
	CENIM	5	No	No	Yes	282.34	694±5	-	-
	CENIM	10	No	No	Yes	285.83	699±2	-	-
	CENIM	25	No	No	Yes	302.57	703±2	-	-
	CENIM	50	No	No	Yes	285.76	726±9	-	-
	CENIM	100	No	No	Yes	293.32	727±5	-	-
R+Mo+Nb	CENIM	1	No	No	Yes	280.07	665±7	3.8	0.05208
	CENIM	5	No	No	Yes	280.3	693±8	-	-
	CENIM	10	No	No	Yes	280	709±3	-	-
	CENIM	25	No	No	Yes	327.4	714±7	-	-
	CENIM	50	No	No	Yes	288.04	712±13	-	-
	CENIM	100	No	No	Yes	279.58	733±5	<2	-
R+C+Mo+Nb	CENIM	1	No	No	Yes	241.34	757±9	-	-
	CENIM	5	No	No	Yes	243.32	797±5	-	-
	CENIM	10	No	No	Yes	242.33	810±11	-	-
	CENIM	25	No	No	Yes	268.42	800±3	-	-
	CENIM	50	No	No	Yes	247.25	813±11	-	-
	CENIM	100	No	No	Yes	255.06	824±11	-	-

Unsorted elements

	Partner	CR (ºC/s)	F/P?	B?	M?	Ms(ºC)	HV10	Vγ /%	Cγ /%
R-Mn	OCAS	0.1	YES	X	X	X		-	-
	OCAS	0.5	YES	X	X	X	272±8	-	-
	OCAS	1	YES	X	X	X	291±6	-	-
	OCAS	2	YES	YES	YES	318	314±21	-	-
	OCAS	5	TRACE	YES	YES	294	575±39	-	-
	OCAS	7.5	X	YES	YES	300	605±22	-	-
	OCAS	10	X	TRACE	YES	299	624±17	-	-
	OCAS	25	X	X	YES	313	633±6	-	-
R+Si	OCAS	0.1	YES	X	X	X	296±6	-	-
	OCAS	0.5	YES	YES	YES	270	603±16	-	-
	OCAS	1	X	X	YES	270	628±10	-	-
	OCAS	2	X	X	YES	272	642±9	-	-
	OCAS	5	X	X	YES	276	660±10	-	-
	OCAS	10	X	X	YES	281	653±12	-	-
	OCAS	25	X	X	YES	279	683±14	-	-
R+Cr	CENIM	1	No	No	Yes	271.79	674±8	-	-
	CENIM	5	No	No	Yes	274.1	704±7	-	-
	CENIM	10	No	No	Yes	274.34	701±6	-	-
	CENIM	25	No	No	Yes	303.31	676±20	-	-
	CENIM	50	No	No	Yes	285.73	685±4	-	-
	CENIM	100	No	No	Yes	276.58	727±7	-	-

Table 8. Summary of the main results obtained from the CCT diagrams. F/P stands for Ferrite/Perlite, B for bainite, M for martensite, Ms is the martensite start T at 25ºC/s, HV is the Vickers hardness, Vγ and Cγ the volume fraction and C content of austenite respectively measured by XRD.

Nb & C effect

	Partner	CR (ºC/s)	F/P?	B?	M?	Ms(ºC)	HV10	Vγ /%	Cγ /%
R+V	CENIM	1	No	No	Yes	294.39	647±11	-	-
	CENIM	5	No	No	Yes	290.89	670±6	-	-
	CENIM	10	No	No	Yes	293.18	686±5	-	-
	CENIM	25	No	No	Yes	316.25	676±6	-	-
	CENIM	50	No	No	Yes	291.47	668±2	-	-
	CENIM	100	No	No	Yes	306.97	707±8	-	-
R+Nb+V	CENIM	1	No	No	Yes	281.53	656±6	-	-
	CENIM	5	No	No	Yes	303.2	683±10	-	-
	CENIM	10	No	No	Yes	287.3	682±2	-	-
	CENIM	25	No	No	Yes	312.3	677±4	-	-
	CENIM	50	No	No	Yes	296.13	678±6	-	-
	CENIM	100	No	No	Yes	296.7	698±4	-	-
R+C+Nb+V	CENIM	1	No	No	Yes	231.7	740±9	-	-
	CENIM	5	No	No	Yes	234.78	769±25	-	-
	CENIM	10	No	No	Yes	227.43	743±22	-	-
	CENIM	25	No	No	Yes	222.64	762±9	-	-
	CENIM	50	No	No	Yes	227.53	757±9	-	-
	CENIM	100	No	No	Yes	208.89	762±5	-	-

3.2.3.ii D-CCT diagrams

The construction of the D-CCT aimed for the evaluation of the deformation effect on the transformation kinetics of different constituents and on the relevant transformation temperatures obtained in the CCTs. As shown in Figure 25, 850°C was chosen as deformation temperature, keeping in mind typical TMCP finish rolling temperature in a strip mill. The deformation and deformation rate were selected considering also the limits of the deformation dilatometers used in this WP. Right before and right after deformation took place, the temperature was decided to be held for 10 and 5 seconds, respectively. Thus the sample temperature could be completely homogenized and the system could also stabilize.

Some examples of the D-CCT diagrams obtained are presented in Figure 26, and a summary of the most relevant results extracted from these diagrams are summarised from Table 10 to Table 12. The main results of this part are as follows:

- No transformation was detected in the first cooling from 1000ºC down to 850ºC.
- Ms Temperatures, for all the alloys decrease as compared to those obtained in the CCT diagrams, and these range between 220ºC for the higher C alloys (0.5C) to 312ºC for the lowest one (0.3C). XRD analysis data came in support of this point, see Table 9, where it was clear that deformation promoted retention of a higher amount of retained austenite, indirectly implying that the Ms-M_f range has decreased.
- There is a small decrease in the hardenability, as F/P is only avoided at slightly higher cooling rates than in the case without deformation. In any case, a cooling rate of over 10ºC/s was still considered sufficient to ensure that, in all alloys, the microstructure was martensitic with no intermediate transformations.

- Also, and as expected, there seems to be an apparent refinement of the microstructure, see for example Figure 27 as compared to Figure 24.
- Hardness generally increased in comparison with those of the CCT samples, but, as pointed out, the decrease of the Ms-M_f temperature range might lead to retention of more retained austenite as compared to the CCT case, which meant the final hardness was lower. This is very evident in the case of the high C steels and some other alloys as for example the R+V and R+Mo+Nb.
- -Alloys containing Nb, Al and Mo exhibit the highest values of the maximum stress measured during deformation at 850ºC, results that are in line with those reported in Task.2.1.

Table 9. Volume fraction of retained austenite ($V_\gamma(\%)$) measured in the martensitic microstructure of R+Mo+Nb alloy after the described conditions.

	1ºC/s	100ºC/s
CCT	4±3	<2
D-CCT	8±3	6±3

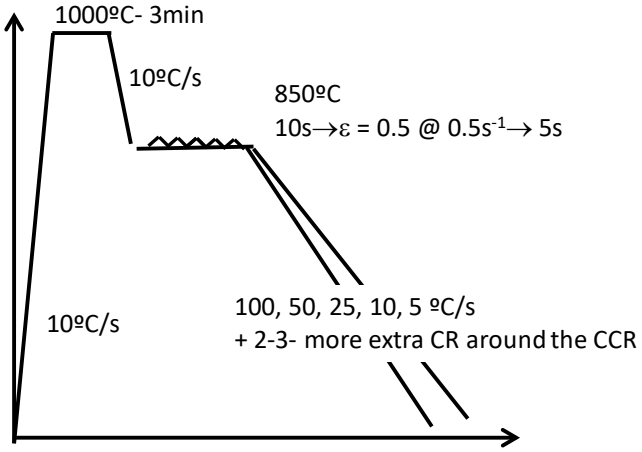

Figure 25. General overview of the parameters used on the construction of the D-CCT diagrams.

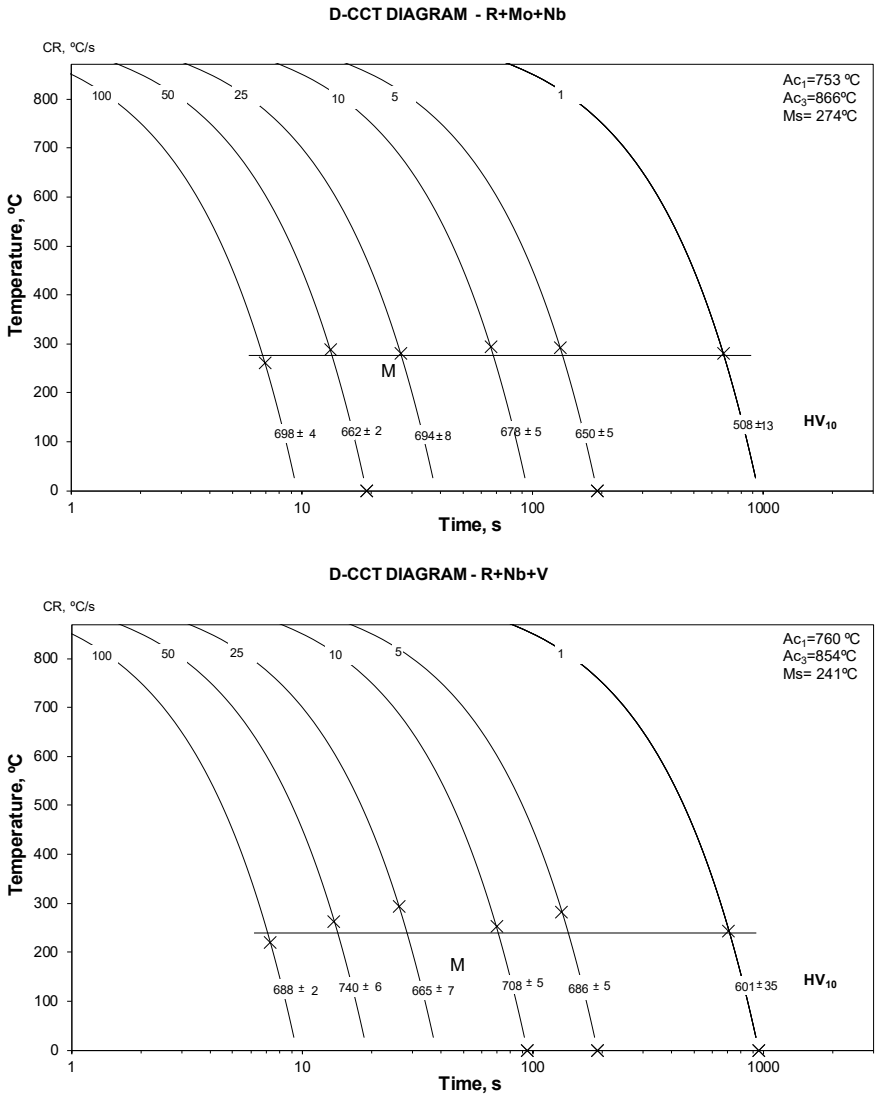

Figure 26. Example of D-CCT diagrams for two selected alloys.

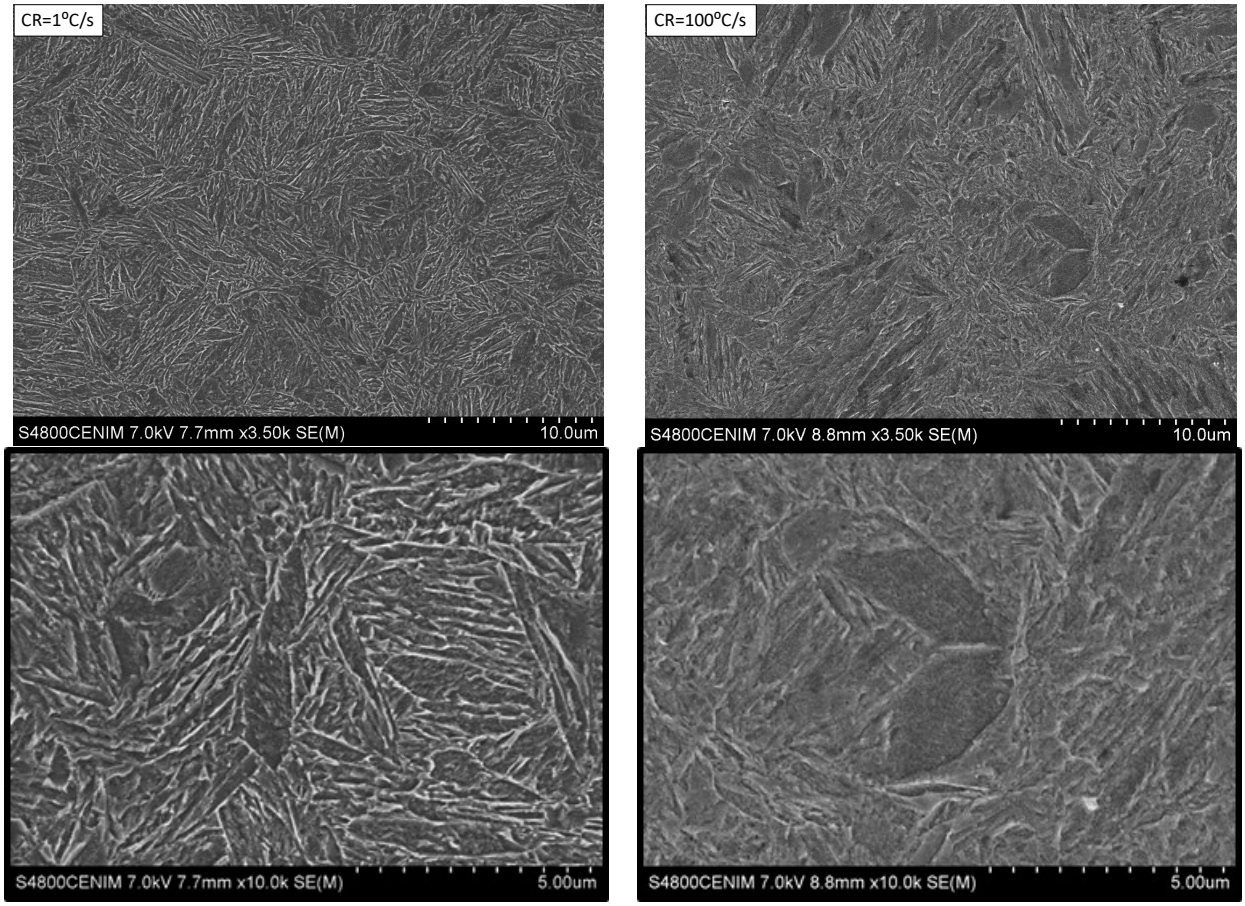

Figure 27. For R+Mo+Nb steel, high magnification detail of the (almost fully) martensitic microstructure obtained after deformation and cooling at 1 and 100ºC/s as described in Figure 25.

Table 10. Summary of the main results obtained from the D-CCT diagrams. F/P stands for Ferrite/Perlite, B for bainite, M for martensite, Ms is the martensite start T at 25ºC/s, HV is the Vickers hardness, Vγ and Cγ the volume fraction and C content of austenite respectively measured by XRD, also reported the maximum stress measured during deformation.

C effect

	Partner	CR (ºC/s)	F/P?	B?	M?	Ms(ºC)	HV10	Vγ /%	Cγ /%	Max. Stress Flow (Mpa)
R-C	OCAS	0.1	YES	X	X	X	247±7	-	-	213
	OCAS	0.5	YES	TRACE	YES	313	524±18	-	-	218
	OCAS	1	YES	X	YES	310	526±10	-	-	229
	OCAS	2	TRACE	X	YES	316	466±30	-	-	234
	OCAS	5	X	X	YES	317	564±5	-	-	235
	OCAS	10	X	X	YES	312	571±3	-	-	230
	OCAS	25	X	X	YES	313	560±5	-	-	231
R	OCAS	0.1	YES	X	X	X	294±9	-	-	200
	OCAS	0.5	YES	X	YES	264	349±19	-	-	227
	OCAS	1	YES	TRACE	YES	274	624±5	-	-	220
	OCAS	2	X	TRACE	YES	278	618±9	-	-	227
	OCAS	5	X	X	YES	278	654±10	-	-	226
	OCAS	10	X	X	YES	276	660±5	-	-	242
	OCAS	25	X	X	YES	270	667±4	-	-	229
R+C	OCAS	0.1	YES	X	X	X	313±6	-	-	194
	OCAS	0.5	YES	X	YES	240	335±6	-	-	230
	OCAS	1	YES	X	YES	239	699±13	-	-	229
	OCAS	2	X	X	YES	242	706±11	-	-	230
	OCAS	5	X	X	YES	237	730±3	-	-	227
	OCAS	10	X	X	YES	237	735±7	-	-	225
	OCAS	25	X	X	YES	235	740±5	-	-	217

Si effect

	Partner	CR (ºC/s)	F/P?	B?	M?	Ms(ºC)	HV5	Vγ /%	Cγ /%	Max. Stress Flow (Mpa)
R-Si+Al	tkSE	0.5	Yes	No	Yes	260.9	483±50	4	-	243.3
	tkSE	1	Yes	No	Yes	277.8	589±10	5.5	-	241.2
	tkSE	2	Yes	No	Yes	283.4	605±7	5.5	-	244.4
	tkSE	5	Yes	No	Yes	285.4	637±1	4	-	244.5
	tkSE	10	No	No	Yes	280.4	648±2	4.5	-	245.3
	tkSE	25	No	No	Yes	280.1	656±1	3	-	237.3
	tkSE	50	No	No	Yes	280.2	643±3	3	-	241
	tkSE	100	No	No	Yes	260.7	645±6	3	-	243.3
R+Al	**tkSE**	0.5	Yes	No	Yes	258.5	433±96	2	-	258.5
	tkSE	1	Yes	Yes	Yes	257.2	595±11	5	-	248.3
	tkSE	2	Yes	No	Yes	275.1	579±1	4.5	-	257.3
	tkSE	5	Yes	No	Yes	278.3	550±3	13	-	260.4
	tkSE	25	No	No	Yes	285.5	661±4	3.5	-	254.2
	tkSE	100	No	No	Yes	255.3	694±2	3.5	-	260.7
R+Si+Al	tkSE	0.5	Yes	No	Yes	250	334±13	<1	-	265
	tkSE	1	Yes	No	Yes	261	559±18	4	-	265
	tkSE	2	Yes	No	Yes	263.5	607±9	5.5	-	266
	tkSE	5	Yes	No	Yes	277.7	648±3	4	-	243
	tkSE	25	No	No	Yes	249.1	669±1	3.5	-	267
	tkSE	100	No	No	Yes	230.4	668±3	3	-	266

Table 11. Summary of the main results obtained from the D-CCT diagrams. F/P stands for Ferrite/Perlite, B for bainite, M for martensite, Ms is the martensite start T at 25ºC/s, HV is the Vickers hardness, Vγ and Cγ the volume fraction and C content of austenite respectively measured by XRD, also reported the maximum stress measured during deformation.

Nb & C effect

	Partner	CR (ºC/s)	F/P?	B?	M?	Ms(ºC)	HV10	Vγ /%	Cγ /%	Max. Stress Flow (Mpa)
R+Mo	CENIM	1	No	No	Yes	269.36	574±25	-	-	270
	CENIM	5	No	No	Yes	269.26	694±5	-	-	274
	CENIM	10	No	No	Yes	267.34	691±3	-	-	271
	CENIM	25	No	No	Yes	310.19	705±9	-	-	278
	CENIM	50	No	No	Yes	256.69	705±9	-	-	276
	CENIM	100	No	No	Yes	240.12	689±5	-	-	275
R+Mo+Nb	CENIM	1	No	No	Yes	267.72	508±13	8.1	0.09304	284
	CENIM	5	No	No	Yes	268.99	650±5	-	-	284
	CENIM	10	No	No	Yes	268.76	678±5	-	-	289
	CENIM	25	No	No	Yes	264.78	694±8	-	-	284
	CENIM	50	No	No	Yes	247.84	662±2	-	-	285
	CENIM	100	No	No	Yes	235.18	698±4	6.5	0.05936	287
R+C+Mo+Nb	CENIM	1	No	No	Yes	228.77	627±18	-	-	282
	CENIM	5	No	No	Yes	230.58	774±6	-	-	286
	CENIM	10	No	No	Yes	224.66	760±3	-	-	277
	CENIM	25	No	No	Yes	257.17	767±9	-	-	280
	CENIM	50	No	No	Yes	224.26	774±3	-	-	277
	CENIM	100	No	No	Yes	211.85	737±18	-	-	278

Unsorted elements

	Partner	CR (ºC/s)	F/P?	B?	M?	Ms(ºC)	HV10	Vγ /%	Cγ /%	Max. Stress Flow (Mpa)
R-Mn	OCAS	0.1	YES	X	X	X	215±4	-	-	214
	OCAS	0.5	YES	X	X	X	264±4	-	-	206
	OCAS	1	YES	X	X	X	269±10	-	-	210
	OCAS	2	YES	X	X	X	280±6	-	-	230
	OCAS	5	YES	X	YES	300	551±34	-	-	221
	OCAS	10	X	X	YES	302	590±11	-	-	240
	OCAS	25	X	X	YES	303	539±10	-	-	213
								-	-	
R+Si	OCAS	0.1	YES	X	X	X	284±6	-	-	196
	OCAS	0.5	YES	X	YES	262	393±31	-	-	232
	OCAS	1	YES	X	YES	X	626±5	-	-	232
	OCAS	2	YES	X	YES	X	652±2	-	-	226
	OCAS	5	YES	X	YES	274	644±4	-	-	228
	OCAS	10	X	X	YES	269	672±4	-	-	223
	OCAS	25	X	X	YES	257	673±4	-	-	188
R+Cr HV5	tkSE	0.5	Yes	No	Yes	267.8	632±8	5	-	237.5
	tkSE	25	No	No	Yes	242.8	667±4	3.5	-	229.9
	tkSE	100	No	No	Yes	231.7	686±8	4	-	227.2

Table 12 Summary of the main results obtained from the D-CCT diagrams. F/P stands for Ferrite/Perlite, B for bainite, M for martensite, Ms is the martensite start T at 25ºC/s, HV is the Vickers hardness, Vγ and Cγ the volume fraction and C content of austenite respectively measured by XRD, also reported the maximum stress measured during deformation.

Nb & C effect

	Partner	CR (ºC/s)	F/P?	B?	M?	Ms(ºC)	HV10	Vγ /%	Cγ /%	Max. Stress Flow (Mpa)
R+V HV5	tkSE	0.5	Yes	Yes	Yes	295.1	545±50	4	-	234.6
	tkSE	1	Yes	Yes	Yes	268.8	631±6	5	-	233.3
	tkSE	2	No	Yes	Yes	274.5	644±8	4	-	229.1
	tkSE	10	No	No	Yes	275.9	653±5	3	-	232.7
	tkSE	25	No	No	Yes	279.7	661±7	3	-	232.3
	tkSE	100	No	No	Yes	227.9	673±2	3	-	233.6
R+Nb+V	CENIM	1	No	No	Yes	267.25	601±35	-	-	269
	CENIM	5	No	No	Yes	267.14	686±5	-	-	271
	CENIM	10	No	No	Yes	268.38	708±5	-	-	269
	CENIM	25	No	No	Yes	280.11	665±7	-	-	270
	CENIM	50	No	No	Yes	248.5	740±6	-	-	270
	CENIM	100	No	No	Yes	256.68	688±2	-	-	272
R+C+Nb+V	CENIM	1	No	No	Yes	231.7	735±12	-	-	271
	CENIM	5	No	No	Yes	234.78	647±11	-	-	264
	CENIM	10	No	No	Yes	227.43	657±82	-	-	270
	CENIM	25	No	No	Yes	222.64	507±12	-	-	276
	CENIM	50	No	No	Yes	227.53	797±5	-	-	274
	CENIM	100	No	No	Yes	208.89	723±7	-	-	270

3.2.3.iii Isothermal tests (preliminary)

Before the construction of the actual TTT diagrams, some preliminary isothermal tests were performed in order to anticipate some conditions, mainly the time for the bainitic transformation to take place. The exact conditions of the new tests are summarised in Figure 28.

Dilatometric signal during isothermal holding showed the typical expansion (Avrami type curve in Figure 29) due to the transformation of austenite into bainitic ferrite. Later, optical microscopy is resorted to confirm this finding, see Figure 30, where the darker features correspond to sheaves of bainite and the lighter phase to retained austenite. It is also clear that for the higher C alloys (R+C+Mo+Nb and R+C+Nb+V) and also for the R+Cr the transformation seems almost completed, in the sense that the typical horizontal plateau describing no further transformation, have not been reached in 1 h, see Figure 29. Even though, except in the R+Cr none of the tested steels showed signs of martensitic transformation after the isothermal treatment, meaning that untransformed austenite at the TTT temperature is sufficiently enriched in C so it remained stable after cooling down to room T (retained austenite).

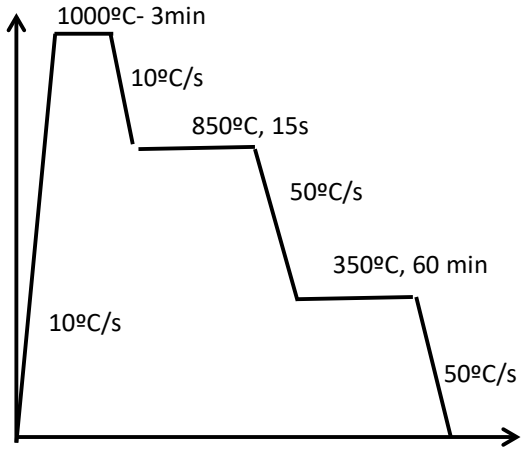

Figure 28. General overview of the parameters used on the new set of isothermal experiments at 350ºC.

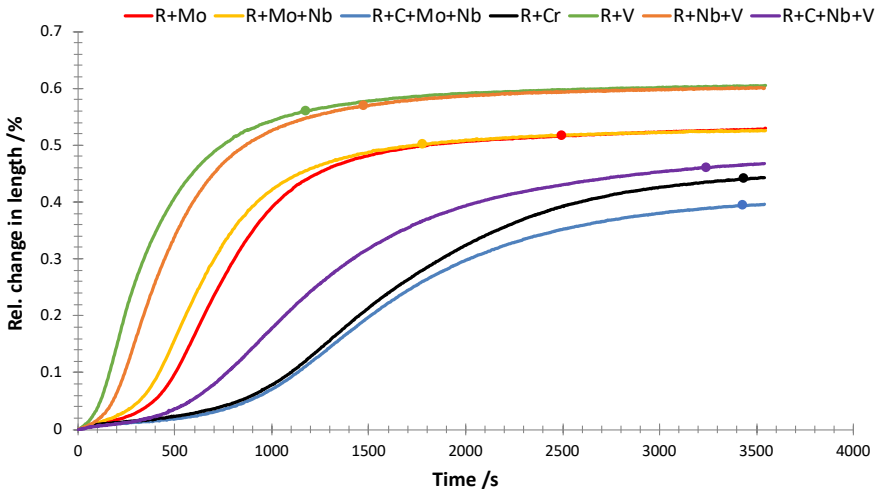

Figure 29. Dilatometric results on the isothermal transformation of austenite into bainite at 350ºC during 60 min.

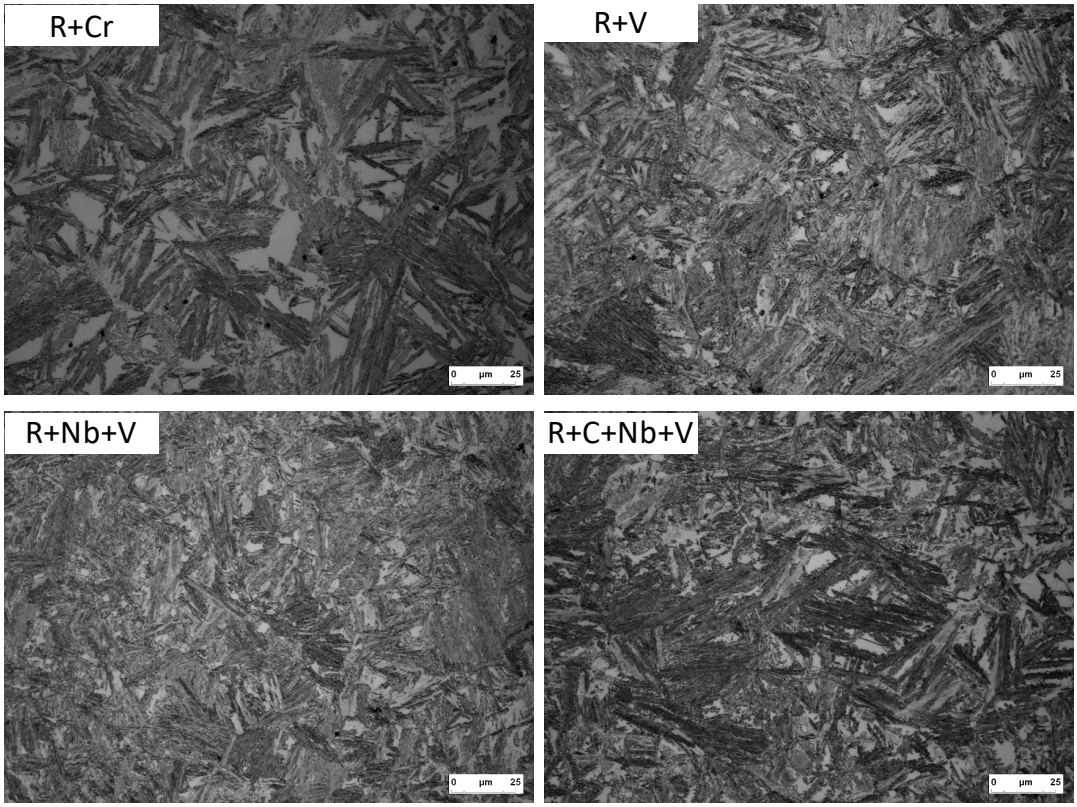

Figure 30. Selected examples of the microstructure obtained after isothermal transformation at 350ºC, according to experimental conditions described in Figure 28.

For the R+Cr alloy a second test was performed increasing the isothermal time up to 1.5 h, see Figure 31, and it seems that the extended time leads to further transformation; the decrease in Vickers hardness is a direct consequence of a lower fraction of martensite forming on cooling down to room T.

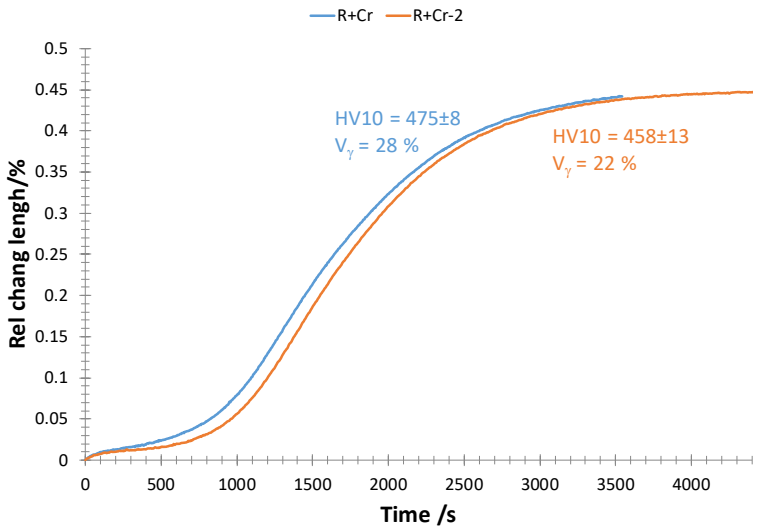

Figure 31. Dilatometric results on the isothermal transformation of austenite into bainite at 350ºC during 60 and 90 min for R+Cr steel.

3.2.3.iv TTT diagrams

Based on the results obtained from the CCT, D-CCT and those first isothermal tests (Figure 28), a set of conditions for the construction of the TTT were agreed, and are summarised in Figure 32. As anticipated, for some high C alloys, 1h of isothermal transformation might be insufficient to complete the transformation, and therefore it was agreed to use 90 min instead, and in some cases, as the results were obtained, even longer. Summary of the main results of the TTT diagrams are collected from Table 13 to

Table 15 and Figure 33. Typical dilatometric curves during the isothermal step, are shown from Figure 34 to Figure 35. The change in length during cooling from the isothermal transformation T down to room T was also analysed to detect the possibility of martensitic transformation.

Some extra experiments were introduced with the aim to ensure that T around 500ºC (as predicted in WP1) correspond to the bay between F/P and B transformation, allowing to use such a temperature for the D-TTT at somewhat medium temperature. Most of the alloys did not show any transformation after isothermal holding at 500ºC for an hour, see for example Figure 34. In the case of R-Mn some transformation products were observed, see Figure 35, the black phases in the optical micrograph corresponds to very fine pearlite and difficult to be resolved in optical micrographs. The dual kinetics is due to the formation of (most likely) Widmanstatten ferrite first and then pearlite. A further test was performed at 450ºC showing no signs of transformation, see Table 13. Also in the case of the R+C (after more than 1h of isothermal holding) some transformation was detected.

An effort has been made in order to obtain experimental bainitic transformation kinetics data, which will allow for a better adjustment of the necessary times for the isothermal treatments. To this purpose a method was assumed by all partners, described in [15], that allows for the determination of the onset and end of transformation, and also, the time for the maximum transformation rate, see data reported from Table 13 to Table 15.

The main results of TTT part are as follows:

- -The intensity of the dilatometric signal increases as the transformation T decreases, a clear indicative that there is more bainite fraction, as expected from the incomplete reaction phenomena, this is also supported by the XRD results shown in Table 13 and
- Table 15.
- The microstructure becomes finer as the transformation T decreases, an example of the evolution of the microstructure with the isothermal T is shown in Figure 36. Dark features correspond to sheaves of bainite while the white features are retained austenite.
- Higher fraction of a finer microstructure leads to higher HV values, therefore HV increases as transformation T decreases. There are cases, when the enrichment of C in austenite is not sufficient to stabilise it down to room T (incomplete transformation or little transformation (high transformation T)), and martensite forms on cooling, leading to an increase in HV, see for example results on R+C+Mo+Nb from 275 to 375ºC. Bainitic microstructures obtained at the lowest transformation T exhibit HV that ranges between 443 and 580, the latest for the higher C alloys.
- On cooling to room T, martensitic transformation is detected in almost all cases after transformation at $T \geq 375$ºC; the white features in Figure 36 then correspond to MA constituent, and, as mentioned, an increase in the HV is also a proof of the presence of high C martensite.

- Some measurements on the plate thickness of bainitic ferrite [16], Table 16 revealed that bainitic ferrite was below 100 nm.
- The times of 1h and 1.5 h for the treatments seem to be enough to reveal the end of the transformation, only in the case of the C bearing steels the times needed to end the transformation are longer than 1.5 h under certain conditions. According to results from Table 13 to
- Table 15, and as expected, Al clearly accelerates the transformation, Mo, C, Mn and Cr retard it and the influence of elements V, Si and Nb is uncertain or difficult to extrapolate.

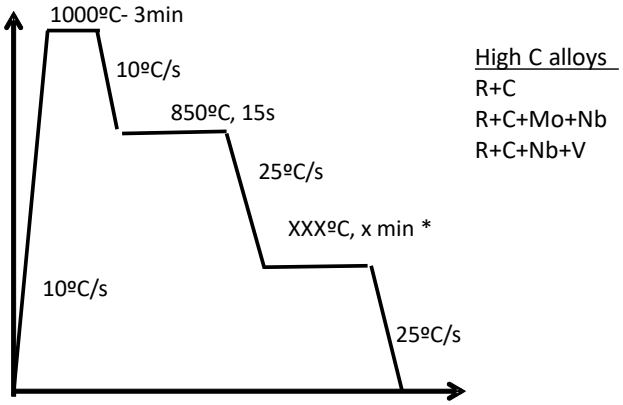

*Isothermal step (intended for bainitic transformation):
High C alloys : (275ºC) 300-350-375ºC 90min
All the other alloys : (325ºC) 350-375-400ºC 60 min

*Isothermal step (to see if ferrite transformation happens after 1h of isothermal):
All alloys 500ºC 60min
If ferrite is not found, T = 500ºC will be used in the MT-DTTT (Is the bay between the nose of ferrite and bainite).

Figure 32. General overview of the parameters used on the construction of the TTT diagrams.

Table 13. Summary of the main results obtained from the TTT diagrams. F/P stands for Ferrite/Perlite, B for bainite, M for martensite, Ms is the martensite start T measured on cooling after isothermal transformation, HV is the Vickers hardness, Vγ and Cγ the volume fraction and C content of austenite respectively measured by XRD. Time for the onset, maximum transformation rate and end of transformation are also provided when possible.

C effect

	Partner	T(ºC)	t(h)	F/P?	B?	M?	Onset time /s	Maximum differential time /s	End of transformation time /s	Ms(ºC)	HV10	Vγ /%	Cγ /%
R-C	OCAS	500	1	X	X	YES	X	X	X	315	647±8	-	-
	OCAS	400	1	X	YES	YES - M/A	X	112	688	165	491±50	-	-
	OCAS	375	1	X	YES	X	8	116	670	X	401±14	-	-
	OCAS	350	1	X	YES	X	15	123	666	X	428±8	-	-
	OCAS	325	1	X	YES	X	X	90	659	X	465±8	-	-
R	OCAS	500	1	X	X	YES	X	X	X	286	547±12	-	-
	OCAS	400	1	X	YES	YES	X	350	1736	229	363±39	-	-
	OCAS	375	1	X	YES	YES	X	332	2290	170	398±8	-	-
	OCAS	350	1	X	YES	X	X	357	1833	X	437±9	-	-
	OCAS	325	1	X	YES	X	72	360	1829	X	476±6	-	-
R+C	OCAS	500	2	YES	X	YES	X	-	X	245	504±65	-	-
	OCAS	450	2	X	X	YES	X	X	X	255	711±13	-	-
	OCAS	400	2	X	YES	YES	X	1440	4256	231	627±87	-	-
	OCAS	375	2	X	YES	YES	267	1980	>7193	212	518±25	-	-
	OCAS	350	2	X	YES	YES	260	1325	5393	178	518±31	-	-
	OCAS	300	2	X	YES	X	367	1274	4917	X	487±7	-	-
	OCAS	275	1.5	X	YES	X	589	1502	>5395	X	487±8	-	-

Si effect

	Partner	T(ºC)	t(h)	F/P?	B?	M?	Onset time /s	Maximum differential time /s	End of transformation time /s	Ms(ºC)	HV10	Vγ /%	Cγ /%
R-Si+Al	tkSE	500	1	No	No	Yes	-	-	-	293	-	-	-
	tkSE	400	1	No	Yes	Yes	51	252	1198	-	360±2	28	0.78
	tkSE	375	1	No	Yes	No	57	259	1122	-	395±1	22	1.17
	tkSE	350	1	No	Yes	No	49	265	1049	-	436±1	18.5	1.23
	tkSE	325	1	No	Yes	No	67	289	1156	-	475±5	14.5	1.17
R+Al	**tkSE**	**500**	1	No	No	Yes	-	-	-	281	-	-	-
	tkSE	**400**	1	No	Yes	Yes	66	269	1171	-	382±7	29	1.08
	tkSE	**375**	1	No	Yes	Traces	48	254	918	-	406±4	25	1.05
	tkSE	**350**	1	No	Yes	No	48	256	928	-	439±3	18.5	1.14
	tkSE	**325**	1	No	Yes	No	136	341	1040	-	465±3	17.5	1.14
R+Si+Al	tkSE	500	1	No	No	Yes	-	-	-	290	-	-	-
	tkSE	400	1	No	Yes	Yes	88	320	1184	-	377±2	29.5	0.90
	tkSE	375	1	No	Yes	No	85	313	925	-	403±1	26	1.08
	tkSE	350	1	No	Yes	No	63	282	940	-	438±2	21	1.14
	tkSE	325	1	No	Yes	No	74	307	1114	-	475±1	17	1.11

Table 14. Summary of the main results obtained from the TTT diagrams. F/P stands for Ferrite/Perlite, B for bainite, M for martensite, Ms is the martensite start T measured on cooling after isothermal transformation, HV is the Vickers hardness, Vγ and Cγ the volume fraction and C content of austenite respectively measured by XRD. Time for the onset, maximum transformation rate and end of transformation are also provided when possible.

Nb & C effect

	Partner	T(ºC)	t(h)	F/P?	B?	M?	Onset time /s	Maximum differential time /s	End of transformation time /s	Ms(ºC)	HV10	Vγ /%	Cγ /%
R+Mo	CENIM	500	1	No	No	Yes	-	-	-	287.76	712±9	-	-
	CENIM	400	1	No	Yes	Yes	76	954	3332	248.98	492±7	-	-
	CENIM	375	1	No	Yes	Yes?	0	842	2734	145.62	426±5	-	-
	CENIM	350	1	No	Yes	No	151	688	2320	-	447±13	-	-
	CENIM	325	1	No	Yes	No	157	702	2302	-	493±0	11.80	1.05
												-	-
R+Mo+Nb	CENIM	500	1	No	No	Yes	-	-	-	275.53	724±5	-	-
	CENIM	400	1	No	Yes	Yes	72	954	2867	242.53	498±5	-	-
	CENIM	375	1	No	Yes	No	72	655	2333	-	439±8	-	-
	CENIM	350	1	No	Yes	No	72	590	1949	-	451±1	-	-
	CENIM	325	1	No	Yes	No	171	641	2187	-	497±3	12.30	0.97
												-	-
R+C+Mo+Nb	CENIM	500	1	No	No	Yes	-	-	-	252.24	804±6	-	-
	CENIM	375	1.5	No	Yes	Yes	0	2246	-	205.45	549±17	-	-
	CENIM	350	1.5	No	Yes	yes	324	1523	4509	-	541±6	-	-
	CENIM	300	1.5	No	Yes	No	626	1895	5073	-	455±2	-	-
	CENIM	275	1.5	No	Yes	No	921	2592	-	-	588±7	13.20	1.87
	CENIM	275	2.5	No	Yes	No	1359	2781	7218	-		-	-

Unsorted elements

	Partner	T(ºC)	t(h)	F/P?	B?	M?	Onset time /s	Maximum differential time /s	End of transformation time /s	Ms(ºC)	HV10	Vγ /%	Cγ /%
R-Mn	OCAS	500	1	YES	YES	X	X	7	X	222	370±64	-	-
	OCAS	400	1	X	YES	X	X	33	260	X	373±6	-	-
	OCAS	375	1	X	YES	X	X	36	227	X	423±10	-	-
	OCAS	350	1	X	YES	X	X	26	242	X	460±8	-	-
	OCAS	325	1	X	YES	X	X	40	281	X	443±1	-	-
R+Si	OCAS	500	1	YES	X	YES	X	-	X	281	646±22	-	-
	OCAS	400	1	X	YES	YES	X	598	2866	236	523±42	-	-
	OCAS	375	1	X	YES	YES	X	486	2383	161	407±20	-	-
	OCAS	350	1	X	YES	X	7	403	1915	X	438±8	-	-
	OCAS	325	1	X	YES	X	101	454	2038	X	447±25	-	-
R+Cr	CENIM	500	1	No	No	Yes	-	-	-	275.05	735±5	-	-
	CENIM	400	1	No	No	Yes	-	-	-	269.33	720±8	-	-
	CENIM	375	1	No	Yes	Yes	317	2041	-	249.46	556±15	-	-
	CENIM	350	1	No	Yes	Yes	464	1390	3488	195.39	468±3	-	-
	CENIM	350	2.5	No	Yes	Yes	450	1422	4109	93.86	461±1	-	-
	CENIM	325	1	No	Yes	Yes	425	1300	3483	142.55	505±5	15.5	1.02
	CENIM	325	2.5	No	Yes	No	540	1386	5351	-	482±8	-	-
	CENIM	300	1	No	Yes	Yes	425	3589	-	127.7	545±14	-	-
	CENIM	300	2.5	No	Yes	No	684	1557	5886	-	516±3	-	-

Table 15. Summary of the main results obtained from the TTT diagrams. F/P stands for Ferrite/Perlite, B for bainite, M for martensite, Ms is the martensite start T measured on cooling after isothermal transformation, HV is the Vickers hardness, Vγ and Cγ the volume fraction and C content of austenite respectively measured by XRD. Time for the onset, maximum transformation rate and end of transformation are also provided when possible.

Nb & C effect

	Partner	T(ºC)	t(h)	F/P?	B?	M?	Onset time /s	Maximum differential time /s	End of transformation time /s	Ms(ºC)	HV10	Vγ /%	Cγ /%
R+V	CENIM	500	1	No	No	Yes	-	-	-	294.72	712±9	-	-
	CENIM	400	1	No	Yes	No	94	223	1318	-	408±4	-	-
	CENIM	375	1	No	Yes	No	76	205	1298	-	436±10	-	-
	CENIM	350	1	No	Yes	No	0	216	1312	-	460±1	-	-
	CENIM	325	1	No	Yes	No	76	320	1746	-	501±2	-	-
R+Nb+V	CENIM	500	1	No	Yes	Yes	-	-	-	289.71	727±7	-	-
	CENIM	400	1	No	Yes	Yes?	0	306	1973	219.11	484±1	21.7	0.83
	CENIM	375	1	No	Yes	No	83	364	1757	-	425±5	-	-
	CENIM	350	1	No	Yes	No	76	356	1606	-	459±2	21.1	1.08
	CENIM	325	1	No	Yes	No	0	371	1957	-	500±3	12.3	1.08
R+C+Nb+V	CENIM	500	1	No	No	Yes	-	-	-	252.42	787±5	-	-
	CENIM	375	1.5	No	Yes	Yes?	0	1131	4344	189.37	446±4	-	-
	CENIM	350	1.5	No	Yes	No	81	842	4055	-	443±4	-	-
	CENIM	300	1.5	No	Yes	No	208	1026	4631	-	536±5	-	-
	CENIM	275	1.5	No	Yes	No	294	1679	5389	-	580±4	-	-
	CENIM	275	2.5	No	Yes	No	774	1881	6314	-	571±2	-	-

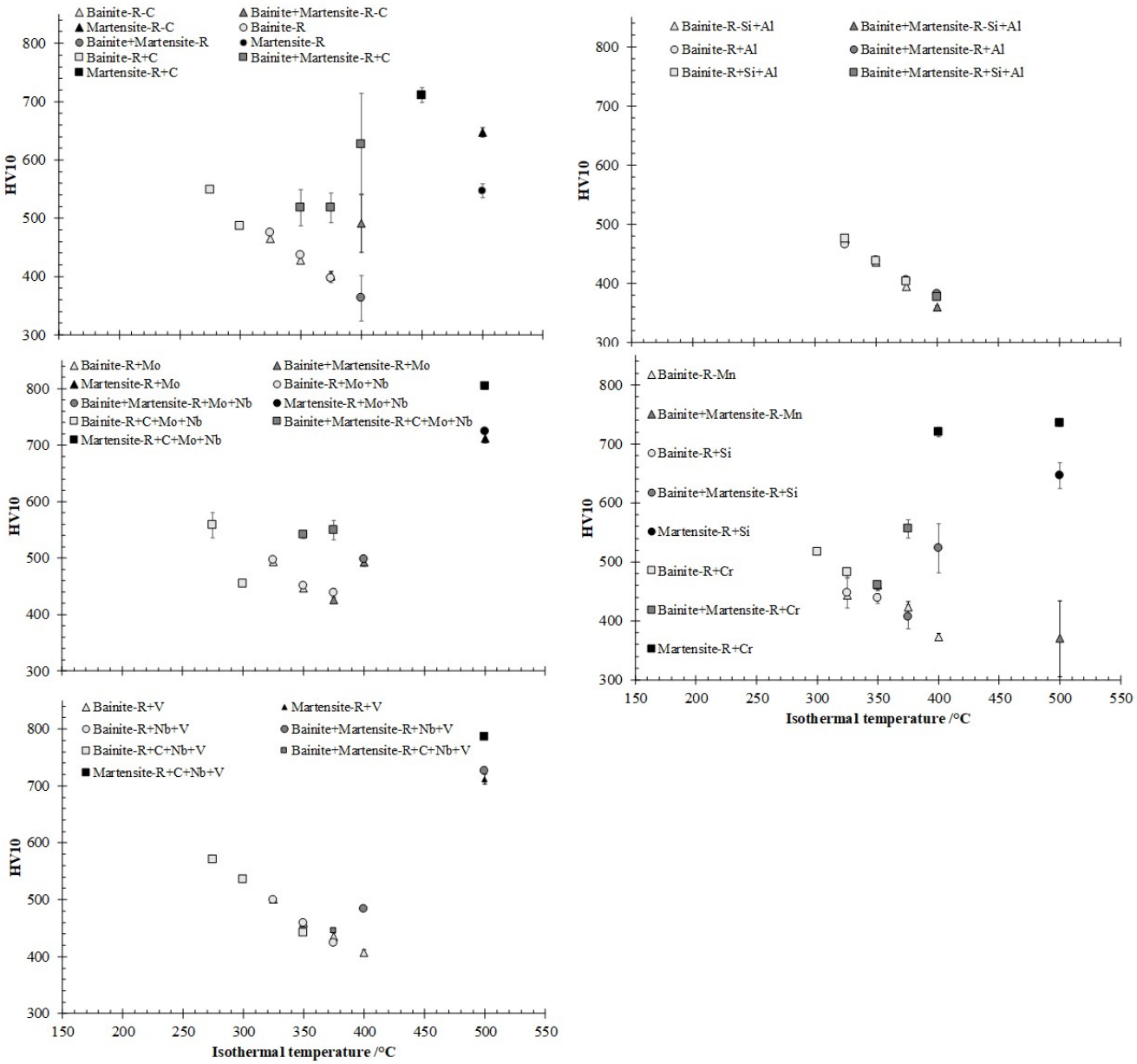

Figure 33. Microstructure and HV values for the TTT experiments.

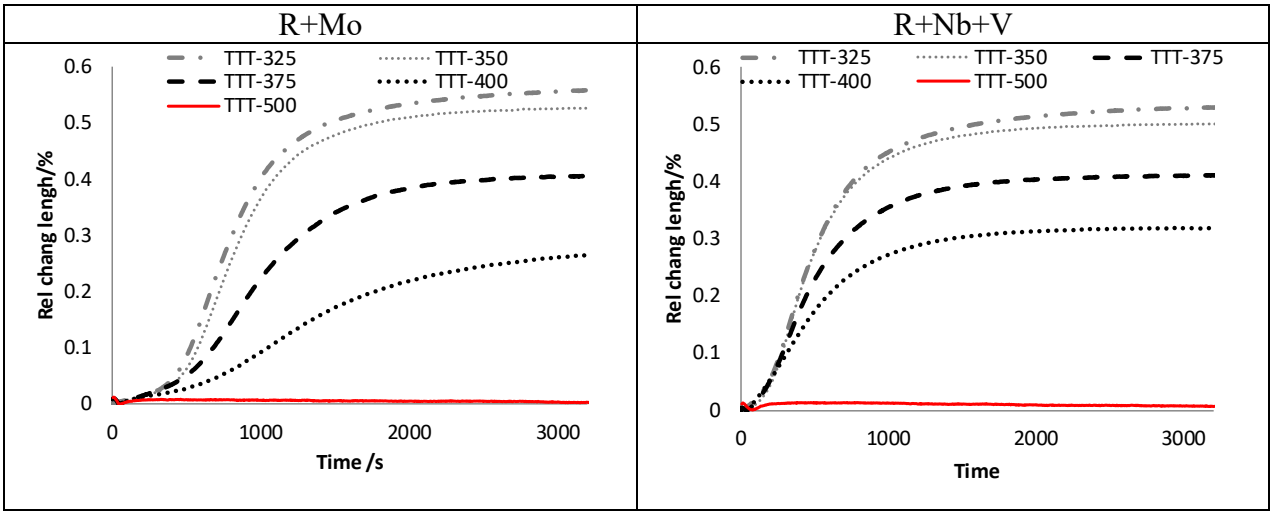

Figure 34. General overview of dilatometric signal of the isothermal transformation at different T for R+Mo and R+Nb+V steel.

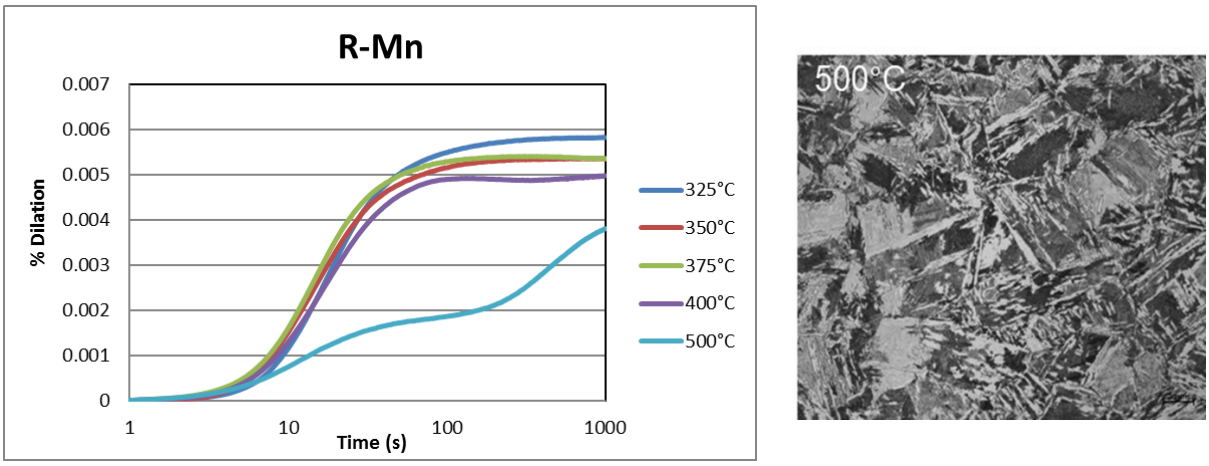

Figure 35. General overview of dilatometric signal of the isothermal transformation at different T for the R-Mn steel. An example of the microstructure obtained after isothermal holding at 500ºC.

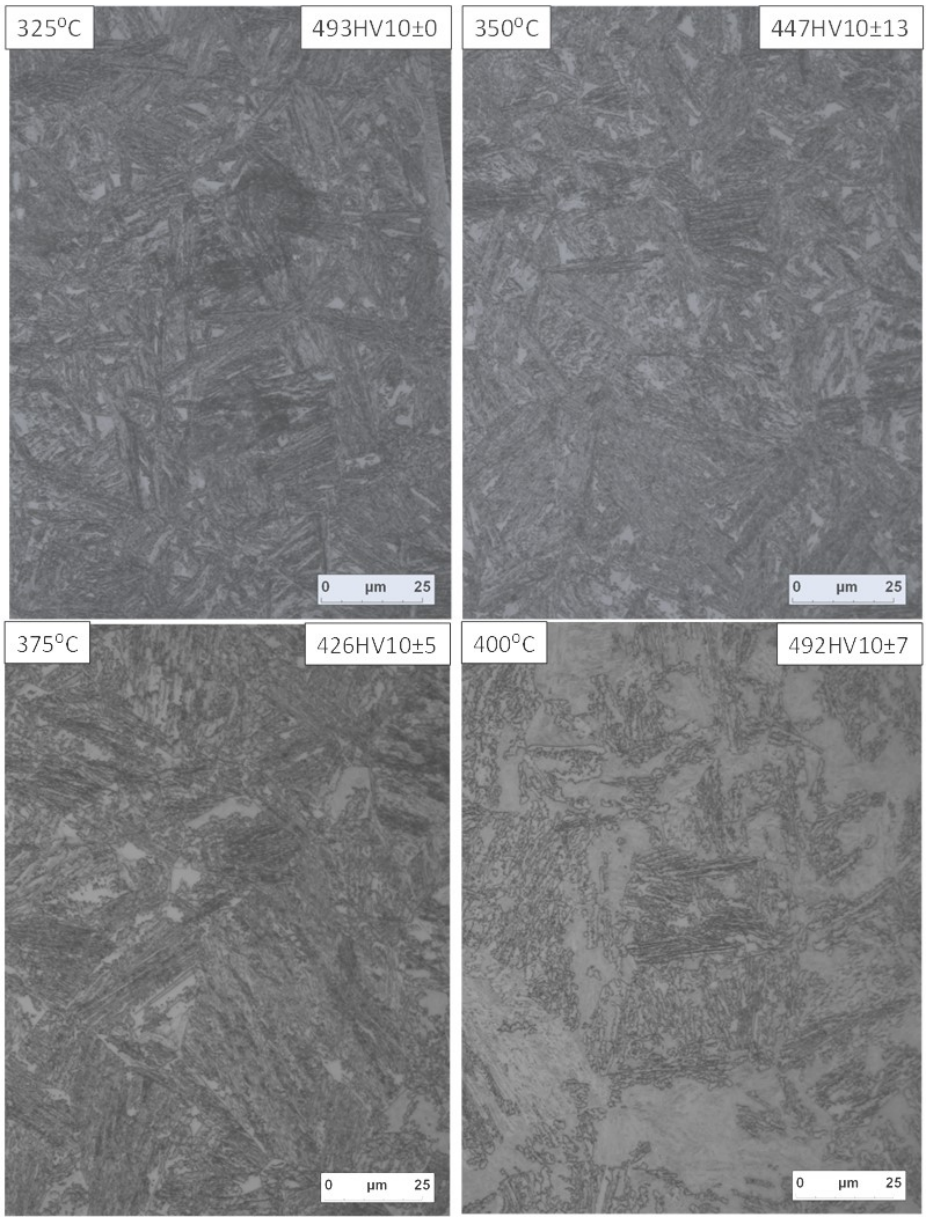

Figure 36. Microstructural evolution as a function of isothermal transformation T for R+Mo steel.

Table 16. Bainitic ferrite plate thickness measurements in some selected cases. The error corresponds to the standard deviation. Error denotes the 95% confidence error.

	T iso/ºC	t iso /h	t /nm	Error /nm
R+Mo+Nb	325	1	94.4	3.8
R+Nb+V	325	1	76.0	3.9
R+C+Mo+Nb	275	1.5	74.3	2.7
R+C+Nb+V	275	1.5	56.3	3.7

3.2.3.v D-TTT diagrams

For the construction of the D-TTT three T ranges were defined for the deformation part, for LT-DTTT deformation was applied at the isothermal transformation T, for the MT-DTTT at 500ºC (bay between F/P and B transformation), and for HT-DTT deformation was applied at 850ºC, see Figure 37.

In general comparison with the TTT data is difficult, as the interpretation of change in length/diameter for dilatometric signal using a compression mode is complicated if not impossible in some cases. In addition to these equipment/experiment related problems, there is a circumstance that add an extra level of difficulty to the interpretation of the effect of ausforming on bainitic transformation based solely on the dilatometry data, i.e. transformation anisotropy. In brief, dilatometric signal, measured in either longitudinal or radial direction is not fully representative of the phase transformation, as bainitic transformation from deformed austenite takes place in a preferential direction, see further details in [17]. There is also the possibility of transformation starting even during the deformation step (mainly at low T) which is not detected as a change in length/radius of the sample. For all those reasons extraction of information regarding the kinetis of the transformation was not always possible.

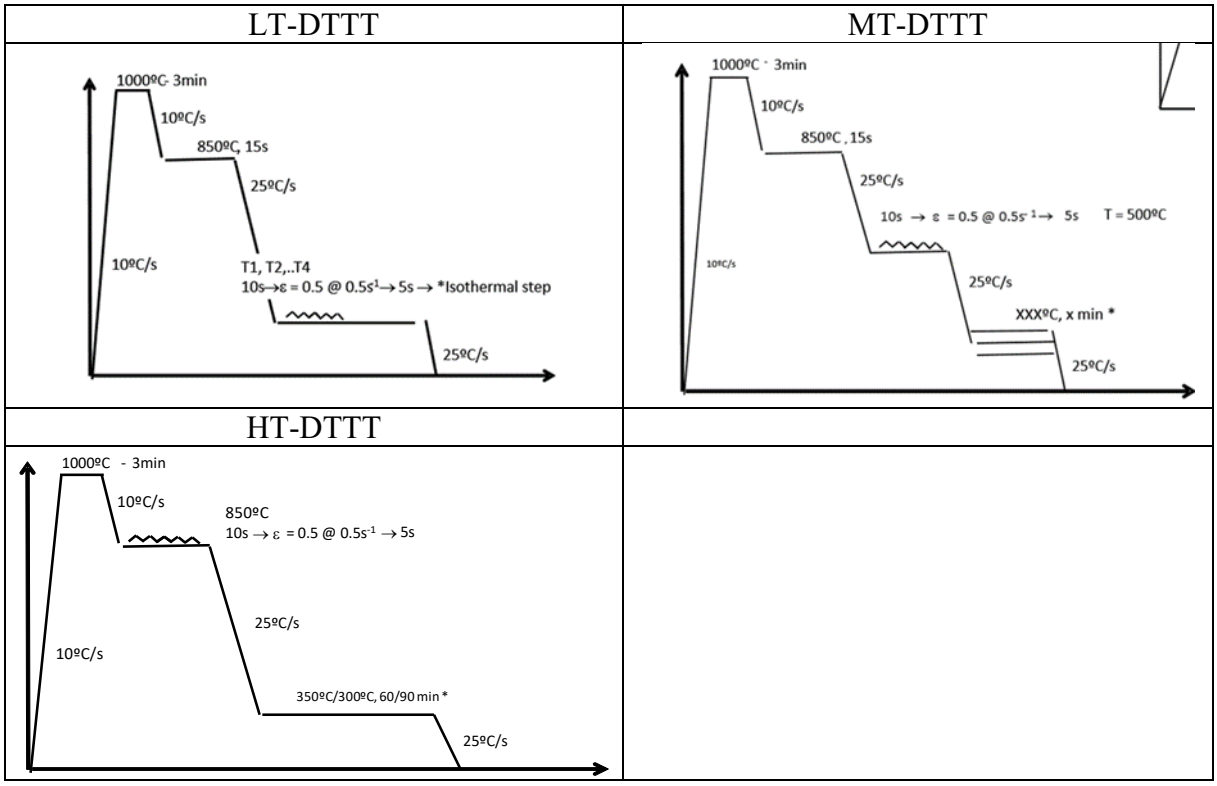

Figure 37. General overview of the parameters to be used on the construction of the D-TTT diagrams.

3.2.3.v.i LT-DTTT

As already mentioned, for this experiments deformation was applied at the same T as the isothermal treatment to obtain bainite. Needless to mention that this was the most challenging part of the D-TTT experiments given the low T and high loads needed to plastically deform the austenite. As already mentioned, it is likely that transformation might start even during the deformation step.

A summary of the most relevant results extracted from these diagrams are summarised from Table 17 to Table 19, and an example of the evolution of the microstructure is shown in Figure 38. The main results of this part, as compared with the TTT, are as follows:

- Introduction of deformation clearly makes retained austenite more stable, following bainitic transformation. XRD shows higher fractions of retained austenite and, when martensitic transformation takes place during final cooling, it occurs at lower T. This austenite stabilisation is

likely to be more related to the constraint effect of the surrounding matrix and its own strength than to the carbon content in the austenite.

- In general, HV values are higher although there is more retained austenite, see for example the R+C+Mo+Nb case at 275ºC with almost twice the amount of austenite, as compared to the TTT case, it has a HV of 617. This is probably a consequence of the deformation hardening of the austenite and the consequent decrease in bainitic ferrite plate thickness.

Table 17. Summary of the main results obtained from the LT-DTTT diagrams. F/P stands for Ferrite/Perlite, B for bainite M for martensite, Ms is the martensite start T, HV is the Vickers hardness, Vγ and Cγ the volume fraction and C content of austenite respectively measured by XRD.

C effect

	Partner	T(ºC)	t (h)	F/P?	B?	M?	Ms(ºC)	HV10	Vγ /%	Cγ /%	Max. stress flow (MPa)
R-C	tkSE	400	1	No	Yes	No	-	418±4	24.5	0.86	804.48
	tkSE	375	1	No	Yes	No	-	455±4	19	0.92	710.4
	tkSE	350	1	No	Yes	No	-	480±7	17	0.95	644.8
	tkSE	325	1	No	Yes	No	-	535±1	14.5	0.86	965.7
R	OULU	400	1	No	Yes	No	-	427	-	-	765
	OULU	375	1	No	Yes	No	-	475	-	-	808
	OULU	350	1	No	Yes	No	-	517	-	-	814
	OULU	325	1	No	Yes	No	-	566	-	-	908
R+C	tkSE	375	1.5	No	Yes	No	-	446±7	38	0.98	893.1
	tkSE	350	1.5	No	Yes	No	-	481±6	33	1.07	898.1
	tkSE	300	1.5	No	Yes	No	-	590±3	25	1.1	942.4
	tkSE	275	1.5	No	Yes	No	-	629±6	25.5	0.92	1057.7

Si effect

	Partner	T(ºC)	t (h)	F/P?	B?	M?	Ms(ºC)	HV10	Vγ /%	Cγ /%	Max. stress flow (MPa)
R-Si+Al	tkSE	400	1	No	Yes	Yes?	-	415±6	28.5	1.02	778.8
	tkSE	375	1	No	Yes	No	-	441±4	27	1.14	840.7
	tkSE	350	1	No	Yes	No	-	499±7	22.5	1.17	903.5
	tkSE	325	1	No	Yes	No	-	528±7	21.5	1.17	888
R+Al	**OULU**	**400**	1	No	Yes	No	-	420			760
	OULU	**375**	1	No	Yes	No	-	517			791
	OULU	**350**	1	No	Yes	No	-	510			818
	OULU	**325**	1	No	Yes	No	-	550			887
R+Si+Al	tkSE	400	1	No	Yes	Yes	-	430±4	34	0.78	765.7
	tkSE	375	1	No	Yes	Yes?	-	438±4	30.5	0.96	807.8
	tkSE	350	1	No	Yes	No	-	489±3	26.5	1.08	831.7
	tkSE	325	1	No	Yes	No	-	524±7	22	1.08	928.9

Table 18. Summary of the main results obtained from the LT-DTTT diagrams. F/P stands for Ferrite/Perlite, B for bainite M for martensite, Ms is the martensite start T, HV is the Vickers hardness, Vγ and Cγ the volume fraction and C content of austenite respectively measured by XRD.

Nb & C effect

	Partner	T(ºC)	t (h)	F/P?	B?	M?	Ms(ºC)	HV10	Vγ /%	Cγ /%	Max. stress flow (MPa)
R+Mo HV5	tkSE	400	1	No	Yes	Yes? (traces of	-	421±2	37	0.74	822.7
	tkSE	375	1	No	Yes	(some	-	440±7	31.5	0.86	866.6
	tkSE	350	1	No	Yes	No	-	481±1	28	0.98	918.1
	tkSE	325	1	No	Yes	No	-	530±4	22.5	1.01	976.5
R+Mo+Nb	OULU	400	1	No	Yes	Yes	150	437	-	-	773
	OULU	375	1	No	Yes	No	-	480	-	-	807
	OULU	350	1	No	Yes	No	-	512	-	-	861
	OULU	325	1	No	Yes	No	-	582	-	-	883
R+C+Mo+Nb HV5	tkSE	375	1.5	No	Yes	(some	-	463±3	36	0.92	923.6
	tkSE	350	1.5	No	Yes	No	-	486±5	37	0.98	937.8
	tkSE	300	1.5	No	Yes	No	-	575±1	27.5	1.13	1107
	tkSE	275	1.5	No	Yes	No	-	617±4	26	0.92	1091

Unsorted elements

	Partner	T(ºC)	t (h)	F/P?	B?	M?	Ms(ºC)	HV10	Vγ /%	Cγ /%	Max. stress flow (MPa)
R-Mn HV5	tkSE	400	4	No	Yes	RA	-	426±1	10.5	1.01	850.8
	tkSE	375	3	No	Yes	No	-	467±2	16	1.19	876.8
	tkSE	350	2	No	Yes	No	-	546±5	14.5	1.22	1011.4
	tkSE	325	1	No	Yes	No	-	588±2	11	1.1	1117.6
R+Si HV5	tkSE	400	1	No	Yes	(Maybe	-	435±2	35.5	0.8	839.9
	tkSE	375	1	No	Yes	(traces of	-	434±10	34.5	0.86	846
	tkSE	350	1	No	Yes	No	-	479±5	28	0.98	937.6
	tkSE	325	1	No	Yes	No	-	532±2	23	1.01	980
R+Cr	OULU	400	1	No	Yes	Yes	180	623	-	-	802
	OULU	375	1	No	Yes	Yes	100	487	-	-	829
	OULU	350	1	No	Yes	No	-	501	-	-	861
	OULU	325	1	No	Yes	No	-	512	-	-	905

Table 19. Summary of the main results obtained from the LT-DTTT diagrams. F/P stands for Ferrite/Perlite, B for bainite M for martensite, Ms is the martensite start T, HV is the Vickers hardness, Vγ and Cγ the volume fraction and C content of austenite respectively measured by XRD.

Nb & C effect

	Partner	T(ºC)	t (h)	F/P?	B?	M?	Ms(ºC)	HV10	Vγ /%	Cγ /%	Max. stress flow (MPa)
R+V HV5	tkSE	400	1	No	Yes	Yes	-	483±6	33.5	0.68	774.3
	tkSE	375	1	No	Yes	Yes?	-	443±1	33.5	0.89	870.6
	tkSE	350	1	No	Yes	Yes?	-	490±3	28	1.01	901.4
	tkSE	325	1	No	Yes	No	-	543±1	23	1.01	977.2
R+Nb+V HV5	tkSE	400	1	No	Yes	Yes?	-	435±2	35	0.8	827.4
	tkSE	375	1	No	Yes	Yes?	-	457±4	31.5	0.92	879.2
	tkSE	350	1	No	Yes	No	-	498±2	23.5	0.95	941.2
	tkSE	325	1	No	Yes	No	-	531±6	22	1.07	953
R+C+Nb+V	OULU	375	1.5	No	Yes	Yes	100	481	-	-	856
	OULU	350	1.5	No	Yes	Yes	120	522	-	-	930
	OULU	300	1.5	No	Yes	No	-	584	-	-	999
	OULU	275	1.5	No	Yes	No	-	627	-	-	1040

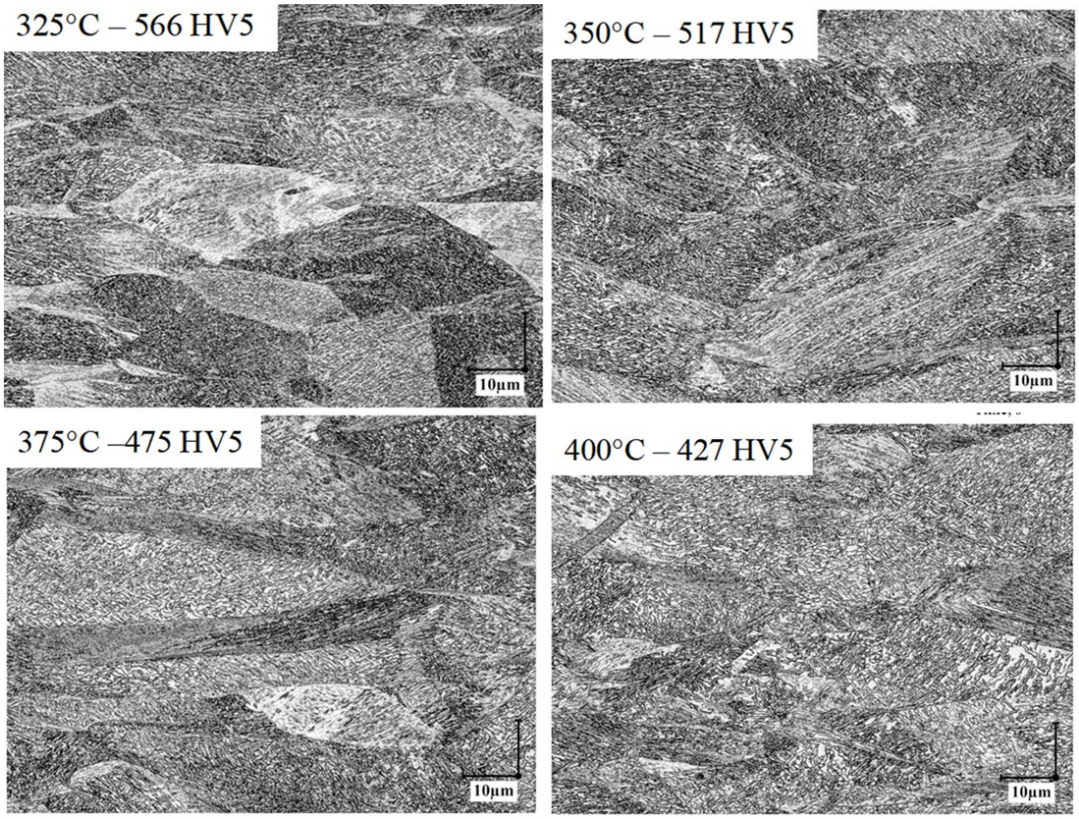

Figure 38. Examples of the bainitic microstructure obtained for the R alloys after the LT-DTTT. T indicates the deformation and isotheral transformation T.

3.2.3.v.ii MT-DTTT

Taking advantage of the bay between the F/P and B transformation curves (TTT), austenite deformation was applied at 500ºC prior to the isothermal bainitic transformation at lower T, see Figure 37.

A summary of the most relevant results extracted from these diagrams are summarised from Table 20 to Table 22, and an example of the evolution of the microstructure is shown in Figure 39. The main results of this part, as compared with the TTT, are as follows:

- Martensite is detected on the room T microstructure after isothermal transformation at lower transform T than those of the TTT case, the calculated Ms in the MT-DTTT tends to be higher than in the TTT, being a clear indication that less bainitic transformation is occurring when austenite is deformed prior to bainitic transformation. The stabilisation of austenite is then mainly controlled by the chemical composition than by deformation/constraint effects.
- In line with those results, HV of the MT-DTTT for bainitic microstructures (no martensite) is lower than in the TTT case. XRD, where available, also confirms this point.
- In terms of transformation kinetics, the onset and end of the transformation as well as the maximum transformation rate indicate that the whole bainitic transformation is shorter than for the TTT. The effect is less pronounced as the isothermal transformation T decreases. Keep in mind, though, that the same fraction of bainite is not achieved in both cases, MT-DTTT and TTT and also that it is very likely that transformation to bainite starts at some point of the deformation process itself (strain induced transformation).

Table 20. Summary of the main results obtained from the MT-DTTT diagrams. F/P stands for Ferrite/Perlite, B for bainite M for martensite, Ms is the martensite start T, HV is the Vickers hardness, Vγ and Cγ the volume fraction and C content of austenite respectively measured by XRD.

C effect

	Partner	T(ºC)	t (h)	F/P?	B?	M?	Onset time /s	Max. differential time /s	End of transformation time /s	Ms(ºC)	HV10	Vγ /%	Cγ /%	Max. stress flow (MPa)
R-C	OULU	400	1	No	Yes	Yes	72	158	381	200	419	17.1	0.41	571
	OULU	375	1	No	Yes	No	79	192	408	-	376	24.2	0.73	577
	OULU	350	1	No	Yes	No	85	202	438	-	411	18.9	0.8	577
	OULU	325	1	No	Yes	No	93	199	470	-	440	13.8	0,88	594
	OULU	300	1	No	Yes	No	-	-	-	-	474	10.6	0.85	576
R	OULU	400	1	No	Yes	Yes	-	181	-	200	470	10.9	0.63	614
	OULU	375	1	No	Yes	Yes	155.9	176	1630.9	200	444	19.3	0.73	605
	OULU	350	1	No	Yes	Yes	100.5	233	1992.5	150	411	28.8	0.92	602
	OULU	325	1	No	Yes	No	86.1	289	1184.1	-	431	23.5	0.92	606
	OULU	300	1	No	Yes	No	89.9	333	1024.9	-	500	13.4	0.66	593
R+C	OULU	375	1.5	No	Yes	Yes	118	441	3811	-	549	19.1	0.66	627
	OULU	350	1.5	No	Yes	Yes	158	458	4598	-	443	32.9	0.99	616
	OULU	300	1.5	No	Yes	No	199	964	4814	-	520	21.4	0.83	605
	OULU	275	1.5	No	Yes	No	228	1323	5023	-	567	20.3	0.47	637

Si effect

	Partner	T(ºC)	t (h)	F/P?	B?	M?	Onset time /s	Max. differential time /s	End of transformation time /s	Ms(ºC)	HV10	Vγ /%	Cγ /%	Max. stress flow (MPa)
R-Si+Al	OULU	400	1	No	Yes	Yes	79	85	407	150	465	-	-	608
	OULU	375	1	No	Yes	Yes	86	152	732	100	363	-	-	605
	OULU	350	1	No	Yes	No	92	162	747	-	378	-	-	598
	OULU	325	1	No	Yes	No	105	189	823	-	458	-	-	602
	OULU	300	1	No	Yes	No	108	221	1101	-	482	-	-	591
	OULU	400	1	No	Yes	Yes	83	103	502	200	534	-	-	618
	OULU	375	1	No	Yes	Yes	90	149	618	120	403	-	-	622
	OULU	350	1	No	Yes	No	95	164	694	-	381	-	-	612
R+Al	OULU	325	1	No	Yes	No	105	191	770	-	404	-	-	621
	OULU	300	1	No	Yes	No	114	212	1061	-	497	-	-	618
R+Si+Al	OULU	400	1	No	Yes	Yes	83	104	652	220	563	-	-	618
	OULU	375	1	No	Yes	Yes	93	177	759	120	412	-	-	630
	OULU	350	1	No	Yes	No	94	165	772	-	405	-	-	626
	OULU	325	1	No	Yes	No	109	201	851	-	491	-	-	620
	OULU	300	1	No	Yes	No	112	258	1009	-	520	-	-	606

Table 21. Summary of the main results obtained from the MT-DTTT diagrams. F/P stands for Ferrite/Perlite, B for bainite M for martensite, Ms is the martensite start T, HV is the Vickers hardness, Vγ and Cγ the volume fraction and C content of austenite respectively measured by XRD.

Nb & C effect

	Partner	T(ºC)	t (h)	F/P?	B?	M?	Onset time /s	Max. differential time /s	End of transformation time /s	Ms(ºC)	HV10	Vγ /%	Cγ /%	Max. stress flow (MPa)
R+Mo	OULU	400	1	No	Yes	Yes	84	163	981	230	572	-	-	596
	OULU	375	1	No	Yes	Yes	88	266	2186	180	477	-	-	612
	OULU	350	1	No	Yes	Yes	95	275	2393	120	427	-	-	616
	OULU	325	1	No	Yes	No	108	386	2104	-	482	-	-	628
	OULU	300	1	No	Yes	No	125	368	2165	-	525	-	-	623
R+Mo+Nb	OULU	400	1	No	Yes	Yes	84	142	782	240	644	-	-	591
	OULU	375	1	No	Yes	Yes	88	186	1786	150	471	-	-	618
	OULU	350	1	No	Yes	Yes	92	312	1890	130	419	-	-	611
	OULU	325	1	No	Yes	Yes	94	353	2293	110	428	-	-	601
	OULU	300	1	No	Yes	No	103	372	2101	-	523	-	-	595
R+C+Mo+Nb	OULU	375	1.5	No	Yes	Yes	85	83	1283	200	606	-	-	626
	OULU	350	1.5	No	Yes	Yes	98	97	3094	150	473	-	-	625
	OULU	300	1.5	No	Yes	No	164	934	5114	-	524	-	-	627
	OULU	275	1.5	No	Yes	No	133	1230	5130	-	611	-	-	634

Unsorted elements

	Partner	T(ºC)	t (h)	F/P?	B?	M?	Onset time /s	Max. differential time /s	End of transformation time /s	Ms(ºC)	HV10	Vγ /%	Cγ /%	Max. stress flow (MPa)
R-Mn	OULU	400	1	No	Yes	No	84	89	296.2	-	392	8.8	0.78	601
	OULU	375	1	No	Yes	No	83	94	331.9	-	403	14.9	1.02	607
	OULU	350	1	No	Yes	No	95	115	564.3	-	417	16.4	1.29	614
	OULU	325	1	No	Yes	No	104	106	672.7	-	412	16.7	1.44	621
	OULU	300	1	No	Yes	No	116	145	1114.1	-	417			615
R+Si	OULU	400	1	No	Yes	Yes	87.3	133	832.3	220	591	-	-	586
	OULU	375	1	No	Yes	Yes	87.1	226	2586.1	160	466	-	-	613
	OULU	350	1	No	Yes	Yes	91.3	240	1790.3	130	428	-	-	622
	OULU	325	1	No	Yes	No	93.9	313	1792.9	-	482	22.7	0.87	612
	OULU	300	1	No	Yes	No	105	326	2101	-	541	17.2	0.67	617
R+Cr	OULU	400	1	No	No	Yes	-	-	-	250	678	-	-	601
	OULU	375	1	No	No	Yes	136	161	1586	230	687	-	-	620
	OULU	350	1	No	Yes	Yes	100	116	3596	230	627	-	-	622
	OULU	325	1	No	Yes	Yes	206	1039	-	190	508	-	-	622
	OULU	300	1	No	Yes	Yes	-	-	-	130	525	-	-	626

Table 22. Summary of the main results obtained from the MT-DTTT diagrams. F/P stands for Ferrite/Perlite, B for bainite M for martensite, Ms is the martensite start T, HV is the Vickers hardness, Vγ and Cγ the volume fraction and C content of austenite respectively measured by XRD.

Nb & C effect

	Partner	T(ºC)	t (h)	F/P?	B?	M?	Onset time /s	Max. differential time /s	End of transformation time /s	Ms(ºC)	HV10	Vγ /%	Cγ /%	Max. stress flow (MPa)
R+V	OULU	400	1	No	Yes	Yes	84	142	1582	200	609	-	-	633
	OULU	375	1	No	Yes	Yes	91	306	1786	180	421	-	-	613
	OULU	350	1	No	Yes	No	141	326	1846	-	472	-	-	635
	OULU	325	1	No	Yes	No	141	347	1906	-	481	-	-	614
	OULU	300	1	No	Yes	No	111	344	1960	-	540	17.3	0.73	610
R+Nb+V	OULU	400	1	No	Yes	Yes	81	120	802	200	490	-	-	629
	OULU	375	1	No	Yes	Yes	82	221	1336	150	421	-	-	611
	OULU	350	1	No	Yes	No	119	241	1496	-	419	-	-	627
	OULU	325	1	No	Yes	No	133	299	1756	-	467	20.8	0.91	613
	OULU	300	1	No	Yes	No	162	298	1810	-	502	17.3	0.8	624
R+C+Nb+V	OULU	375	1.5	No	Yes	Yes	92.1	122	2033.1	160	515	-	-	630
	OULU	350	1.5	No	Yes	No	-	-	-	-	420	-	-	649
	OULU	300	1.5	No	Yes	No	137.7	732	4613.9	-	502	18.7	0.84	627
	OULU	275	1.5	No	Yes	No	148.3	899	-	-	544	23.0	0.43	599

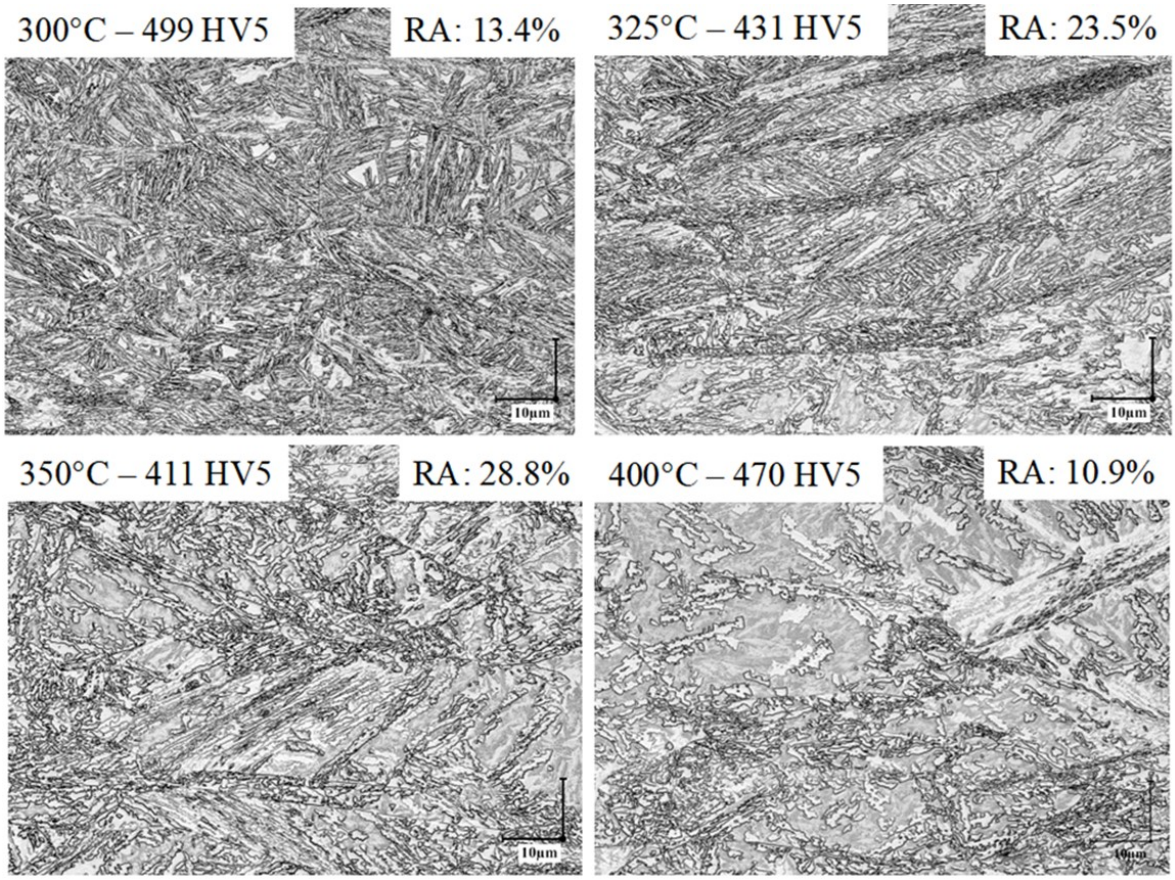

Figure 39. Examples of the bainitic microstructure obtained for the R alloys after the MT-DTTT. Deformation was applied at 500ºC, and the isotheral transformation T is indicated in each micrograph together with HV and volume fraction of retained austenite (RA).

3.2.3.v.iii HT-DTTT

A set of experiments, where deformation is applied at 850ºC and then isothermal transformed at 350ºC or 300ºC was performed as described in Figure 37.

A summary of the most relevant results extracted from these tests are summarised in Table 23. The main results of this part, as compared with the TTT, are as follows:

- There seems to be a certain degree of austenite stabilisation in some cases, owing to lesser extent of bainitic transformation, which leads to a higher fraction of M and higher HV values.
- In other cases the results are very similar to those reported for the TTT.

Table 23. Summary of the main results obtained from the HT-DTTT diagrams. F/P stands for Ferrite/Perlite, B for bainite M for martensite, Ms is the martensite start T, HV is the Vickers hardness, Vγ and Cγ the volume fraction and C content of austenite respectively measured by XRD.

C effect

	Partner	T(ºC)	t (h)	F/P?	B?	M?	Onset time /s	Maximum differential time /s	End of transformation time /s	Ms(ºC)	HV10	Vγ /%	Cγ /%	Maximum stress flow (MPa)
R-C	OCAS	350	1	No	Yes	No	X	126	648	No	430±10	-	-	247
R	OCAS	350	1	No	Yes	Yes	X	342	1854	202	438±16	-	-	231
R+C	OCAS	300	1.5	No	Yes	Yes	605	1458	5336	179	492±17	-	-	242

Si effect

	Partner	T(ºC)	t (h)	F/P?	B?	M?	Onset time /s	Max. differential time /s	End of transformation time /s	Ms(ºC)	HV10	Vγ /%	Cγ /%	Max. stress flow (MPa)
R-Si+Al	OCAS	350	1	No	Yes	No	47	188	1124	No	412±11	-	-	239
R+Al	OCAS	350	1	No	Yes	No	46	216	1116	No	424±4	-	-	255
R+Si+Al	OCAS	350	1	No	Yes	No	72	242	1012	No	438±11	-	-	263

Nb & C effect

	Partner	T(ºC)	t (h)	F/P?	B?	M?	Onset time /s	Max. differential time /s	End of transformation time /s	Ms(ºC)	HV10	Vγ /%	Cγ /%	Max. stress flow (MPa)
R+Mo	OCAS	350	1	No	Yes	Yes	432	767	3150	203	500±60	-	-	250
R+Mo+Nb	OCAS	350	1	No	Yes	Yes	X	980	>3600	200	444±26	-	-	250
R+C+Mo+Nb	OCAS	300	1.5	No	Yes	No	1242	2614	>5395	No	539±10	-	-	248

Unsorted elements

	Partner	T(ºC)	t (h)	F/P?	B?	M?	Onset time /s	Max. differential time /s	End of transformation time /s	Ms(ºC)	HV10	Vγ /%	Cγ /%	Max. stress flow (MPa)
R-Mn	OCAS	350	1	No	Yes	Yes	0	40	281	226	459±9	-	-	230
R+Si	OCAS	350	1	No	Yes	Yes	X	540	2060	197	421±9	-	-	235
R+Cr	OCAS	350	1	No	Yes	Yes	853	2387	>3600	236	561±70	-	-	243

Nb & C effect

	Partner	T(ºC)	t (h)	F/P?	B?	M?	Onset time /s	Max. differential time /s	End of transformation time /s	Ms(ºC)	HV10	Vγ /%	Cγ /%	Max. stress flow (MPa)
R+V	OCAS	350	1	No	Yes	Yes	76	270	1508	214	427±5	-	-	233
R+Nb+V	OCAS	350	1	No	Yes	Yes	X	486	2506	184	421±11	-	-	235
R+C+Nb+V	OCAS	300	1.5	No	Yes	Yes	936	1306	>3600	190	524±17	-	-	252

A summary of the effects and observations made, based on the results of the different D-TTT experiments, is shown Table 24.

Table 24. General effects and observations made based on the results of the different D-TTT experiments.

Compared to	MT-DTTT	HT-DTTT
LT-DTTT	-HV decreases -Austenite is less stable, more M on cooling. -More bainitic transformation takes place	-HV decreases -Austenite is less stable, more M on cooling. -More bainitic transformation takes place
MT-DTTT		-More martensite forms on cooling. -Austenite is less stable -Al bearing steel changes the tendency. -In general there is an increase of HV. -More bainitic transformation

3.3 Work Package 4. Microstructural investigation

3.3.1 Task 4.1: Microstructural investigations (All).

The needed microstructural characterisation for the construction of the CCT, TTT, D-TTT, D-CTT diagrams has been already presented in their corresponding section. Thus, identification of phases such as polygonal ferrite, pearlite, bainite/martensite and retained austenite was performed using light optical microscopy (LOM) and aided with hardness measurements. Examination of selected bainitic microstructures required the use of higher magnification-resolution microscopy, as FEG-SEM. In particular cases the scale of bainitic ferrite plates was also determined as in ref [16].

3.3.2 Task 4.3: TEM & characterization of precipitation (All)

In the four alloys that contain Nb, and right after the homogenisation and rolling process, Figure 5, a precipitation analysis was performed to ensure that all the Nb was is solid solution. To do so, ICPMS (induced coupled plasma mass spectrometry) was used. In order to extract the precipitates from the steel matrix, electrolysis is performed to dissolve the samples. The solution is filtered and analysed by ICP. The amount of Nb found in the filtrate (measured with ICP-OES) corresponded almost perfectly to the total amount of Nb in the steel. As such, it was concluded that the amount of Nb that could be present as Nb(C,N) precipitate is negligible in the hot rolled starting condition, see Table 25.

Table 25. Amount of Nb in solid solution after homogenisation and hot rolling process in Figure 5.

Name	Nb in s.s. (wt.%)	Nb total (wt.%)
R+Mo+Nb	0.021	0.023
R+C+Mo+Nb	0.022	0.025
R+Nb+V	0.018	0.020
R+C+Nb+V	0.021	0.023

The alloys R+Nb+V and R+C+Nb+V and, in particular, the microstructures obtained following the D-CCT after cooling at 1ºC/s, were analysed for the possibility of precipitation (induce by deformation or during cooling). For this purpose, microanalysis fitted to an FEG-SEM was used. The results of the analysis allowed us to conclude that there was no precipitation in any of the alloys and for the selected conditions, as only a few scarce V-rich precipitates were found in the case of the R+Nb+V alloy, see Figure 40.

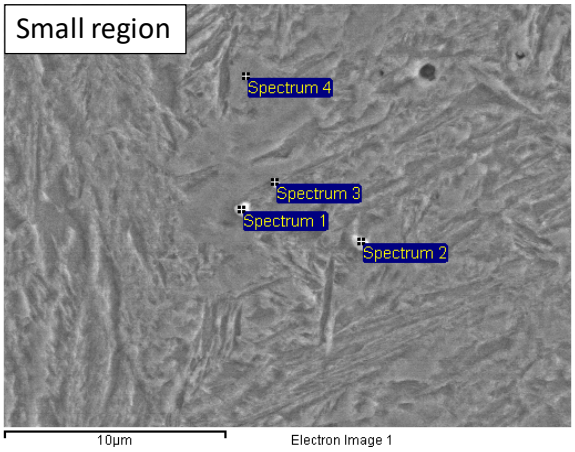

Spectrum	C	Si	Ti	V	Cr	Mn	Fe	Nb
Spectrum 1	52.41	0.88	1.47	0.89	0.20	0.62	26.84	16.69
Spectrum 2	42.11	1.82	0.76	0.59	0.51	0.96	43.33	9.92
Spectrum 3	58.96	0.90	2.04	0.34	0.39	0.71	26.25	10.40
Spectrum 4	40.69	1.77	-0.12	-0.04	0.48	1.38	55.88	-0.03

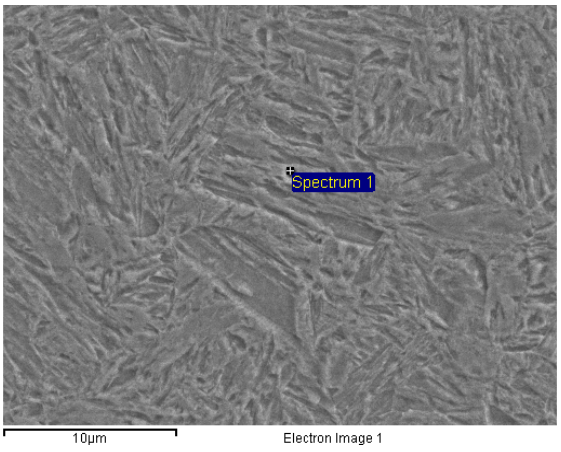

Spectrum	In stats.	C	Si	V	Cr	Mn	Fe	Nb
Spectrum 1	Yes	7.31	1.54	0.13	1.02	1.91	88.11	-0.01

Figure 40. For the R+Nb+V alloy after D-CCT 1ºC/s, only a small region with some scarce Nb precipitates were found.

What is more, tkSE undertook a TEM study on the alloy R+Nb+V to evaluate the possibility of precipitation induced by deformation, for this purpose the LT-DTTT at 400ºC condition was selected.

The microstructure is shown in Figure 41. It consists of very fine lamellar, brownish areas (grey arrows) and brighter, coarser structured areas (yellow arrows). Both areas can be distinguished in the extraction carbon replica in Figure 41.

Precipitation in both areas has been investigated using TEM and EDX. The results of the very fine lamellar areas are shown in Figure 42. In the bainitic ferrite (blue arrows), fine (Nb,V,Ti,Cr)(C,N) precipitates were found. The precipitation diameter is between 2 and 15 nm with an average diameter of approximately 6 nm. No precipitates were found in the retained austenite (green arrows).

The results of the coarser structures are shown in Figure 43. Again fine precipitates of similar size were found in the bainitic ferrite (brown arrows). No precipitates were found in the retained austenite (light green arrows) and martensite (dark green arrows).

The results of the analysis show that, in contrast to the D-CCT results, precipitation can occur during the LT-DTTT process in the bainitic ferrite.

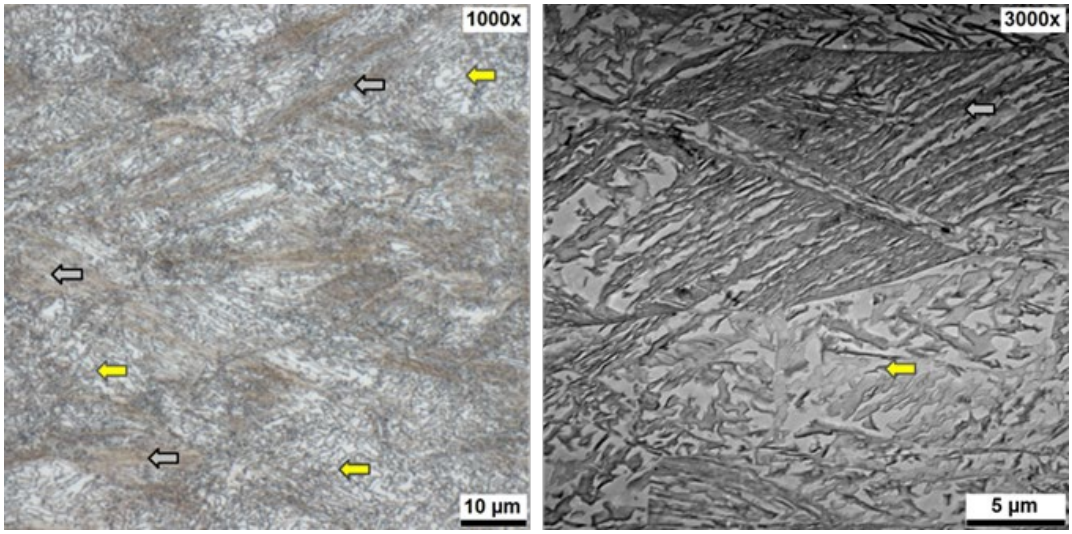

Figure 41. LOM (left) and TEM image of extraction carbon replica (right) after D-TTT at 400 °C of R+Nb+V. Very fine lamellar, brownish areas (grey arrows) and brighter, coarser structured areas (yellow arrows) can be distinguished.

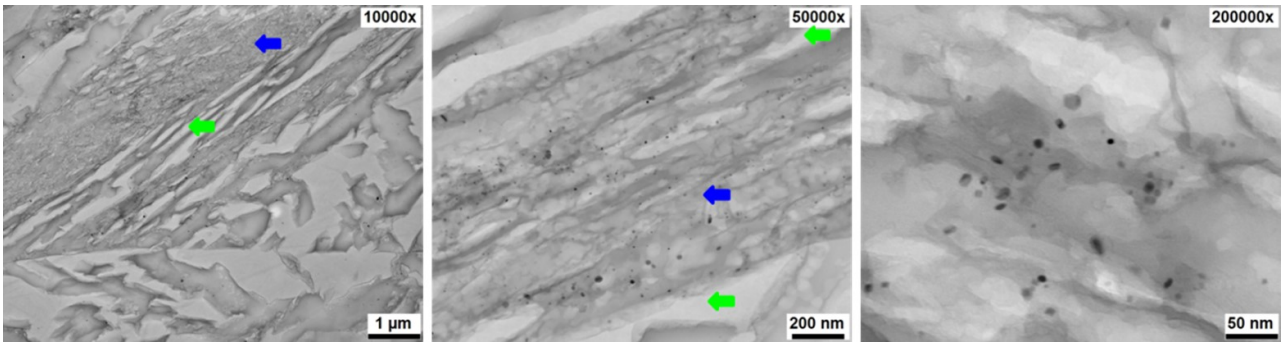

Figure 42. TEM images with different resolution of the very fine lamellar areas after D-TTT at 400 °C of R+Nb+V.

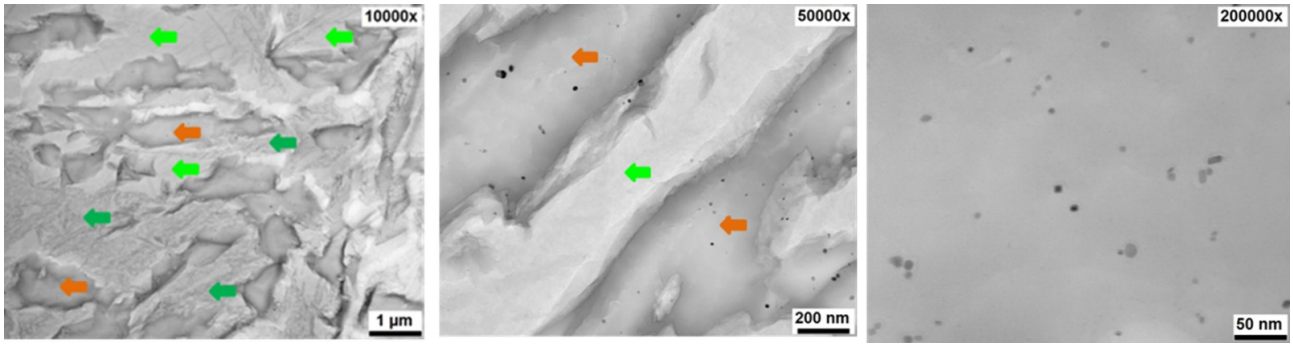

Figure 43. TEM images with different resolution of the coarse areas after D-TTT at 400 °C of R+Nb+V.

3.3.3 Task 4.4: Retained austenite measurements. (All)

Before undertaken any XRD measurements, a round robin was agreed and performed among the consortium. The chosen microstructure was a high carbon high silicon nanostructured bainite, obtained by isothermal transformation at 250ºC for 70h in the frame of another RFCS project. All partners included in their sample preparation procedure, a step dedicated to remove the deformed surface layer, cycles of etching and polishing being the most common. The final outcome of the round robin allowed us to conclude that within the margin of error, all partners reported similar values in terms of volume fraction and lattice parameters.

Measurements of residual austenite content and its lattice parameter, have been performed in selected microstructures. Results thus obtained have been presented and discussed in the frame of the WP2 results.

4 Stage 2. Pilot Plant/Rolling Simulators approach.

4.1 Work Package 3.Pilot Plant Simulators/ Lab rolling production of TMCP material.

4.1.1 Task 3.1: Production of optimized material (tkSE).

Based on the results obtained in WP2, CCT/DCCT and TTT/DTT diagrams, a decision was made in terms of the chemical compositions to be studied in this WP3. Among others such considerations could be summarised as follows:

- As a lean alloying concept is pursued, and Mo is quite expensive, a maximum of one alloy with this element can be selected. There seems to be a synergic effect of Mo+Nb into accelerating the transformation.
- Al content must be limited or otherwise, if the level of N is not controlled well below 30ppm during casting, big AlN precipitates can be present regardless of the heat treatment, with the consequent impairment of resultant mechanical properties irrespective of optimized processing.
- Suffice Mn content isrecommended as there is need of hardenability.
- High C alloys seem to results in more refined microstructures. Though coiling a material/microstructure with very high hardness is challenging.

The alloys selected are the ones shown in the Table 26. All alloys except one (Nº 19) correlate to the one mentioned in Table 3, N in front of the name stands for New. Alloy 19 is a completely new alloy, where Si was reduced in order to minimize the surface quality problems associated with high concentrations of this element and Al was added on one hand to compensate for the lower Si content in avoiding cementite precipitation during bainitic transformation, and on the other hand for its capability to accelerate bainitic transformation.

Table 26. Selection of chemical compositions for pilot plant/rolling simulator all in wt.%.

No	Name	ID	C	Si	Mn	Mo	Cr	V	Al	Nb	P	S	N
16	NR	2	0.4	1.3	2	0	0.7	0	0	0	< 0.012	< 0.003	< 0.003
17	NR+Mo+Nb	8	0.4	1.3	2	0.3	0.7	0	0	0.02			
18	NR+Nb+V	14	0.4	1.3	2	0	0.7	0.1	0	0.02			
19	NR+Nb+V+Al	NEW	0.4	1	2	0	0.7	0.1	0.5	0.02			
20	NR+C+Nb+V	15	0.5	1.3	2	0	0.7	0.1	0	0.02			

One melt of ~300 kg was casted for each of the five selected steels, Table 26, at tkSE. From each melt three 150x150x500 mm^3 blocks of about 100 kg each have been cast. The S content was aimed to be below 20 ppm, and the N content below 30 ppm. The chemical compositions of the alloys/blocks were measured and it only minor deviations in the element contents were detected, the castings were considered to be successful.

As it was stated, a final product thickness of 3 and 12 mm was targeted, thus, roughing was performed after homogenization of the 100kg blocks at 1250°C for 24 hours (to promote elemental diffusion and reduce the segregation), following the scheme in Figure 44. Two out of three cast blocks were rough rolled to 45 mm. The third cast block was rough rolled down to 65 mm to have enough deformation above RST during HT-TMCP-12 mm to get fine recrystallized grains. Note that the exact roughing schedule was performed after concluding Task 3.5 (Processing Data Analysis).

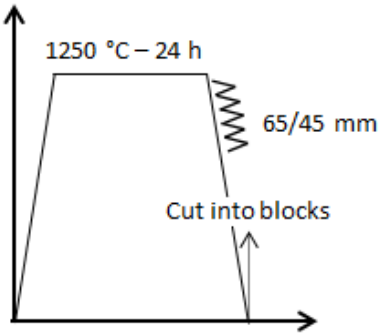

Figure 44. Scheme of the applied homogenisation and roughing procedures.

In order to avoid the decarburised layer of the blocks, a LOM in combination with a composition analysis using a microprobe, allowed to conclude that milling down 2-3 mm should be sufficient to avoid it. Thus, the 45mm blocks were milled down to 40-38 mm and the 65 mm down to approximately 58 mm.

4.1.2 Task 3.2: Grain growth and recrystallization kinetics studies (OULU)

4.1.2.i Recrystallization behaviour. Stress –relaxation (SRX) experiments.

This study was performed using a Gleeble 3800 thermomechanical simulator on Ø10x12mm cylindrical specimens from the NR, NR+Mo+Nb, NR+Nb+V and NR+C+Nb+V alloys.

Keeping in mind that deformation at 850ºC (typical FRT in a strip mill) would be enough to ensure that no recrystallization takes place, and the fact that for the Nb-bearing steels the RST temperatures are well above 850 °C (1000 – 1025 °C), and for the NR steel it is well above 850 °C, no stress relaxation experiments

were conducted at 850 °C. Even experiments conducted at 900-950 °C with NR steel showed only partial or no recrystallization.

The SRX characteristics of the four steels were evaluated and kinetics modelled using a fractional softening approach to determine the time for 50 % recrystallization as a function of strain, strain rate, grain size and temperature by applying stress-relaxation (SRX) tests, in accordance with the regression modelling performed previously by Somani et al. [18] for various steels. A set of experiments were planned for each of the four steels to establish fractional softening equations of the following type for predicting SRX rates in terms of times for 50% recrystallization:

$$t_{50} = A\varepsilon^{p}\dot{\varepsilon}^{q}{d_0}^{s}e^{\frac{Q_{app}}{RT}}$$

where A is a material constant, ε is strain, $\dot{\varepsilon}$ is strain rate, Q_{app} is the apparent activation energy of recrystallization, d is grain size, R is the gas constant and T is absolute temperature. The material dependent constants p, q and s describe the powers of the strain, strain rate and the grain size, respectively. Using t_{50} in combination with an Avrami-type equation, the recrystallized fraction can be predicted as a function of temperature and time.

In order to determine the Q_{app} and material dependent constants (or powers) of different experimental parameters i.e., strain, strain rate, grain size, to establish the equations describing the kinetics of recrystallization, stress relaxation tests were planned, divided in four different groups, see Figure 45, for instance :

- Effect of temperature (900-1250ºC) (7 tests)
- Effect of strain (0.125-0.4) (5 tests)
- Effect of strain rate (0.01-5 s^{-1}) (4 tests)
- Prior austenite grain size (1 test) reheating at 1250 °C for 2 minutes and quenching

Additional tests were carried out to verify the equation of grain size power (s), as suggested by Somani et al. [18] .The equation seems to predict reasonably well for different grain sizes even for the current four steels. However, separate attempts were not made to find the power of grain size, as it is a function of grain size itself.

The temperature dependence of the SRX kinetics for the four steels can be discerned by plotting the t_{50} times estimated at different temperatures for specimens deformed to 0.2 strain at 0.1 s^{-1} against the inverse absolute temperature. The slopes of the plots were used to estimate the apparent activation energies of recrystallization (Q_{app}). When doing this, the cases of incomplete recrystallization (at low temperatures) and metadynamic recrystallization (MDRX) at high temperatures were carefully excluded. The estimated Q_{app} values for the four steels are shown in Table 27.

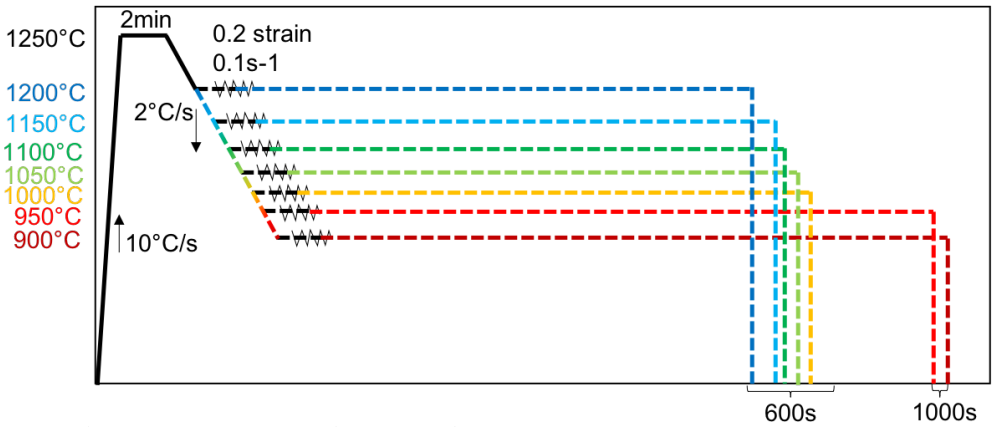

Figure 45. Schematic illustration of a series of stress-relaxation experiments, which is used to investigate effect of temperature (Qapp) on the kinetics of the recrystallization.

The powers of strain (p) and strain rate (q) have been estimated based on the plots of (i) t_{50} vs. strain at 0.1 s^{-1} at a given deformation temperature (1050°C or 1100°C) and (ii) t_{50} vs. strain rate following compression to 0.2 strain at the deformation temperature. The powers of strain (p) estimated from the slopes of the line fits were estimated to be about -2.6, -2.5, -2.0 and -2.0 for the NR, NR+Mo+Nb, NR+Nb+V and NR+C+Nb+V steels, respectively. Similarly, the slopes of the linear fits for the powers of strain rate (q) were estimated as -0.26, -0.23, -0.28 and -0.33 for the NR, NR+Mo+Nb, NR+Nb+V and NR+C+Nb+V steels, respectively. The powers of strain and strain rate are also shown in Table 27.

Table 27. Material dependent constants of the static recrystallization

Steel	Q_{app} (kJ/mol)	p	q
NR	225	-2.6	-0.26
NR+Mo+Nb	261	-2.5	-0.23
NR+Nb+V	260	-2.0	-0.28
NR+C+Nb+V	268	-2.0	-0.33

Taking the power of grain size to be described by the relation $s = 2.13d^{-0.105}$ [18,19] , together with the above values for the other parameters (Q_{app}, p and q) in Equation 1 gives the constant A for the four steels. The SRX rate, therefore, can be reasonably described by the following SRX equations:

NR: $t_{50} = 1.4 \times 10^{-13} \varepsilon^{-2.6} \varepsilon'^{-0.26} d^{s} \exp(225000/RT)$

NR+Nb+Mo: $t_{50} = 2.2 \times 10^{-14} \varepsilon^{-2.5} \varepsilon'^{-0.23} d^{s} \exp(261000/RT)$

NR+Nb+V: $t_{50} = 2.3 \times 10^{-14} \varepsilon^{-2.0} \varepsilon'^{-0.28} d^{s} \exp(260000/RT)$

NR+C+Nb+V: $t_{50} = 1.2 \times 10^{-14} \varepsilon^{-2.0} \varepsilon'^{-0.33} d^{s} \exp(268000/RT)$

Validity of the model for each steel independently is presented in Figure 46 . The lowest competence of predictions versus experimental values was found for steel NR+C+Nb+V, for which the experimental results deviated ±20% of the predicted values, whereas for steels NR, NR+Mo+Nb and NR+Nb+V the accuracies were ±14%, ±9% and ±2%, respectively.

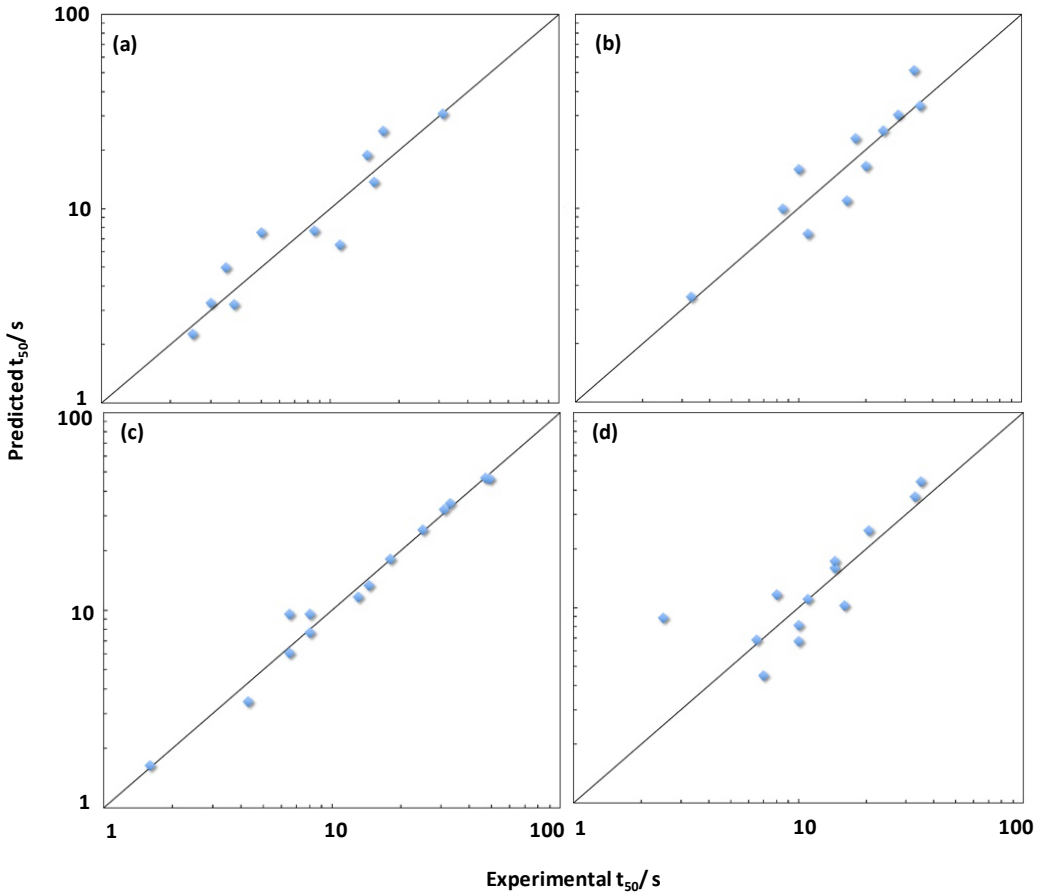

Figure 46. Predicted and experimental t_{50} values for steel a) NR b) NR+Mo+Nb c) NR+Nb+V and d) NR+C+Nb+V.

The equations were used to estimate interpass times in hot-rolling schedules and the results (Table 28 and Table 29) obtained were shared with the project partners. Equations used for estimating t_{99} were based on Avrami type fitting of t_{50} **:**

$$t_{99} = t_{50} * \frac{\ln(1-0.99)}{k}^{1/n} \Rightarrow \text{interpass time: } t_{99} + 20\%$$

An additional 20% time was added because the predictions by stress relaxation may deviate by about 20%, as stated above and the additional time will not cause any significant change in grain size, especially in presence of microalloying elements. For grain size after each pass. D_{rex} was determined using the following equation:

$$D_{rex} = 1.1 D_0^{0.67} \varepsilon^{-0.67}$$

Table 28. Kinetics of static recrystallization for proposed rolling schedule, strain rate $10s^{-1}$.

Test No.	Initial Grain size	RH Temp.,°C	Temp., °C	1/T (1/K)	Reduction %	Strain	Strain rate, s-1	Grain size	Rex'ed t50	Avrami t99	Interpass time s t99+20%
Alloy 2: 0.4C-1.4Si-2.0Mn-0.71Cr-0.005Mo-0.001Nb								652			
1st pass	652,0	1250	1150	0,00070274	10	0,09531018	10	408,2	6,85	24,23	29
2nd pass	408,2		1100	0,00072833	25	0,223143551	10	168,7	1,43	5,06	6
3rd pass	168,7		1050	0,00075586	20	0,182321557	10	106,9	4,75	16,77	20
Alloy 8: 0.4C-1.3Si-2.0Mn-0.71Cr-0.3Mo-0.026Nb											
1st pass	461,0	1250	1150	0,00070274	10	0,09531018	10	323,6	3,23	11,43	14
2nd pass	323,6		1100	0,00072833	25	0,223143551	10	144,4	1,01	3,57	4
3rd pass	144,4		1050	0,00075586	20	0,182321557	10	96,3	5,06	17,88	21
Alloy 14: 0.4C-1.3Si-2.0Mn-0.5Al-0.7Cr-0.005Mo-0.018Nb-0.1V											
1st pass	461,0	1250	1150	0,00070274	10	0,09531018	10	323,6	4,96	17,52	21
2nd pass	323,6		1100	0,00072833	25	0,223143551	10	144,4	1,31	4,65	6
3rd pass	144,4		1050	0,00075586	20	0,182321557	10	96,3	5,52	19,52	23
Alloy 15: 0.5C-1.3Si-2.0Mn-0.7Cr-0.005Mo-0.021Nb-0.1V											
1st pass	461,0	1250	1150	0,00070274	10	0,09531018	10	323,6	4,82	17,04	20
2nd pass	323,6		1100	0,00072833	25	0,223143551	10	144,4	1,32	4,66	6
3rd pass	144,4		1050	0,00075586	20	0,182321557	10	96,3	5,72	20,22	24

Table 29. Kinetics of static recrystallization for proposed rolling schedule, strain rate $50s^{-1}$.

Test No.	Grain size	Initial RH Temp.,°C	Temp., °C	1/T (1/K)	Reduction %	Strain	Strain rate, s-1	Rex'ed Grain size	t50	Avrami t99	Interpass time s t99+20%
Alloy 2: 0.4C-1.4Si-2.0Mn-0.71Cr-0.005Mo-0.001Nb								652			
1st pass	652,0	1250	1150	0,00070274	10	0,09531018	50	408,2	5,74	20,30	24
2nd pass	408,2		1100	0,00072833	25	0,22314355	50	168,7	1,20	4,24	5
3rd pass	168,7		1050	0,00075586	20	0,18232156	50	106,9	3,98	14,05	17
Alloy 8: 0.4C-1.3Si-2.0Mn-0.71Cr-0.3Mo-0.026Nb											
1st pass	461,0	1250	1150	0,00070274	10	0,09531018	50	323,6	2,23	7,89	9
2nd pass	323,6		1100	0,00072833	25	0,22314355	50	144,4	0,70	2,46	3
3rd pass	144,4		1050	0,00075586	20	0,18232156	50	96,3	3,49	12,35	15
Alloy 14: 0.4C-1.3Si-2.0Mn-0.5Al-0.7Cr-0.005Mo-0.018Nb-0.1V											
1st pass	461,0	1250	1150	0,00070274	10	0,09531018	50	323,6	4,15	14,68	18
2nd pass	323,6		1100	0,00072833	25	0,22314355	50	144,4	1,10	3,89	5
3rd pass	144,4		1050	0,00075586	20	0,18232156	50	96,3	4,63	16,36	20
Alloy 15: 0.5C-1.3Si-2.0Mn-0.7Cr-0.005Mo-0.021Nb-0.1V											
1st pass	461,0	1250	1150	0,00070274	10	0,09531018	50	323,6	4,04	14,27	17
2nd pass	323,6		1100	0,00072833	25	0,22314355	50	144,4	1,10	3,90	5
3rd pass	144,4		1050	0,00075586	20	0,18232156	50	96,3	4,79	16,94	20

4.1.3 Task 3.5: Processing data analysis (OCAS)

Although there was information regarding the maximum flow stresses attained during the different simulations performed at lab scale, see Table 30, it was considered paramount to perform a number of trials to see if the different pilot plants would be able to stand the required loads mainly for the MT-TMCP and LT-TMCP. The same trials allowed for the determination of other vital parameters as number of passes and temperatures, cooling before coiling etc. Note that this task was performed even before any roughing of the casts was performed in Task 3.1.

Table 30. Maximum flow stresses obtained during D-TTT in WP2.

		Max. flow stress /MPa		
	Tiso/°C	HT-TMCP (Def T 850ºC)	MT-TMCP (Def T. 550ºC)	LT-TMCP (Def T = Tiso)
R	300		593	
	325		606	908
	350	231	602	814
	375		605	808
	400		614	765
R+Mo+Nb	300		595	
	325		601	883
	350	250	611	861
	375		618	807
	400		591	773
R+Nb+V	300		624	
	325		613	953
	350	235	627	941.2
	375		611	879.2
	400		629	827.4
R+C+Nb+V	275		599	1040
	300	252	627	999
	350		649	930
	375		630	856

Among the proposed chemistries in Table 26, the highest C alloy NR+C+Nb+V was selected, and a separate cast was prepared in a laboratory induction casting furnace in a series of 3 consecutive cast ingots, each weighing ~30kg. For homogenization, the ingots were annealed at 1200ºC for 24h under N_2 atmosphere to promote elemental diffusion and reduce the segregation. The 100mm thick ingots then, were reheated at 1250ºC and rough-rolled to 40mm plates to break the initial cast structure. Afterwards, multiple blocks in 90x140x40 mm3 (LxWxt) dimension each, were cut from the rough-rolled plates and reheated again at 1250ºC for at least 1.5h before finish rolling down to 12mm. The 90x140x40 mm3 (LxWxt) cut blocks were rotated 90º for finish rolling along the width (90mm) direction to minimize the rolling loads at the mill. The finish rolling temperature (FRT) was decreased incrementally from one block to another from 850ºC to 350ºC in steps of 50ºC as shown in Table 31. Typical hot strip rolling schedule is used as shown in Table 31 for TMCP-1 with two passes of 25% reduction at the FRT. The FRTs can be divided into three regions. High temperature (HT)-TMCP: FRT=850-700ºC; Medium temperature (MT)-TMCP: FRT=650-500ºC and Low temperature (LT)-TMCP: FRT≤450ºC.

Table 31. TMCP-1 Rolling schedules with 2 passes at decreasing finish rolling temperatures.

TMCP-1	Thickness (mm)	Reduction (%)	Tempera-ture(°C)											
Initial passes >TnR	40.0	-	1250											
	36.0	10	1200											
	27.0	25	1100											
	21.6	20	1000	Decreasing FRT→										
Finish passes <TnR	16.2	25	850	800	750	700	650	600	550	500	450	425	400	375
	12.15	25	850	800	750	700	650	600	550	500	450	425	400	375
TnR=No-recrystallisation temperature	Block No.		1	2	3	4	5	6	7	8	9	10	11	12

The mean and peak rolling loads and corresponding flow stresses were recorded during each pass. Also, at FRT's≤600ºC, the rolls were continuously monitored for any material related imprint on the rolls. The temperature evolution on the material during the rolling passes was recorded. Post-rolling cooling parameters were varied to finalise the cooling stop temperature and coiling parameters.

An alternative rolling schedule for LT-TMCP was attempted with a single finishing pass of 25% reduction at the FRT to reduce rolling loads on the mill. The rolling schedule is shown in Table 32 as TMCP-2. The rolling loads, flow stresses and temperature evolution during rolling was recorded.

Table 32. TMCP-2 Rolling schedules with 1 pass at low finish rolling temperatures.

Alternative rolling for low FRT					
TMCP-2	Thickness (mm)	Reduction (%)	Tempera-ture(°C)		
Initial passes >TnR	40.0	-	1250		
	36.0	10	1150		
	27.0	25	1100		
	21.6	20	1000		
Finish passes <TnR	16.2	25	850	Decreasing FRT	
	12.15	25	400	375	350
TnR=No-recrystallisation	Block No.		13	14	15

4.1.3.i Rolling loads

The rolling loads and corresponding mean and peak flow stresses are summarised in Figure 47. Though it was possible to finish roll at 375ºC with two consecutive finishing passes each of 25% reduction in TMCP-1 it is not recommended to roll multiple blocks at such a low temperature to avoid damage on rolls. For the alternative TMCP-2 rolling scheme with a single 25% reduction at the low FRTs. the rolling loads and flow stresses are significantly lower than TMCP-1. However, continuous rolling of multiple blocks at such low temperatures should be carefully monitored to avoid any material imprint on rolls. Another critical point is the cooling rate and cooling medium (air or water cooling) used before the finishing passes at low FRTs (≤500ºC) which is discussed later. Till now the TMCP-1 and TMCP-2 plates were air-cooled (~1.5-3.5ºC/s cooling rate) before the finishing passes at low FRTs.

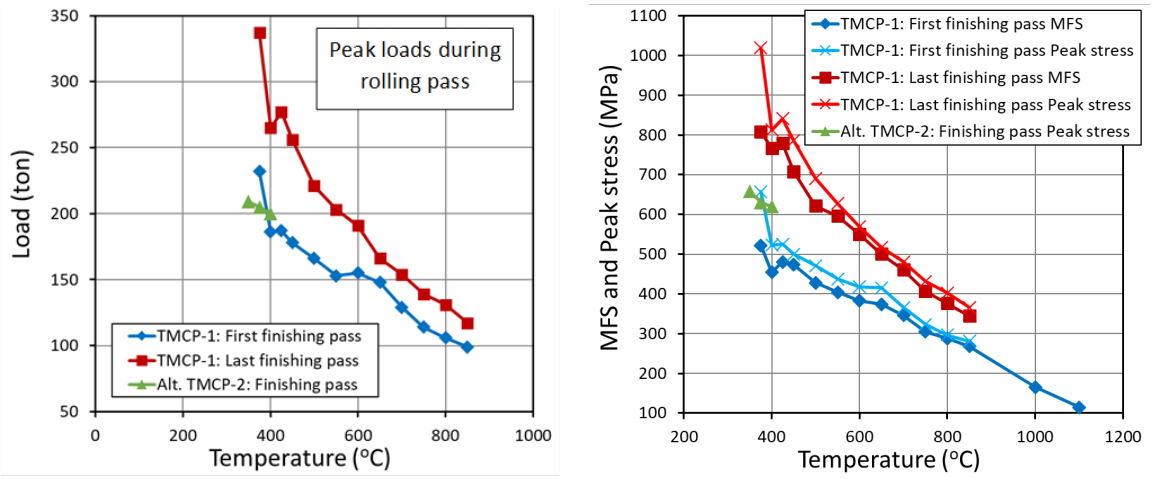

Figure 47. (a) Peak load at the finish rolling pass at different FRTs. (b) Peak stress and mean flow stress (MFS) at the finish rolling pass at different FRTs.

4.1.3.ii Temperature rise during rolling passes.

Temperature of the rolled plates was recorded during the rolling passes and summarized in Figure 48. Due to the intense rolling pressure in TMCP-1, the temperature on the plates increases by ~20-40ºC for FRT≥600ºC (Figure 48a) and by ~50-90ºC for FRT<600ºC (Figure 48b). Even for the alternative TMCP - 2 rolling schedules the temperature on the plates rose by ~30ºC (Figure 48c) during 25% reduction at FRTs=400ºC or 375ºC or 350ºC.

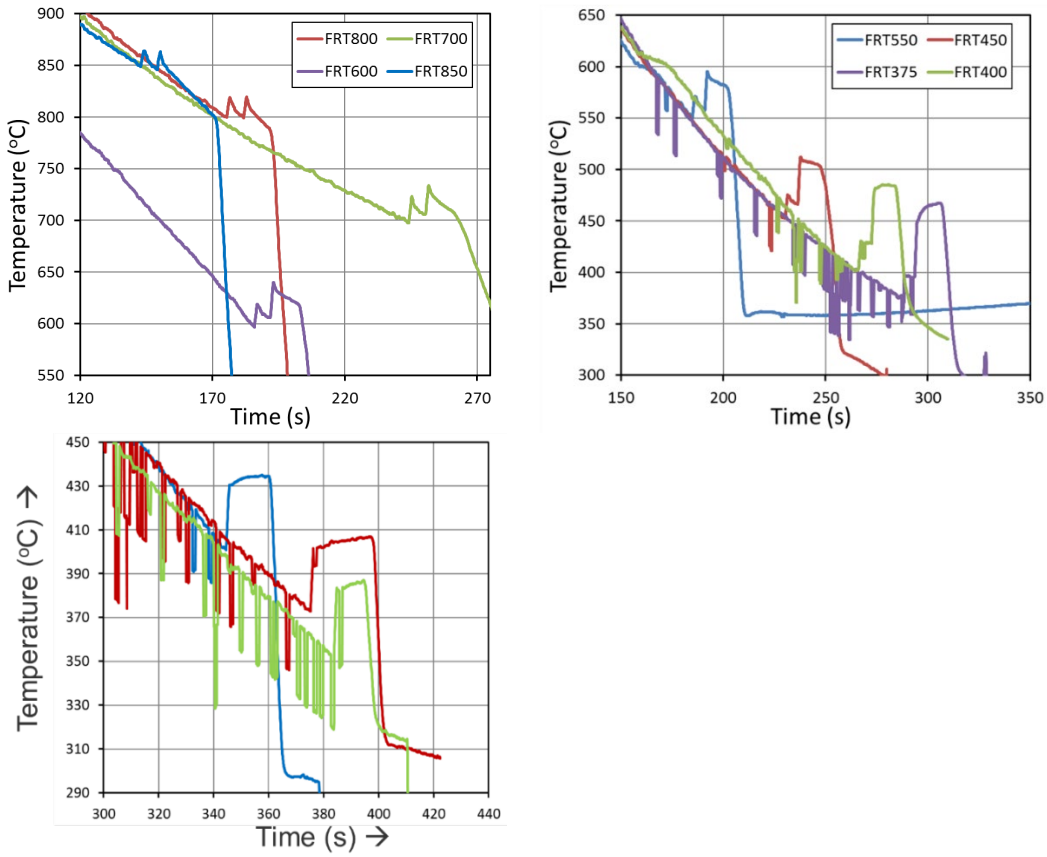

Figure 48. (a) Plate T increases by ~20-40ºC during finishing passes for FRT≥600ºC in TMCP-1. (b) Plate T increases by ~50-90ºC during finishing passes for FRT<600ºC in TMCP-1. (c) Plate T increases by ~30ºC during finishing passes for FRT≤400ºC in TMCP-2.

4.1.3.iii Cooling rates before coiling

The critical cooling rate needs to be more than 1ºC/s to avoid the ferrite-pearlite bay for these compositions. The rolled plates were water cooled before coiling and the cooling rates were varied to simulate laminar cooling in run-out tables. As shown in Figure 49, even with slow initial cooling rates ~7-10ºC/s the cooling rate sharply increased to ~30ºC/s when the temperature drops below 550-600ºC due to the breakage of steam film (Leidenfrost effect) on the hot rolled plates. The cooling stop temperature before coiling is difficult to control at such high cooling rates ~30ºC/s. So it is recommended to stop the water cooling before 550-600ºC and let the hot rolled plates be cooled by free air cooling (free cooling rate at 12mm thickness ~1.5ºC/s). If this cooling rate is superimposed on the deformation continuous cooling diagram as shown in Figure 49b. it can be observed that the ferrite-pearlite bay can be avoided.

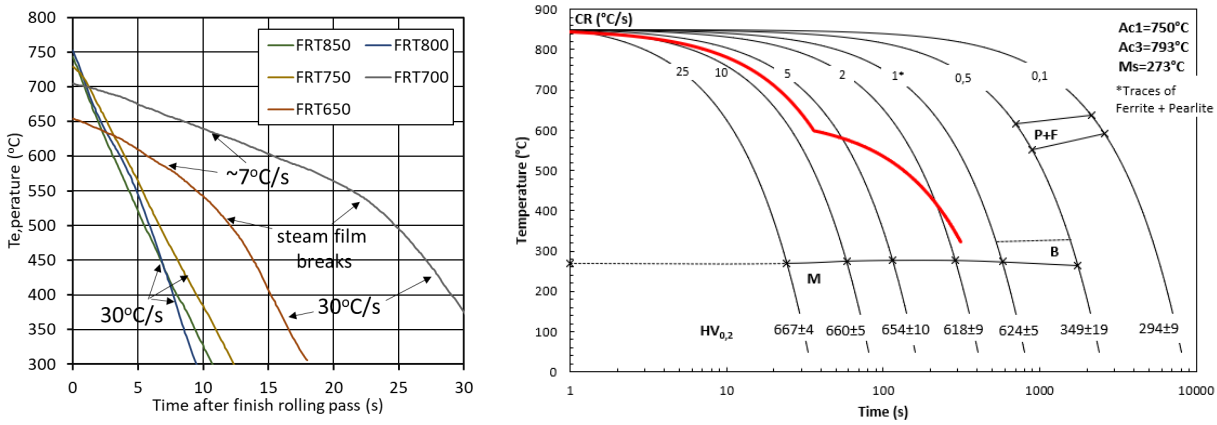

Figure 49. (a) Different water cooling rates at 12mm thick plates after finish rolling pass. (b) The combined water cooling (~7-10ºC/s) and free air cooling (~1.5ºC/s) to avoid ferrite-pearlite bay.

4.1.3.iv Cooling rates before LT-TMCP last pass(es) at low FRT

For LT-TMCP schedules with low FRT≤450ºC, the plates were free air-cooled before the finish rolling temperature. The thickness of the plates was 22mm before the finishing passes at FRT and the free air-cooling rate for the 22mm plates were ~1.5ºC/s (Figure 50) which is borderline to the critical cooling rate of 1ºC/s. For alternate TMCP-2 schedules, the plate thickness was 16mm during cooling before the last pass at low FRT. In that case, free air cooling before the last pass may increase the cooling rate to ~2ºC/s which may not be sufficiently high enough to avoid the ferrite-pearlite bay. Forced air-cooling was attempted which increased the cooling rate to ~3.5ºC/s (Figure 50). But forced-air cooling is not recommended for final trials as this leads to very inhomogeneous cooling of the plates.

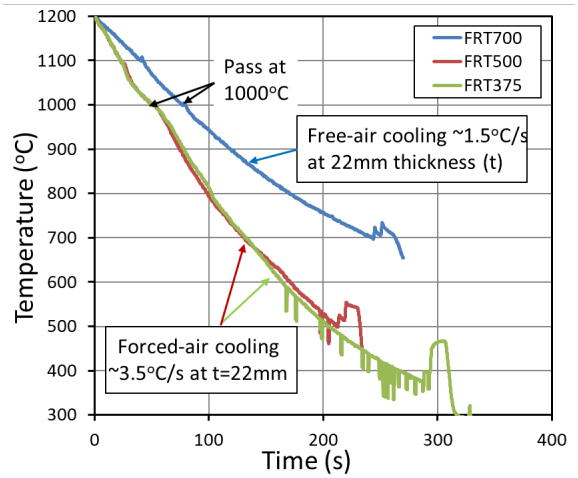

Figure 50. Free air-cooling and forced air-cooling rates before finishing passes at low temperatures for TMCP-1.

The combined water and air cooling scheme as proposed in Figure 49b was attempted on two blocks with alternate TMCP-2 rolling schemes with FRT=400ºC. Even though only one 25% reduction pass was given at FRT=400ºC, the rolling loads were as high as rolling loads for TMCP-1 as shown in Figure 51. Possible martensite or other hard oxide formation at the plate surfaces due to high surface-cooling rates may lead to such higher loads. In this scenario, based on the rolling load or flow stress analysis, and considering chances of roll damage at low temperature rolling, no water will be used during cooling before the LT-TMCP last pass and finish rolling will be done at 400°C.

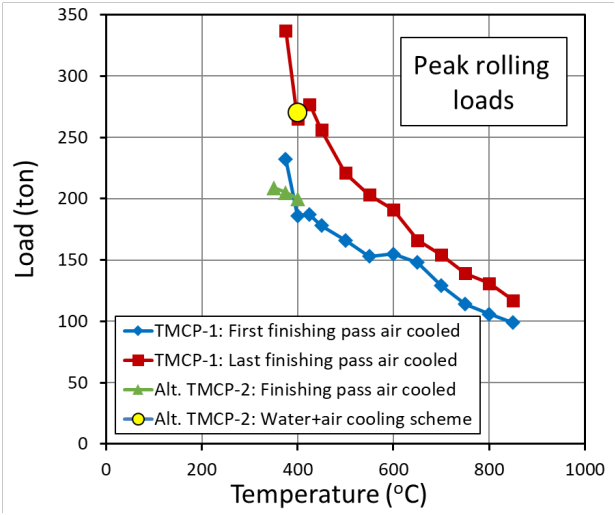

Figure 51. High rolling loads during TMCP-2 last pass after combined water and air cooling as Figure 4b.

4.1.3.v Coiling Temperature.

The temperature evolution in a steel coil after hot rolling has been simulated by tkSE with a finite element model. The model considers air between coil windings, different heat transfer coefficients for the coil eye, shell and front and was validated with thermos camera measurements of produced coils (Reheating due to phase transformation is not considered for the presented simulations). For the coil a strip width of 850 mm. a thickness of 3 mm and a length of about 970 m was assumed. Six positions at the coil have been considered, see Figure 52. On one hand the outer coil, which typically undergoes fast cooling and as a

contrast the coil center, which cools down rather slowly. The results for the coiling simulations considering coiling temperatures of 350°C. 325°C and 300°C are presented in Figure 53.

Considering the simulation results a rather low coiling temperature of 300 (and maybe also 325 °C) might be too low to avoid martensitic transformation during coiling considering the high end of transformation times determined in WP2 (DTTT. TTT). Using a coil cooling rate of 0.01 °C/s for the TMCPs is a realistic cooling rate for a coiling temperature of 350 °C.

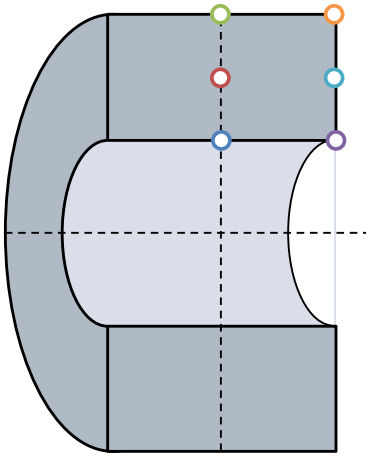

Figure 52. Geometry used for the coiling simulations.

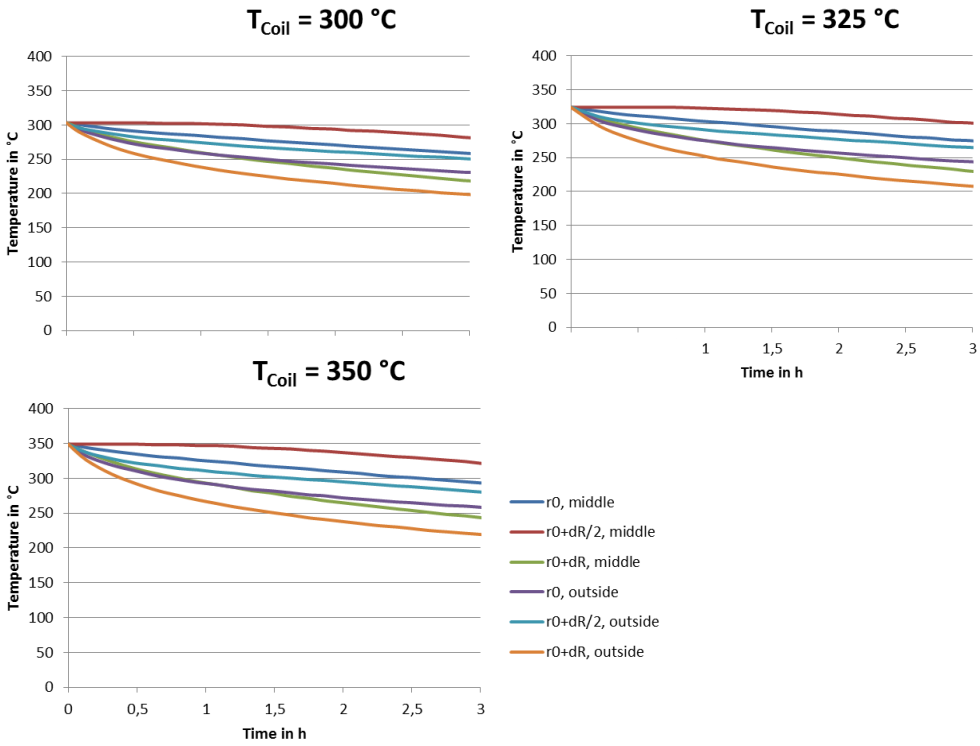

Figure 53. Results of the T profiles of the coiling simulations on different positions of the coil, as in Figure 52.

4.1.3.vi Conclusions

To increase the total hot reduction for HT-TMCP, 60mm will be used as the starting thickness for finish rolling down to 12mm. The HT-TMCP plates will be water-cooled at ~7-10ºC/s cooling rate till 500ºC and after that will be free air-cooled till the coiling temperature. For LT-TMCP the starting thickness is kept as 40mm similar to the above trials. No water will be used and the LT-TMCP plates will be only free air-cooled before the last pass at low FRT. The finalized rolling schedules are shown in Table 33. The final coiling temperature (T_{iso}) was selected as 350ºC.

Table 33. Finalized HT-TMCP and LT-TMCP rolling parameters.

HT-TMCP			
TMCP	Thickness (mm)	Reduction (%)	Temperature(°C)
Initial passes >TnR	60.0	-	1250
	51.0	15	1200
	33.2	35	1150
	21.5	35	1100
Finish passes	16.2	25	820
	12.12	25	820

LT-TMCP			
TMCP	Thickness (mm)	Reduction (%)	Temperature(°C)
Initial passes >TnR	40.0	-	1250
	36.0	10	1200
	27.0	25	1150
	21.6	20	1100
Finish passes <TnR	16.2	25	850
	12.15	25	400

4.1.4 Task 3.3 & 3.4: Simulation of Thermomechanical schedules (HT, MT and LT) (tkSE, OULU, OCAS).

With the information gathered in Task 3.5 and Task 3.2, the consortium was now ready for the application of the TMCP treatments.

4.1.4.i Final distribution of Thermomechanical schedules

Due to technical limitations of some of the equipment to be used by different partners, the final distribution of TMCP as well as the final thickness aimed and the mentioned type of equipment is listed in Table 34.

Note that the same Table 34 contains a Benchmark Isothermal-TMCP performed by OULU for 12mm product.

Table 34. Final distribution by partners and TMCP, and the type of equipment used.

	tkSE	OULU	OCAS
LT-TMCP	3 mm (HDS-V40 -Plain strain)		12 mm (laboratory rolling mill)
MT-TMCP	3 mm (HDS-V40 -Plain strain)	12 mm (Rolling mill)	
HT-TMCP	3 mm (Rolling mill)		12 mm (Rolling mill)
Benchmark (Isothermal-TMCP)		12 mm (Rolling mill)	

4.1.4.ii Isothermal-TMCP (Benchmark)

The sole purpose of this TMCP was to provide information of the microstructure obtained after following a regular rolling schedule (above the RST), see Figure 54, followed by isothermal treatment at 350 ºC in a 12mm product, providing then a benchmark to compare with the others TMCP. Further details on some of the procedures are provided in the MT-TMCP (OULU) section few pages after.

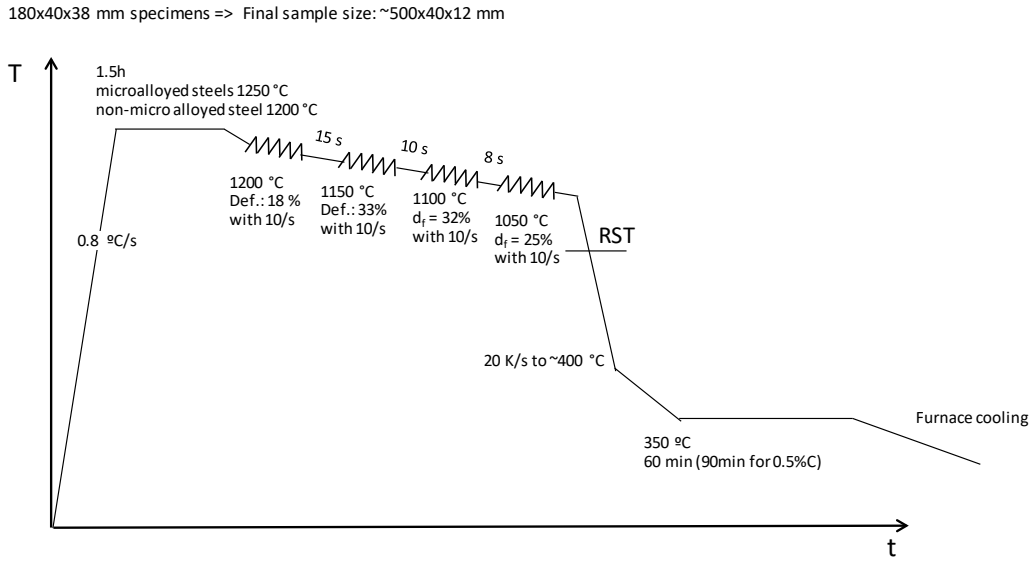

Figure 54. Isothermal-TMCP applied for the 12 mm product (OULU).

4.1.4.iii HT-TMCP

The details on the parameters and partner for the HT-TMCP are shown in Figure 55.

In the 3 mm case at tkSE, water-cooling was applied down to approximately 600 °C. The 3 mm plates are thin enough that subsequent air cooling is sufficient to avoid phase transformation during cooling according to the DCCTs from WP2. An example of the measured air cooling time-temperature curve of an HT-TMCP-3mm sample is shown in Figure 56. Using the rolling force and the rolling geometry the mean flow stress was calculated for the five rolling passes at tkSE. Figure 57 shows the results for NR+C+Nb+V. Above RST the mean flow stress steadily increases with each rolling pass up to 155 N/mm^2 according to the decreasing thickness (and the different reduction). The final rolling pass, which takes place at a much lower temperature (820°C) shows a much higher mean flow stress of 402 N/mm^2.

Based on the microstructural characterisation and preliminary tensile tests of the 1st campaign, tkSE divided the tests in different campaigns, where the isothermal part was changed. It was decided to increment the time at the isothermal T (in case bainitic transformation were not completed) and also to decrease the transformation T down to 325ºC, 2nd & 3^{d} campaign.

1st Campaign: Isothermal at 350ºC-30 min. All alloys except NR

2nd & 3^{d} Campaign: Isothermal at 350ºC-3h & 325ºC-3h. All alloys.

In the case of OCAS (12 mm), the HT-TMCP was applied according to Figure 55. It has to be pointed out that cooling a 12mm thickness plate from 800ºC down to the isothermal temperature (350ºC), represented a big challenge. A first forced cooling (water cooling) from 800ºC to 450ºC was applied, then air cooling to 350ºC. Once the plates were stabilized at 350ºC they were transferred to a furnace at 350ºC. Due to the continuous character of the process, the plates spend, within the 350ºC furnace, different times according to the order of entry that varied from 20 to 80 min. The ulterior analysis of the cooling curves revealed that different plates of the same alloys would also present different cooling profiles from 800 to 350ºC, see some examples in Figure 58 and Figure 59. The profiles showed that after switching between forced cooling into air cooling, there were different scenarios. Some where the switch T was above or below 450ºC, and other cases where some transformation was detected by the increase in T, in any case, the time to reach 350ºC, moment at which is transferred to the isothermal furnace, could be as long as 350-400s and some phase transformation can be anticipated in that period. Plates were identified in all cases so a complete history of their cooling profile was recorded.

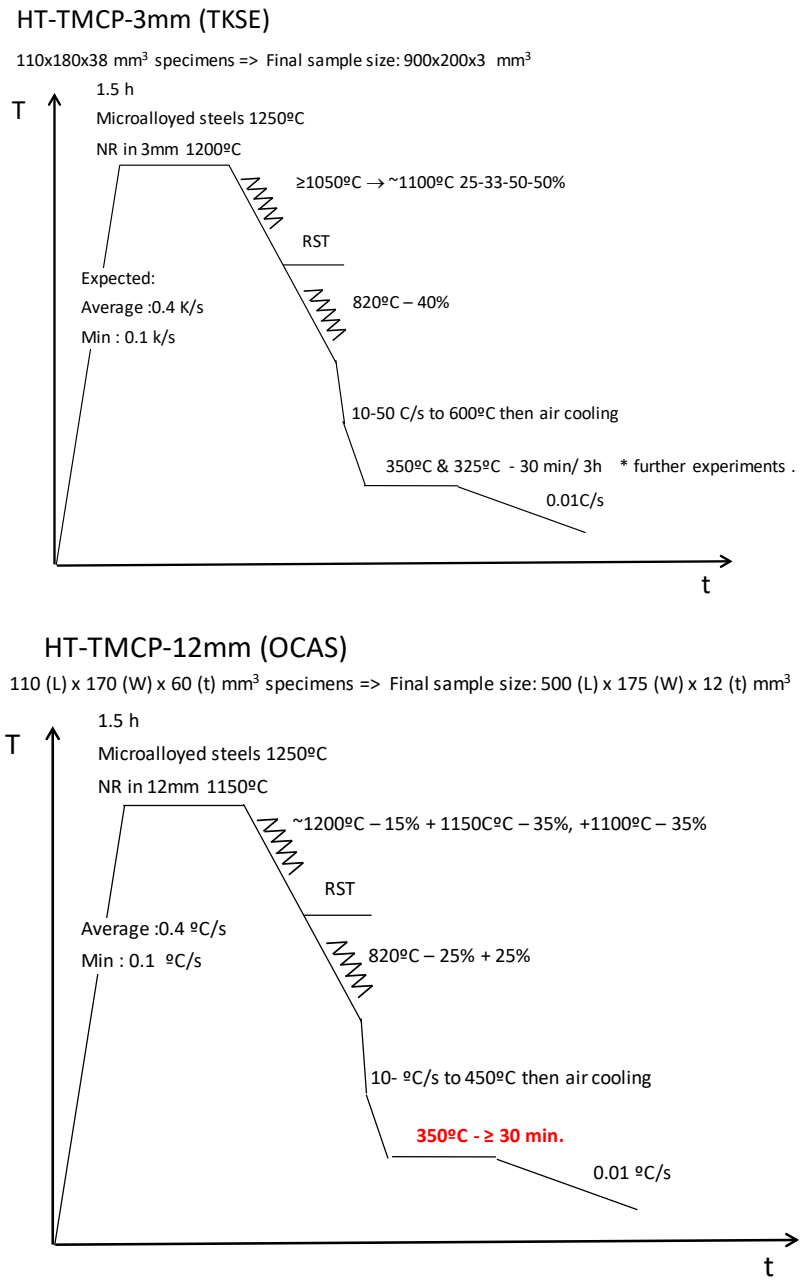

Figure 55. HT-TMCP applied for the 3mm (tkSE) and 12 mm (OCAS) product.

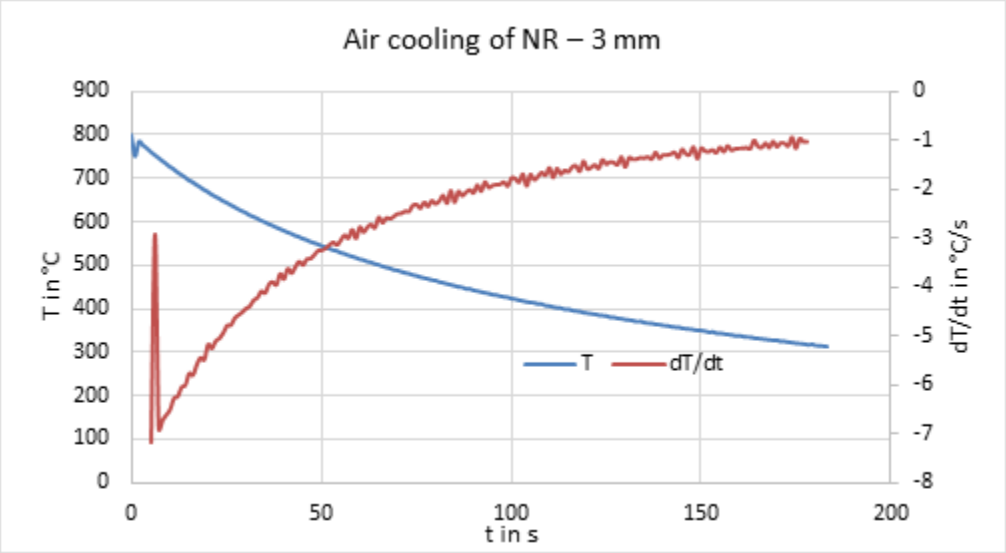

Figure 56 Air cooling curve of a 3 mm NR plate.

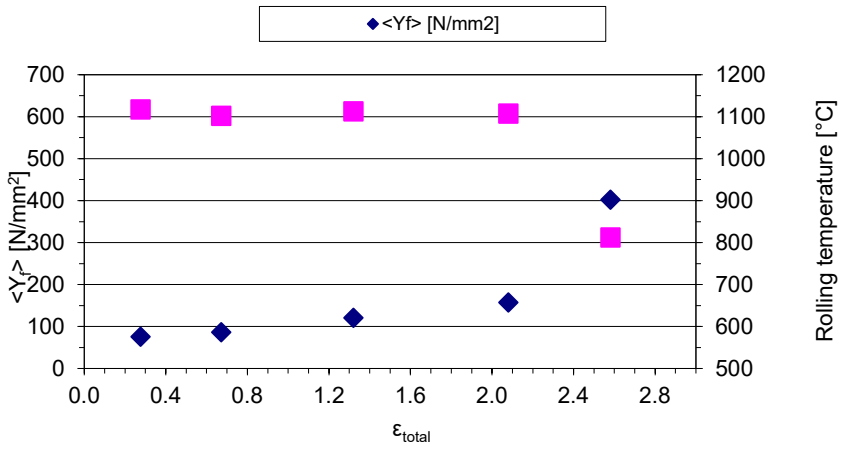

Figure 57: Mean flow stress and rolling temperature for the HT-TMCP-3mm of NR+C+Nb+V at tkSE

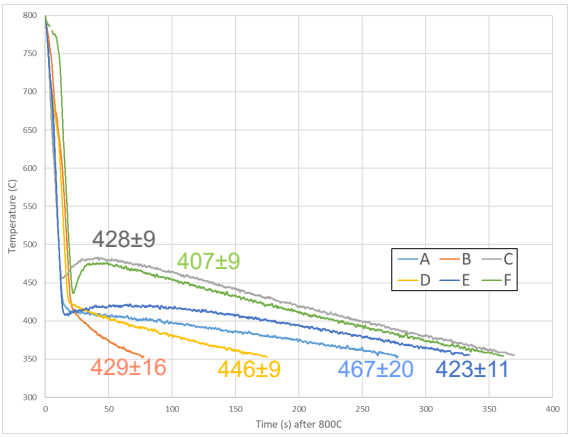

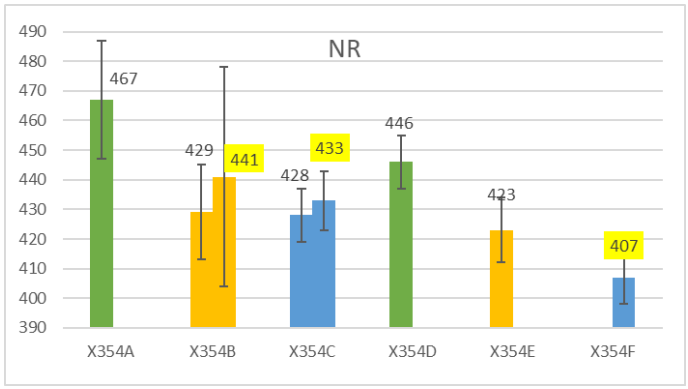

Plates	Partners	Isothermal time at 350C	HV10	Stdev
X354A	TKS	70 min	467	20
X354B	OULU	60 min	429	16
			441	37
X354C	OCAS	50 min	428	9
			433	10
X354D	TKS	40 min	446	9
X354E	OULU	30 min	423	11
X354F	OCAS	20 min	407	9

HV10 on through-thickness cross-section

HV10 on surface

Figure 58. After rolling cooling profiles obtained in 6 plates of the NR alloy. Also indicated the HV and the partner in possession of the plate for WP4 and WP5.

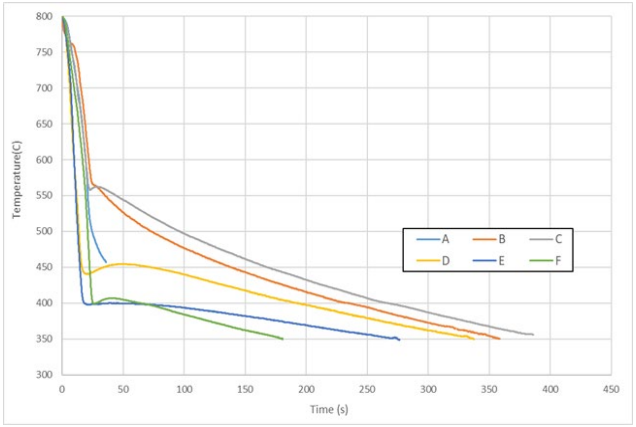

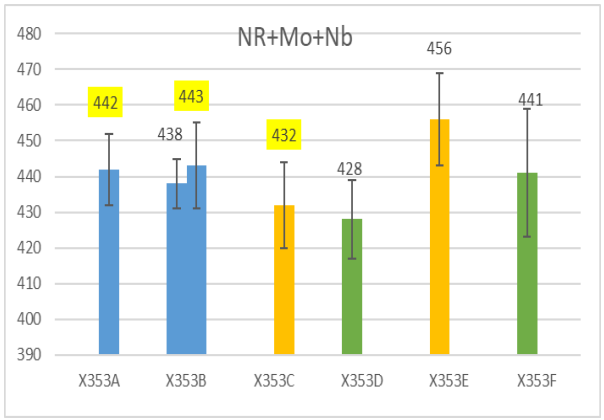

Plates	Partners	Isothermal time at 350C	HV10	Stdev
X353A	OCAS	60 min	442	10
X353B	OCAS	50 min	438	7
			443	12
X353C	OULU	40 min	432	12
X353D	TKS	30 min	428	11
X353E	OULU	20 min	456	13
X353F	TKS	60 min	441	18

HV10 on through-thickness cross-section

HV10 on surface

Figure 59. After rolling cooling profiles obtained in 6 plates of the NR+Mo+Nb alloy. Also indicated the HV and the partner in possession of the plate for WP4 and WP5.

4.1.4.iv MT-TMCP

For details on the parameters and partner for the MT-TMCP see Figure 60.

The MT-TMCP with a final thickness of 3 mm was done at tkSE with a Gleeble HDS-V40 using plane strain compression samples. The HDS-V40 has a 40 ton hydraulic system. Due to the low deformation temperature of the final deformation, the standard sample size of 50x150x10 mm^3 required too high deformation forces and led to the breakage of the deformation stamps. Thus a smaller sample size of 25x150x10 mm^3 was used. The deformed area of the sample is thus 25x10 mm^2. Selected stress-strain curves are shown in Figure 62. A peak stress of approximately 1500 MPa was observed.

The HDS-V40 samples are heated by Joule heating. The current is adjusted to reach the set temperature at position 1 (T1) in the undeformed area (see Figure 61). The deviation from T1 in the deformed area was measured by applying three additional thermocouples on an already deformed sample. An approximately 10 °C higher temperature compared to T1 can be expected in the center of the deformed area.

The MT-TMCP with a final thickness of 12 mm was performed at Oulu with a two-high, reversible laboratory rolling mill equipped with direct quenching facilities. The maximum width of the sample will depend on the available load (maximum of 1 MN) and temperature of rolling. The dimensions of the rolls are 250 mm in diameter and width 250 mm as well. Normally, the width of the plate never exceeds about 80-100 mm for high temperature rolling, for instance. The cooling section consists of 80 nozzle jets, 40 of them above the run-out table and 40 below the table, powered by high pressure water pump capable of delivering water jets in range of 1–16 bars through the nozzles. In addition, the mill is capable of cold rolling when equipped with another pair of rolls.

Blocks of 110x40x38 mm (length x width x thickness) were rolled to a plate with final thickness of 12 mm according to schedule shown in Table 35. In between third and fourth pass, 19 mm thick plate was water-cooled from 1050°C to 550°C at cooling rate of 20K/s. A typical time-temperature curve is shown in Figure 63. As seen in the same figure, cooling system is kept up to approx. 400°C moment at which the coiling system is turn off to allow to enter the coiling step. Results in Figure 64 shows that regardless of the attempts the plates spent most of the coiling at temperatures higher than 350°C, where the transformation already started, leading to coarser structure than in MT-DTTT with corresponding isothermal holding temperature

Table 35. Rolling schedule for MT-TMCP 12 mm applied at OULU

	Thickness mm	Reduction %	Temperature ºC
Hot passes	40		
	36	10	≅1200
	27	25	≅1150
	19	30	≅1050
MT passes	15	21	550
	12	20	550

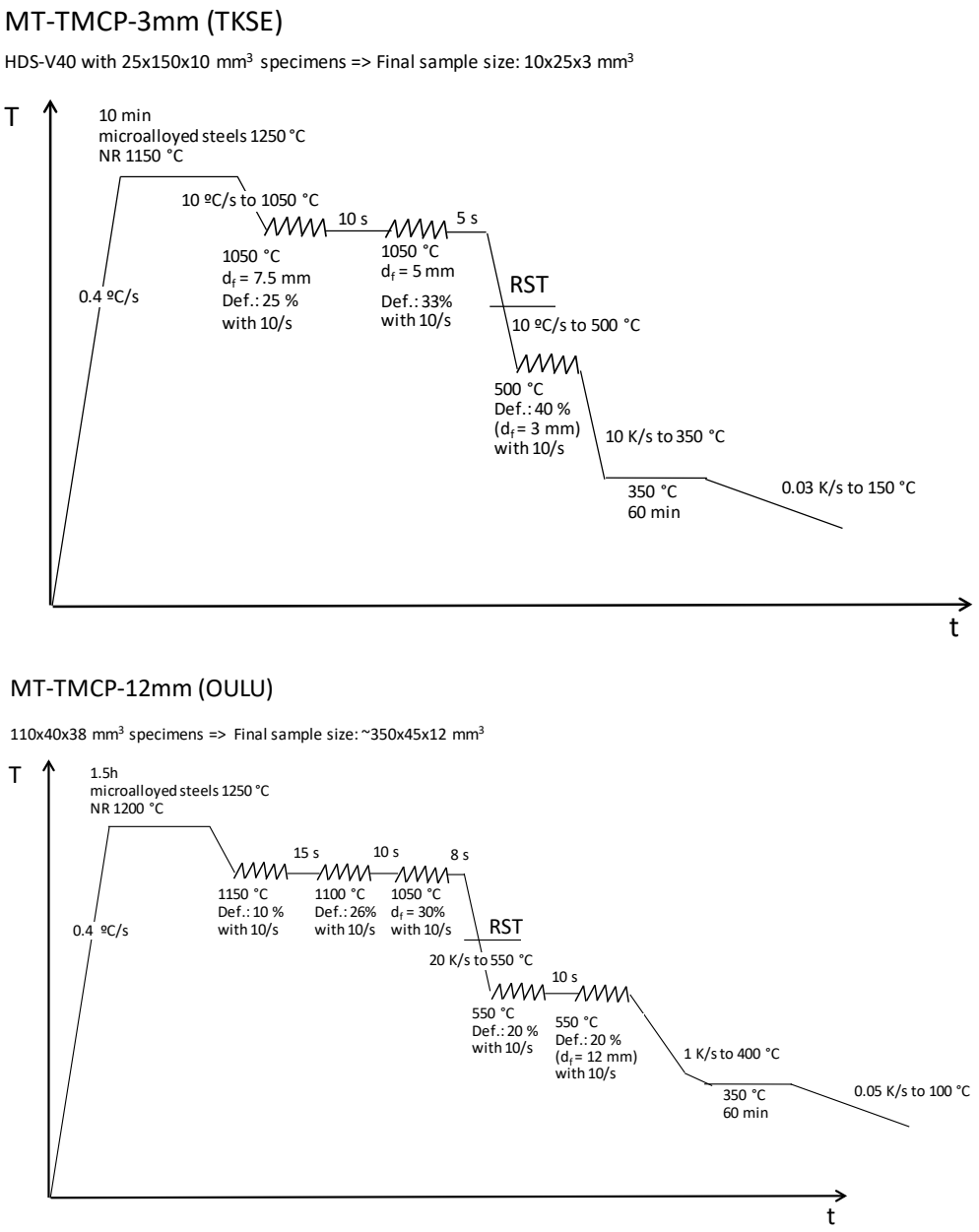

Figure 60. MT-TMCP applied for the 3mm (tkSE) and 12 mm (OULU) product.

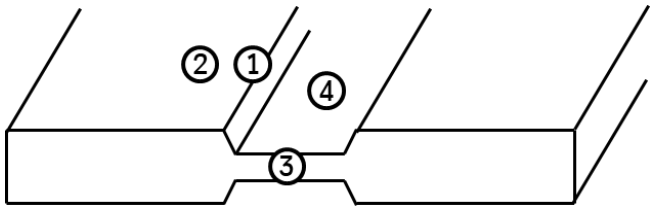

Figure 61. Position of thermocouples on an already deformed HDS-V40 plain strain compression sample to measure the temperature homogeneity in the sample. With a set temperature at position 1 of 350 °C the following temperatures were measured: T2 = 338 °C. T3 = 362 °C. T4 = 363 °C.

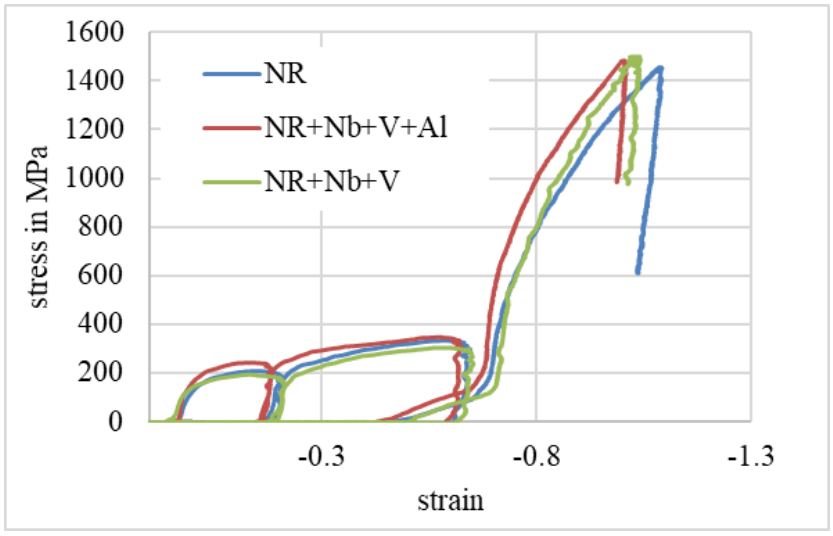

Figure 62. Selected HDS-V40 stress strain curves of the three MT-TMCP-3mm deformation steps.

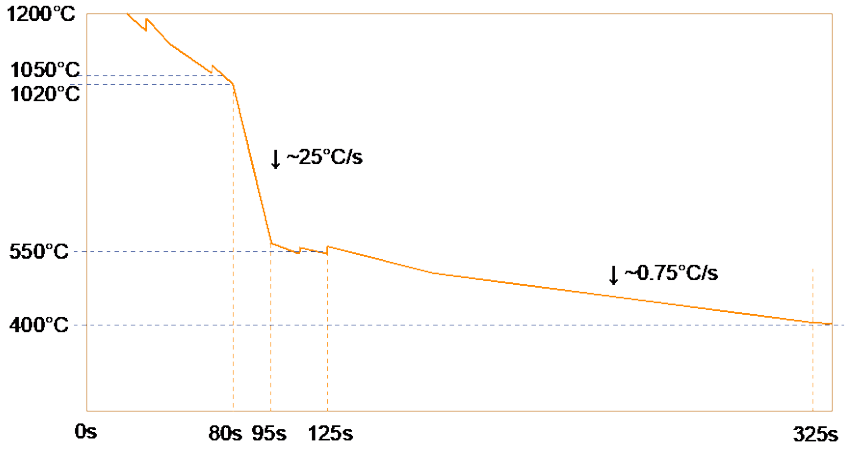

Figure 63. Typical temperature-time profile obtained in MT-TMCP rolling at Oulu.

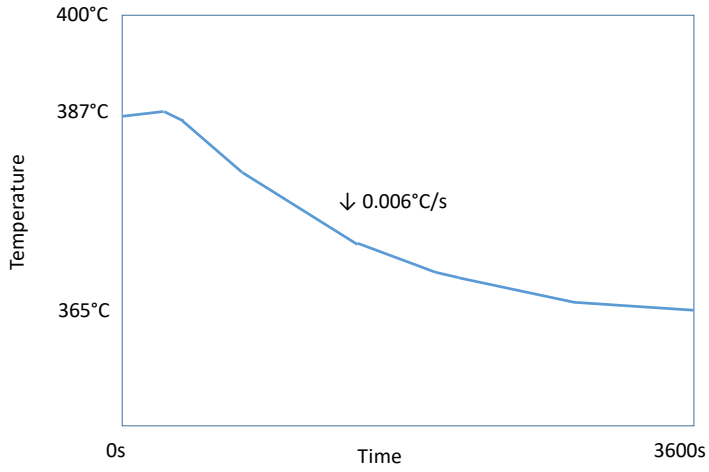

Figure 64. Typical temperature-time profile after switching cooling at 400ºC to enter coiling T of 350ºC obtained in MT-TMCP rolling at Oulu.

4.1.4.v LT-TMCP

For details on the parameters and partner for the LT-TMCP see Figure 67.

Like the MT-TMCP-3mm the LT-TMCP-3mm was done at tkSE with a Gleeble HDS-V40. Again, a sample size of 25x150x10 mm^3 was used. Despite the small sample size, the high deformation force at 350 °C often led to the breakage of the deformation stamps and visible imprints in the material (Figure 65). In some samples also cracks at the boundary of the deformed area were observed (Figure 66). Meaningful stress-strain curves could not be measured due to the mentioned problems.

For the 12mm product, OCAS performed the mentioned rolling schedule, and an example of the typical temperature profile measured is shown in Figure 68. As it is shown after deformation at 400ºC, and before reaching the isothermal temperature of 350ºC, there is some phase transformation (detected as an increase in the temperature after the sharp increase due to applied deformation) and therefore 400ºC should be considered as the starting isothermal transformation temperature.

Figure 65. LT-TMCP-3mm HDS-V40 samples with imprints from the deformation stamps broken during the deformation at 350 °C.

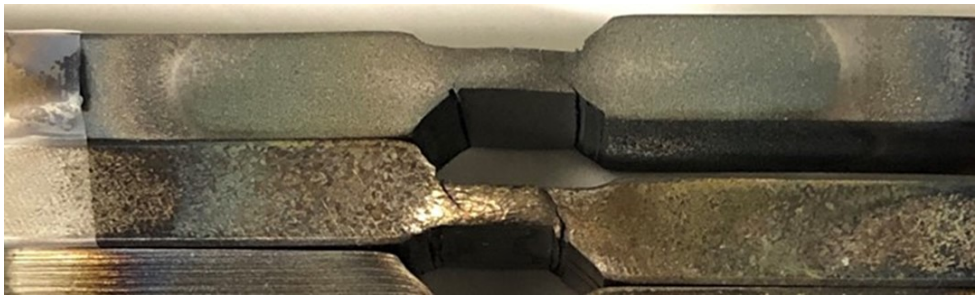

Figure 66. LT-TMCP-3mm HDS-V40 samples with cracks at the boundary of the deformed area.

LT-TMCP-3mm (TKSE)

HDS-V40 25x150x10 mm^3 specimens => Final sample size: 10x25x3 mm^3

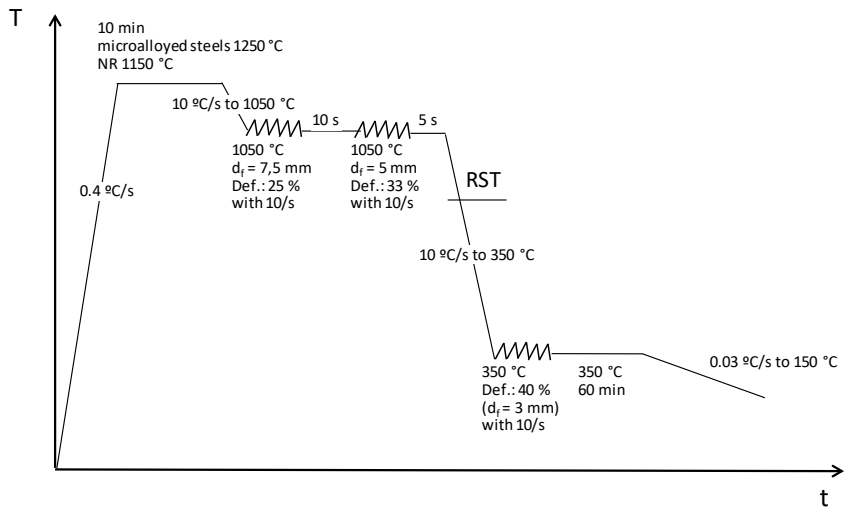

LT-TMCP-12mm (OCAS)

110 (L) x 80 (W) x 40 (t) mm^3 specimens => Final sample size: 300 (L) x 85 (W) x 12 (t) mm^3

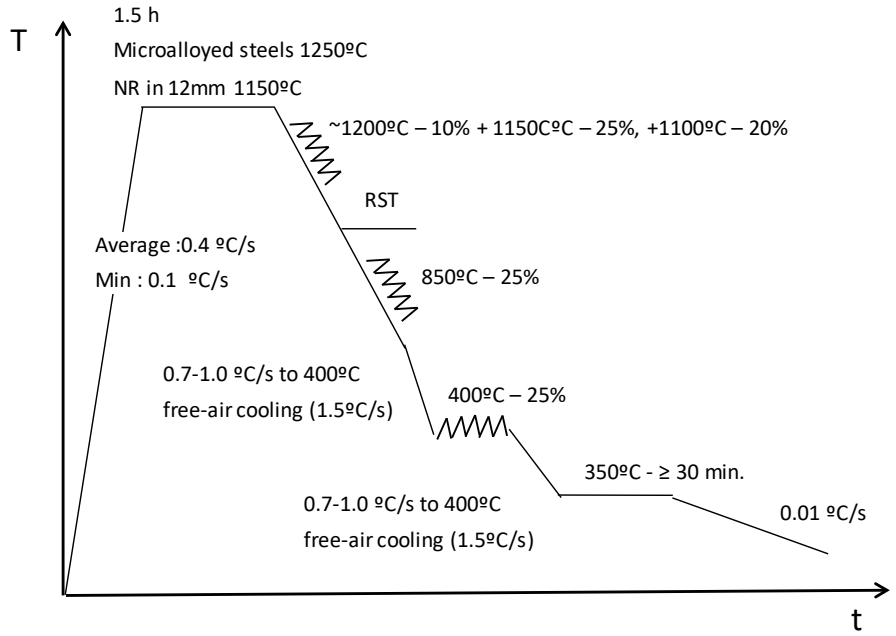

Figure 67. LT-TMCP applied for the 3mm (tkSE) and 12 mm (OCAS) product.

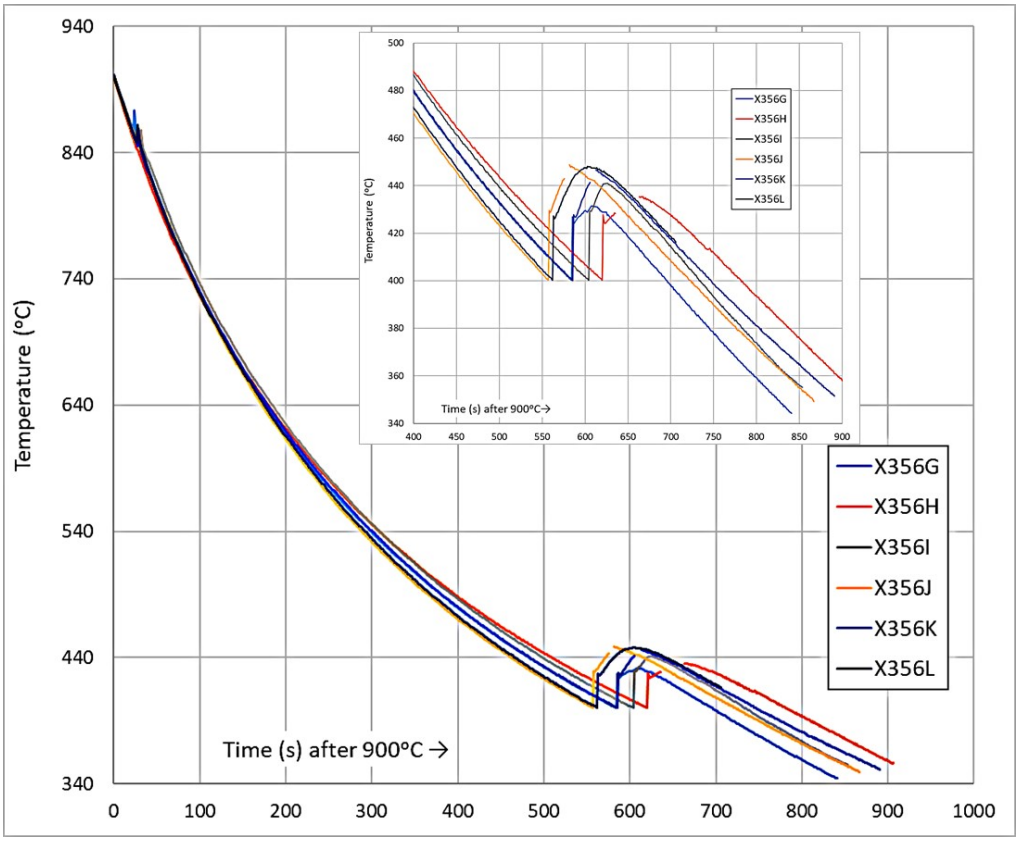

Figure 68. Example thermal profiles for the LT-TMCP NR 12mm product (OCAS).

4.2 Work Package 4. Microstructural investigation.

4.2.1 Task 4.2: Crystallographic texture analysis of deformed microstructures. Parent austenite (PA) grain reconstruction. (All).

This section focuses on the parent austenite (PA) grain reconstruction as a way to ensure that bainitic transformation takes place from a fully recrystallized or deformed austenite as requested. For such purpose the two steels which generally present the best results, NR+Nb+V and NR+C+Nb+V, have been selected.

First of all, the isothermal TMCP have been analysed to be sure that full recrystallization has occurred during the last deformation step at 1050 °C (> RST), see Figure 54. EBSD data were subjected to a reconstruction technique developed by Nyyssönen et al. [20]. This technique required using the Matlab toolbox MTEX [21], obtaining an average misorientation of approximately 2°, indicating a good fit for the reconstructed result. The reconstruction PA maps can be found in Figure 69 a) and b), images from which it can be concluded that full recrystallization occurred as grain sizes are not elongated or inhomogeneous, in good agreements with the PA grain equivalent diameter histograms shown in Figure 69 c) and d), where it can be observed that all grain equivalent diameters are below 40 μm. Note that, due to the successive deformations above the RST there is an important refinement in the PA, as the achieved size is much smaller than that obtained right after austenitization at 1050 °C, ~100 μm.

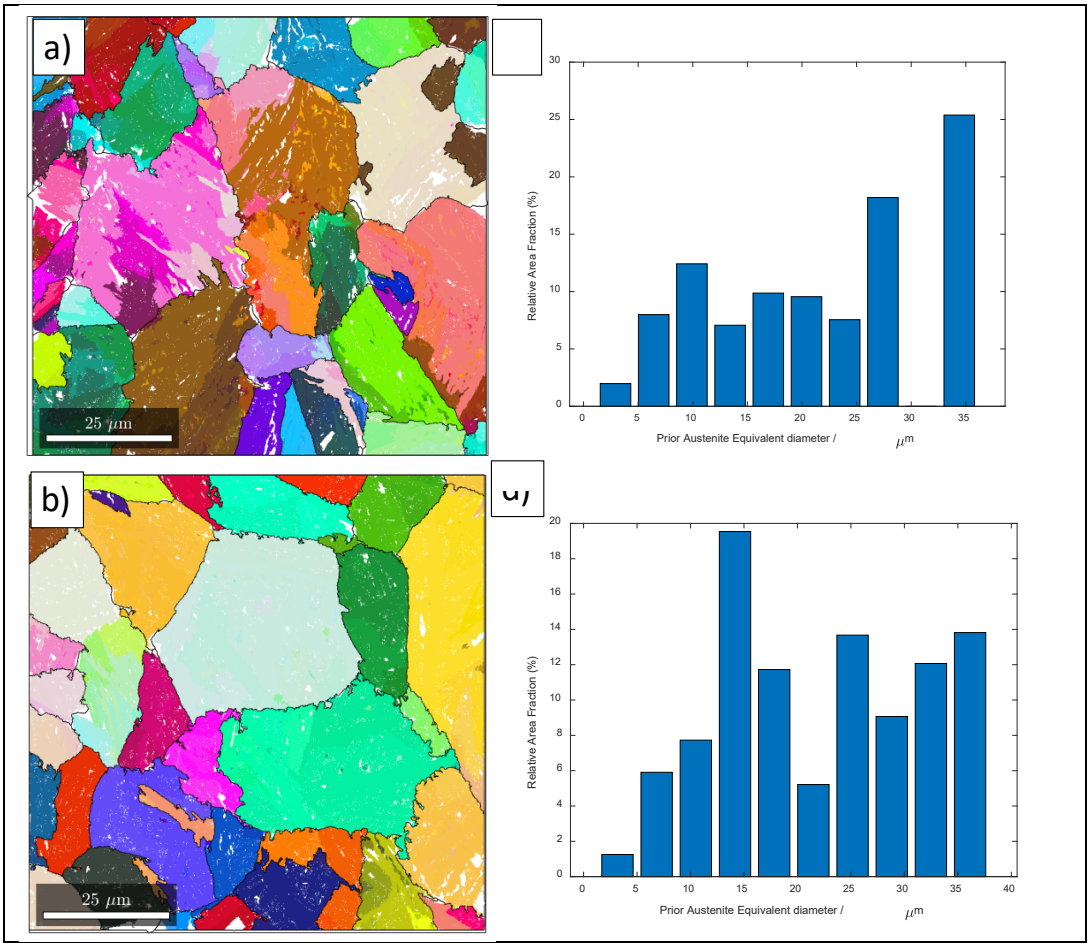

Figure 69. Isothermal TMCP Prior austenite (PA) reconstructed by PAG_GUI software [20] and Prior austenite grain equivalent diameter histograms, a) and c) NR+Nb+V and b) and d) NR+C+Nb+V steel. Measurements made on the longitudinal direction (RD-ND).

In order to make sure that the applied deformation for the different TMCP was indeed below the RST, an equivalent study to that just presented has been made on NR+C+Nb+V subjected to 12 mm HT, MT and LT-TMCP, Figure 55, Figure 60 and Figure 67 respectively. The study is performed in the longitudinal direction (RD-ND).

Figure 70 a) to c) shows the reconstructed PA maps, where the elongated morphology typical of deformed and unrecrystallized austenite is visible. This elongation indirectly affects the PA grain equivalent diameter, which increases as this value has only been measured on the longitudinal section. As can be seen in Figure 70 d) to f), the equivalent diameter histogram shifts towards higher values as the deformation is applied at lower temperatures.

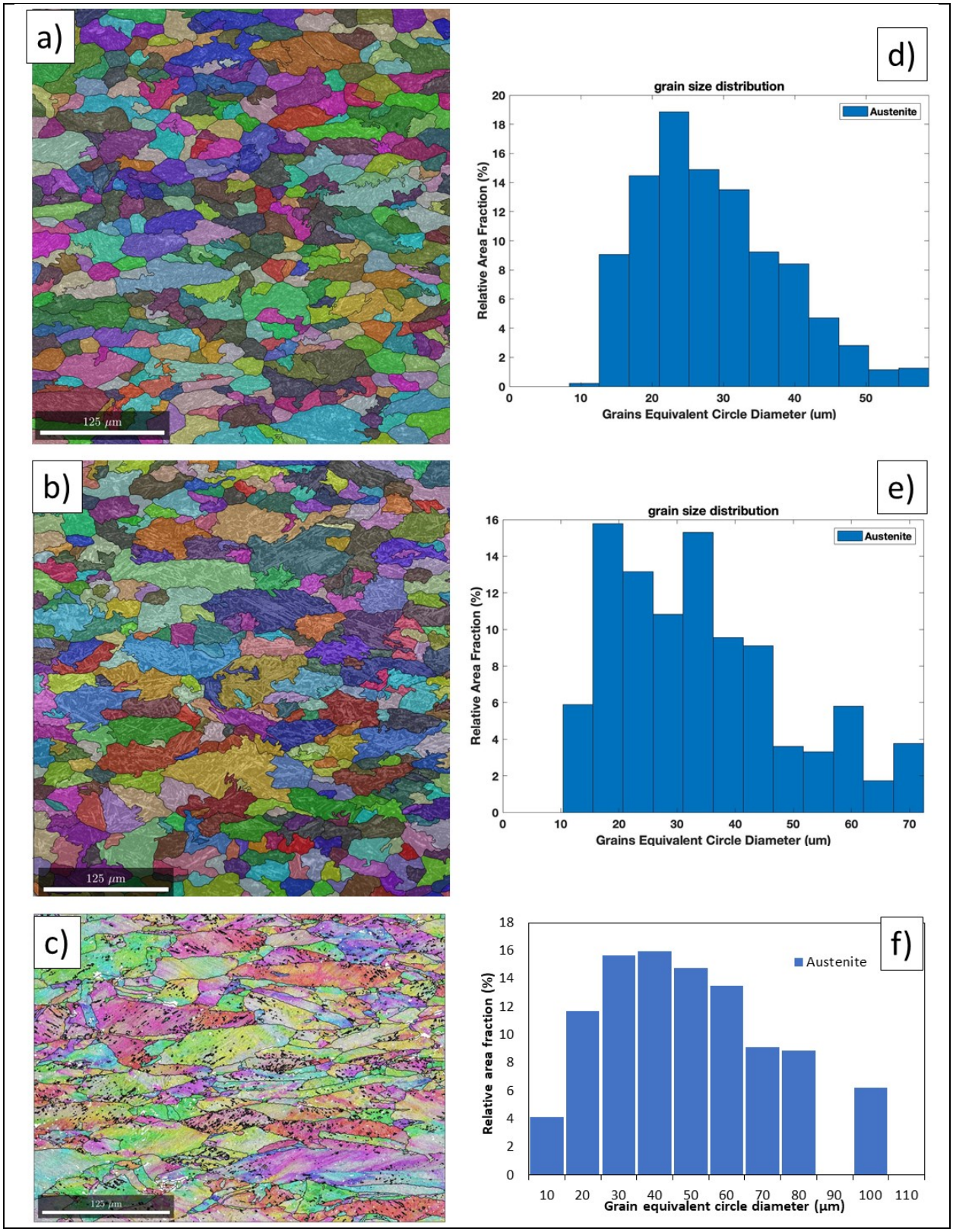

Figure 70. For NR+C+Nb+V Prior austenite (PA) reconstructed by PAG_GUI software [20] and Prior austenite grain equivalent diameter histograms, a) and d) HT-TMCP, b) and e) MT-TMCP and c) and f) LT-TMCP.

4.2.2 Task 4.1 & Task 4.4: Microstructural investigations & XRD retained austenite measurements. (All)

This section applies to the characterization of the microstructures produced in WP3. On a regular basis on all the TMCP conditions developed, including the isothermal holding (benchmark), hardness has been measured, and, on selected conditions, Optical Microscopy (OM), Scanning Electron Microscopy (SEM) and X-Ray Diffraction were performed. Thus, Task 4.1 and 4.4 will be presented together. The determination of the C content, based on the lattice parameters obtained by XRD, was not possible due to the uncertainty in its determination because of the applied deformation, therefore XRD analysis is restricted to the fraction of retained austenite (RA).

Note that in a later section, Task 5.6, and based on WP4 and WP5 results, two grades were selected for a deeper microstructural and mechanical characterization.

In the next paragraphs, the analysis of these results will enable distinguishing the phases present in the microstructures and to understand why the hardness levels change depending on the treatment. To do so, information described in WP2 regarding the transformation start temperature and the formation of martensite will be reminded so that the later discussion can be fully understood.

Longitudinal direction refers to RD-ND, while transversal refers to TD-ND.

4.2.2.i Isothermal-TMCP (Benchmark)

Figure 71 shows a Vickers Hardness (HV) vs. austenite volume fraction (Vɣ) scatter plot corresponding to isothermal TMCP, and are compared to the hardness ranges obtained for martensite and bainite (transformed at 350 °C) in the previous CCT and TTT studies in the same steels (WP2). It is observed that microstructures are mainly bainitic with some traces of martensite, in good agreement with the micrographs, see Figure 72 and Figure 73. Regarding the austenite volume fractions, most of the samples contain 20-30 % austenite, except the NR steel which only retains 12 %.

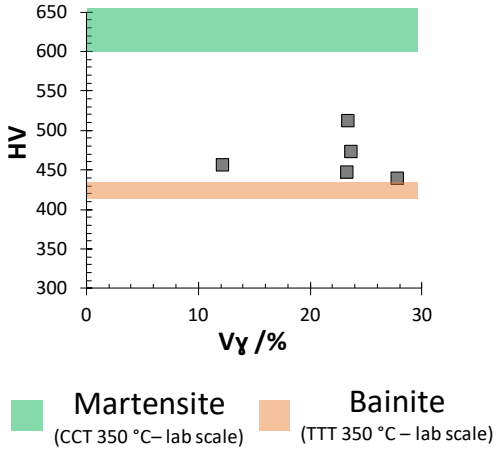

Figure 71. Scatter plot of the Vickers Hardness (HV) vs. austenite volume percentage (Vɣ) of the microstructures obtained by isothermal TMCP, where the martensite and bainite hardness values obtained for the corresponding conditions are shown by shadowed green and orange areas.

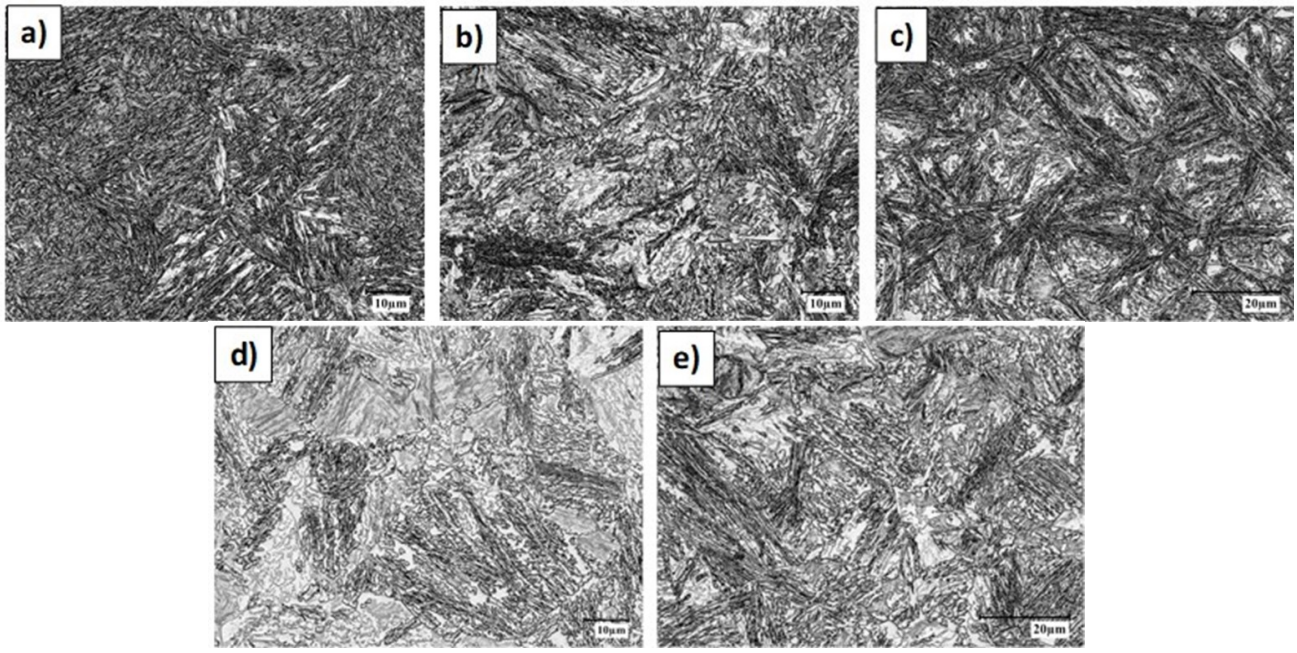

Figure 72. 12 mm isothermal TMCP microstructures, etched with Nital 2 %: a) NR steel; b) NR+Mo+Nb; c) NR+Nb+V; d) NR+Nb+V+Al and e) NR+C+Nb+V.

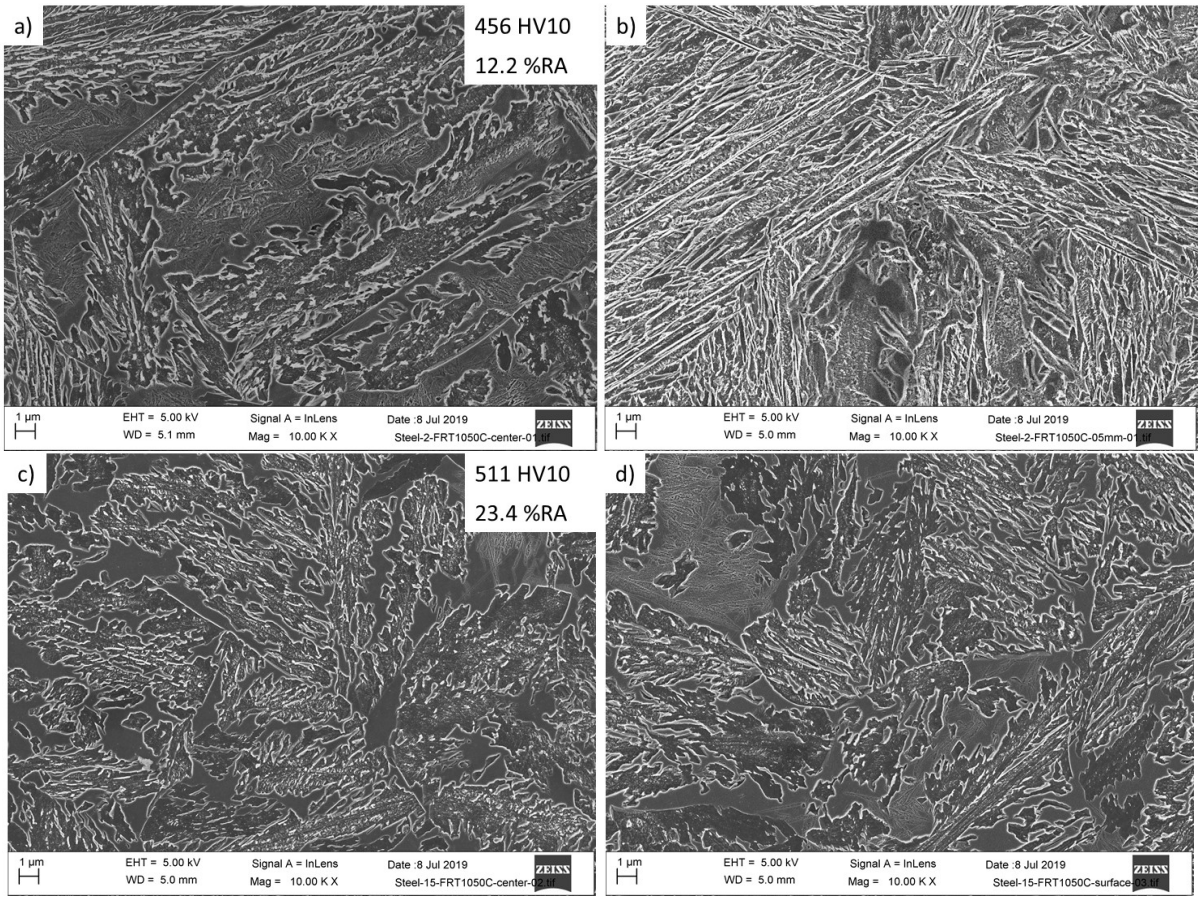

Figure 73. Selected examples of 12 mm isothermal TMCP microstructures at higher magnification, etched with Nital 2 %: a) and b) NR steel; c) and d) NR+C+Nb+V steel. RA stands for retained austenite.

Figure 74 shows Vickers Hardness (HV) vs. austenite volume percentage (Vɣ) scatter plots, classified depending on the TMCP and the thickness of the final product. The hardness ranges obtained for martensite and bainite (transformed at 350 °C) in the previous D-CCT and D-TTT studies in the same steels (WP2)

will be considered as references and are shown as shadowed green and orange regions, respectively. Please note that microstructures obtained at the lab scale are not as deformed as the ones that have gone through a whole TMCP, but their hardness can be indicative of the expected hardness for a given microstructure. A grey region range of the hardness and austenite volume fraction obtained in 12 mm specimens subjected to isothermal TMCP is also included to study the effect of deformation on the microstructures.

Optical micrographs of all microstructures obtained for HT (transformed at 325 and 350 °C), MT and LT-TMCP and for both kinds of final product thickness can be found in Figure 75 to Figure 85.

4.2.2.ii 3 mm HT-TMCP

As already explained, different coiling conditions have been tested, 350ºC-30 min, 350ºC-3h and 325°C-3h, Figure 55. As seen in Figure 75 and Figure 76, small fractions of martensite are present in almost all microstructures, which are predominantly bainitic. The main difference that arises from the coiling temperature is the refinement of the microstructure, see Figure 75 a-e) for finest microstructures (transformed at 325 °C) and Figure 75 f-j) for the coarsest ones (transformed at 350 °C). These differences also affect both the hardness and the austenite volume fraction, in accordance with the current theory of bainitic transformation [2], Figure 74. While the points on the top left of Figure 74 a) would correspond to the finest bainite, with the highest hardness and the lowest austenite volume fractions, the ones on the bottom right of the same figure would belong to the microstructures transformed at the highest temperature. Varying the isothermal time also modifies the hardness and the volume fraction (hardness decreases as more retained austenite is present) although the influence is not as significant as the one of the isothermal temperature, find an example of the difference in Figure 77.

Although there is no reference for HV levels of microstructures transformed at 325 °C by a isothermal TMCP or in the D-TTT experiments at the lab scale, we do have these results for the highest (350ºC) isothermal TMPC temperature, from which it can be concluded that the hardness and austenite volume fraction levels for this TMCP are in the range of the ones obtained by the isothermal TMCP. Moreover, the presence of martensite is evident in some cases in which the hardness approaches the hardness range defined for the reference martensite.

It is also worth noticing that in some cases segregation, in the form of bands with different constituents, is also very noticeable, see for example Figure 75 j) and h) where martensite (darker phases) seem to be preferential.

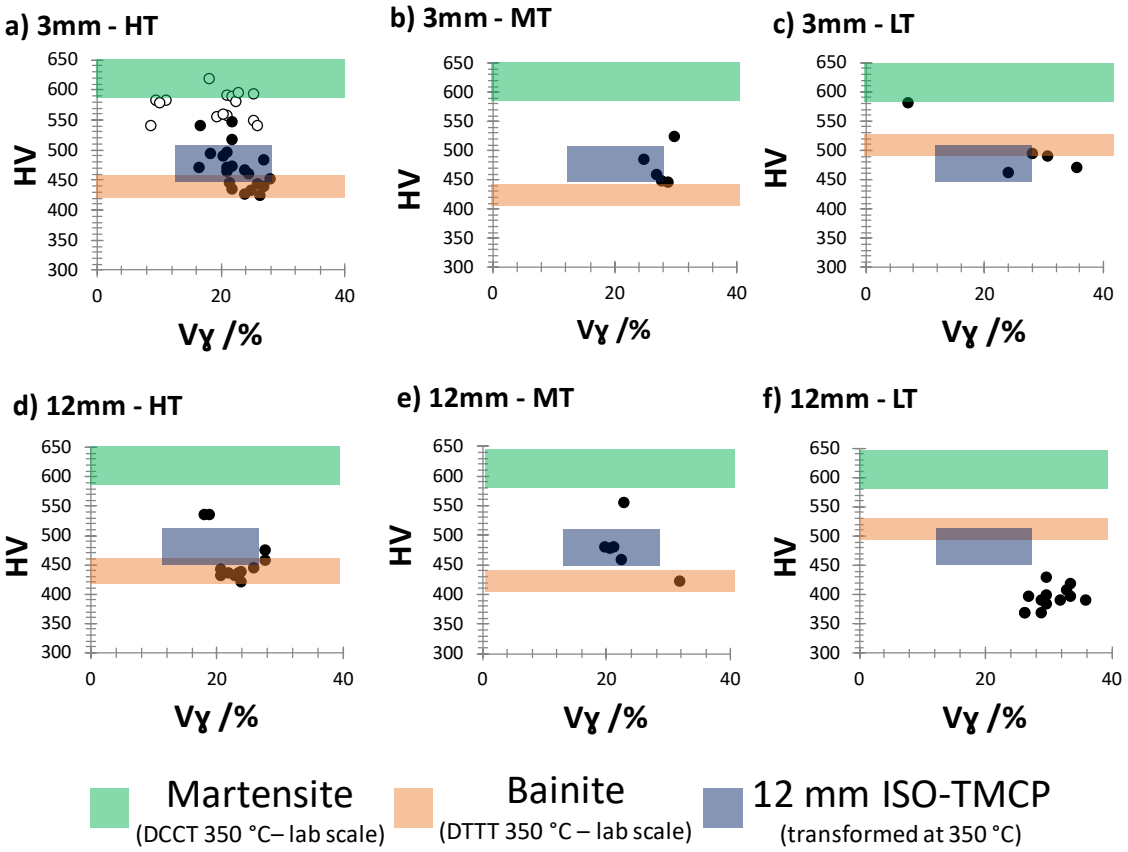

Figure 74. Vickers Hardness (HV) vs. austenite volume percentage (Vɣ) scatter plots, where the martensite and bainite hardness values obtained for the corresponding conditions are shown by shadowed green and orange areas. A grey region range of the hardness and austenite volume fraction obtained in 12 mm specimens subjected to isothermal TMCP is also included. Note that the black points are those transformed at 350 °C, whereas the white ones have been transformed at 325°C.

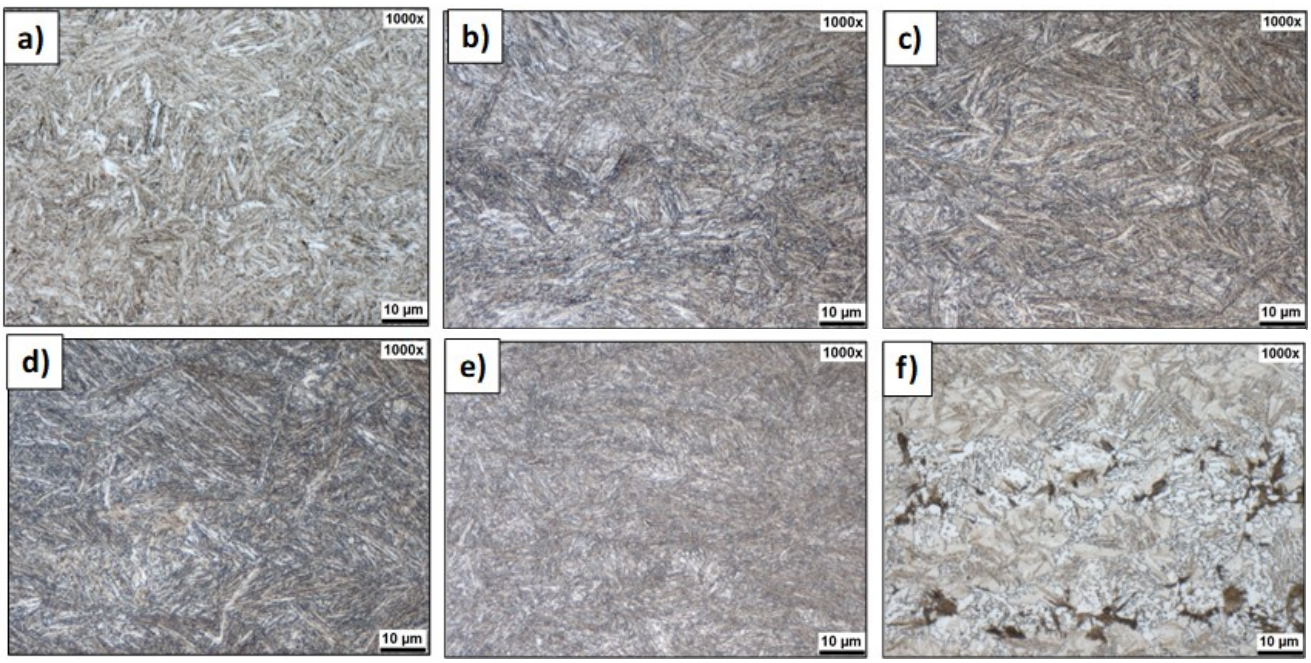

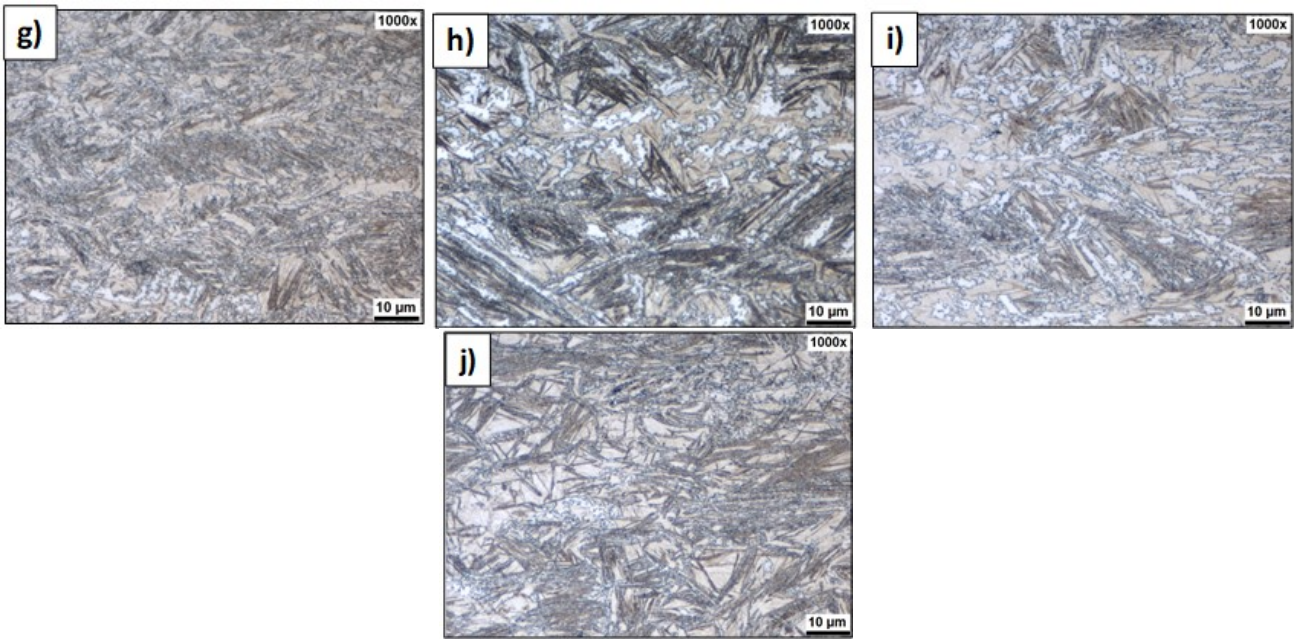

Figure 75. 3 mm HT-TMCP microstructures, etched with Nital 2 %, where the microstructures shown in a-e) have been transformed at 325 °C whereas the ones f-j) have been transformed at 350 °C: a,f) NR steel; b,g) NR+Mo+Nb; c,h) NR+Nb+V; d,i) NR+Nb+V+Al and e,j) NR+C+Nb+V.

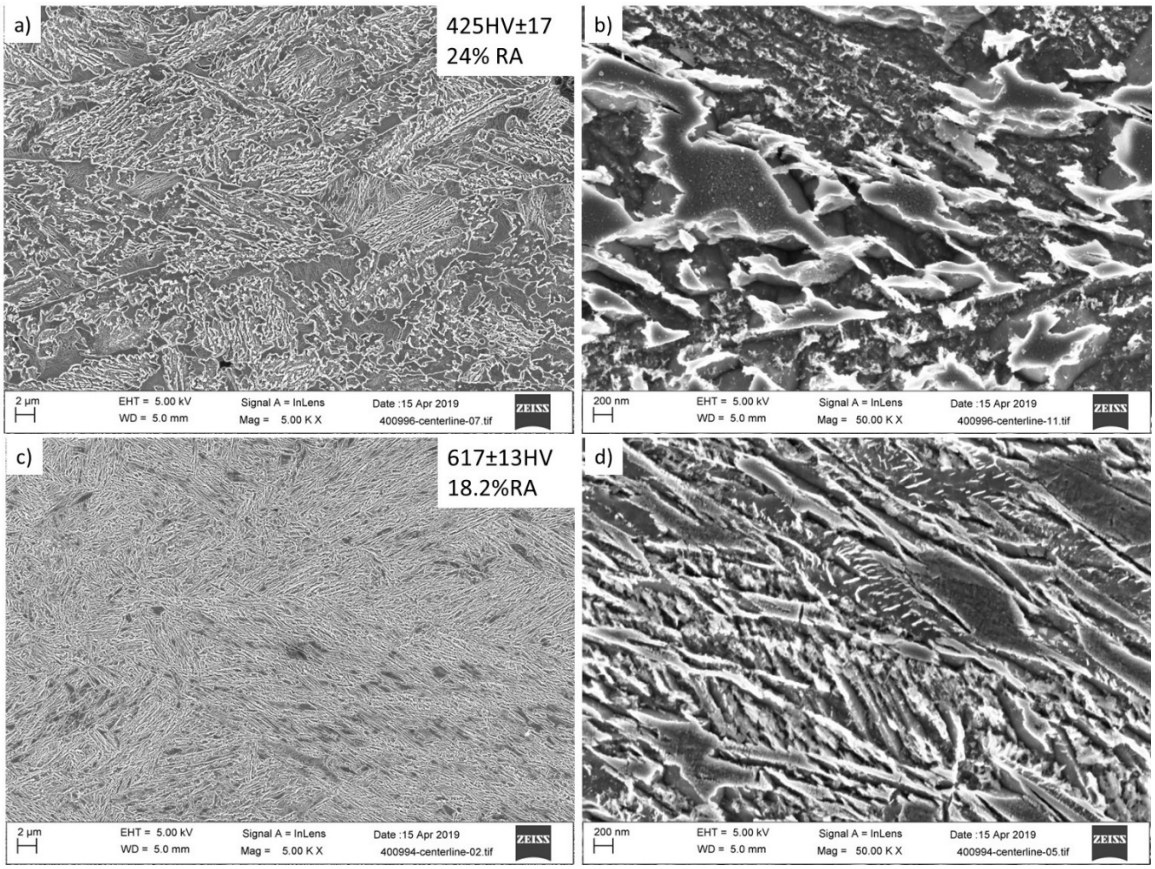

Figure 76. Selected examples of 3 mm HT-TMCP microstructures at higher magnification (SEM), etched with Nital 2 % : a) and b) NR+Nb+V+Al treated at 350ºC-3h and c) and d) NR+C+Nb+V treated at 325ºC-3h. RA stands for retained austenite.

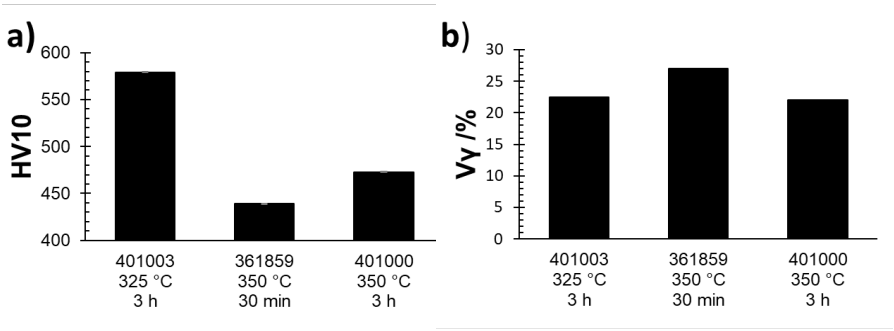

Figure 77. For NR+Nb+V variation of the a) HV and b) Vγ measurements for the 3mm HT-TMCP microstructures.

4.2.2.iii 3 mm MT-TMCP

In 3 mm MT-TMCP, Figure 60, deformation has been applied by Plain Strain Compression. Due to the accumulative deformations applied at different temperatures, a problem that has been encountered is the inhomogeneity of the deformation. Figure 78 a) shows macrographs of the 3 mm NR+Nb+V product subjected to the mentioned treatment, where it can be seen that, the compression has not strictly been plane strain and some shear stresses have also been applied. It is also possible to observe big differences in the size of the final microstructure between the center and close to the surface, thus hardness and volume fractions have been measured on the central part of the specimens, where the local plastic strain approaches the macroscopic strain [22], and the shear seems to be minimal, Figure 74.

Samples subjected to MT-TMCP 3mm are predominantly bainitic, bainitic ferrite and retained austenite, with some traces of martensite, as it can be observed in Figure 79 and as indicated by the hardness values in Figure 74. It can be also seen that most of the microstructures exhibit a certain degree of alignment, see Figure 79 c) and e), characteristic for microstructures obtained through ausforming processes [23]. Vγ values are slightly higher than the reference value, indicative of certain degree of mechanical stabilisation, but the hardness values are similar, probably due to the contribution of slightly finer bainite and some martensite.

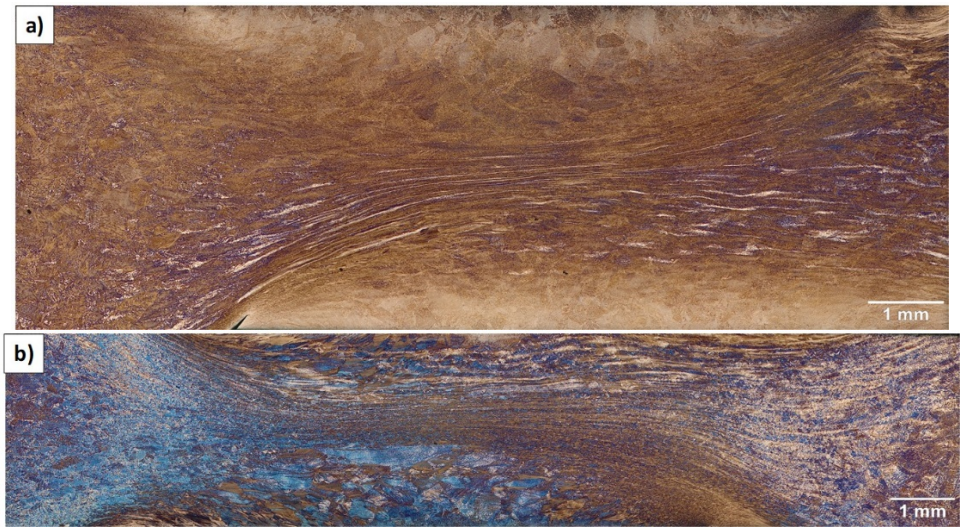

Figure 78. Macrographs of the 3 mm plates of the NR+Nb+V steel subjected to a) MT-TMCP and b) LT-TMCP microstructures.

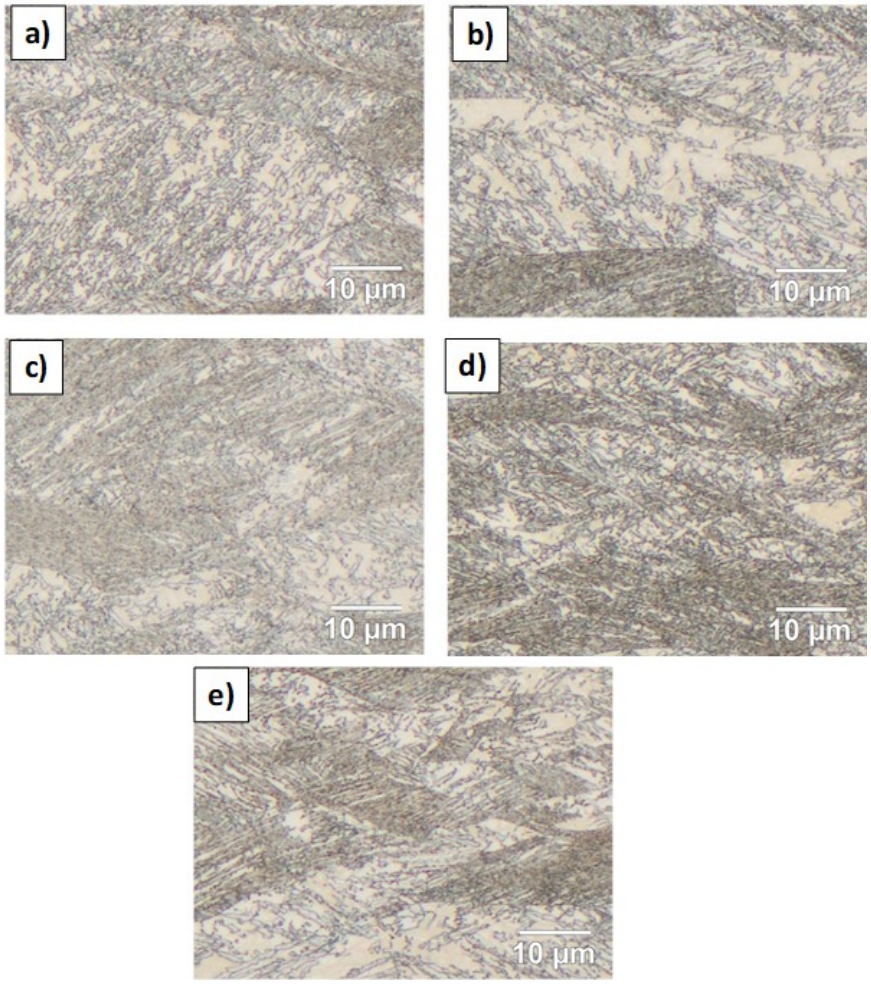

Figure 79. 3 mm MT-TMCP microstructures, etched with Nital 2 %: a) NR steel; b) NR+Mo+Nb; c) NR+Nb+V; d) NR+Nb+V+Al and e) NR+C+Nb+V.

4.2.2.iv 3 mm LT-TMCP

The LT-TMCP have also been performed by Plane Strain Compression, Figure 67, and, thus, the problems mentioned in the previous subsection regarding the inhomogeneity of the deformation are also present, see Figure 78 b). The revealed microstructures are a mixture of bainite, retained austenite and martensite, Figure 80. In spite of the higher austenite volume fractions, austenite mechanical stabilization, their hardness values are similar to the lab specimens, Figure 74, being this probably the combined effect of finer bainitic ferrite and the presence of martensite. As it happened with the 3mm MT-TMCP, most of the ferritic plates are rather aligned, see Figure 80, characteristic for microstructures obtained through ausforming processes.

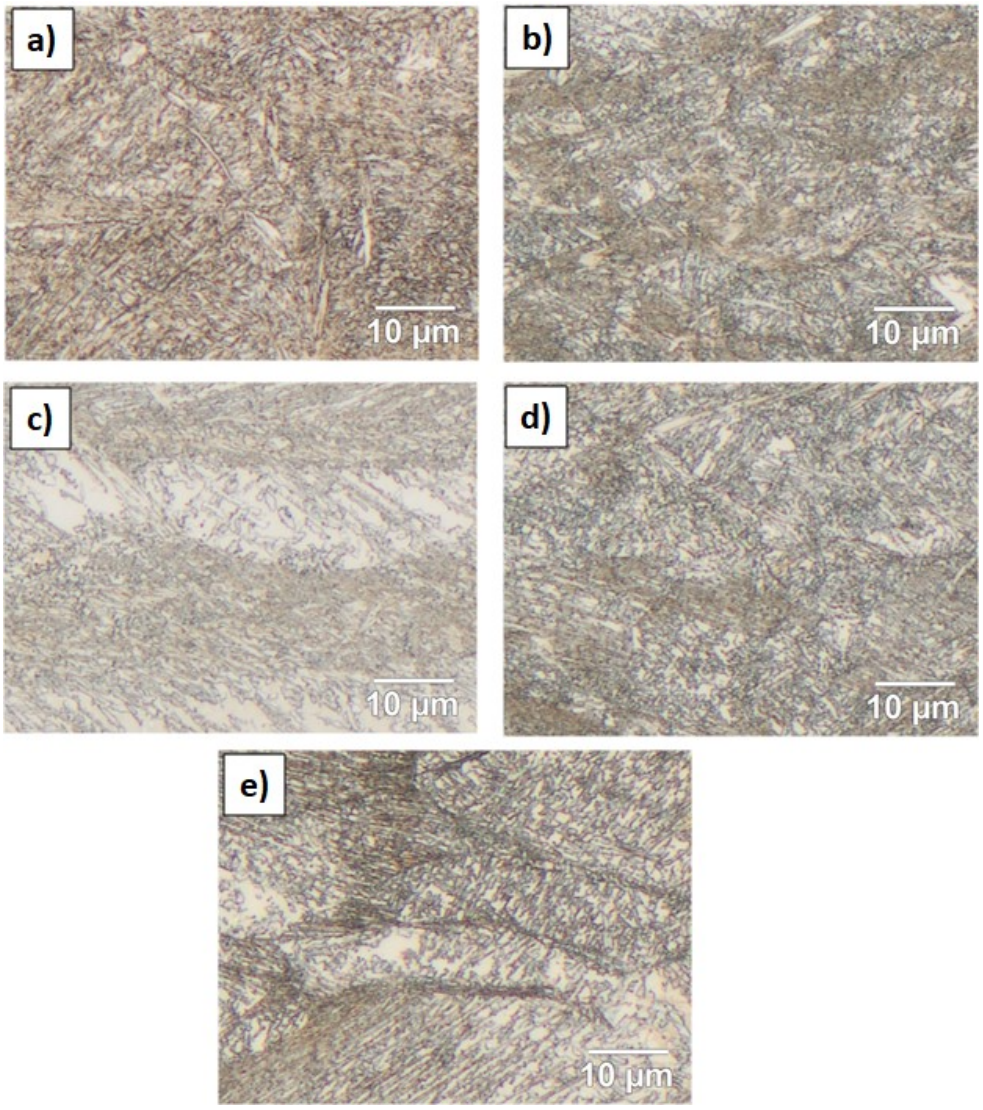

Figure 80. 3 mm LT-TMCP microstructures, etched with Nital 2 %: a) NR steel; b) NR+Mo+Nb; c) NR+Nb+V; d) NR+Nb+V+Al and e) NR+C+Nb+V.

4.2.2.v 12 mm HT-TMCP

All microstructures produced in the 12 mm HT-TMCP, Figure 55, have been etched with Klemm's reagent, which colours differently the phases (bainitic ferrite is blue, martensite is brown and austenite is white), see Figure 81, where it can be observed that whereas NR (Figure 81 a)) and NR+C+Nb+V (Figure 81e)) are composed of bainite and a high fraction of martensite, the remaining steels mainly consist of bainite and some traces of martensite. This is directly reflected to the hardness values and the austenite volume fraction, Figure 74 d) shows that two of the five points have been shifted to the left top, being their closer to the martensitic range of reference. In addition, as previously elucidated, because cooling rates could not be as rapid as possible when cooling down after deformation, the transformation might have started at higher temperatures than 350 °C, see WP3 and Figure 58 and Figure 59, meaning that the bainitic ferrite plates are coarser than expected, which could explain the fact that there is no hardness increase. High magnification images of selected microstructures can be seen in Figure 82.

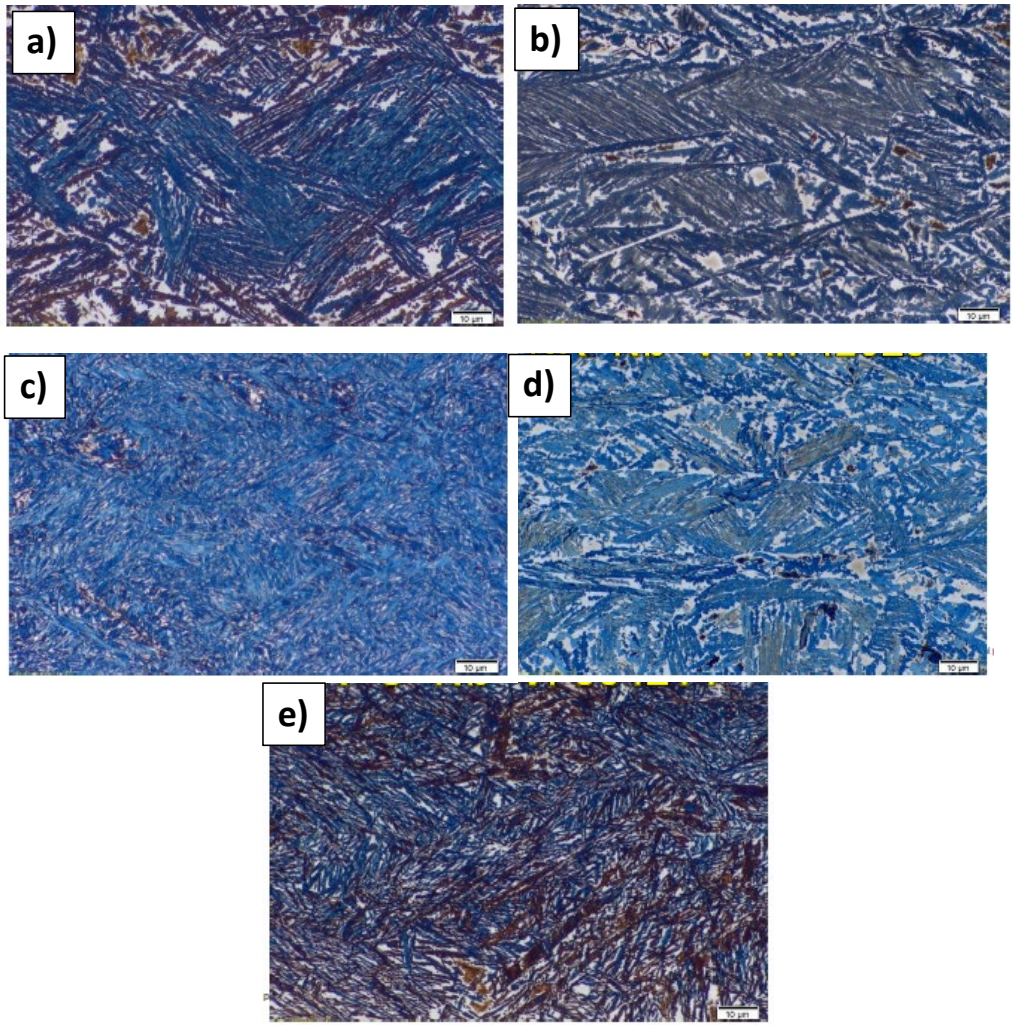

Figure 81. 12 mm HT-TMCP microstructures, etched with Klemm's reagent to distinguish martensite (brown), bainite (blue) and austenite (white): a) NR steel; b) NR+Mo+Nb; c) NR+Nb+V; d) NR+Nb+V+Al and e) NR+C+Nb+V.

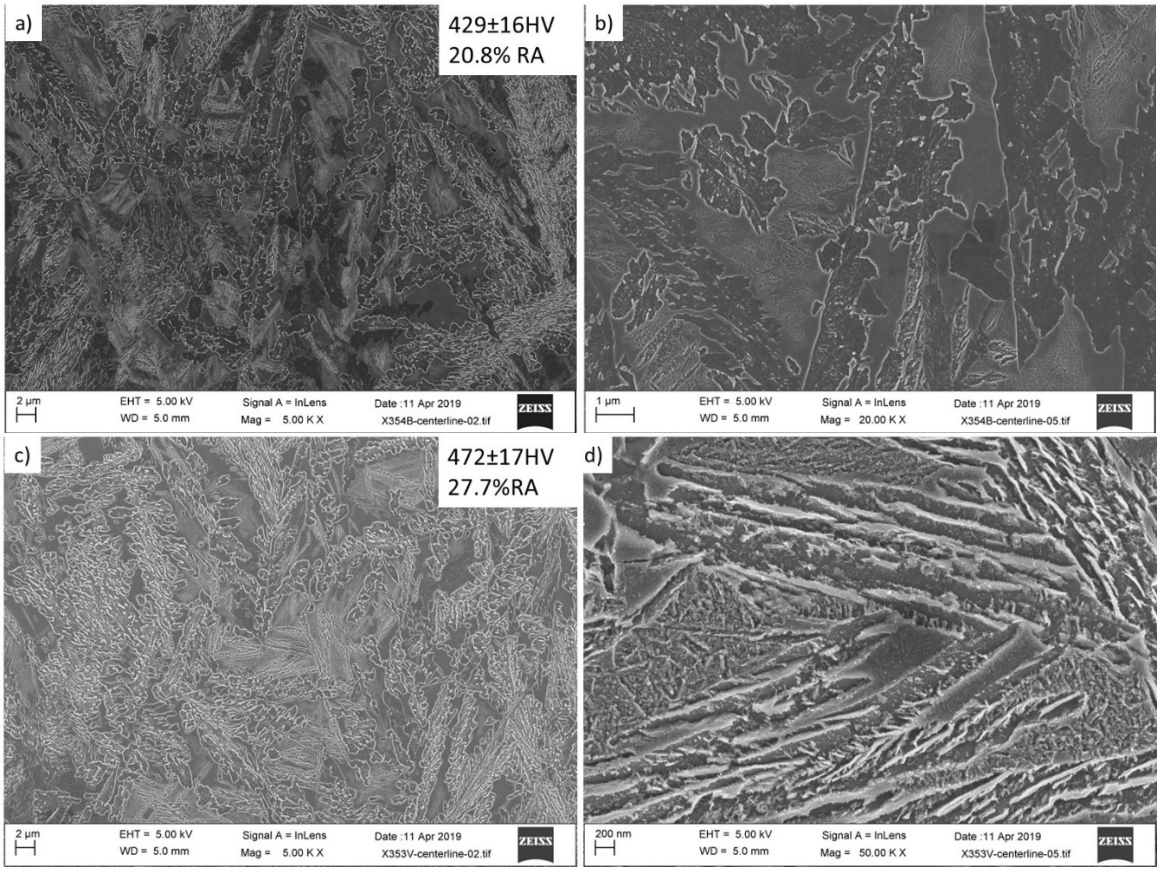

Figure 82. Selected examples of 12 mm HT-TMCP microstructures at higher magnification (SEM), etched with Nital 2% : a) and b) NR steel; c) and d) NR+C+Nb+V. RA stands for retained austenite.

4.2.2.vi 12 mm MT-TMCP

Regarding the microstructures obtained by MT-TMCP, Figure 60, the micrographs in Figure 83 show that they consist of a mixture of a high fraction of martensite with bainite and retained austenite. The presence of thick bainite, due to high transformation temperatures, Figure 64, and martensite does not increase HV to higher values than those obtained in the lab bainite, see Figure 74 e). Examples of selected microstructures at higher magnification can be found in Figure 84.

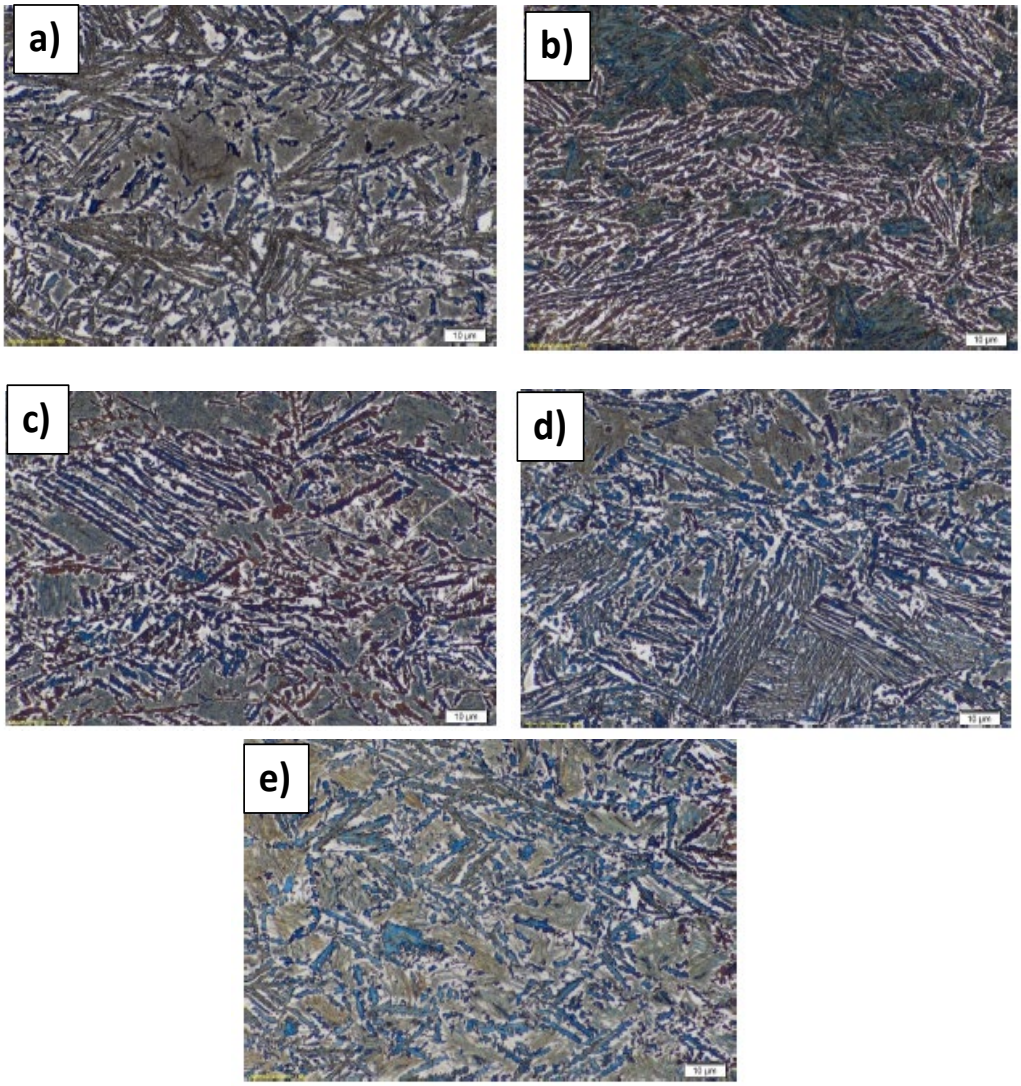

Figure 83. 12 mm MT-TMCP microstructures, etched with Klemm's reagent to distinguish martensite (brown), bainite (blue) and austenite (white): a) NR steel; b) NR+Mo+Nb; c) NR+Nb+V; d) NR+Nb+V+Al and e) NR+C+Nb+V.

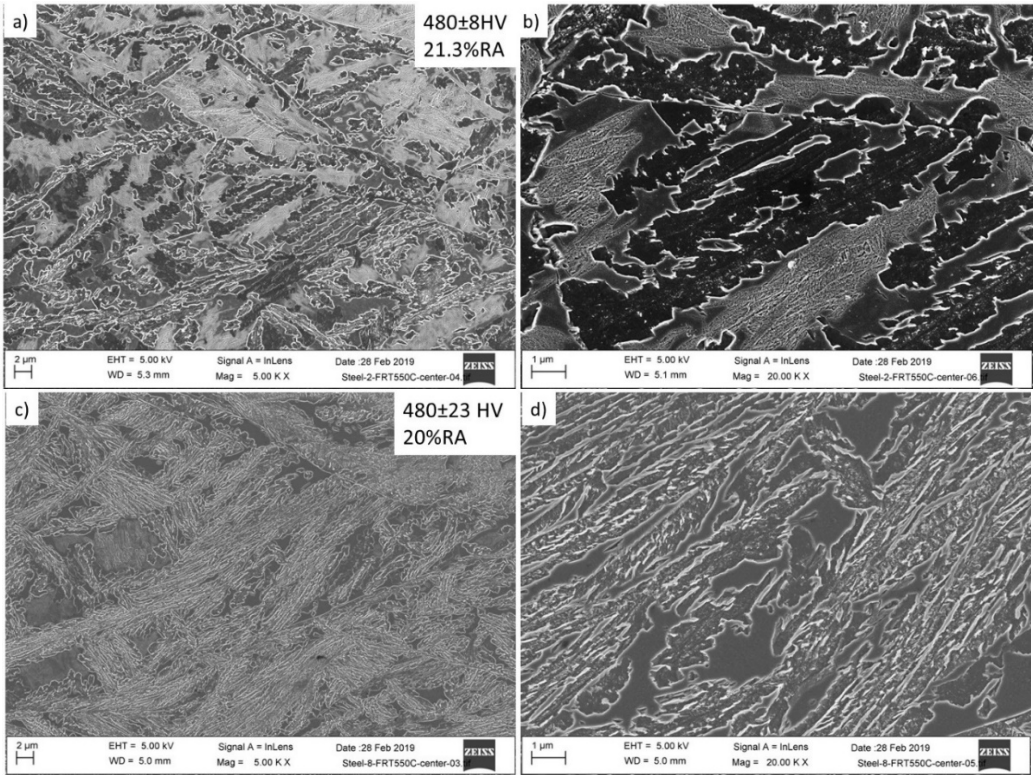

Figure 84. Selected examples of 12 mm MT-TMCP microstructures at higher magnification (SEM), etched with Nital 2% : a) and b) NR steel; c) and d) NR+Mo+Nb; RA stands for retained austenite.

4.2.2.vii 12 mm LT-TMCP

Microstructures obtained by LT-TMCP in 12 mm product, Figure 67, can be found in Figure 85, where it can be observed that NR+Nb+Mo contains a high fraction of martensite in addition to bainite, the remaining steels mainly consist of bainitic ferrite, austenite in a higher fraction than observed for the isothermal TMCP (see Figure 74 f) and some traces of martensite. In addition, as previously elucidated, because cooling rates could not be as rapid as possible when cooling down after deformation, Figure 68, the transformation started at higher temperatures than 350 °C, meaning that the bainitic ferrite plates are coarser than expected. For that reason and also because of mechanical stabilization of austenite (higher austenite volume fraction), the hardness values are even lowered with respect to the reference isothermal TMCP and the lab bainite hardness levels. It has to be also noted that, in the LT-TMCP last pass was 25% deformation at 400°C compared with the 50% deformation at 350°C for the DTTT , which might also contribute to the differences in HV. Examples of selected microstructured at higher magnification can be found in Figure 86.

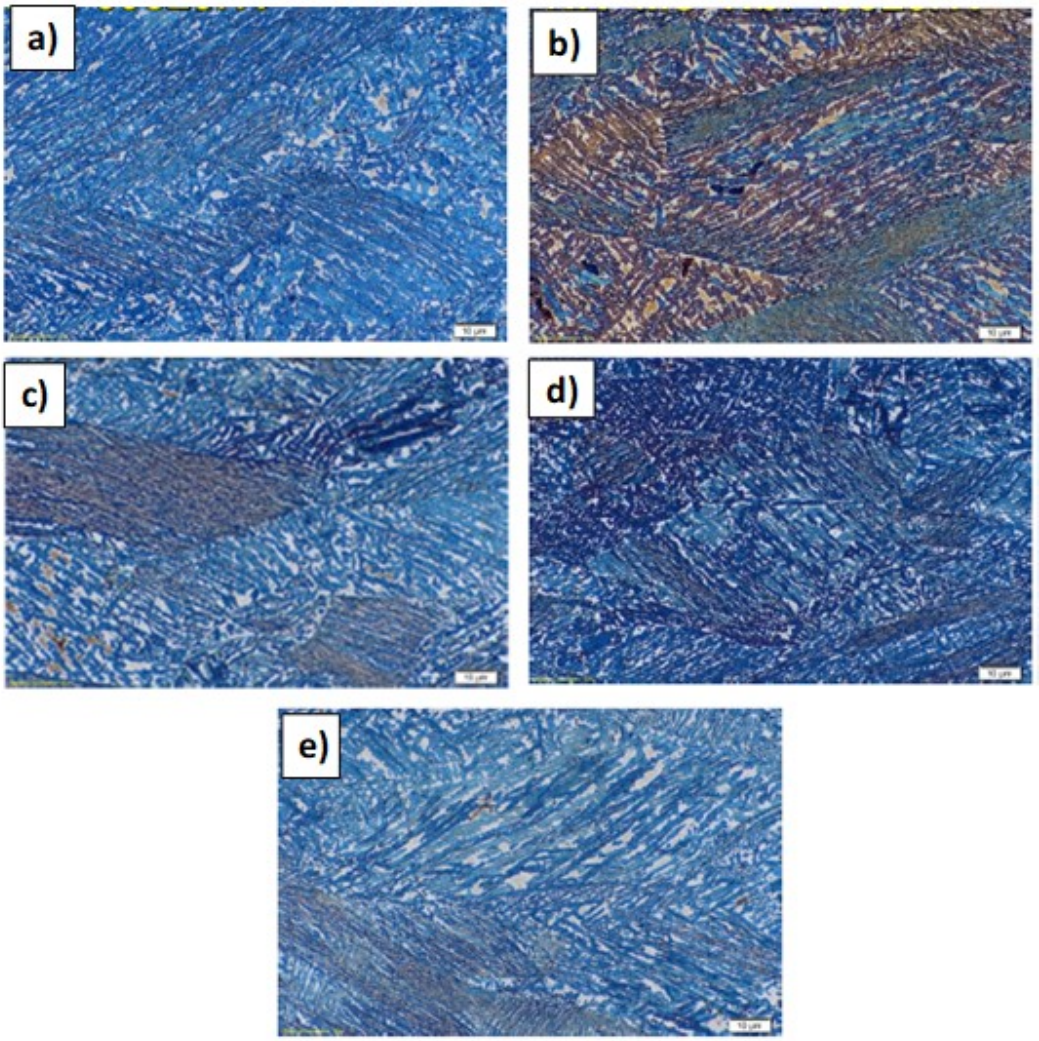

Figure 85. 12 mm LT-TMCP microstructures, etched with Klemm's reagent to distinguish martensite (brown), bainite (blue) and austenite (white): a) NR steel; b) NR+Mo+Nb; c) NR+Nb+V; d) NR+Nb+V+Al and e) NR+C+Nb+V.

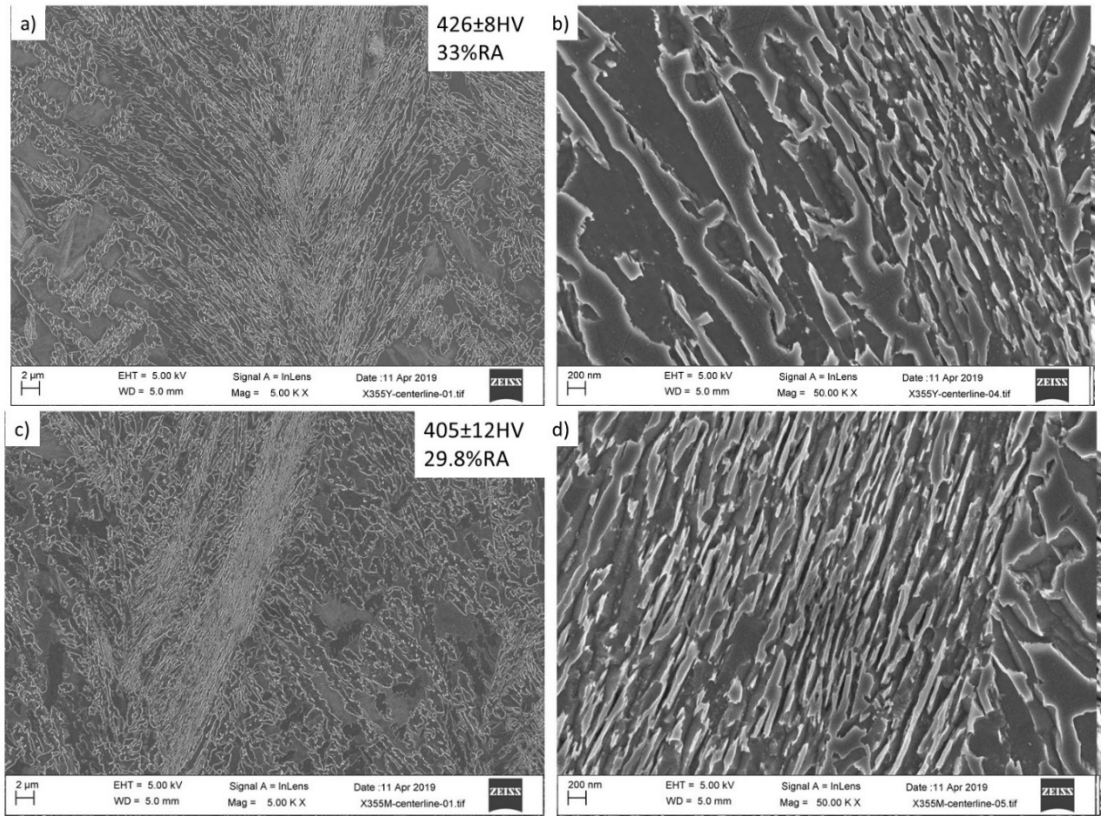

Figure 86. Selected examples of 12 mm LT-TMCP microstructures at higher magnification (SEM), etched with Nital 2% : a) and b) NR+C+Nb+V steel; c) and d) NR+Nb+V; RA stands for retained austenite.

4.2.3 Task 4.3: TEM & characterization of precipitation (OULU, OCAS)

4.2.3.i Precipitation characterization by ICP-OES

ICP-OES (inductively coupled plasma-optical emission spectrometer) was used to determine the microalloying elements (Nb, V, Mo) dissolved in solid solution and microalloyed precipitate fraction in the 12mm rolled plates at the HT/MT and LT-TMCP conditions. In order to extract the precipitates from the steel matrix, electrolysis is performed to dissolve the steel samples and the solution is filtered. The filter and filtrate samples are analysed with ICP-OES to determine the amount of Nb, V, Mo. The samples are nebulised and atomised in plasma. Atoms and ions are excited by the plasma, subsequently emitting a characteristic spectrum. The optical emission is split in the monochromator in different characteristic wavelengths from the elements present in the sample, which are simultaneously detected on a CID detector. The intensity is a measure for the quantity.

Figure 87 shows the amount of dissolved and precipitated microalloying elements in the TMCP 12 mm rolled plates. In the case of the HT and LT-TMCPs, for all Nb-microalloyed plates, approximately half of the total Nb is precipitated.

In all cases it is assumed that a certain amount of Nb remains undissolved even after the homogenisation and roughing of the plates, see Figure 88, which corresponds to similar analysis performed on homogenised+roughed plates used in the WP2. Then during hot rolling and deformation at high T (< RST) some precipitation might also occurs, the exceptional high amount of precipitated Nb found in the LT-

TMCP could be explained by the slow air-cooling after the penultimate pass at 850ºC to the final pass at 400ºC, see Figure 67.

For all the analysed conditions, approximately 15% Mo is precipitated for the Mo containing plate while V precipitation is negligible and almost all of it remains in solid solution Figure 87.

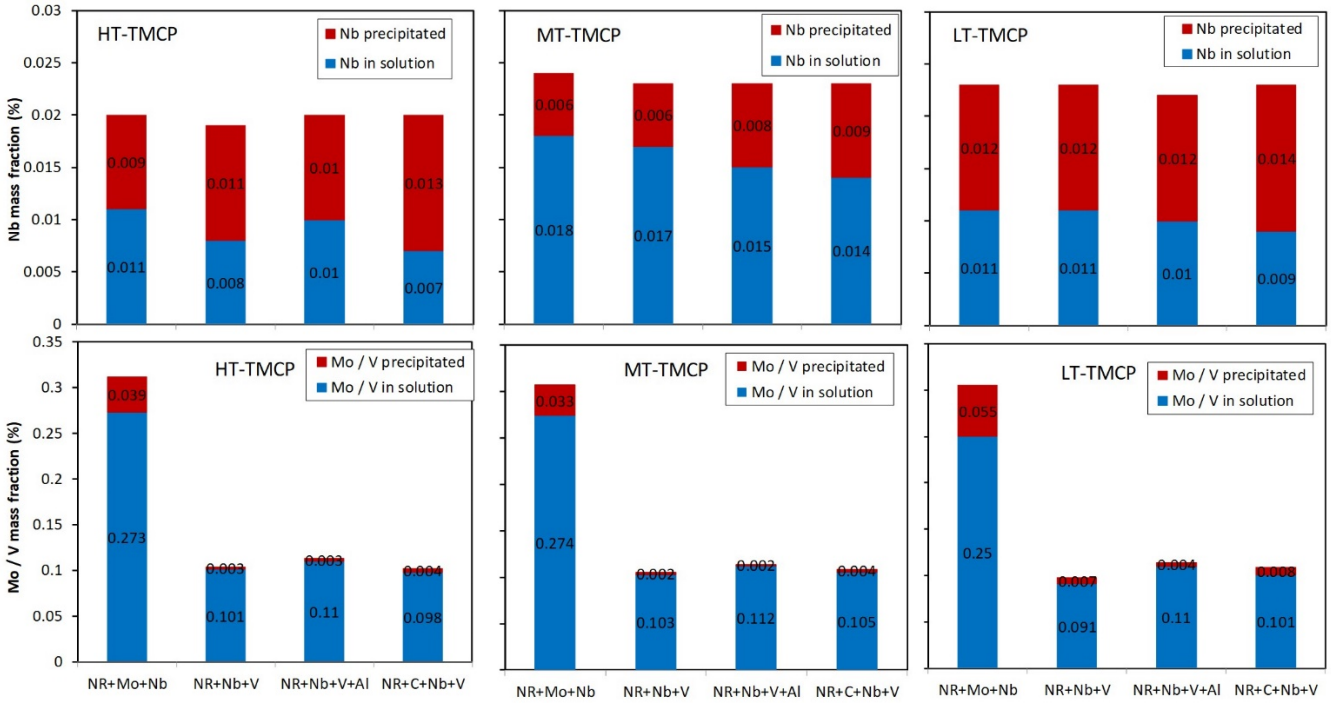

Figure 87. Overview of ICP-OES results for HT/MT and LT-TMCP 12mm plates.

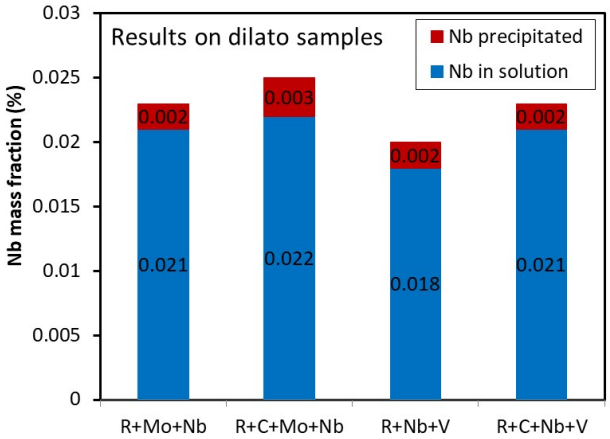

Figure 88. Overview of ICP-OES results for homogenised+roughed plated from WP2.

4.2.3.ii TEM characterization

Further characterisation of the microstructure of steel NR MT-TMCP 12 mm was performed in order to detect and identify the presence and scale of the of bainitic ferrite plates and also of the fine inter-lath austenite films, by means of transmission electron microscope TEM-JEOL JEM-2200FS. The specimen was thinned down to a thickness of 100 µm, and then discs with diameter of 3 mm were punched out for TEM observations. Accelerating voltage was 200 kV.

A bright field (BF) image of NR MT-TMCP 12 mm is shown in Figure 89. In the location studied, there are 150–400 nm thick bainite laths with some cementite within, and 100 nm interlath films of retained austenite. Selected area diffraction pattern (SADP) and corresponding dark field image (DF) of the austenite spo and the BF image are shown in Figure 90. The zone axis in SAD was austenite <113> and thus, retained austenite with matching orientation is presented in DF image, in the form of interlath films with thickness of 15–50 nm along the boundaries of bainite laths (100–200 nm). It should be emphasized that the sample could not be tilted due to strong magnetic behaviour and thus, austenite may be only partially visible, since it was only observed in given orientation. However, presence of thin films of retained austenite is clearly evident in the microstructure. In addition, the microstructures were also examined in terms of plausible existence of carbides, and they were found inside the bainitic laths, which is typical for lower bainite. Figure 91 presents two Fe_3C carbides inside a bainite lath, bigger of them being a 300 nm long, 30 nm thick, in approximately 35° angle to the lath growth direction (lath boundary, LB, marked with red line in the figure). In overall, carbides seem to exist only in small fraction of cross-sectional area, and mass fraction is even minor as the density of the carbide is less than matrix density. Corresponding SAED Figure 91 was taken with such an aperture that only bainite (α-Fe) and cementite (Fe_3C) were present.

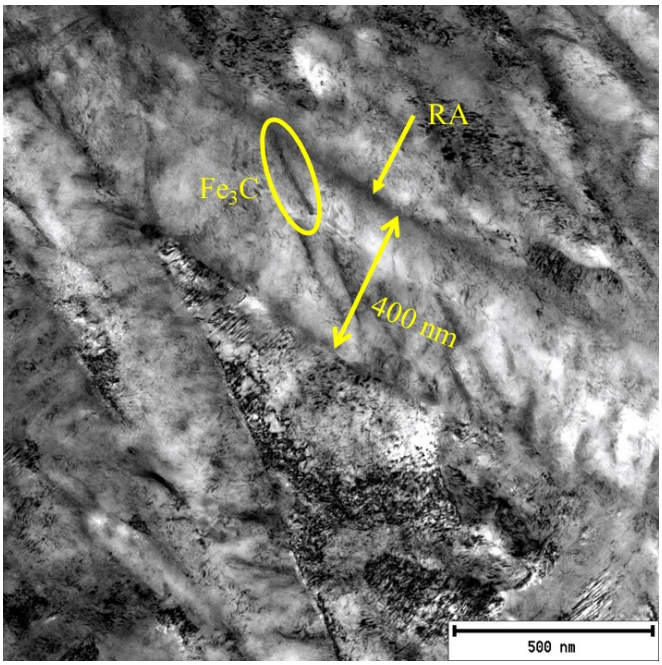

Figure 89. BF image of Steel NR MT-TMCP.

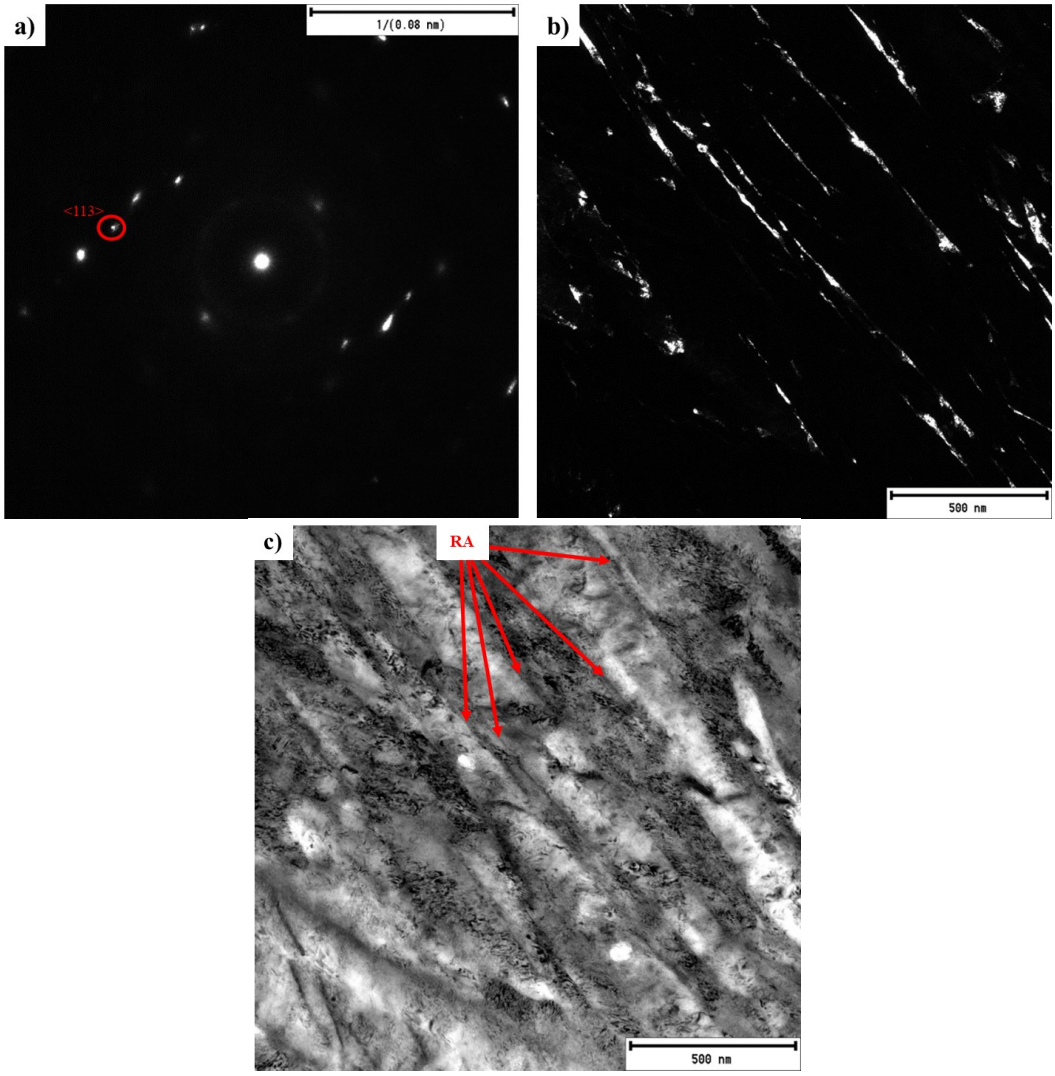

Figure 90. a) Selected area diffraction pattern of austenite with a <113> zone axis, corresponding b) dark field image and c) bright field image.

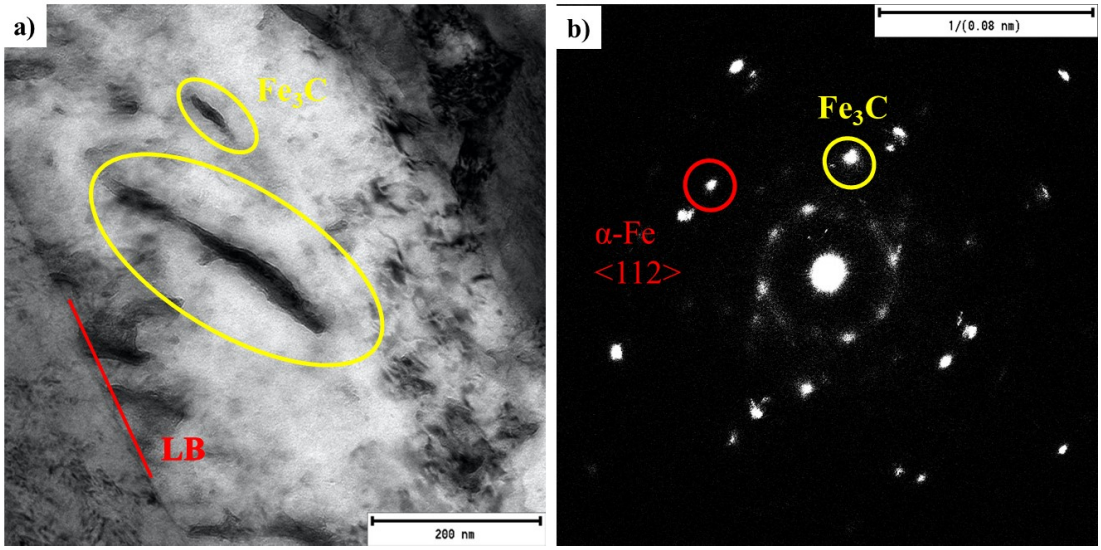

Figure 91. a) BF image of steel NR MT-TMCP showing in-lath cementite (Fe3C) and b) corresponding SAED. Red line in BF image illustrates lath boundary (LB).

4.3 Work Package 5. Properties testing.

Microstructures obtained after TMCP processes in WP3, with final product thickness of 3 and 12 mm, have been tested in this WP to determine their properties.

Note that in a later section, Task 5.6, and based on WP4 and WP5 results, two grades were selected for a deeper microstructural and mechanical characterization.

*In the case of LT-TMCP and MT-TMCP 3 mm product, where plain compression press had to be used to simulate the process, and due to the low deformation temperature of the final deformation, the standard sample size of 50x150x10 mm^3 required too high deformation forces and led to the breakage of the deformation stamps. Thus, a smaller sample size of 25x150x10 mm^3 was used. The deformed area of the sample is thus 25x10 mm^2, which made properties characterization unviable.

Table 36 shows as a function of final thickness and the different TMCP applied, the partner in charge of mentioned mechanical properties (on selected conditions).

Table 36. As a function of final thickness and the different TMCP applied, partner in charge of mentioned mechanical properties (on selected conditions). L refers to longitudinal direction and T to transversal.

			Tensile	Charpy	Wear	Bending	Hole Exp.
HT-TMCP	3 mm	HT-350C-30min	tkSE (L&T)			tkSE	tkSE
	3 mm	HT-350C-3h	tkSE(T) OULU(L&T)		OULU	tkSE	tkSE
	3 mm	HT-325C-3h	tkSE(T) OULU(L&T)		OULU OCAS	tkSE	tkSE
	12 mm	HT-350C - ≥ 30min	OULU	tkSE	OULU OCAS	OCAS	
MT-TMCP	3 mm	MT-350C-60min	*				
	12 mm	MT-350C-60min	OULU	tkSE	OULU OCAS		
LT-TMCP	3 mm	LT-350C-60min	*				
	12 mm	LT-350C - ≥ 30min	OULU	tkSE	OULU OCAS	OCAS	

A general scheme of the typical position of the sample blanks extracted from the sheets is shown in Figure 92.

Longitudinal direction refers to RD-ND, while transversal refers to TD-ND.

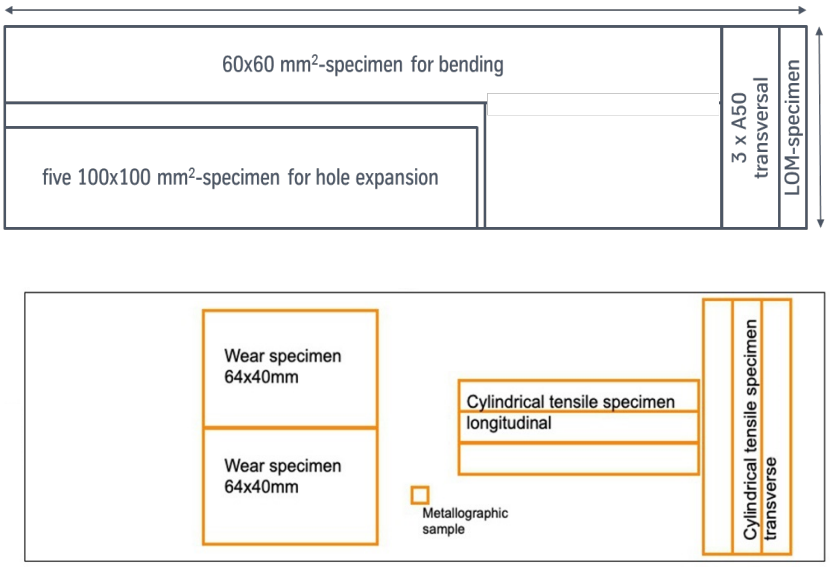

Figure 92. Representative scheme of sample extraction for properties tests.

4.3.1 Task 5.1: Tensile tests on 3mm and 12 mm material (tkSE,OULU)

4.3.1.i Experimental conditions

For the 3 mm product both partners (tkSE and OULU) conducted the tests according to DIN EN ISO 6892-1 standard with A50 samples (12.5 mm width and a gauge length of 75 mm). In accord with the ISO standard, a slow deformation rate of 0.00025 s^{-1} was applied during the initial elastic deformation, followed by an abrupt raise in strain rate to 0.0067 s^{-1} to determine the tensile behaviour and properties in a reasonable time. An extensometer was always used during the experiments.

4.3.1.i.i tkSE:

While sheets with a holding time of 30 min were tensile tested both in transverse as well as longitudinal direction, sheets with a holding time of 3 h were tested only in the transverse direction.

4.3.1.i.ii OULU:

From the 3mm rolled samples, A50 flat tensile specimens were machined in both longitudinal as well as transverse directions.

For the 12mm product, cylindrical tensile specimens according to EN 10002-1 standard were machined from both longitudinal as well as transverse directions, except the MT-TMCP specimens, for which only the longitudinal specimens were used. The specimens had a gauge length of 40 mm and diameter 6 mm, with M10x1.5 metric threads at both the ends for attaching the specimens to the grips in the 100-kN Zwick Roell tensile testing device. A strain rate of 0.00025 s^{-1} was applied during initial elastic deformation, followed by an abrupt raise in the strain rate to 0.008 s^{-1} to characterize the tensile behaviour and properties.

In all cases YS refers to the 0.2% yield strength.

4.3.1.ii HT-TMCP

4.3.1.ii.i 3mm materials (tkSE)

The engineering stress-strain curves of the transverse HT-TMCP-3 mm specimens measured at tkSE are shown in Figure 93. In accord with WP3, during test rolling of the HT-TMCP-3 mm sheets in the rolling setup, air cooled sheets of four out of the select five steels (Table 37, except NR steel) were produced. Due to realization of sufficiently fast air cooling, martensitic microstructures formed (~10 % retained austenite) in the rolled samples, identified by t_{coil} = 0 in in Table 37. For favour of comparison, tensile tests were performed for these air-cooled martensitic sheets as well. Since the rolling simulations were performed using samples from the ends of the casting blocks, strong segregations existed, which in turn could negatively affect the tensile test results.

As expected samples with martensitic microstructures showed the highest yield and ultimate tensile strengths, see Table 37. Except for the NR+Nb+V+Al steel, the ultimate elongations measured for these steels were lowest accordingly (around 5 %). The NR+C+Nb+V samples were, in fact, so brittle that some of them broke even during the elastic deformation.

A strong influence of the coiling temperature and holding time on the tensile properties is clearly visible, Table 37. Increasing the holding time from 30 min to 3 h led to an increase in the tensile strength to a tune of 150-200 MPa, though accompanied by nearly halving of the total elongation as a consequence. Reducing the coiling temperature from 350 to 325°C is favourable for high tensile properties. The ultimate tensile strength is increased by about 200 to 350 MPa, while the ultimate elongation stays at the same level, except the NR+Nb+V+Al steel, which shows nearly halving of the ultimate elongation as a result.

A summary of the tensile properties is shown in Table 37. No significant difference between the results in longitudinal and transversal direction for 30 min holding was found. As expected, NR+C+Nb+V steel showed the highest tensile strength (about 1937 MPa) for each coiling condition. Only at the coiling temperature of 325°C, NR+Mo+Nb steel showed a similar tensile strength as NR+C+Nb+V.

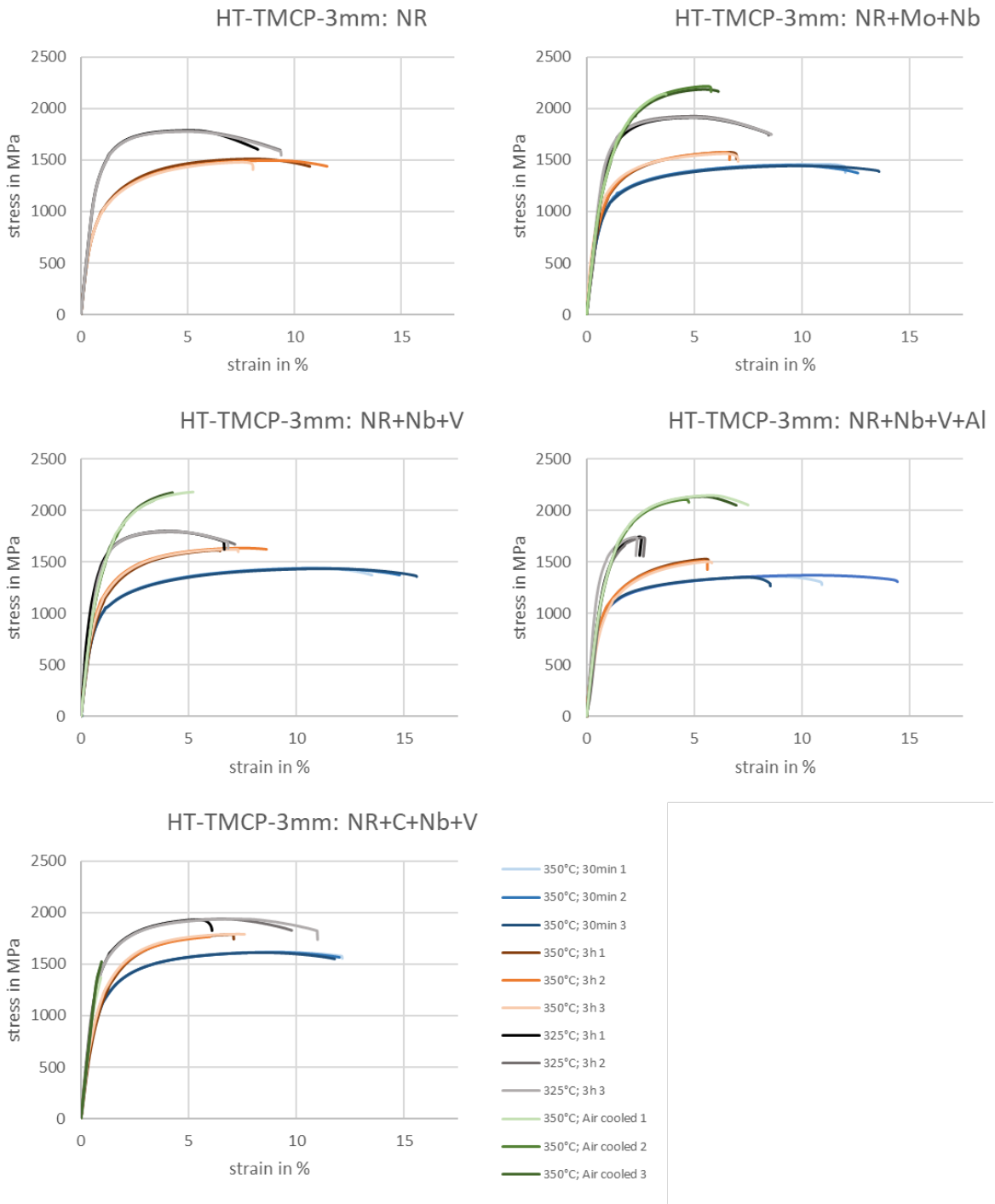

Figure 93: Stress-strain curves of the HT-TMCP-3 mm A50 samples taken transversal to the rolling direction tested at tkSE.

Table 37: Summary of the tensile test results for the HT-TMCP-3 mm material tested at tkSE (average of 3 tests). The standard deviation is given into brackets.

Alloy	T_{coil} /ºC	t_{coil} /h	Plate ID	Direction	YS/ MPa	UTS/ MPa	εu/ %	εt/ %
NR	350	3	401905	Transverse	810 (± 14)	1497 (± 15)	7.5 (± 0.8)	10.2 (± 2.4)
	325		401908		1337 (± 15)	1783 (± 6)	4.1 (± 0.1)	9.9 (± 0.4)
NR+Mo+Nb	350	0		Longitudinal	1266 (± 44)	2156 (± 110)	3.7 (± 1)	3.7 (± 1)
				Transverse	1289 (± 13)	2182 (± 37)	3.8 (± 1.1)	4.1 (± 1.3)
		0.5	361855	Longitudinal	885 (± 18)	1448 (± 13)	8.7 (± 0.1)	13.2 (± 0.5)
				Transverse	881 (± 20)	1451 (± 7)	9.3 (± 0.6)	12 (± 0.8)
		3	401004		870 (± 56)	1573 (± 12)	5.9 (± 0.3)	6.3 (± 0.4)
	325		401006		1577 (± 25)	1920 (± 10)	3.8 (± 0.1)	7.5 (± 0.2)
NR+Nb+V	350	0		Longitudinal	1279 (± 12)	1989 (± 84)	1.8 (± 0.7)	1.8 (± 0.7)
				Transverse	1269 (± 20)	2152 (± 45)	3.3 (± 0.9)	3.3 (± 0.9)
		0.5	361859	Longitudinal	826 (± 24)	1430 (± 14)	9.5 (± 0.2)	10 (± 0.2)
				Transverse	838 (± 13)	1439 (± 3)	10.3 (± 0.4)	13.9 (± 1.1)
		3	400999		899 (± 90)	1627 (± 12)	6.2 (± 0.9)	6.7 (± 1.3)
	325		401001		1360 (± 122)	1797 (± 6)	3.3 (± 0.2)	6.1 (± 0.2)
NR+Nb+V+Al	350	0		Longitudinal	1296 (± 13)	2144 (± 16)	4.5 (± 0.2)	5.6 (± 0.9)
				Transverse	1281 (± 3)	2130 (± 20)	4.2 (± 0.6)	5.4 (± 1.5)
		0.5	361862	Longitudinal	871 (± 13)	1341 (± 10)	9.5 (± 0.3)	14.3 (± 0.7)
				Transverse	864 (± 52)	1361 (± 10)	8.2 (± 1.6)	10.7 (± 3)
		3	400995		823 (± 82)	1513 (± 15)	4.9 (± 0.2)	5 (± 0.1)
	325		400997		1463 (± 101)	1743 (± 6)	1.5 (± 0.2)	1.6 (± 0.1)
NR+C+Nb+V	350	0		Longitudinal	1304 (± 6)	2002 (± 322)	1 (± 0.6)	1 (± 0.6)
				Transverse		1453 (± 78)	0.2 (± 0.1)	0.2 (± 0.1)
		0.5	361864	Longitudinal	922 (± 3)	1598 (± 27)	8.7 (± 0.4)	12.3 (± 1.9)
				Transverse	882 (± 47)	1615 (± 4)	7.9 (± 0.4)	11.2 (± 0.3)
		3	400991		929 (± 53)	1783 (± 12)	5.9 (± 0.8)	6 (± 0.9)
	325		400993		1373 (± 60)	1937 (± 6)	5.5 (± 0.9)	8.1 (± 2.6)

4.3.1.ii.ii 3mm material (OULU)

As an example, the engineering stress – strain curves of the 3 mm HT-TMCP steels are displayed in Figure 94, which clearly depicts the influence of bainitic holding temperature on the stress-strain behaviour and tensile properties. Even a small change of bainitic holding from 350 to 325 °C makes appreciable difference in respect of yield and tensile strengths as well as elongation values. Obviously, a higher strength at lower holding temperature (325°C) corroborates the corresponding lower tensile elongation, particularly the low uniform elongation. One interesting exception, however, was NR+C+Nb+V steel with 0.5C%, which had almost a similar level of elongation at both holding temperatures, while at the same time there was a gain of 200 MPa in the tensile strength at lower holding temperature (325ºC). In order to be able to readily compare the curves for different steels, all stress-strain curves have been plotted with same scales.

A summary of the results is shown in Table 38, which shows an average of at least 3-5 tests for a particular steel. As can be seen from the table, a high tensile strength was obtained after holding at 325°C for individual steels and the corresponding elongation, however, was relatively low. The highest tensile strength measured was 1946 MPa for NR+C+Nb+V steel with 0.5C%.

It is important to highlight the fact that no relevant differences were found between the results of both partners in same conditions.

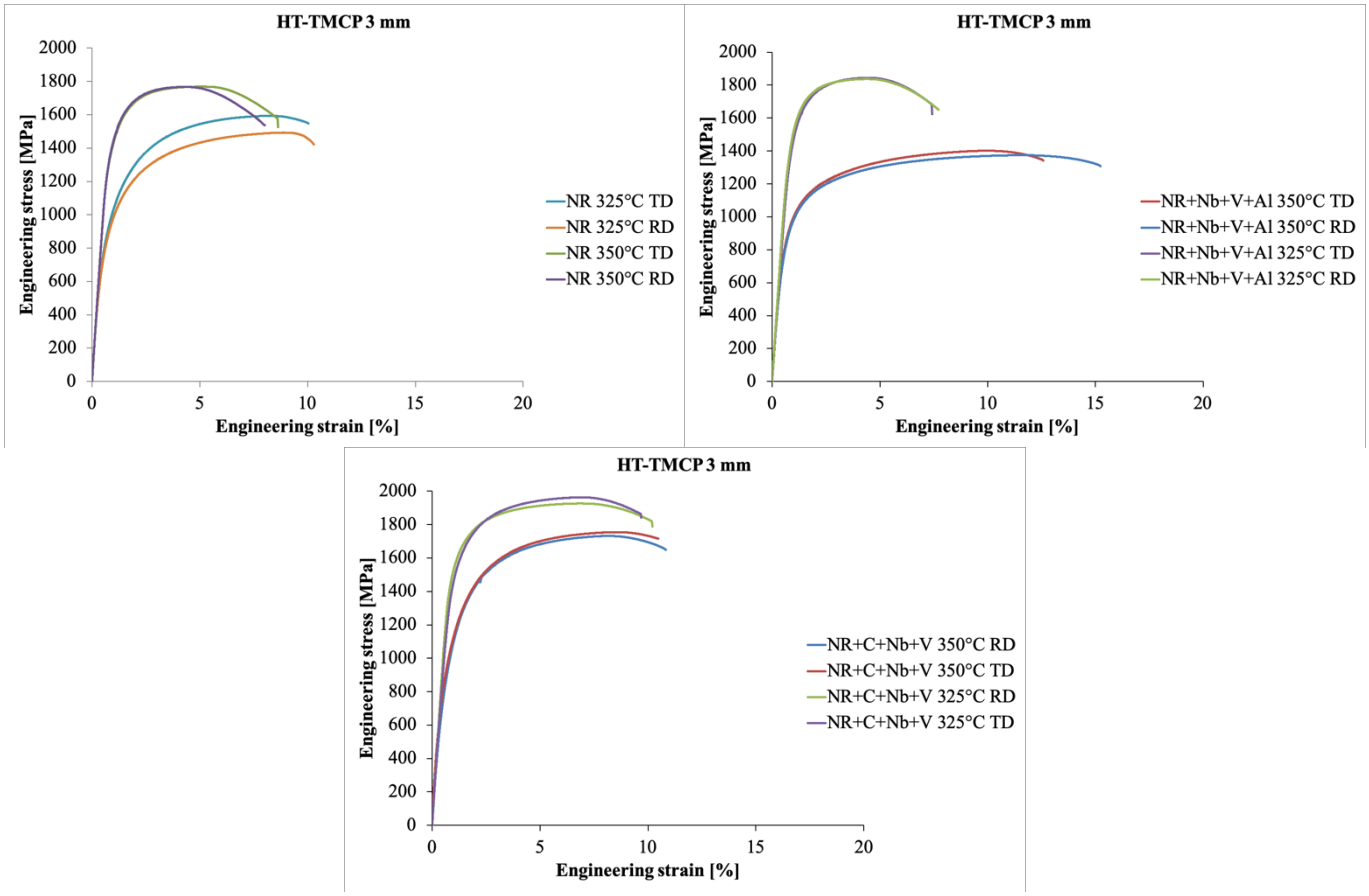

Figure 94. Examples of stress-strain curves of the HT-TMCP 3 mm samples tested at Oulu.

Table 38. Summary of the tensile test results for the HT-TMCP 3 mm material tested at Oulu. Transverse direction: average of 3 tests. Longitudinal direction: average of 5 tests. Standard error is in the brackets.

Alloy	T_{coil} /ºC	t_{coil} /h	Plate ID	Direction	YS/ MPa	UTS/ MPa	εu/ %	εt/ %
NR	325	3 h	401909	Transverse	1307 (± 2)	1773	4.1	8.3
	325	3 h	401909	Longitudinal	1327 (± 14)	1727	3.4	7.9
	350	3 h	401907	Transverse	788 (± 15)	1489	7.6	10.1
	350	3 h	401907	Longitudinal	780 (± 10)	1481	8.1	10.5
NR+Mo+Nb	325	3 h	401007	Transverse	1397 (± 9)	1858	3.9	6.6
	325	3 h	401007	Longitudinal	1319 (± 26)	1782	3.9	7.4
	350	3 h	401005	Transverse	866 (± 10)	1515	8.7	12.4
	350	3 h	401005	Longitudinal	854 (±15)	1486	8.4	11.8
NR+Nb+V	325	3 h	401003	Transverse	1483 (± 23)	1837	2.7	6.4
	325	3 h	401003	Longitudinal	1288 (± 40)	1799	4.5	8.4
	350	3 h	401000	Transverse	865 (± 6)	1564	8.1	10.8
	350	3 h	401000	Longitudinal	900 (± 46)	1540	6.8	10.7

NR+Nb+V+Al	325	3 h	400998	Transverse	1431 (± 30)	1845	3.4	7.4
	325	3 h	400998	Longitudinal	1404 (± 27)	1826	3.4	7.3
	350	3 h	400996	Transverse	791 (± 12)	1404	9.6	12.2
	350	3 h	400996	Longitudinal	787 (± 8)	1390	10.8	15.1
NR+C+Nb+V	325	3 h	400994	Transverse	1385 (± 14)	1946	5.7	9.1
	325	3 h	400994	Longitudinal	1456 (± 39)	1929	5.9	10.1
	350	3 h	400992	Transverse	848 (± 31)	1753	7.7	10.5
	350	3 h	400992	Longitudinal	855 (± 32)	1717	7.5	10.7

4.3.1.ii.iii 12 mm materials (OULU)

An illustration of engineering stress – strain curves for two steels in two different directions is shown in Figure 95, which clarifies that there is no significant difference in tensile behaviour between longitudinal and transverse directions. Both the uniform and tensile elongations are impressive, but the tensile strength seems to be relatively low in comparison to the high tensile strengths obtained at 325°C holding in the case of flat 3mm samples.

A summary of the tensile results is shown in Table 39. The results presented in the table are the averages of three tests in each direction for a given steel. Generally speaking, the strength of these steels was quite close in the range of 1400–1500 MPa, which was apparently not very high, but keeping in view their high elongations, particularly uniform elongations (ε_u), these are considered reasonably good. Total elongations obtained in the longitudinal direction varied in the range 17–19%, irrespective of the steel type. However. NR+Mo+Nb steel showed lower elongations in the transverse direction (12%). Tensile properties of the NR+Mo+Nb and NR+Nb+V+Al steels were pretty similar in rolling direction, both of them had tensile strengths of about 1425 MPa and total elongations of about 19%. It is, however, emphasized that the current plate of NR+Nb+V+Al steel was held at 350°C for only 50 minutes to enable bainitic transformation, while the NR+Mo+Nb plate was held for just 20 minutes at 350°C, prior to continuous cooling to room temperature, based on the results of the Gleeble simulations.

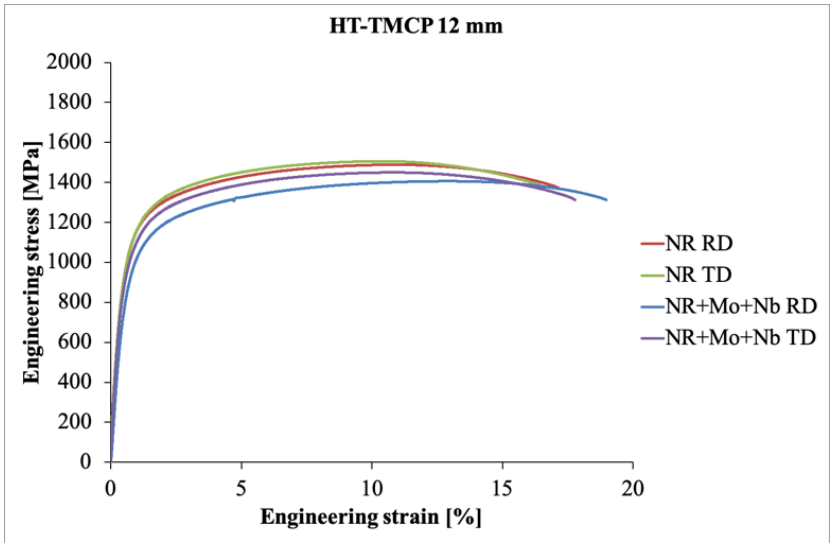

Figure 95. Examples of stress-strain curves of the HT-TMCP 12 mm samples tested at Oulu.

Table 39. Summary of tensile test results (average of three tests) for the HT-TMCP 12mm material.

Alloy	T_{coil} /ºC	t_{coil} /h	Plate ID	Direction	YS/ MPa	UTS/ MPa	εu/ %	εt/ %
NR	350	60 min	X354B	Transverse	874 (±69)	1505	9.7	16.5
	350	60 min	X354B	Longitudinal	828 (± 80)	1490	11.0	17.0
NR+Mo+Nb	350	20 min	X353E	Transverse	921 (± 7)	1413	7.7	12.0
	350	20 min	X353E	Longitudinal	856 (± 3)	1423	12.0	19.0
NR+Nb+V	350	40 min	X353H	Transverse	814 (± 39)	1456	10.9	16.8
	350	40 min	X353H	Longitudinal	713 (± 20)	1436	12.0	18.0
NR+Nb+V+Al	350	50 min	X353N	Transverse	865 (± 8)	1451	10.1	17.4
	350	50 min	X353N	Longitudinal	914 (± 39)	1425	11.0	19.0
NR+C+Nb+V	350	40 min	X353V	Transverse	945 (± 27)	1494	10.3	14.8
	350	40 min	X353V	Longitudinal	935 (± 23)	1469	14.0	18.0

4.3.1.iii MT-TMCP

4.3.1.iii.i 12 mm materials (OULU)

An example of the engineering stress-strain behaviour of the three steels isothermally held for bainitic transformation at 350°C/1 h is shown in Figure 96, depicting the influence of prior strain (about 0.4 strain at 500°C) and alloying elements on the transformation behaviour and resultant tensile properties. While Mo+Nb alloying tends to increase the tensile strength (with somewhat lower ductility) in comparison with that of the reference steel, an increase in C content to 0.5% besides addition of microalloying elements, however, resulted in lower tensile strength but enhanced ductility, presumably as a consequence of a higher fraction of retained austenite in the steel, and this suggests use of a still lower temperature of bainitic holding for improving the tensile properties.

A summary of the tensile results is shown in Table 40. The results in the table are the averages of three tests for a given steel. In general, total elongations (8.9–16.5%) of 12 mm MT-TMCP steels were lower and the tensile strengths (1500–1912 MPa) higher than those of 12 mm HT-TMCP samples. The tensile strength recorded for the NR+C+Nb+V steel with 0.5% C was the highest and reached almost 2GPa (1912 MPa), but the total elongation as a result was somewhat reduced.

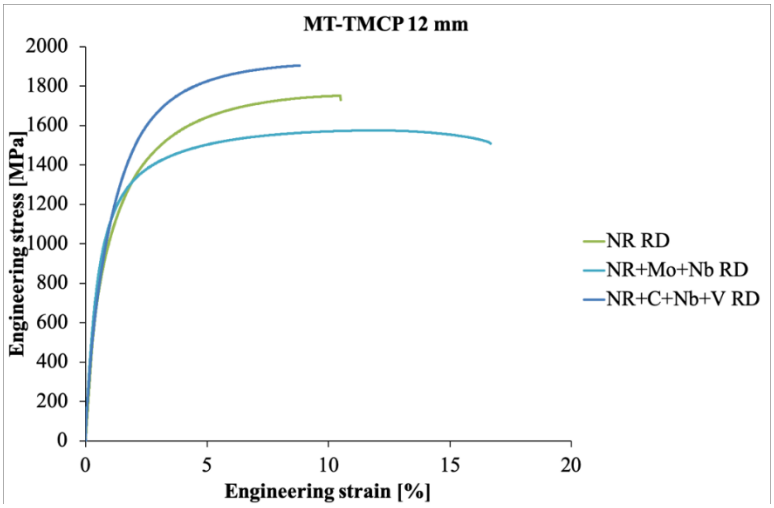

Figure 96. Examples of stress-strain curves of the MT-TMCP 12 mm samples tested at Oulu.

Table 40. Summary of tensile test results (average of three tests) for the MT-TMCP 12mm material

Alloy	T_{coil} /°C	t_{coil} /h	Plate ID	Direction	YS/ MPa	UTS/ MPa	εu/ %	εt/ %
NR	350	60 min	2-1	Longitudinal	802	1628 (±)	10.6	12.7
	350	60 min	2-14	Longitudinal	792 (± 62)	1739 (± 11)	9.1	9.9
NR+Mo+Nb	350	60 min	8-1	Longitudinal	870 (± 28)	1566 (± 5)	11.0	16.5
NR+Nb+V	350	60 min	14-12	Longitudinal	758 (± 15)	1626 (± 18)	11.3	14.9
NR+Nb+V+Al	350	60 min	16-12	Longitudinal	712 (± 11)	1500 (± 4)	11.5	15.7
NR+C+Nb+V	350	60 min	15-12	Longitudinal	821 (± 6)	1912 (± 5)	7.9	8.9

4.3.1.iv LT-TMCP

4.3.1.iv.i 12 mm materials (OULU)

Another example of engineering stress-strain curves recorded on LT-TMCP steels is shown in Figure 97. Contrary to the expectations of high strengths in these steels, most steels showed mediocre strengths and relatively high elongations owing to the fact that the deformation temperature was actually relatively high and most of the transformation occurred during the slow cooling (about 0.1°C/s) to the isothermal holding temperature. Hence, most of the transformation was realized in the upper bainitic regime during cooling itself. It also points to the fact that it is nearly impossible to cool thick samples fast enough from an intermediate temperature of about 400°C) to the lower bainitic holding temperatures without the occurrence of phase transformation.

A summary of the tensile results is presented in Table 41. The results in the table are averages of three tests for a given steel. In general, tensile strengths of 12 mm LT-TMCP steels were surprisingly low, in the range of 1294–1506 MPa, whereas total elongations (19.2–28.1%) were higher than those of HT-TMCP or MT-TMCP samples, obviously as a result of slow cooling from the deformation temperature resulting in somewhat coarse bainite.

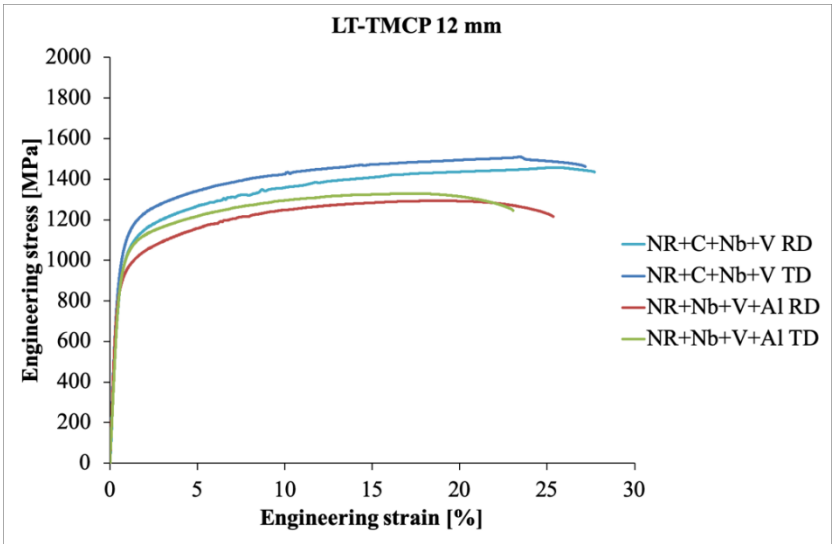

Figure 97. Examples of stress-strain curves of the LT-TMCP 12 mm samples tested at Oulu

Table 41. Summary of tensile test results (average of three tests) for the LT-TMCP 12mm material.

Alloy	Tcoil /ºC	tcoil /min	Plate ID	Direction	YS/ MPa	UTS/ MPa	εu/ %	εt/ %
NR	350	30	X356I	Transverse	887 (± 6)	1376 (± 2)	19.3	25.0
	350	30	X356I	Longitudinal	807 (± 12)	1342 (± 10)	19.8	25.7
NR+Mo+Nb	350	70	X355D	Transverse	834 (± 3)	1434 (± 1)	14.8	19.2
	350	70	X355D	Longitudinal	819 (± 16)	1391 (± 14)	18.4	23.7
NR+Nb+V	350	40	X355M	Transverse	833 (± 50)	1488 (± 13)	18.1	23.5
	350	40	X355M	Longitudinal	781 (± 11)	1413 (± 10)	18.8	23.8
NR+Nb+V+Al	350	30	X355T	Transverse	919 (± 37)	1330 (± 2)	16.6	23.2
	350	30	X355T	Longitudinal	833 (± 4)	1294 (± 2)	18.2	25.0
NR+C+Nb+V	350	20	X356Y	Transverse	918 (± 36)	1506 (± 11)	21.0	25.0
	350	20	X356Y	Longitudinal	910 (± 5)	1462 (± 12)	25.2	28.1

4.3.1.v General analysis

Figure 98 shows different tensile properties as a function of hardness for all the tested conditions in 3 mm and 12 mm product subjected to HT, MT and LT-TMCP, all of them compared with the reference properties obtained by isothermal TMCP in 12 mm product.

Regarding the 3 mm HT-TMCP, when data is plotted as a function of hardness, Figure 98 a,b), two clear regions proportional to HV are found in the case of the Yield Strength (YS) and Ultimate Tensile Stress (UTS), the same regions that were present in the microstructural analysis and that were associated to different isothermal temperatures, Figure 74. As expected, lower isothermal temperatures, finer bainitic microstructures, lead to higher YS and UTS and lower UE and TE. Obviously the hardening capacity of

the microstructure, measured as the YS/UTS ratio, developed at 350ºC is better (lower ratio) than that of the 325ºC microstructure, Figure 99.

Figure 100 is representative of the tensile behaviour with temperature and time. Although the increase of isothermal time also makes the YS and the UTS increase and the UE and TE decrease, it can be observed that the isothermal temperature is the most significant parameter, as the highest variations are observed among microstructures heat treated at different temperatures.

Regarding the comparison with the reference, if only the cloud on the bottom left (results for 350 °C as isothermal temperature) is considered, not improvements are detected, the YS values are always in the range observed for isothermal TMCP microstructures.

No tensile properties have been measured for the 3 mm MT and LT-TMCP.

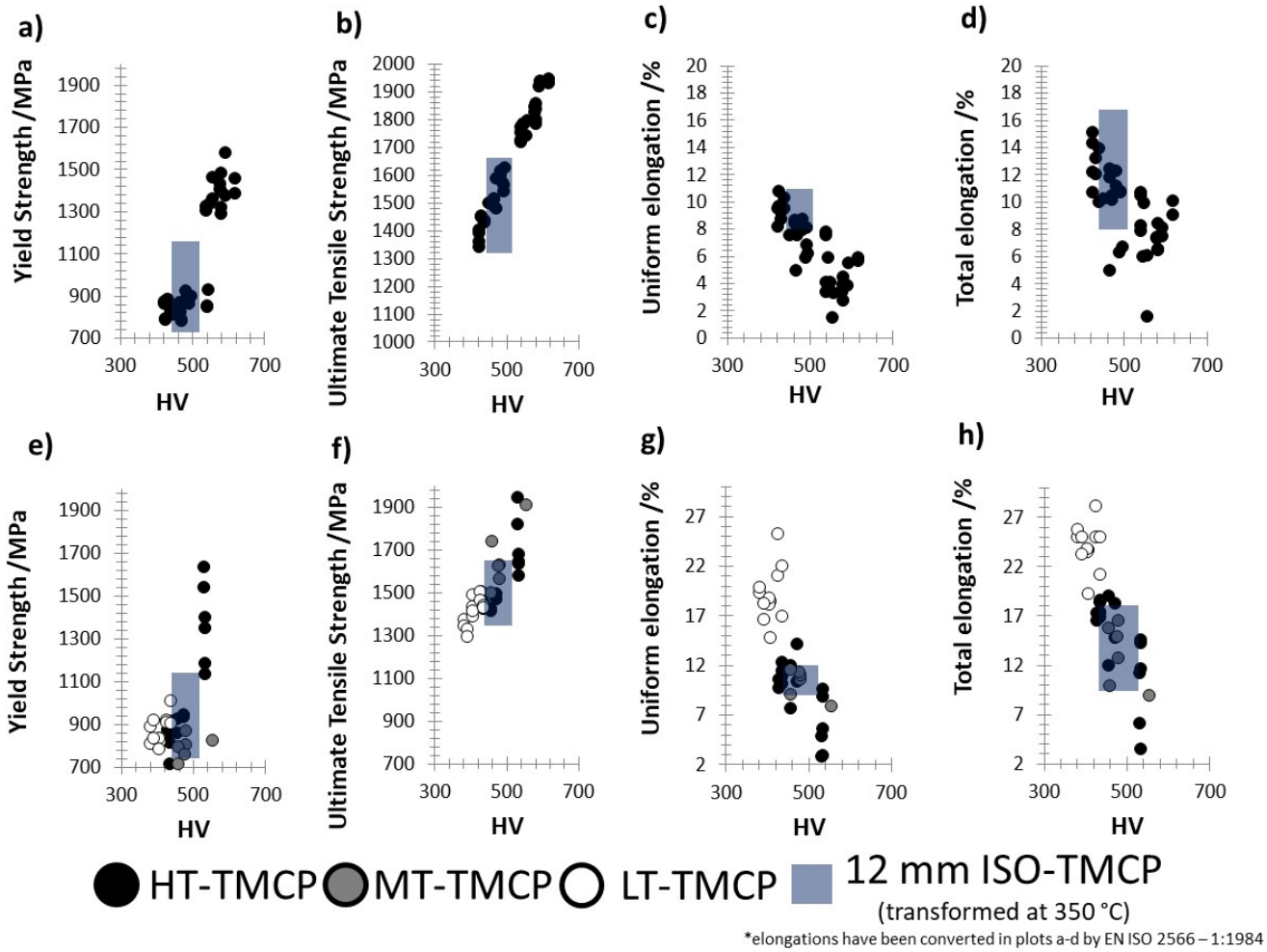

Figure 98. Different mechanical properties obtained by tensile tests represented as a function of the Vickers Hardness (HV), where the type of TMCP can by distinguished by its color. A grey region range of the values obtained in 12 mm specimens subjected to isothermal TMCP at 350 °C is also included. Subfigures a-d) correspond to 3 mm product, whereas the subfigures e-h) correspond to 12 mm product. Due to the different geometries of the tensile specimens of the ISO-TMCP and LT-TMCP (3mm), the elongation results of the former has been corrected according to [24].

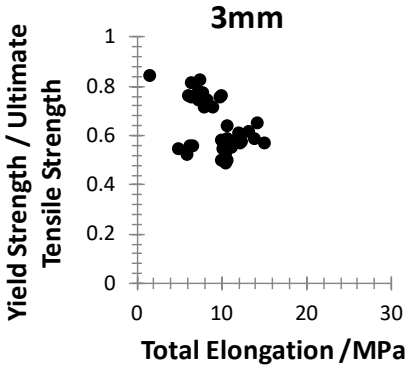

Figure 99. Yield strength / Ultimate tensile strength ratio of the 3mmm HT-TMCP.

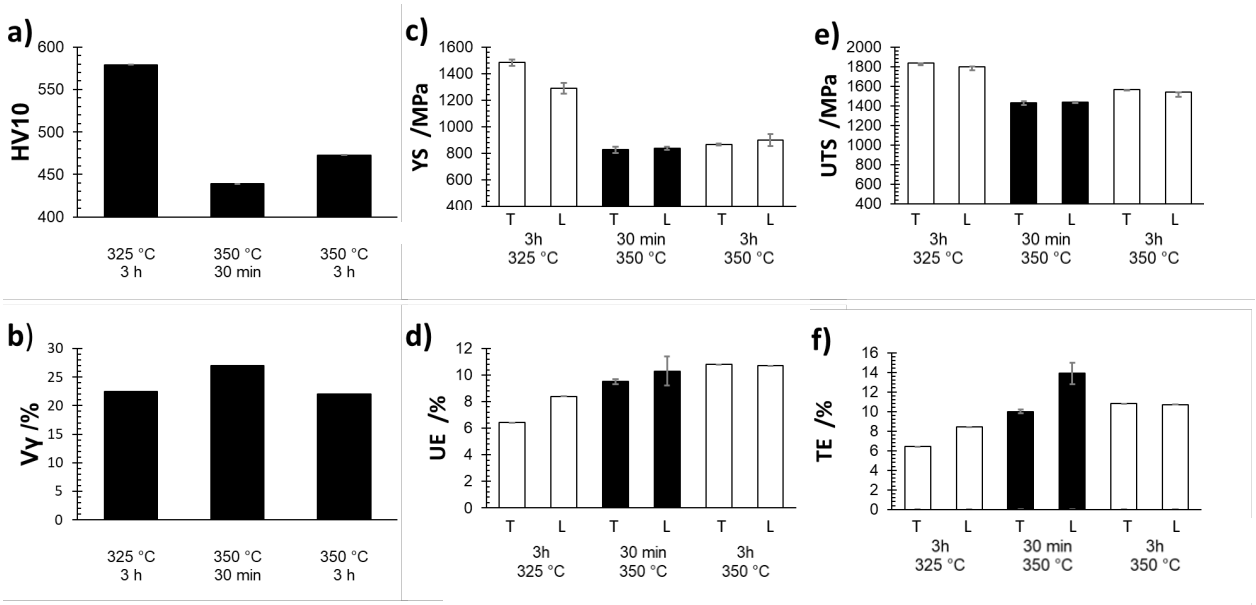

Figure 100. For the 3 mm HT-TMCP product, different parameters for three different conditions of NR+Nb+V steel, where the isothermal temperature and time are indicated below each bar: a) Hardness; b) austenite volume fraction; c) yield strength; d) uniform elongation; e) ultimate tensile strength; f) total elongation.

Note that, because of already described technical reasons the 12 mm TMCP plates have been isothermally treated for different times and temperatures. Therefore, no effect of transformation start temperature or isothermal time can be studied. The analysis has been focused on whether the properties improve the ones of the reference isothermal TMCP.

On average, the MT-TMCP and HT-TMCP exhibits similar values of HV and UTS values, while the presence of martensite in the case of the MT reduces the YS as compared to HT-TMCP. While the HT-TMCP properties are barely improved with respect to the reference isothermal TMCP, the MT-TMCP shows an improvement in the UTS values. The slightly higher fraction of retained austenite and lower fraction of martensite in the HT-TMCP could also explain the better ductility results, that pairs, and in some cases exceed, that of the isothermal TMCP.

The LT-TMCP on the other hand, having a much higher fraction of retained austenite and lower HV than the other two TMCP cases, has similar YS, lower UTS but much better ductility, exceeding also that of the

isothermal TMCP. Regardless of the TMCP, it is evident from the results that most of the elongation is uniform.

The discussed results have also a direct reflect on the product of strength and ductility, where the best combination is obtained for the LT followed by the MT and HT, which are on pair, see Figure 101. In the same figure the hardening capacity (YS/UTS ratio) shows that the highest capability is shown by the MT-TMCP microstructures, probably due to a stable austenite embedded in a fairly strong ferritic matrix.

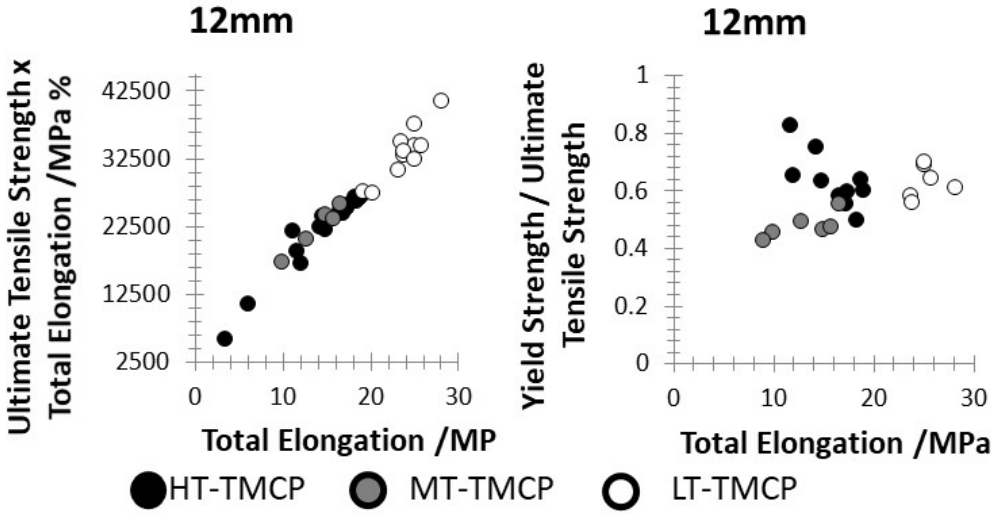

Figure 101. For the 12 mm TMCP product, strength ductility product and YS/UTS ratio.

If we look individually at the tensile properties of the 12 mm microstructures, which are in Figure 102, Figure 103 and Figure 104, we can make several conclusions that are valid regardless the TMCP:

- No significant differences are found on the tensile properties measured on the longitudinal or transversal direction.
- in the case of the HT-TMCP treatments, properties are of the same level or even better in comparison with the reference isothermal TMCP. Among all steels, the NR+Nb+V and NR+C+Nb+V steels present the best properties, as they present a low reduction of ductility and strength, respectively, and still they show improvements in strength and ductility with respect to the reference treatment, respectively
- the MT-TMCP microstructures present equalled or slightly improved strength properties with respect to the isothermal TMCP microstructures, whereas the elongation is equalled or slightly worsened.
- although the LT-TMCP microstructures generally present much better ductility than the reference, their strength is slightly worsened, as previously mentioned. The microstructures developed in steels NR+Nb+V and NR+C+V+Al show the best properties among all the microstructures obtained by LT-TMCP.

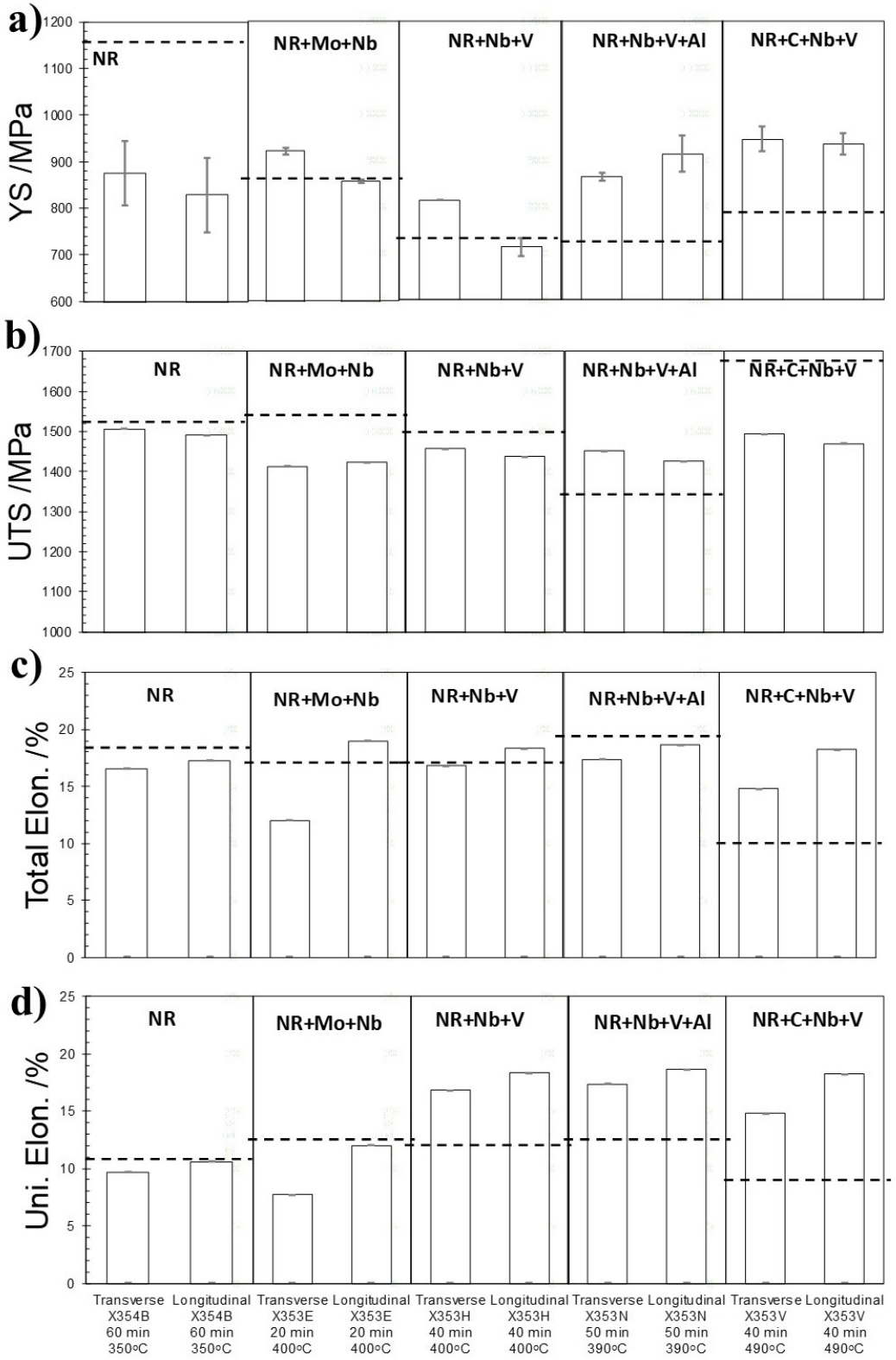

Figure 102. Obtained tensile properties for 12 mm HT-TMCP, as a function of section, start of transformation temperature and isothermal time. All the isothermal treatments were performed at 350 °C, although the indicated T and t corresponds to an estimation at which the transformation started according to plots of the type found in Figure 58. The results obtained for the isothermal TMCP specimens are depicted by dashed lines.

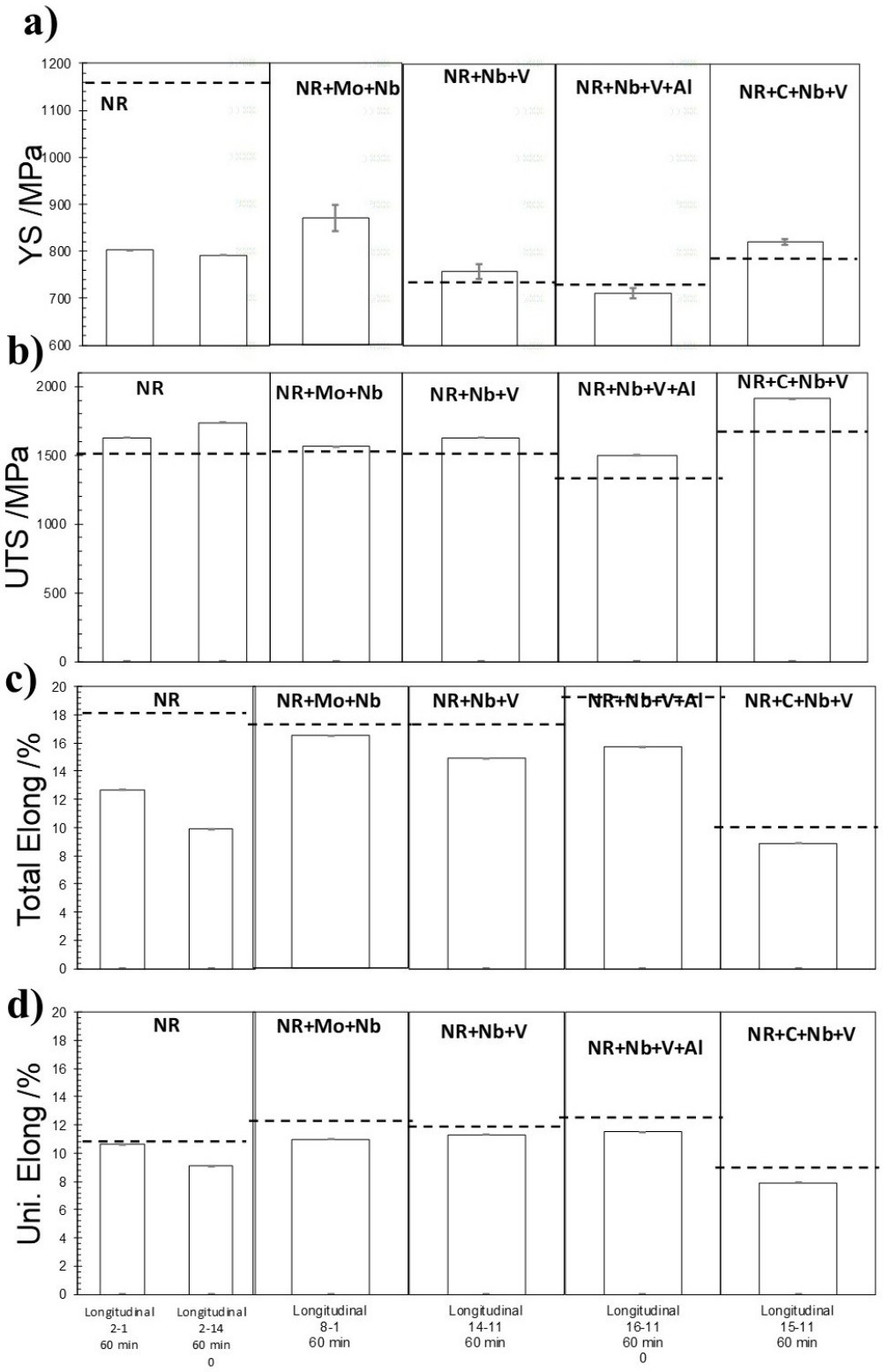

Figure 103. Obtained tensile properties for 12 mm MT-TMCP, as a function of section and isothermal time. All the isothermal treatments were performed at 350 °C. The results obtained for the isothermal TMCP specimens are depicted by dashed lines.

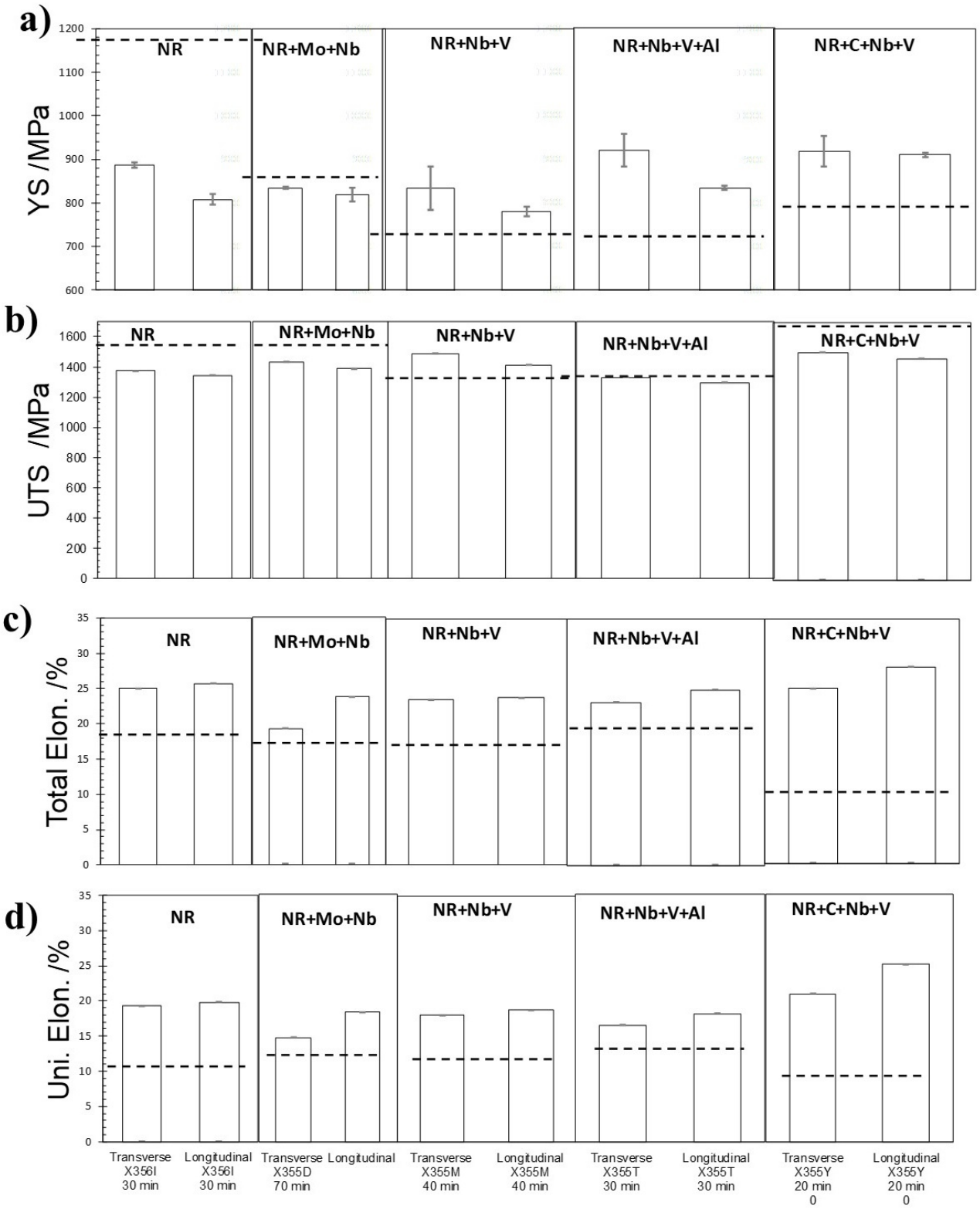

Figure 104. Obtained tensile properties for 12 mm LT-TMCP, as a function of section and isothermal time. All the isothermal treatments were performed at 350 °C, although the indicated T and t corresponds to an estimation at which the transformation started according to plots of the type found in Figure 68. The results obtained for the isothermal TMCP specimens are depicted by dashed lines.

4.3.2 Task 5.2: Charpy on 12 mm materials (tkSE)

4.3.2.i Experimental conditions

At tkSE, charpy tests were done according to DIN EN ISO 148-1:2011-01 with 12 mm samples from the HT-, MT- and LT-TMCP materials. The standard sample size of 55 x 10 x 10 mm3 with a V-notch was used. The V-notches had a notch angle of 45, a notch depth of 2 mm and a notch root radius of 0.25 mm. The hammer fin had a radius of 2 mm.

In principle, samples were tested in the temperature range between -40 and 100 °C (-40, -20, 0, 20, 50 and 100 °C). Depending on the amount of material available for the different TMCP conditions, not all temperatures could be tested for each material/plate. Due to the limitation of the available material and the width of the MT-TMCP strips, samples were prepared only parallel to the rolling direction. For each condition, three samples were tested.

4.3.2.ii HT-TMCP

Two plates of each steel were available for testing. Due to the possibility of different cooling conditions prevailing prior to the isothermal holding at 350 °C, both the plates were tested at -20 and -40 °C. Only one plate was tested at higher temperatures. For full characterization of some plates with a comparable high hardness (X353K and X353S), some additional charpy tests were done using the remaining material from wear test samples from OCAS. Due to the limitation of the plate thickness, only sample sizes of 55 x 7 x 10 mm^3 could be used. For comparison, the impact energy was rescaled to the standard geometry. The measured average impact energies are shown in Table 42. In Figure 105 the average and minimum impact energies of the three tests are plotted as a function of the test temperature. In addition, an impact energy of 27 J is shown as the reference since material testing standards frequently require a minimum impact energy of 27 J.

None of the steels shows impact energies above 27 J for the relevant test temperatures -20 and -40 °C. The exception being the NR+Nb+V X353K plate with more than 27J on average at -20ºC. At a temperature of 50 °C, all steels except NR have a minimum impact energy above 27 J.

Table 42: Summary of average Charpy impact energy results for the HT-TMCP-12 mm material (average of 3 tests). The energy values are in Joule for full size Charpy geometry. The standard deviation is given in brackets.

Alloy	Plate ID	T_{coil} /ºC	t_{coil} /min	-40 °C	-20 °C	+20 °C	+50 °C	+100 °C
NR	X354A	350	70	16.3 (±5.4)	18 (±5)	25.7 (±2.9)		
	X354D		40	11.7 (±0.5)	12.7 (±0.9)		28.7 (±3.7)	40.3 (±2.9)
NR+Mo+Nb	X353D		30	13.3 (±0.5)	18 (±0)	26 (±0.8)		
	X353F		60	18 (±4.5)	12 (±0.8)		38.7 (±8.2)	49.7 (±2.5)
NR+Nb+V	X353I		30	11.3 (±0.9)	15.3 (±2.1)	25.3 (±0.9)		
	X353L		70	12 (±0.8)	16 (±1.6)		41.3 (±3.7)	43.3 (±0.5)
	X353K		80		34.2 (±8.3)	38.2 (±12)		

NR+Nb+V+Al	X353P		30	17 (±0)	18 (±1.4)	34.3 (±2.1)		
	X353Q		20	16.3 (±0.9)	20.3 (±3.3)		42.3 (±0.5)	57.3 (±2.6)
NR+C+Nb+V	X353T		60	10.3 (±0.9)	12.3 (±1.2)	20 (±0.8)		
	X353W		30	10.3 (±0.5)	14 (±2.2)		31.7 (±0.5)	33.7 (±1.7)
	X353S		70		22.2(±6.7)	27.1(±7.1)		

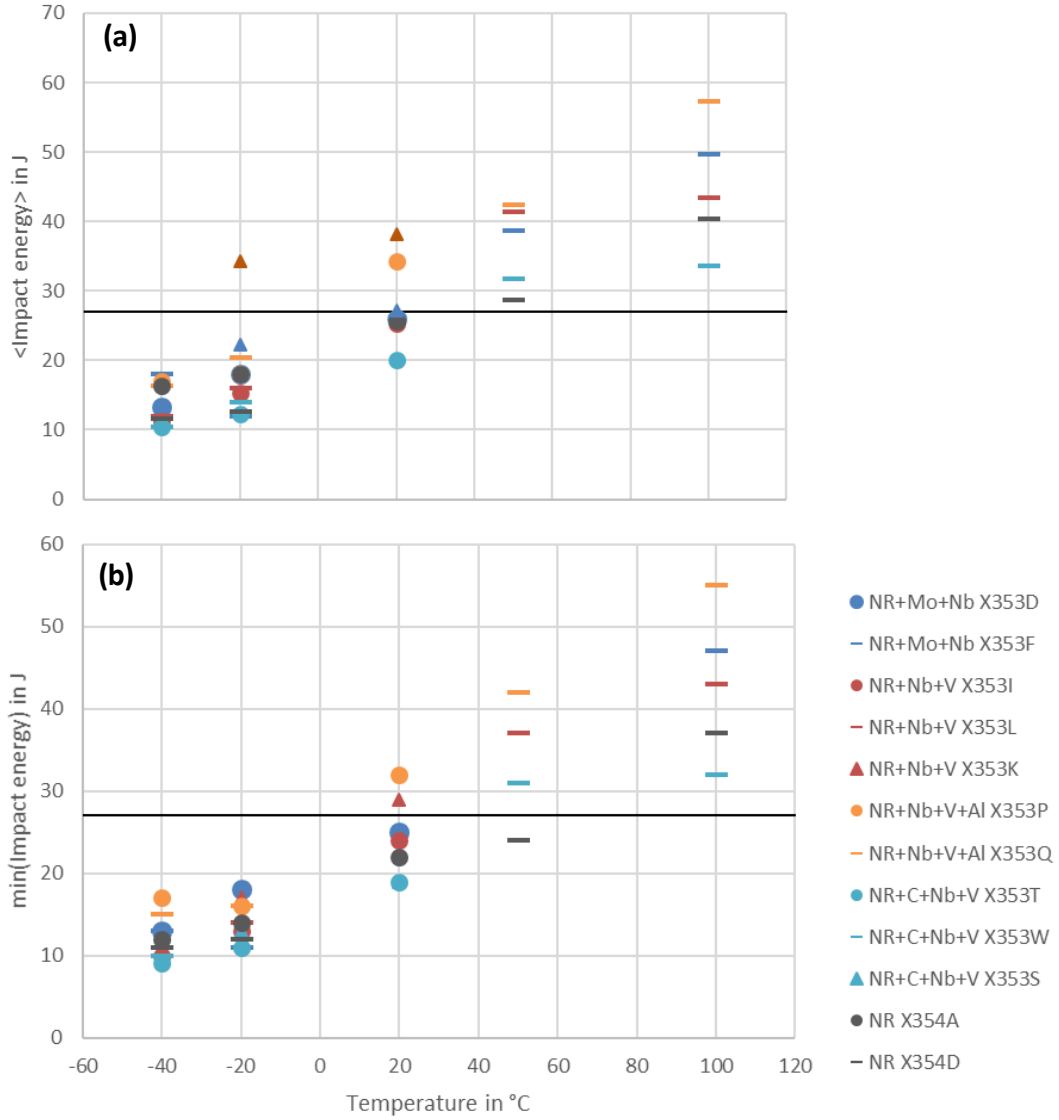

Figure 105: (a) Average and (b) minimum impact energy of the Charpy test as a function of the test temperature for HT-TMCP-12 mm material (average of 3 tests).

4.3.2.iii MT-TMCP

Due to the limited amount of available MT-TMCP-12 mm material, samples extracted from the 350ºC-60 min plates of the five steels were tested at different test temperatures in the range -40 to 100°C (five plates were used in total). The measured average impact energies are shown in in Table 43. In Figure 105, the average and minimum impact energies are plotted as a function of the test temperature.

Table 43: Summary of Charpy impact energy results for the MT-TMCP-12 mm (350ºC-60min) material (average of 3 tests). The energy values are in Joule for full size Charpy geometry. The standard deviation is given in brackets.

Alloy	-40 °C	-20 °C	0 °C	RT	50 °C	100 °C
NR	11.3 (± 2.9)	11 (± 2)	14.3 (± 2.1)	26.7 (± 9.5)	24.7 (± 10.3)	32.3 (± 12.9)
NR+Mo+Nb	10.3 (± 1.2)	10.3 (± 0.6)	14 (± 3.6)	16 (± 2.6)	27.3 (± 4.2)	33.3 (± 5.5)
NR+Nb+V	7 (± 1)	11.3 (± 3.2)	10.3 (± 1.2)	15.3 (± 8.4)	22.3 (± 9.5)	27.3 (± 10.5)
NR+C+Nb+V	9 (± 3.5)	7.7 (± 1.2)	11.3 (± 2.1)	16.7 (± 6.4)	16.3 (± 1.2)	24.3 (± 3.2)
NR+Nb+V+Al	9.7 (± 1.2)	11.3 (± 5.1)	20 (± 7)	18 (± 1.7)	26.7 (± 4.7)	38 (± 7)

The measured impact energies are even lower than those of the HT-TMCP-12 mm material despite a lower ausforming temperature (MT-TMCP). Only the NR+Nb+V+Al steel has a minimum impact energy above 27 J for the highest test temperature of 100 °C. With the exception of only 100 °C tested samples (~5 % ductile fracture), no samples showed any features of ductile fracture (0 %).

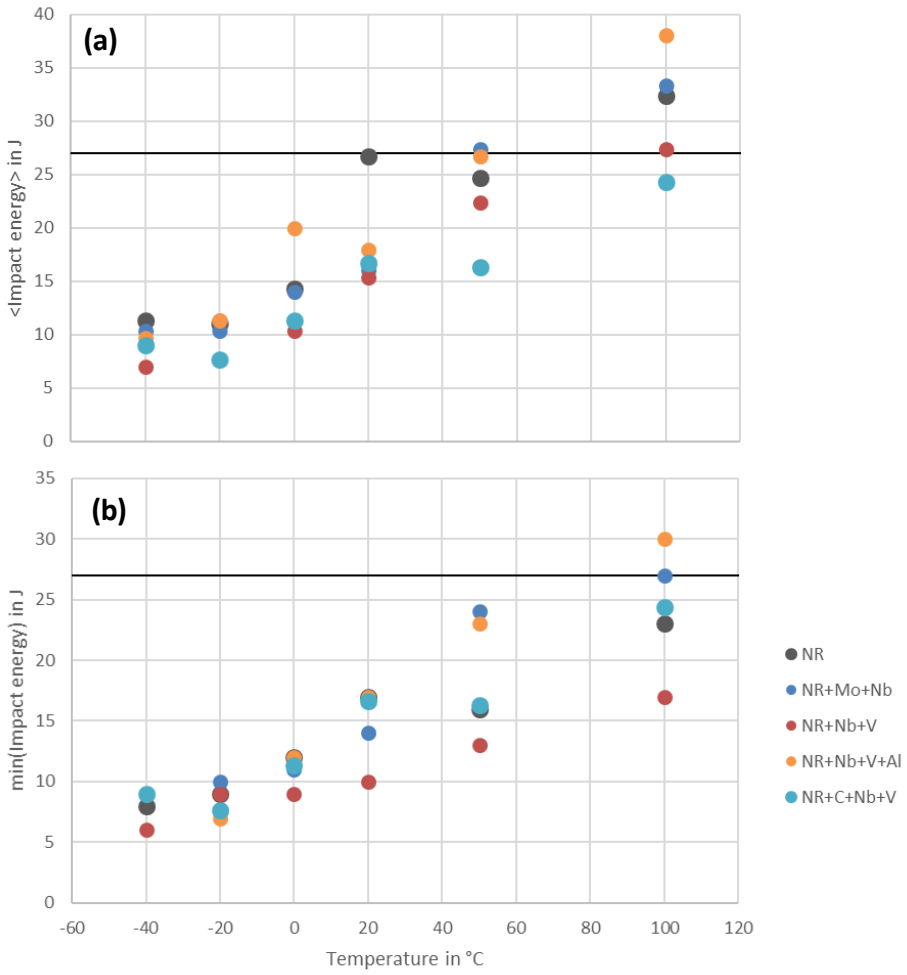

Figure 106: (a) Average and (b) minimum impact energy of the Charpy test as a function of the test temperature for MT-TMCP-12 mm material (average of 3 tests).

4.3.2.iv LT-TMCP

Two plates of each steel held at 350ºC were available for testing. Both plates were tested at -20 and -40 °C. For the additional tests at higher temperatures, only one plate was tested at each temperature. For full characterization of some plates with a comparable high hardness (X353N and X353Z), some additional charpy tests were done using the remaining material from wear test samples from OCAS (55 x 7 x 10 mm3). The measured average impact energies are shown in Table 44. In Figure 107, the average and minimum impact energies of the three tests are plotted as a function of the test temperature.

The measured impact energies are higher than those of the HT-TMCP-12 mm samples. With the exception of NR+C+Nb+V steel, all other steels already have shown a minimum impact energy of more than 27 J at 20 °C. The NR+Nb+V steel, on the other hand, is the only steel that showed a minimum impact energy of more than 27 J at -20 °C.

Table 44: Summary of Charpy impact energy results for the LT-TMCP-12 mm material (average of 3 tests). The energy values are in Joule for full size Charpy geometry. The standard deviation is given in brackets.

Alloy	Plate ID	350ºC t_{coil} /h	-40 °C	-20 °C	+20 °C	+50 °C
NR	X356L	40	18.7 (±0.5)	28.3 (±3.4)	40.3 (±4)	
	X356M	30	17.7 (±0.9)	24.7 (±3.3)		63.3 (±4.2)
NR+Mo+Nb	X355C	50	24 (±4.1)	27 (±1.6)	47 (±1.4)	
	X355E	60	14 (±0.8)	19.7 (±1.2)		47 (±0.8)
NR+Nb+V	X355O	60	21.7 (±1.2)	31.3 (±2.1)	54.3 (±6.9)	
	X355P	40	22.3 (±1.7)	25 (±5.1)		61.3 (±4.6)
	X355N	40		31.1 (±2.5)	59.1 (±7.9)	
NR+Nb+V+Al	X355W	40	22.3 (±0.5)	28.3 (±1.9)	56.7 (±3.3)	
	X355X	30	19.7 (±1.7)	25.3 (±0.9)		61.7 (±3.9)
NR+C+Nb+V	X356A	20	12.7 (±2.1)	15 (±0)	28.3 (±2.1)	
	X356F	20	11.7 (±0.9)	19.3 (±1.2)		40.3 (±1.7)
NR+C+Nb+V	X355Z	20		21.8 (±5.4)	44 (±5.8)	
	X356D	20		23.3±(3.1)	40.7 (±8.3)	
	X355M	20		28.3±(3.1)	57.7 (±8)	

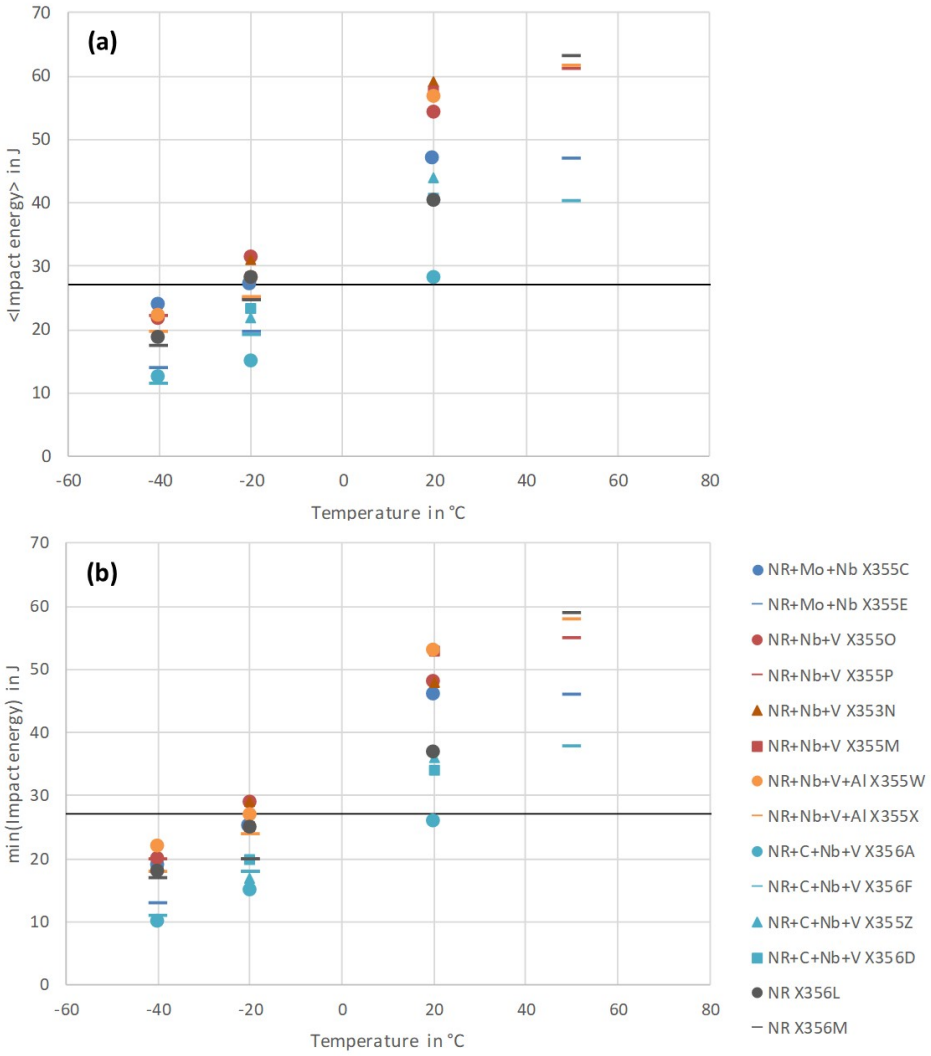

Figure 107: (a) Average and (b) minimum impact energy of the Charpy test as a function of the test temperature for LT-TMCP-12 mm material (average of 3 tests).

4.3.2.v General analysis

Toughness has been evaluated by Charpy tests, whose results are represented in Figure 108. Although the tests have been performed at several temperatures, the brittle-ductile transition temperature cannot be estimated, as more Charpy tests at higher and lower temperatures would be required. When comparing with the charpy energies corresponding to the isothermal TMCP samples, it can be observed that only the MT-TMCP, characterized by having larger fractions of martensite (and lower retained austenite) than the rest of the samples, only exceeds 27 J (typical material testing standard) at 100ºC, whereas the HT and LT-TMCP have superior behaviour, in ascending order.

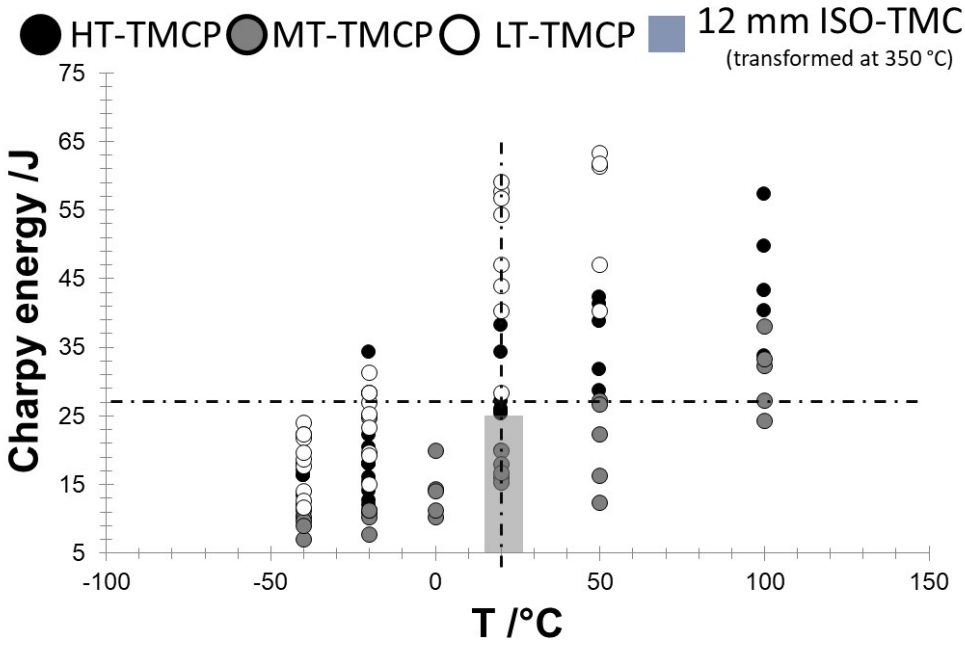

Figure 108. Charpy energy obtained as a function of the test temperature for 12 mm HT, MT and LT-TMCP. In the isothermal TMCP, the Charpy tests have only been carried out at room temperature and the range of their Charpy energies can be found in a grey shadowed area.

4.3.3 Task 5.3: Wear on 3 mm and 12 mm material (OULU,OCAS)

Two types of wear tests have been performed, and the characteristics and results are described in the following paragraphs.

4.3.3.i Dry-pot Experimental conditions (OULU.).

Dry-pot experiments were carried out for all 12 mm materials at the Tampere Wear Center. For the experiments, two pieces of 64x40x10 mm specimens were machined for each experimental steel from 12 mm plates so that the thickness was reduced by milling down 1 mm on both sides of the plates. The wear tester device used a pin mill type sample arrangement, where three experimental samples and a reference sample of a known material were attached to the vertical main shaft at different height levels at an angle of 45° (Figure 109). After attaching the samples, the shaft was lowered down to the pot and the slurry was added. The slurry used in the experiment was 9 kg of granite with particle size of 8/10 mm. Each test consisted of four cycles, each of which lasted 15 minutes. The slurry was replaced after each cycle and the samples were weighed before and after each of the four cycles. Sample positions were changed after each cycle to reduce the differences, if some position was causing less or more wear for the sample than the others [25,26]. After four cycles the weights of the samples were compared to their original weights in terms of calculating mass loss of each sample, which were then compared to the mass loss of the reference sample. The reference material used was a commercial steel with a hardness of 500 HB (530HV) and high abrasive resistance.

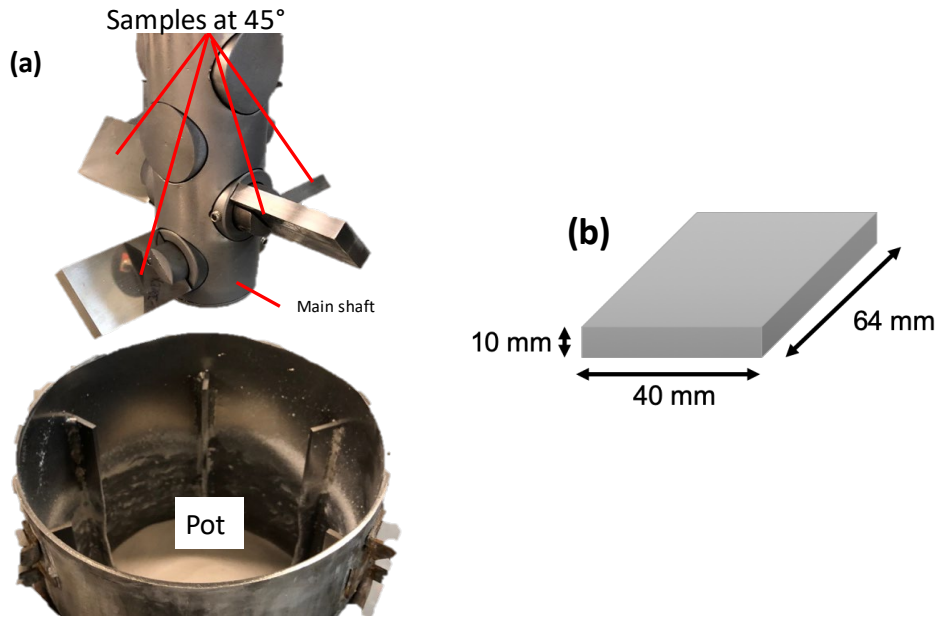

Figure 109. a) Sample arrangement and b) sample dimensions of the dry-pot test.

4.3.3.ii Results on HT/MT & LT-TMCP (Dry Pot)

The wear test results in respect of mass loss caused by the dry-pot testing are presented as a summary in Figure 110, and in detail in Table 45 as absolute values (g) and as relative differences (%) to the corresponding reference material. Generally speaking, the abrasive wear performance was correlating well with the initial hardness of the steels. As expected, the lowest mass loss (worn 7.7 % less than the reference steel) i.e. the best wear performance was measured for the sample with the highest initial hardness

(NR+C+Nb+V-MT-TMCP; 535 ± 22 HV10), while the highest mass loss (14.2 % more than the reference steel) was obtained for the sample with the lowest hardness (NR-LT-TMCP; 375 ± 7 HV10). However, another interesting result was exhibited by those steels presenting lower hardness than the reference steel, but similar level of mass loss. This indicates that the initial hardness may not be the only contributor describing the abrasive wear resistance, but also the fraction, location and the morphology of retained austenite too had a significant effect on the wear performance. For instance, NR+Nb+V-LT-TMCP showed relatively low mass loss despite its low hardness (429 HV) owing to the high retained austenite content (36%)

Table 45. Summary of Dry-pot results for the 12 mm material.

Alloy	Route	T_{coil} /ºC	t_{coil} /min	Plate ID	Mass loss g	%Difference to ref
NR	HT-TMCP	350	60	X354B	1.605	+3%
NR+Mo+Nb	HT-TMCP	350	20	X353C	1.572	+1.2%
NR+Nb+V	HT-TMCP	350	40	X353H	1.660	+3.9%
NR+Nb+V+Al	HT-TMCP	350	50	X353N	1.631	+2.1%
NR+C+Nb+V	HT-TMCP	350	40	X353V	1.560	-2.4%
NR	MT-TMCP	350	60	2-14	1.583	+1.6%
NR+Mo+Nb	MT-TMCP	350	60	8-13	1.616	+1.4%
NR+Nb+V	MT-TMCP	350	60	14-12	1.591	-0.1%
NR+Nb+V+Al	MT-TMCP	350	60	16-12	1.653	-3.8%
NR+C+Nb+V	MT-TMCP	350	60	15-12	1.470	-7.7%
NR	LT-TMCP	350	50	X356K	1.773	+14.2%
NR+Mo+Nb	LT-TMCP	350	50	X355F	1.665	+7.2%
NR+Nb+V	LT-TMCP	350	50	X355L	1.547	+3.3%
NR+Nb+V+Al	LT-TMCP	350	20	X355Q	1.653	+10.4%
NR+C+Nb+V	LT-TMCP	350	60	X356E	1.588	+6.0%

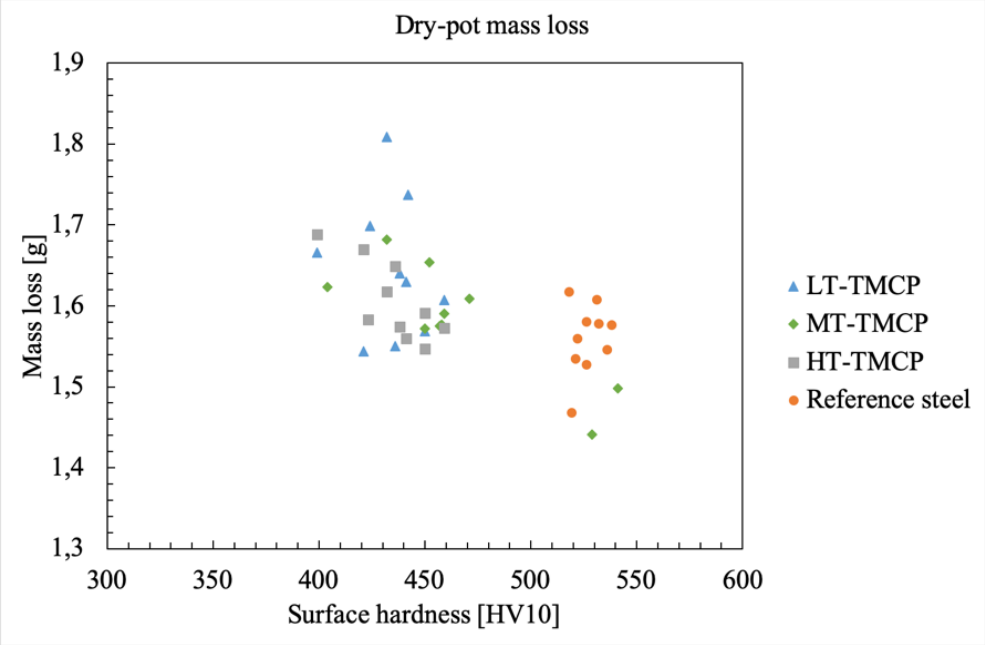

Figure 110. Summary of the results of the Dry-pot experiment at Tampere Wear Center.

4.3.3.iii ASTM-G65 abrasion test conditions (OCAS).

The ASTM G65 test (or dry sand - rubber wheel abrasion test) is widely used to evaluate low-stress abrasive wear of material, particularly in the mining and agricultural machinery industries. In the course of this abrasion test, a specimen is loaded against the rim of a rotating rubber wheel (Figure 111a). A sand flow is directed in the same direction of the wheel rotation and is oriented to the gap between the wheel and the specimen, abrading the specimen surface under an applied normal load at a given sliding speed. Abrasion resistance of the material is evaluated by measuring volume loss after the test. Tester preparation is explicitly detailed in the ASTM G65-16 standard, [27]. The reference steel used is a standard commercial wear resistant steel with 488HV hardness with average volume loss 80mm^3.

For the experiment. 75mm x 25 mm (RD x TD) specimens were machined from the 12 mm and 3 mm plates. For each material (plate), at least 3 wear specimen were tested.

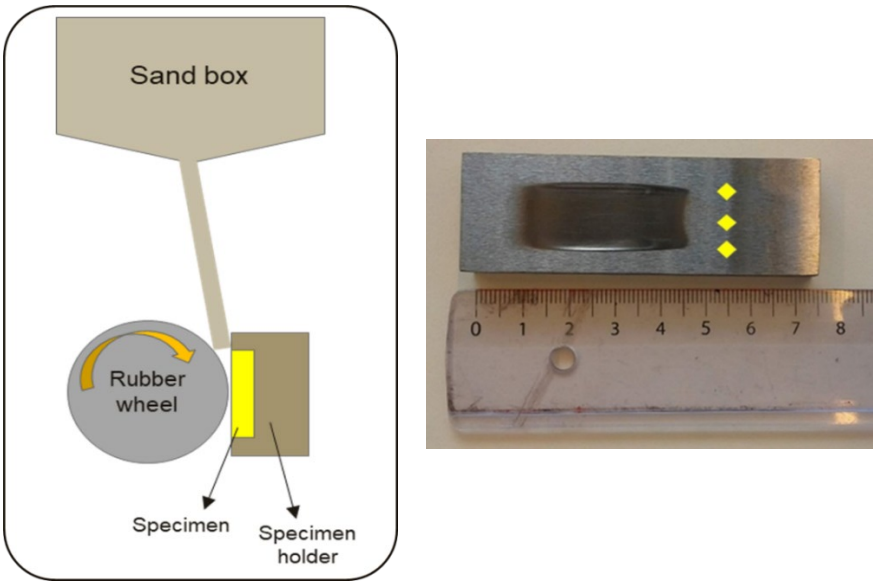

Figure 111: (a) ASTM G65 test set-up; (b) G65 specimens after the test and hardness locations.

4.3.3.iv ASTM G-65 abrasion HT/MT & LT-TMCP results.

The average volume loss after the test is reported in Table 46 along with standard deviation. The surface hardness of the wear specimens are also measured as shown in Figure 111 b) and reported in Table 46.

Table 46: Summary of ASTM G65 abrasion test results.

Alloy			Plate ID	T_{coil} /ºC	t_{coil} /min	HV10	Aver. Vol. loss (mm^3)
NR	HT-TMCP	12 mm	X354C	350	50	433±10	78.9±1.2
NR+Mo+Nb			X353B	350	50	443±12	75.5±71.3
NR+Nb+V			X353K	350	80	534±14	71.3±1.4
NR+Nb+V+Al			X353M	350	60	429±17	76.5±6.0
NR+C+Nb+V			X353S	350	70	556±25	63.6±3.2
NR	MT-TMCP		18055100-2	350	60	468±26	69.6±2.5
NR+Mo+Nb			18058100-7	350	60	498±18	67.9±3.0
NR+Nb+V			18061100-6	350	60	496±22	72.7±2.7
NR+Nb+V+Al			18064100-6	350	60	473±18	76.6±3.3
NR+C+Nb+V			18068100-6	350	60	554±25	64.9±2.4
NR	LT-TMCP		X356G	350	50	416±21	78.7±1.0
NR+Mo+Nb			X355H	350	50	420±15	78.9±0.6
NR+Nb+V			X355N	350	40	428±14	78.9±0.7
NR+Nb+V+Al			X355V	350	50	413±11	82.2±1.1
NR+C+Nb+V			X355Z	350	20	440±23	73.0±0.1

NR+C+Nb+V	HT-TMCP	3 mm	400991	350	180	560±20	61.1±1.9
NR+C+Nb+V			400993	325	180	625±15	65.1±2.1
NR+Nb+V+Al			400995 HE.4	350	180	457±15	78.1±2.1
NR+Nb+V+Al			400995 HE.5	350	180	450±10	80.2±1.4
NR+Nb+V+Al			400997	325	180	593±20	69.7±3.3
NR+Nb+V			400999 HE.4	350	180	500±17	76.1±3.4
NR+Nb+V			400999 HE.5	350	180	513±20	75.7±1.2
NR+Nb+V			401001	325	180	602±4	66.8±1.5
NR+Mo+Nb			401004	350	180	500±13	74.8±0.7
NR+Mo+Nb			401006	325	180	597±21	67.2±1.2
NR			401905	350	180	459±11	76.9±2.0
NR			401908	325	180	553±20	65.5±1.6

Figure 112 and Figure 113 show the average mass volume loss as a function of the surface HV for the different TMCP conditions in Table 46. The plots also contain (into brackets) the fraction of retained austenite of the tested microstructure, and a big red cross indicates the levels for the reference steel.

It is clear that both the surface HV and the amount of retained austenite play an important role, i.e. a higher fraction of retained austenite with a high HV seems to be the optimal combination for lower wear rates. Except for the LT-TMCP, for similar levels of HV, and even lower, the obtained microstructures behave better than the reference steel.

In most cases, the alloy showing the worst wear rate is the NR+Nb+V+Al steel and the one with the best performance is the NR+C+Nb+V steel.

In the results, the 3 mm microstructures transformed at lower isothermal temperature (325ºC) seem to have a better response than those obtained at higher T (350ºC).

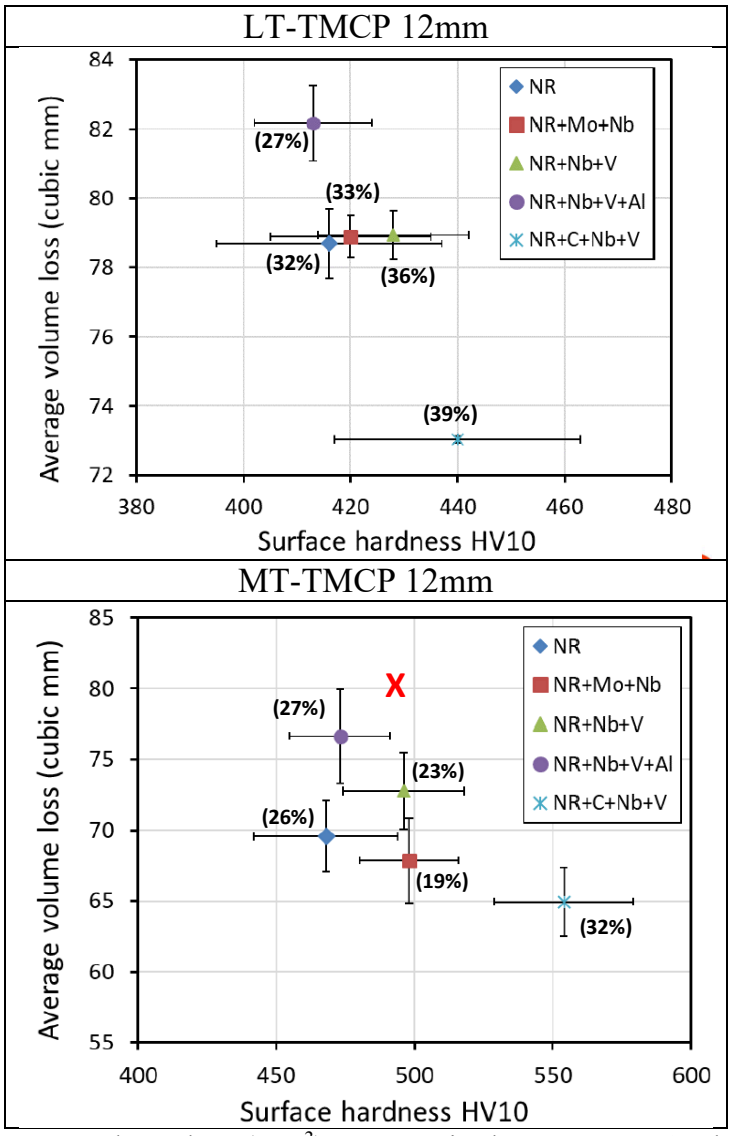

Figure 112. Average volume loss (mm^3) measure in the ASTM G-65 abrasion tests for LT and MT –TMCP (12 mm) material. Volume fraction of retained austenite into brackets. Big red cross indicates the levels for the reference steel.

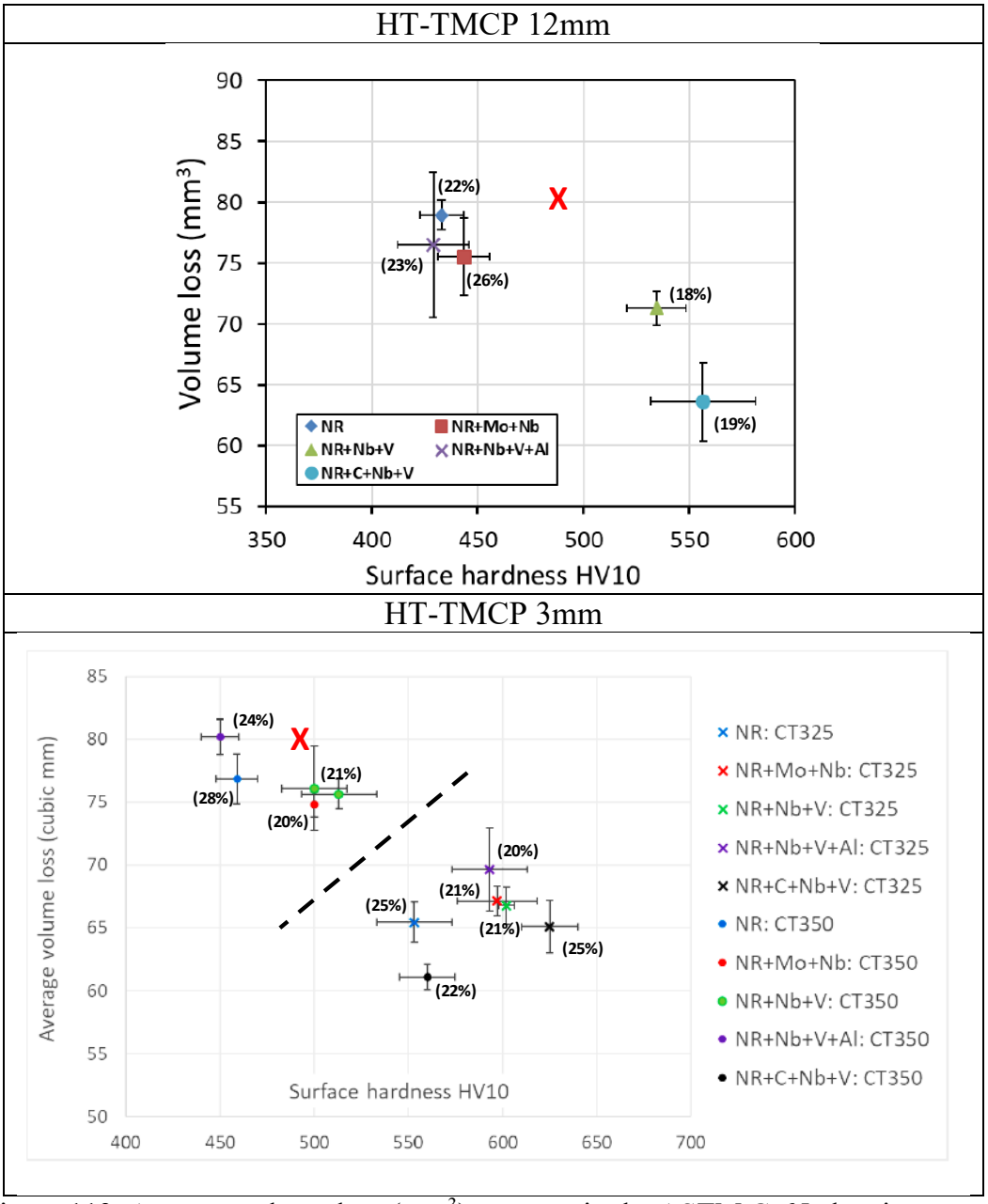

Figure 113. Average volume loss (mm^3) measure in the ASTM G-65 abrasion tests for HT – TMCP (12 & 3 mm material. Volume fraction of retained austenite into brackets. Big red cross indicates the levels for the reference steel.

4.3.4 Task 5.4: Bending on 3mm and 12 mm material (tkSE,OCAS)

4.3.4.i HT-TMCP 3 mm material (tkSE)

For testing the 3 mm thick material, the VDA238-100 standard tight radius bending test [28] was first applied. A scheme of the test is shown in Figure 114. A square sheet metal specimen (60 x 60 mm^2) resting on two bearing rollers is bent with a bending sword until it fails (crack). The bending sword velocity is 20 mm/min and its radius is 0.4 mm. The crack of the specimen is indicated by the drop in the bending force. The stop-criterion is a drop of 1 % of the Max-Force. At tkSE the deformation of the sample (bending angle) is measured directly by means of an optical system synchronized in time with the force-displacement curve.

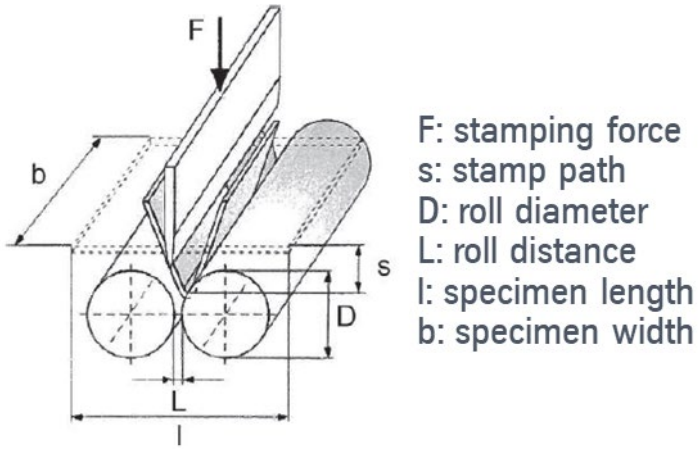

Figure 114: Scheme of the VDA238-100 standard tight radius bending test (taken from [28]).

Four samples of each material and coiling condition were tested with the bending line transverse and longitudinal to the rolling direction. In most samples deep cracks at the outer radius were present after testing (Figure 115) and no springback after the release of the force was observed. Some samples even broke during testing (NR and NR+C+Nb+V steels with 3 h holding at 350 °C and NR+Nb+V steel with 3 h holding at 325 °C).

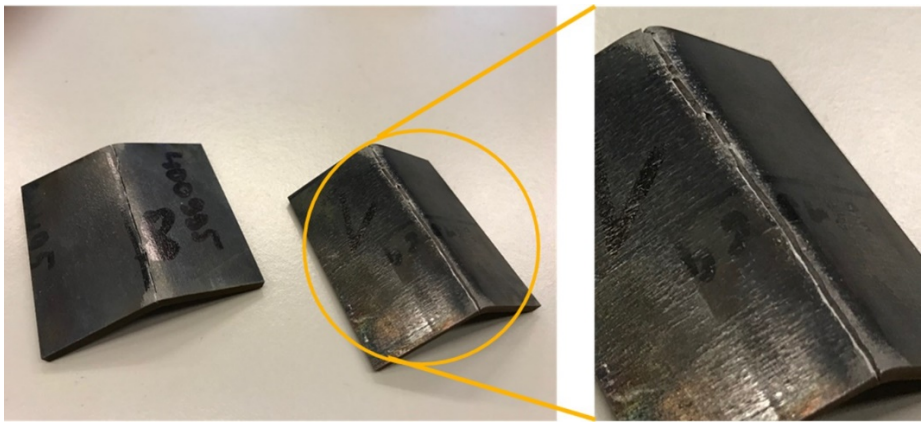

Figure 115: NR+Nb+V+Al (350 °C; 3 h. longitudinal) and NR+C+Nb+V (350 °C; 0.5 h)

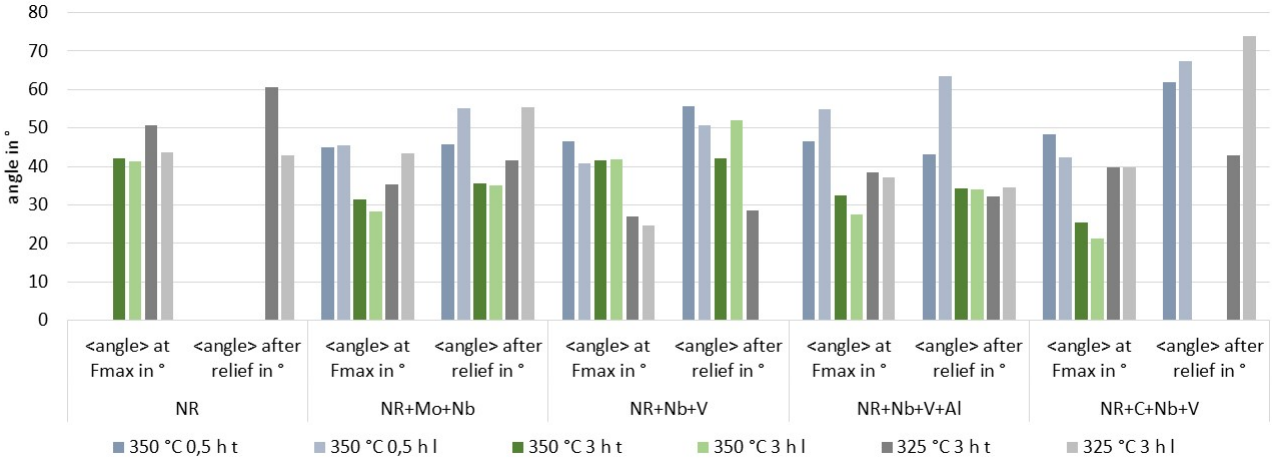

Figure 116: Summary of standard tight radius bending angles at F_{max} and after force release for the HT-TMCP-3 mm material. The results are bundled according to the different steels. Results are shown for the different coiling temperatures and holding times and bending lines transversal (t) and longitudinal (l) to the rolling direction (average of 4 tests).

The results of the bending angles at F_{max} and after force release are shown in Figure 116 bundled according to different steels. Due to the severe cracking of some samples the angle after relief is sometimes higher compared to the angle at F_{max}. The bending angles are smaller when the holding time is increased from 30 min to 3 h for all steels. With the exception of NR+Nb+V steel, reducing the coiling temperature from 350 to 325 °C lead to an increase of the bending angles at F_{max}. The anisotropy of the bending angles is small and varies depending on the steel and the coiling conditions. As expected, in most of the cases, the bending angle with the bending line transverse to the grain or rolling direction is greater than or equal to the corresponding bending angle with the bending line longitudinal to the rolling direction.

Figure 117 shows the bending angles at F_{max} again, this time bundled according to the different coiling conditions. NR steel generally shows comparable high bending angles on account of a lower hardness compared to the microalloyed steels. NR+C+Nb+V steel with a coiling temperature of 325 °C stands out, in particular, exhibiting the highest hardness the bending angle is on the same level or even higher than the other steels.

Since the plate thickness of 3 mm is larger compared to material typically tested by the tight radius bending test, no comparison to a reference material is available. Only the bendability of the steels among themselves under different process conditions can be compared.

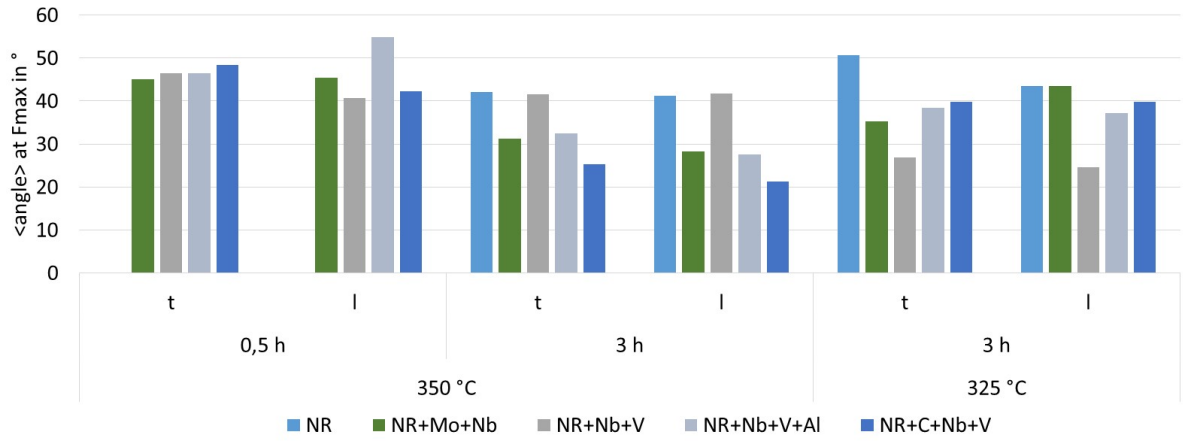

Figure 117: Summary of standard tight radius bending angles at F_{max} for the HT-TMCP-3 mm material. The results are bundled according to the different coiling temperatures and holding times and bending lines transversal (t) and longitudinal (l) to the rolling direction (average of 4 tests).

In addition to the original plan, 3 mm samples of four steels were also tested with additional bending radii to determine the critical bending radius according to DIN EN ISO 7438:2016-07. Samples of the plates with 3 h holding at 325 and 350 °C were available except for the NR steel (not from the same plate as the tight binding test material). The experimental setup is shown in Figure 118. The samples had a dimension of 200 x 30 x 3 mm^3. Since only a limited amount of material was available, only samples with the bending line transverse to the rolling direction were tested. In addition, only single samples of each steel with the bending line longitudinal to the rolling direction could be tested.

The results of the bending tests are shown in Table 47. The tested minimum bending ratio (bending punch radius (R)/sample thickness (th)) for full (180°) bending and the maximum bending ratio at which a crack occurs are given. In transverse direction, two samples could be tested, whereas in longitudinal direction, only one sample could be tested. Figure 119 shows the results as a function of the material hardness with the bending line transverse and longitudinal to the rolling direction. As expected the bending ratio for full bending with the bending line longitudinal to the grain or rolling direction is always greater than or equal to the corresponding bending angle with the bending line transverse to the rolling direction.

A trend can be seen in respect of the dependence of the bending ratio on the hardness. The higher the hardness is, the larger the bending ratio is. Except for the NR+Nb+V sample with the coiling temperature of 350 °C, the critical bending ratio for the hardness below 580 HV was 3.3 or smaller.

For comparison, the bending ratio for the standard tight radius bending test would have been $0.1\overline{3}$.

The measured critical bending ratios of approximately 3 to 4 are within the bending recommendations for 90° bending of commercial steels of similar hardness [29]. Cold bending of the project steels is therefore possible under the conditions typical at these strengths.

MT-TMCP 3 mm material (tkSE). The 10x25 mm^2 MT- TMCP 3mm material samples are too small for bending tests.

LT-TMCP 3 mm material (tkSE). The 10x25 mm^2 LT- TMCP 3mm material samples are too small for bending tests.

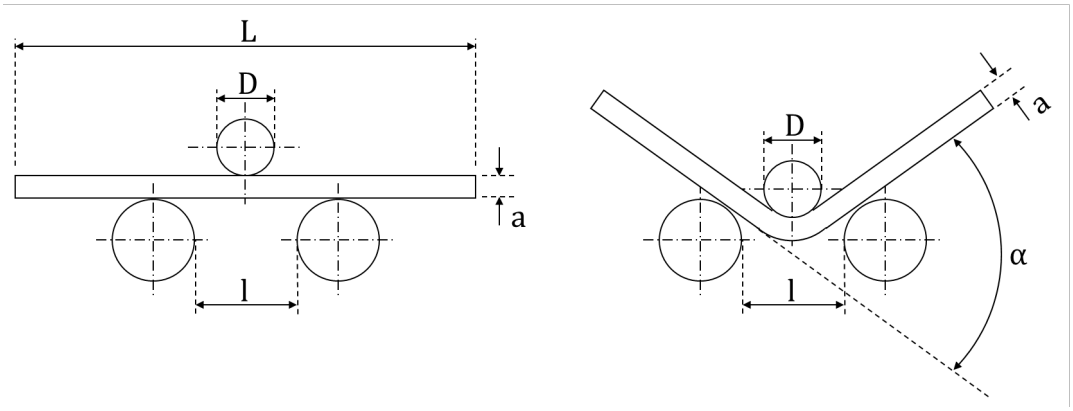

Figure 118: Scheme of the bending device with two support rollers and a bending punch to determine the critical bending radius according to DIN EN ISO 7438:2016-07. The bending punch has a diameter of D.

Table 47: Summary of critical bending ratio results for the HT-TMCP-3 mm material. 2 samples tested in longitudinal and 1 tested in transversal direction respectively).

Alloy	Plate ID	T_{coil} /ºC	t_{coil} /h	HV	Orientation	min bending ratio 180°	Max bending ratio broken
NR+C+Nb+V	400992	350	3	516	trans.	3.3	2.75
	400992	350		516	longi.	5	3.7
	400994	325		595	trans.	4.2	3.3
	400994	325		595	longi.	5	4.2
NR+Nb+V+Al	400996	350		445	trans.	2.5	2
	400996	350		445	longi.	>2.5	2.5
	400998	325		559	trans.	3.3	2.75
	400998	325		559	longi.	>3.3	3.3
NR+Nb+V	401000	350		473	trans.	4.2	3.7
	401000	350		473	longi.	4.2	
	401003	325		579	trans.	3.3	2.75
	401003	325		579	longi.	3.3	2.75
NR+Mo+Nb	401005	350		469	trans.	2.75	2.5
	401005	350		469	longi.	>2.75	2.75
	401007	325		588	trans.	3.7	3.3
	401007	325		588	longi.	3.7	

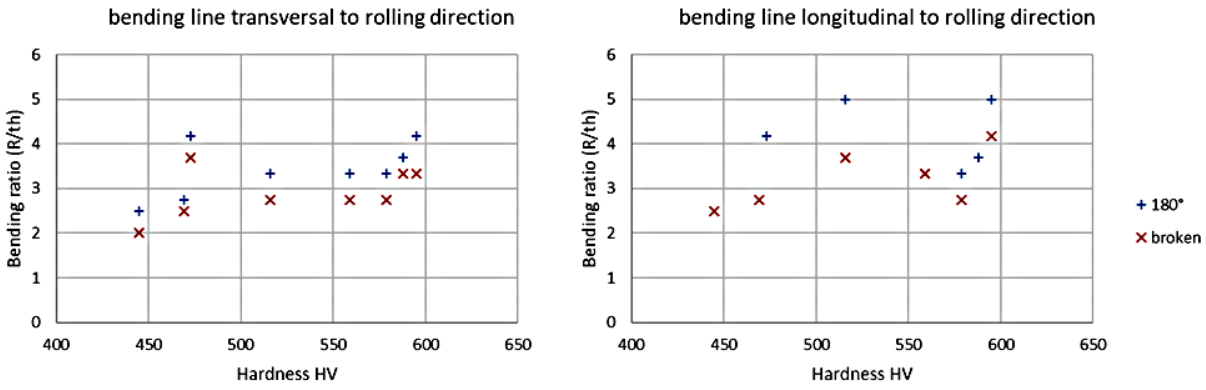

Figure 119: Smallest measured bending ratio for a bending angle α = 180° and breakage/cracking of the sample as a function of the material hardness with the bending line transversal and longitudinal to the rolling direction, respectively.

4.3.4.ii HT-TMCP and LT-TMCP 12mm material (OCAS)

Air-bending or free-bending is carried out for the 12mm thick (th) HT-TMCP and LT-TMCP specimens along rolling direction (RD) as shown in Figure 120. With limited number of samples available (only 1 sample for RD bending per grade and per processing conditions), the objective of the bending test was to get a first idea on the critical bending ratio for these kinds of bainite microstructures. The width (b) of the bend specimen was at least 8 times the thickness to satisfy plane-strain condition at the bend. Different punch radius (Rp) was used to test different bending ratios (Rp/th) depending upon the hardness of the plates. Table 48 enlists different parameters and results from the bending tests. 'Green' indicates no cracking while 'Red' indicates that the samples cracked during bending. The estimation of critical bending ratio is shown in Figure 121 by the red dotted line. More bending tests were required to be done to determine the critical bending ratio more accurately. The pictures of the bent samples are summarised in Figure 122 and Figure 123.

Due to the limited number of sample availability, most of the sample hardness is ~400-450HV with critical bending ratio ~2.0 which is at par or even better than the bending recommendations for 90° bending of commercial steels of similar hardness [29]. The presence of a significant amount of retained austenite in bainitic microstructures provides a better bendability of these steels compared to a fully martensitic microstructure based steel. More samples are required to be tested at higher hardness levels to identify the critical bending ratio at high hardness levels.

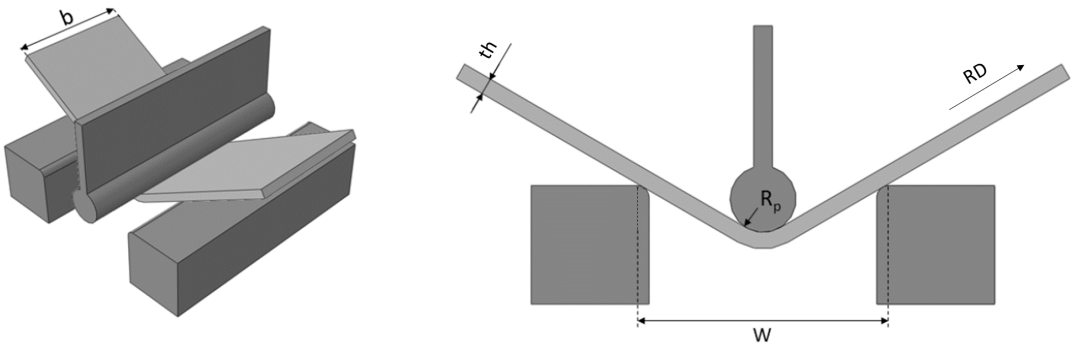

Figure 120: Typical bending set-up for 12mm thick HT-TMCP and LT-TMCP specimens.

Table 48: Summary of bending results for 12mm HT-TMCP and LT-TMCP plates.

Route	Grade	Plate ID	HV10	Punch radius Rp (mm)	Bending Ratio (Rp/th)	Bend angle (°)	Status
HT-TMCP Thickness (th)=12mm	NR	X354C	433	30	2.5	139	No crack
	NR+Mo+Nb	X353B	443	36	3.0	121	No crack
	NR+Nb+V	X353K	534	24	2.0	143	No crack
	NR+Nb+V+Al	X353M	429	20	1.7	51	Cracking
	NR+C+Nb+V	X353S	556	24	2.0	27	Cracking
LT-TMCP Thickness (th)=12mm	NR	X356G	393	20	1.7	120	No crack
	NR+Mo+Nb	X355H	409	24	2.0	105	No crack
	NR+Nb+V	X355N	425	20	1.7	67	Cracking
	NR+Nb+V+Al	X355V	394	20	1.7	113	Cracking
	NR+C+Nb+V	X355Z	423	24	2.0	93	No crack

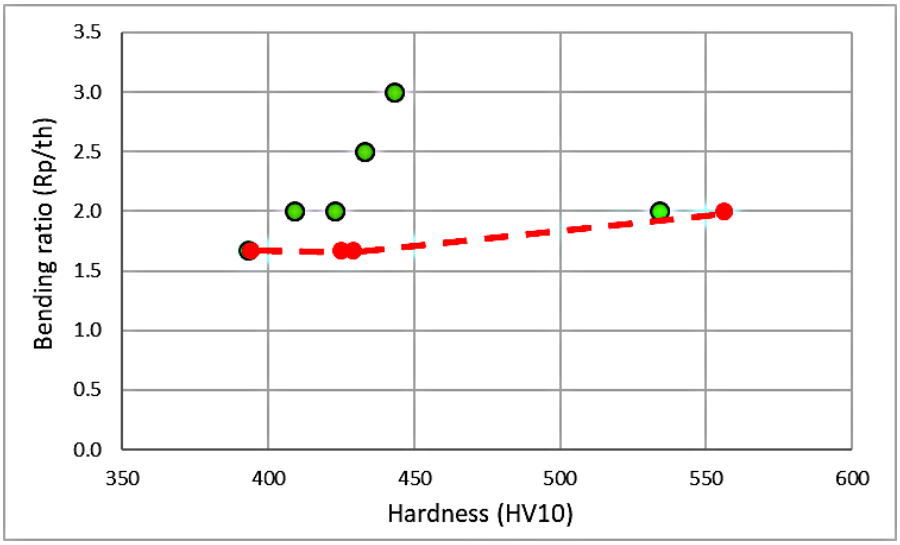

Figure 121: RD bending ratio vs hardness for the 12mm HT-TMCP and LT-TMCP plates. Green circles indicate no cracking while red circles indicate cracking during bending. The red dotted line indicates approximate critical bending ratio.

Figure 122. Examples of 12mm HT-TMCP bend samples.

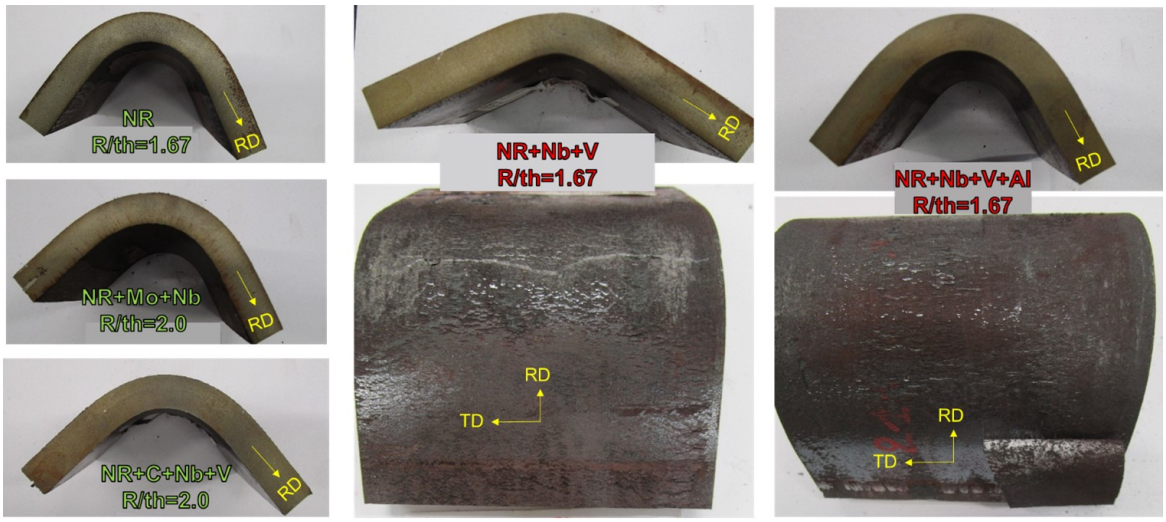

Figure 123. Examples of 12mm LT-TMCP bend samples.

4.3.5 Task 5.5: Hole expansion on 3 mm material (tkSE)

4.3.5.i HT-TMCP

At tkSE hole expansion tests according to ISO 16630 were carried out with samples from the HT-TMCP-3 mm material. The standard sample size is 100 x 100 mm^2 with a punched 10 mm hole. During the hole expansion test, the hole is expanded with a 60° conical punch until a crack becomes visible at the edge of the hole. The punch is moved at a speed of 0.8 mm/s. During the test, the sample is clamped in a die with a diameter of 50 mm. The hole expansion ratio λ is defined as

$$\lambda(\%) = 100\left(\frac{D_f - D_0}{D_0}\right)$$

D_0 is the initial hole diameter and D_f is the mean hole diameter after cracking. D_f is averaged from the diameter determined lengthwise, crosswise and in both diagonal directions. Typically 4 to 5 tests of each material have been carried out.

A summary of the results with punched holes is shown in Table 49. Four sheets with a holding time of 30 min were tested and two sheets with a holding time of 3 h at 350 °C. Except for NR+Nb+V+Al with 30 min holding time, no material has shown any hole expansion before cracking, and the hole expansion of NR+Nb+V+Al steel is also very low. The cutting edge is pre-damaged due to work hardening and manifestation of micro cracks (Figure 124). In addition, some retained austenite at the edge may have already transformed during preparation. The sheets with a holding time of 3 h at 325 °C could not be tested, since a hole could not be punched out due to the high hardness of the material.

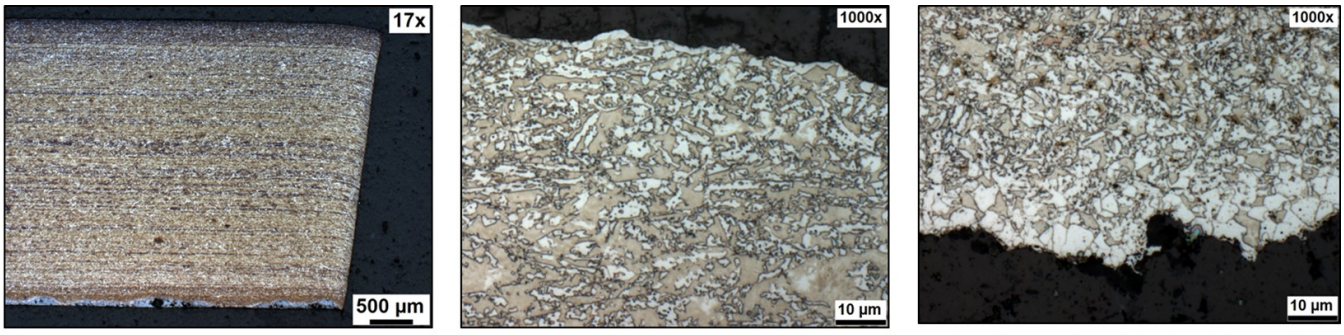

Figure 124: Light optical microscopy images of the hole edge of an untested hole expansion test sample of NR+Nb+V (plate ID 400999, nital etched).

Table 49. Summary of hole expansion test results for the HT-TMCP-3 mm material with punched holes (average of 4 to 5 tests). The standard deviation is given in brackets.

Partner	Alloy	Thickness	T_{coil} /°C	t_{coil} /h	Plate ID	D_f in mm	λ in %
tkSE	NR+Mo+Nb	3.22 mm	350	30 min	361855	10.02 (±0.04)	0.2 (±0.4)
tkSE	NR+Nb+V	3.23 mm	350	30 min	361859	10	0
tkSE	NR+Nb+V	3.23 mm	350	3 h	400999	10	0
tkSE	NR+Nb+V+Al	3.25 mm	350	30 min	361862	11.25 (±0.06)	12.5 (±0.6)
tkSE	NR+Nb+V+Al	3.25 mm	350	3 h	400995	10	0
tkSE	NR+C+Nb+V	3.23 mm	350	30 min	361864	0	0

To compare the impact of the alloying and processing conditions, additional hole expansion tests with wire eroded holes were done. The pre-existing damage at the edge is much smaller compared to that of the punched holes, leading to much higher λ values [30,31]. Since some sheets have already been used up for sample preparation with punched holes, not all materials could be tested with eroded holes. A summary of the obtained results is shown in Table 50. In addition. the λ values are plotted in Figure 125. As expected, the λ values are much higher compared to the previous results. For a deformed NR+Mo+Nb sample the retained austenite fraction was measured near the edge and 20 mm from the hole. While 20.5 % retained austenite was measured in the bulk sample, only 10.5 % was left near the edge of the hole (due to TRIP effect).

λ is generally larger with the lower coiling temperature of 325 °C compared to 350 °C. NR has shown the highest λ values. The steel with the lowest hardness, i.e. NR+Nb+V+Al steel, showed a comparable small λ as well as the hardest material NR+C+Nb+V. This is in accord with the corresponding stress-strain curves and total elongations shown in Figure 93.

In view of the results presented, punching the examined steels is not a suitable processing method. The risk of the formation of edge cracks is too high. Nevertheless, high formability of the cut edges can be achieved with adapted processing (e.g. wire eroding).

Table 50. Summary of hole expansion test results for the HT-TMCP 3mm material with eroded holes (average of 4 to 5 tests). The standard deviation is given in brackets.

Alloy	Thickness	T_{coil} /°C	t_{coil} /h	Plate ID	D_f in mm	λ in %
NR	3.1	350	3 h	401905	11.9 (±0.4)	19.3 (±3.9)
	3.3	325	3 h	401908	17.5 (±1.1)	75.3 (±11.4)
NR+Mo+Nb	3.2	350	3 h	401004	10.4 (±0.8)	3.9 (±3.1)
	3.2	325	3 h	401006	13.5 (±0.2)	35.3 (±1.6)
NR+Nb+V	3.2	325	3 h	401001	14.6 (±0.8)	45.5 (±8.4)
NR+Nb+V+Al	3.1	325	3 h	400997	12.6 (±0.7)	25.8 (±7.2)
NR+C+Nb+V	3.1	350	3 h	400991	10	0
	3.1	325	3 h	400993	12.4 (±0.7)	23.5 (±6.6)

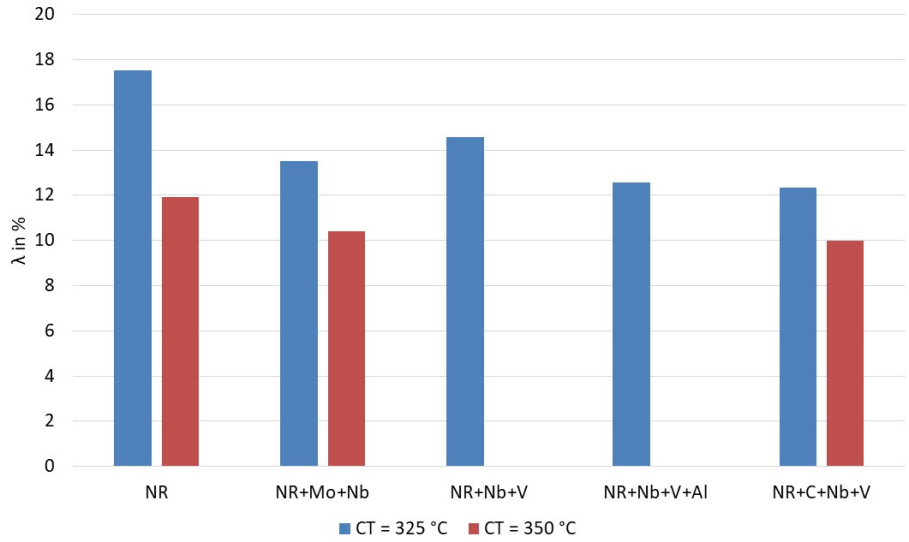

Figure 125: Hole expansion ratio results for the HT-TMCP-3 mm material with eroded holes and a holding time of 3 h at 325 or 350 °C respectively.

The 10 x 25 mm^2 MT- and LT-TMCP 3mm material samples are too small for the hole expansion test.

5 Task 5.6: Detailed Microstructural and Mechanical Characterization in Selected Conditions (ALL)

Considering that in many cases there are different isothermal temperatures and times for every plate, and the fact that properties have been measured on different plates, from all the discussed results, it is difficult to decide which alloy under which TMCP treatment provides an optimal combination of properties. Even more difficult is the correlation of the obtained properties with the tested microstructure. For that reason, the two steels which generally present the best results, NR+Nb+V and NR+C+Nb+V, have been selected for a more detailed mechanical and microstructural characterization. Note that according to Table 26, the only difference in the chemical composition of these alloys is the C content. For the purpose of this part of the study only the 12 mm product has been used, as it is the condition where suffice material remained for further tests. In order to avoid the mentioned variability, the selected plates always had been heat treated under similar conditions, time and temperature, and they also have similar hardness. As it has been done previously, the reference isothermal TMCP have also been characterized. The parameters describing all these treatments can be found in Table 51.

Table 51. Selected conditions for further characterization.

	TMCP	Steel	Plate	Coiling T /°C
Thickness 12mm	Iso	NR+Nb+V	61-1050-1	350
	Iso	NR+C+Nb+V	68-1050-1	350
	HT	NR+Nb+V	x353K	350
	HT	NR+C+Nb+V	x353U/x353S	350
	MT	NR+Nb+V	1-5,6,11,12	350
	MT	NR+C+Nb+V	1-5,6,11,12	350
	LT	NR+Nb+V	X355 J/X355 M/X355N	350
	LT	NR+C+Nb+V	x356D/x355Y/x355Z	350

The effect of the deformation on the final bainitic microstructure has also been evaluated. Figure 127 shows the micrographs of the microstructures obtained for both steels by means of the different TMCPs. Although all microstructures are mainly composed of a mixture of bainitic ferrite and retained austenite, they also contain some martensite, being the MT-TMCP where the highest fraction is observed, see Figure 127 e) and f). It is worth noticing that increasing the C content of the alloy seems to lead always to a refinement of the microstructure with the subsequent increase in HV for very similar, or slightly higher, fractions of austenite.

Figure 126 clearly shows the previously discussed mechanical stabilisation of austenite (against bainitic transformation) when moving from HT to LT-TMCP, as the fraction of austenite tends to increase as well. This austenite fraction increase has been proved to be not enough to soften the final microstructure since hardness seems to be very sensitive to the presence of this strengthen austenite and the ferritic matrix.

In terms of refinement, it can be observed that, in comparison to the microstructures obtained by pure isothermal TMCP (Figure 127 (a,b)), the microstructure is only finer when subjected to HT-TMCP, whereas it is coarser for the remaining two TMCPs. This microstructural changes are also evident when analysing the ferrite grains by EBSD [32,33]. Figure 128 shows the three IPF-Z ferrite (grain boundaries set for misorientations of 6 °) maps, on which the ferrite grain boundaries are depicted by solid black lines. At first sight it is clear that only the HT is finer than that of the ISO-TMCP, and the MT and LT tend to be coarser. This effect is also found when the ferrite grain equivalent diameter is computed and represented by histograms, as in Figure 129. While the mean equivalent diameter is similar for both the isothermal and the HT-TMCP conditions, the latter with higher fraction of smaller grains, being their maximum values about 25 nm, the equivalent diameters of the MT-TMCP and the LT-TMCP condition can go up to 50 μm.

A study of boundaries has also been performed, see Figure 128, the low angle boundaries (2-15°), related to the microstructure scale, are depicted by red solid lines, whereas the high angle boundaries (above 15 °) are plotted by black solid lines. As can be observed, the conditions that presents the highest amount of low angle boundaries is the microstructures obtained by the HT-TMCP, followed by that of the TMCP and isothermal TMCP, almost on par. Regarding the high angle boundaries, their frequency seems to be comparable among all three conditions.

In the case of the LT-TMCP treatment, an additional map was scanned on the transverse section to study how prior deformation could have affected in terms of anisotropy, see summary of results in Figure 130. If these results are compared to those in Figure 127, Figure 128 and Figure 129, it can be concluded that there are no significant differences between sections, longitudinal and transversal.

The increase in the scale of the microstructure as the deformation T decreases could be explained if we consider the following two facts

- Although the intended coiling for all conditions was 350ºC in the case of MT and LT-TMCP, Figure 64 and Figure 68, the transformation started around 380 and 440-400ºC respectively, which results in thicker microstructures
- during the deformation process (mainly at LT and MT) bainitic transformation might be induced by deformation, and it would be thicker than that obtained purely by isothermal treatment at lower temperatures [34].

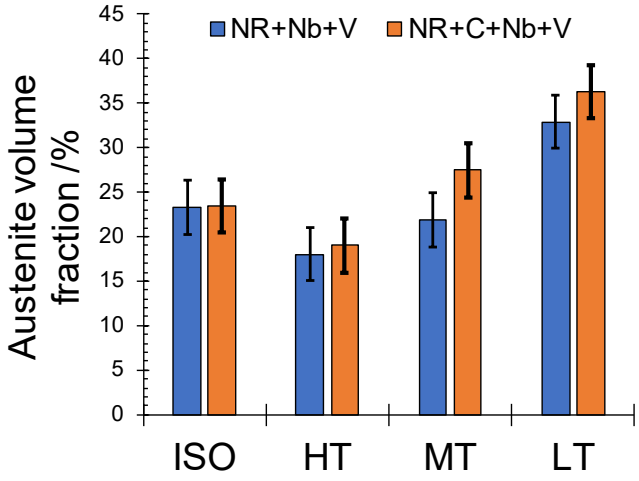

Figure 126. Austenite volume fractions obtained by XRD for the four conditions that were further characterized, classified according to the steel and the TMCP.

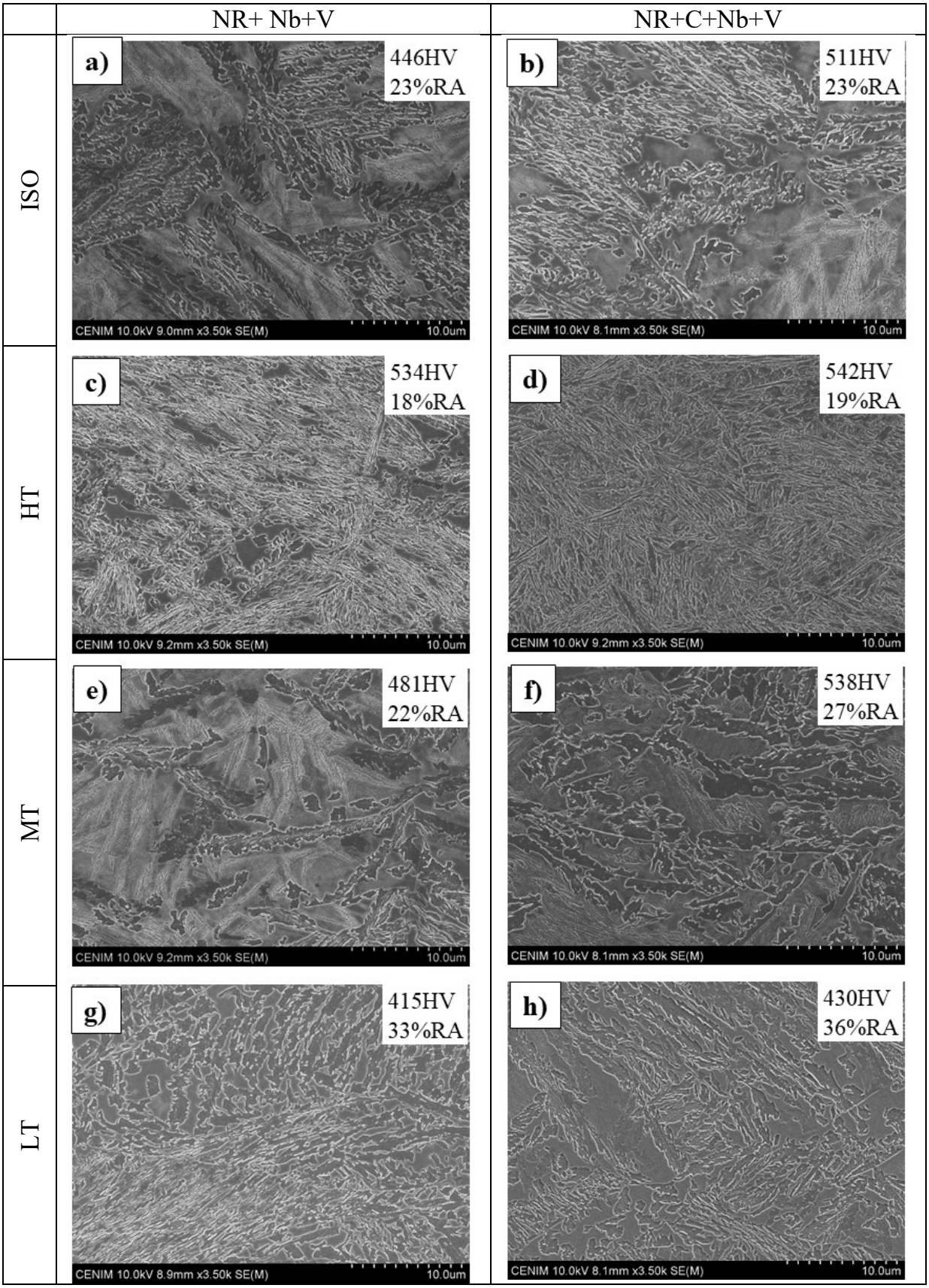

Figure 127. Longitudinal SEM images of selected microstructures, conditions indicated in the same figure together with HV and fraction of retained austenite (RA).

TMCP	Z-axis IPF map	**Low** (2-15 ° **red**) and **high (>15 °,** black) angle boundaries map
ISO	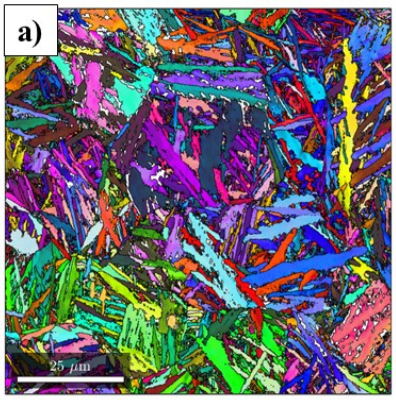	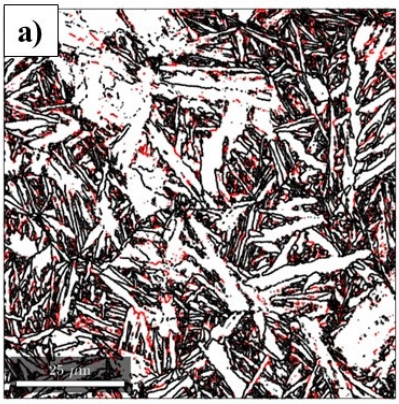
HT-TMCP	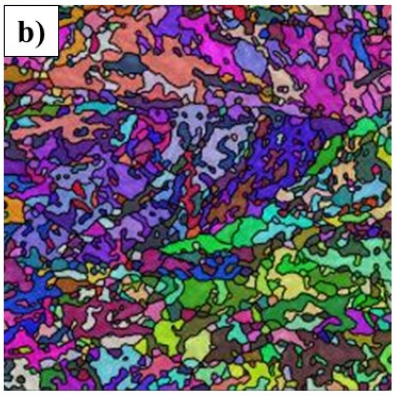	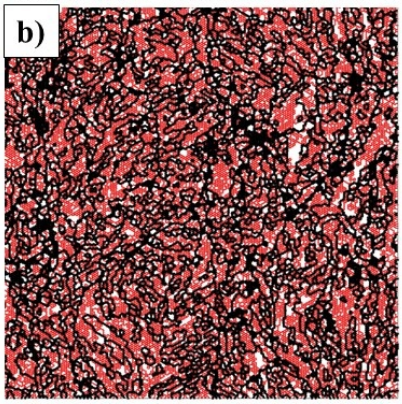
MT-TMCP	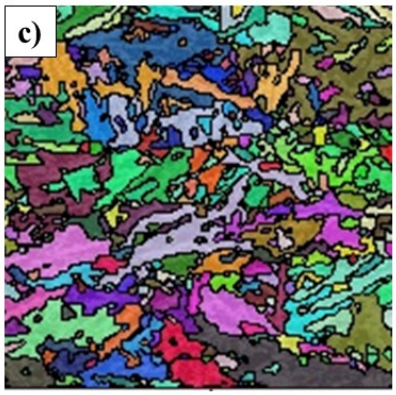	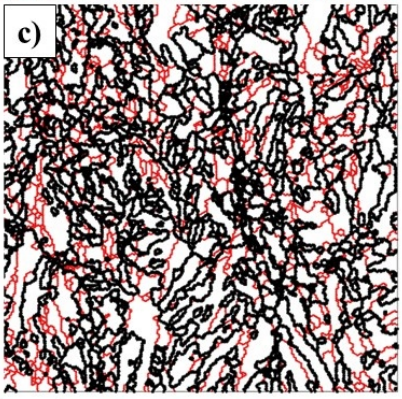
LT-TMCP	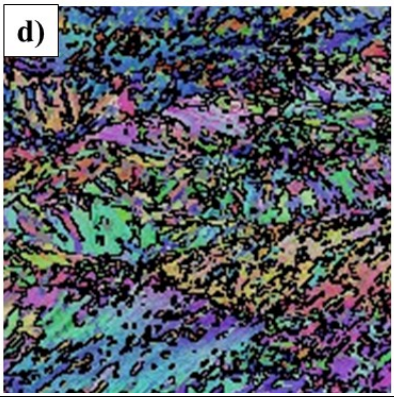	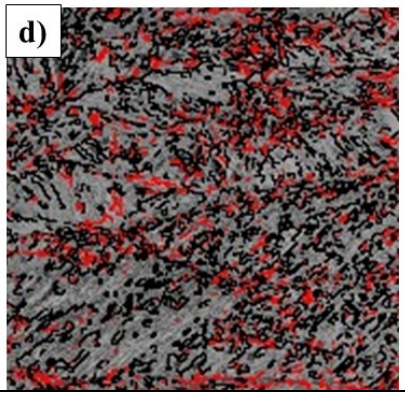

Figure 128. For NR+C+Nb+V steel, EBSD analysis on the longitudinal section of selected microstructures: TMCP conditions and analysis type indicated. The scale on the first map belongs to all of them.

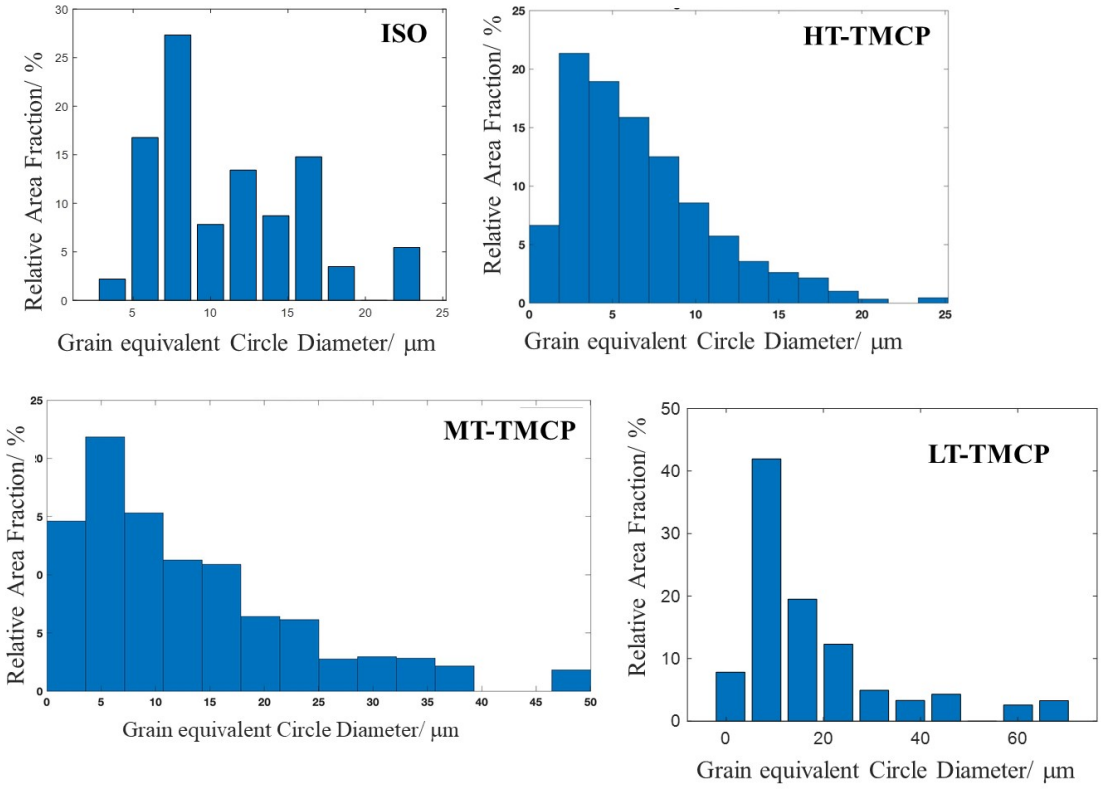

Figure 129. For NR+C+Nb+V steel, ferrite grain equivalent diameter histograms extracted from the IPF maps.

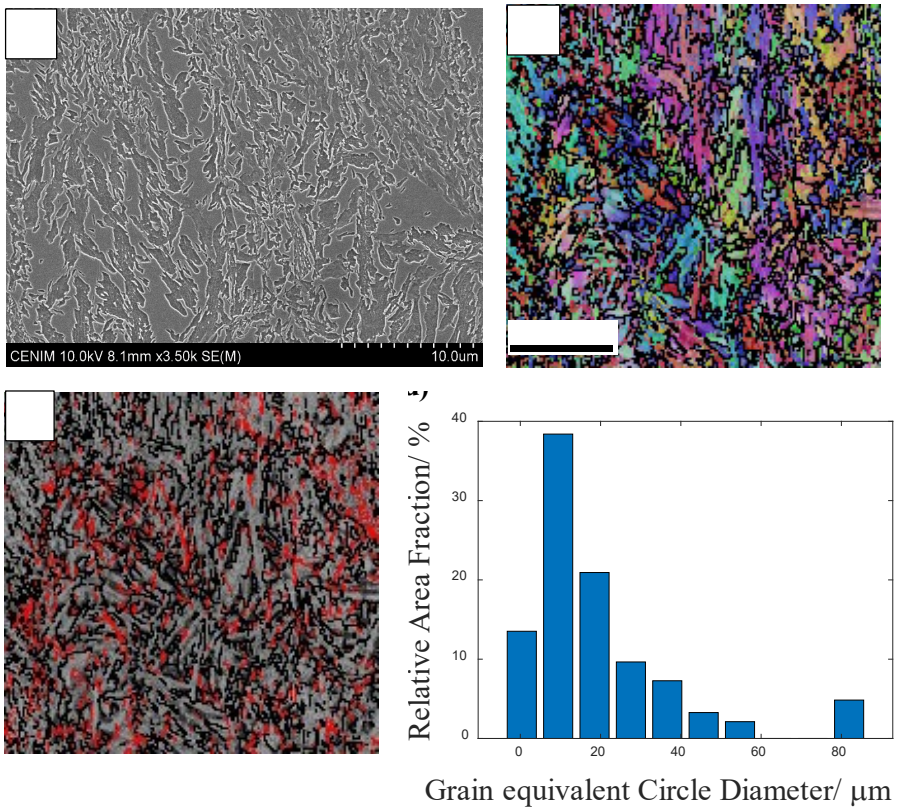

Figure 130. For NR+C+Nb+V steel subjected to LT-TMCP, SEM micrograph, IPF-Y map, low and high angle boundaries map and ferrite grain equivalent diameter histogram obtained from a transverse direction (TD-ND) map.

These microstructural characteristics directly affect the tensile properties, always keeping the usual trend which associates higher carbon content to higher strength and lower ductility, see Figure 131.

The mentioned refinement of the microstructure detected for the HT-TMCP in addition to the presence of some martensite, as compared to the ISO-TMCP, invariably leads to an important increase of the YS and moderately of the UTS. The low fraction of austenite with low hardening capacity (TRIP effect) might be beyond the decrease in ductility.

On the other hand, the microstructure obtained with the MT-TMCP although thicker it contains more martensite and it explains the similar YS but higher UTS values achieved, the higher fraction of more stable austenite is capable of maintaining the levels of ductility similar to those of the iso-TMCP. Finally the LT-TMCP microstructure, composed of lower fraction of thicker ferrite and a high fraction of more stable austenite is only capable of excelling in terms of ductility.

Based on that, the strain hardening capacity of the microstructures seems is better for the MT as its YS/UTS is the lowest followed by Iso, LT and finally HT, Figure 132. The strength-ductility product if far better in the LT and for the NR+C+Nb+V alloy, and the HT microstructures showing the lowest values, Figure 132.

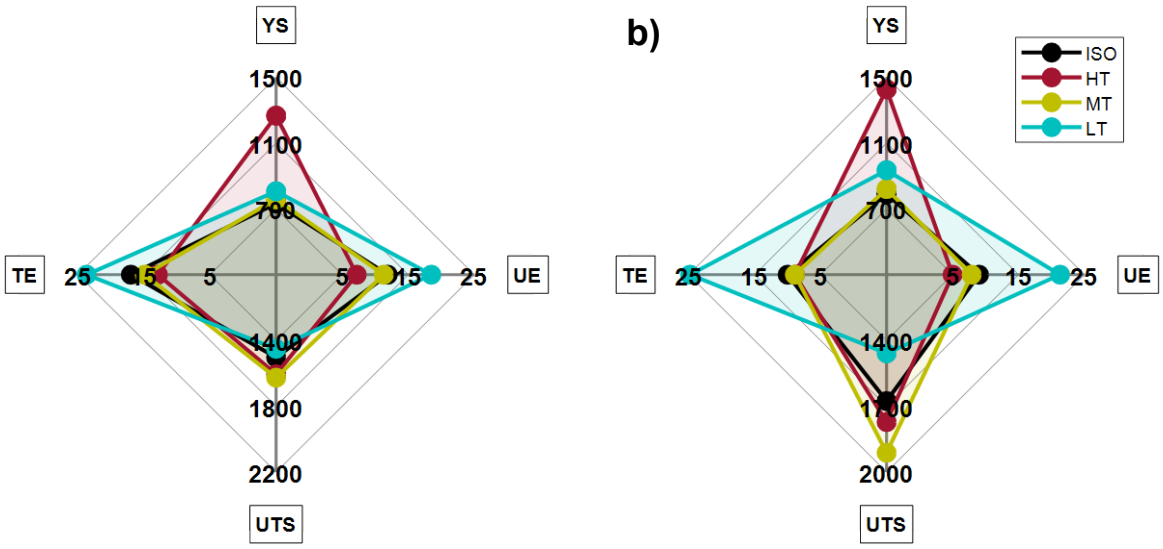

Figure 131. Spider plot showing the tensile results of the selected conditions of a) the NR+Nb+V steel and b) the NR+C+Nb+V steel.

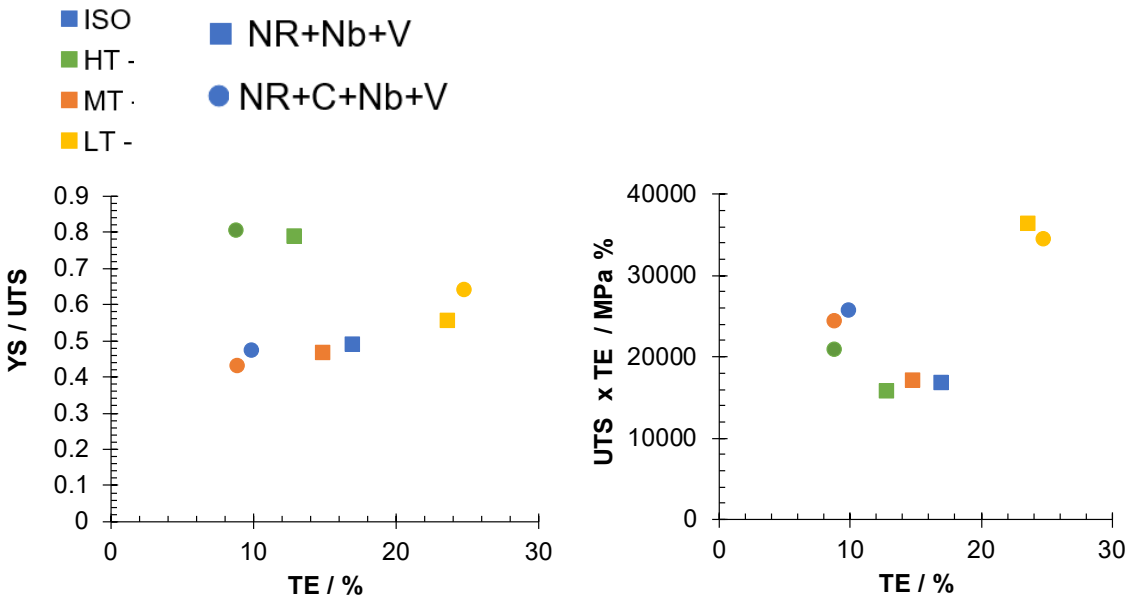

Figure 132. Strain hardening capacity, YS/UTS ratio, and strength-ductility product.

Wear results need to be discussed considering the reference material used for each type of experiment, i.e. for the ASTM G-65 a HV_{ref} = 488 steel with a 80 mm^3 of volume loss was used, while for the dry pot a HV_{ref} =530 steel. In order to facilitate the discussion the plots in Figure 133 contains the value Δ (= HV_{ref}-HV).

For the ASTM G-65 the developed microstructures exhibit wear fractions inferior to that of the reference material, being even lower for the higher C alloy (harder microstructures). It is also interesting to note that even for softer microstructures, those in LT-TMCP with Δ > 0, the wear behaviour is better than in the reference steel. Although in principle it seems that HV is controlling the wear response, when comparing the HT (hard) and the MT-TMCP (softer) results, it is clear that similar levels of wear fraction can be attained with a softer microstructure containing a higher fraction of more stable austenite.

As for the dry pot results, the trends are not so conclusive, while the microstructure of MT-TMCP exceeds the behaviour of the reference material, that of LT-TMCP seems to be too soft to have a good wear behaviour. As the MT microstructures, in terms of HV, are similar or lower than the reference, the role of retained austenite in conjunction with HV on the wear behaviour becomes again evident.

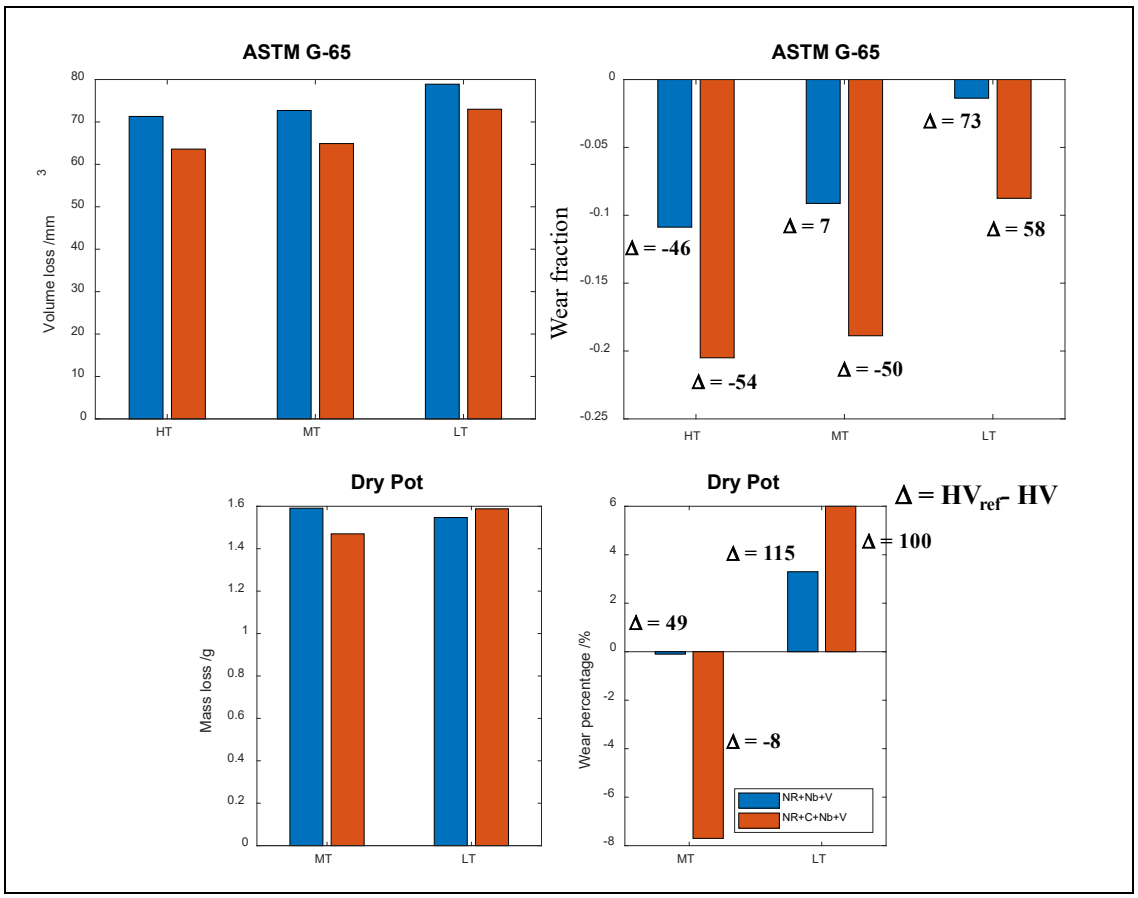

Figure 133. Bar plot showing the wear results obtained in the selected conditions by a) ASTM G-65 wear tests, reference material is 488HV, and b) Dry Pot wear tests, reference material is 530HV. $\Delta = HV_{ref}- HV$.

Regarding the toughness, Figure 134 includes results of Charpy tests performed at different temperatures, where is can be observed that the charpy energy obtained in the pure isothermal microstructures is equal or lower than the energies obtained by other TMCPs at the same temperature. In addition, it can be seen that the best results are usually obtained for samples subjected to LT-TMCP, followed by the ones which underwent HT-TMCP. While the LT results could be explained by a relatively soft microstructure with a high fraction of retained austenite, the results of the HT would be directly related to the scale of the microstructure, which is finer. The presence of martensite in the MT-TMCP is the most likely reason behind the low absorbed energies.

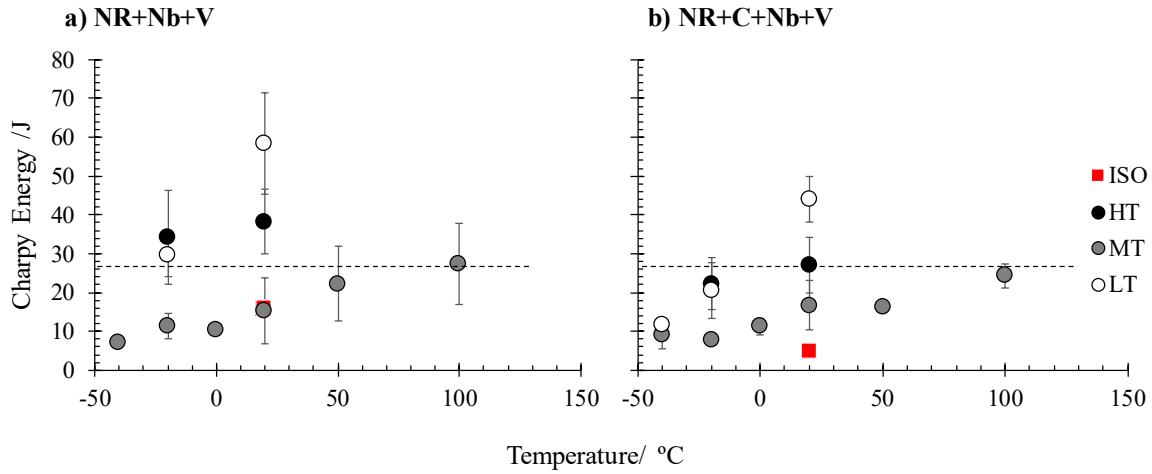

Figure 134. Charpy energy vs. temperature plots obtained in selected conditions.

6 Stage 3. Modelling (WP6)

In the course of the project different models has been created with very specific purposes.

6.1.1 Coupled heat transfer, conduction and phase transformation model (OULU).

In order to realistically simulate the austenite to bainite transformation in the steels through the plate thickness during cooling, we applied the fully coupled heat transfer, conduction and phase transformation model, which has been described in refs. [35,36]. The coupling of the models is achieved by passing the temperature information at each time-step from the heat conduction model to the phase transformation model, calculating the phase evolution and the release of latent heat during the time-step, and returning the heat released to the heat conduction calculations. Naturally the heat transfer between the cooling water and the hot steel plate is modeled. The flowchart describing the coupling between the heat conduction and phase transformation models is shown in Figure 135.

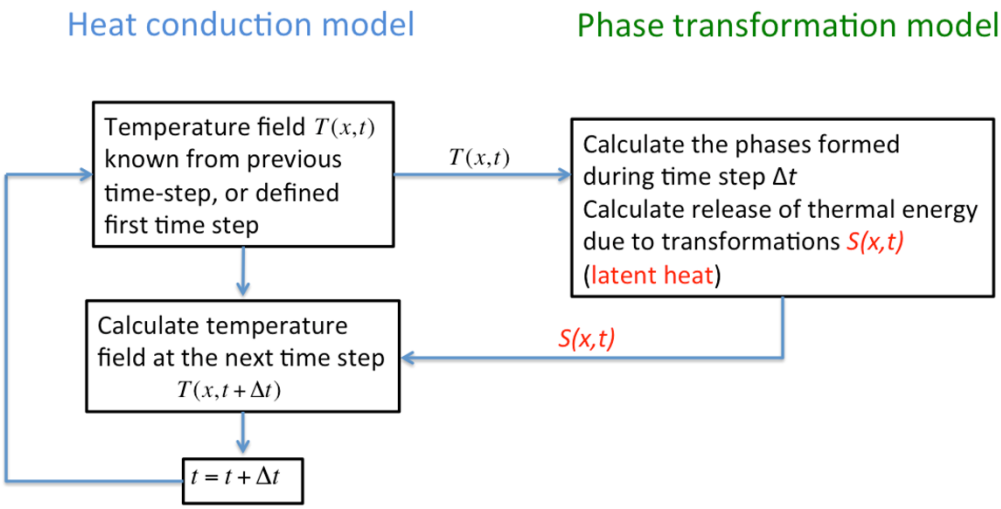

Figure 135. The fully coupled heat conduction and phase transformation model described in [35,36] was applied to simulate the austenite to bainite transformation during cooling.

For realistic estimates, the models need to be calibrated to experimental results, or use literature data. We performed the phase transformation model calibration by numerical fitting to the experimental data obtained from Gleeble simulations, in the similar way as described in [37] but including experimentally deduced maximum fraction of bainite that can form at each holding temperature. We tested two different phase transformation models, namely the Kolmogorov-Johnson-Mehl-Avrami (KJMA) [35–37] and the Austin-Rickett (AR) [38] model. According to the KJMA model, the fraction of bainite χ_b as function of time t during isothermal holding is described by Eq. 6

$$\chi_b = [1 - \exp([-k(t - t_0)]^n)]\chi_{b,max} \quad \text{Eq. 6}$$

where k is the temperature dependent rate parameter, n constant exponent and $\chi_{b,max}$ the maximum fraction of bainite that can form. The AR model applies Eq. 7

$$\chi_b = \left(1 - \frac{1}{1 + [k(t - t_0)]^n}\right)\chi_{b,max} \quad \text{Eq. 7}$$

For non-isothermal holding, the differential forms of the equations Eq. 6 and Eq. 7 were applied, as described in [35–37] for KJMA model and in [38] for the AR model. It was found that both models were capable of describing the data well, but KJMA model required separate fittings for the early and later stages of the transformation while the AR model was capable of describing the transformation behavior with single set of fitted parameters. For this reason we chose to use the AR model for the coupled simulations. The comparison of the fitted model to the experimental data is shown in Figure 136.

The heat transfer model was calibrated to reproduce the cooling in experimental laboratory water cooling line, as described in [39]. For the heat conduction model, we applied the literature data for heat conductivity, specific heat capacity and latent heat as explained in [36].

Once the computational model had been calibrated, it was applied for designing the cooling path from the last deformation pass in the lab rolling mill to the coiling temperature (which was then physically simulated by holding in furnace).

Although the computational model was sufficiently accurate for the initial design of the water-cooling operation, it slightly underestimated the cooling power of the water jets. The reason for this was most likely that the width of the sample used in the current study was smaller than the one used in the calibration, as shown in Figure 137.

A simulation with 20 % higher heat transfer coefficient between the cooling water and the steel plate yielded a good agreement between the simulated and measured temperatures in the middle of the steel plate, as shown by the red lines (dashed experimental, solid simulated) in Figure 138.

The calibrated and fully coupled model was constructed to simulate water-cooling of a steel plate in a laboratory water cooling line. This provides useful tool for designing the water-cooling schedule and serves as an important first step towards simulating the processing conditions in an industrial setting.

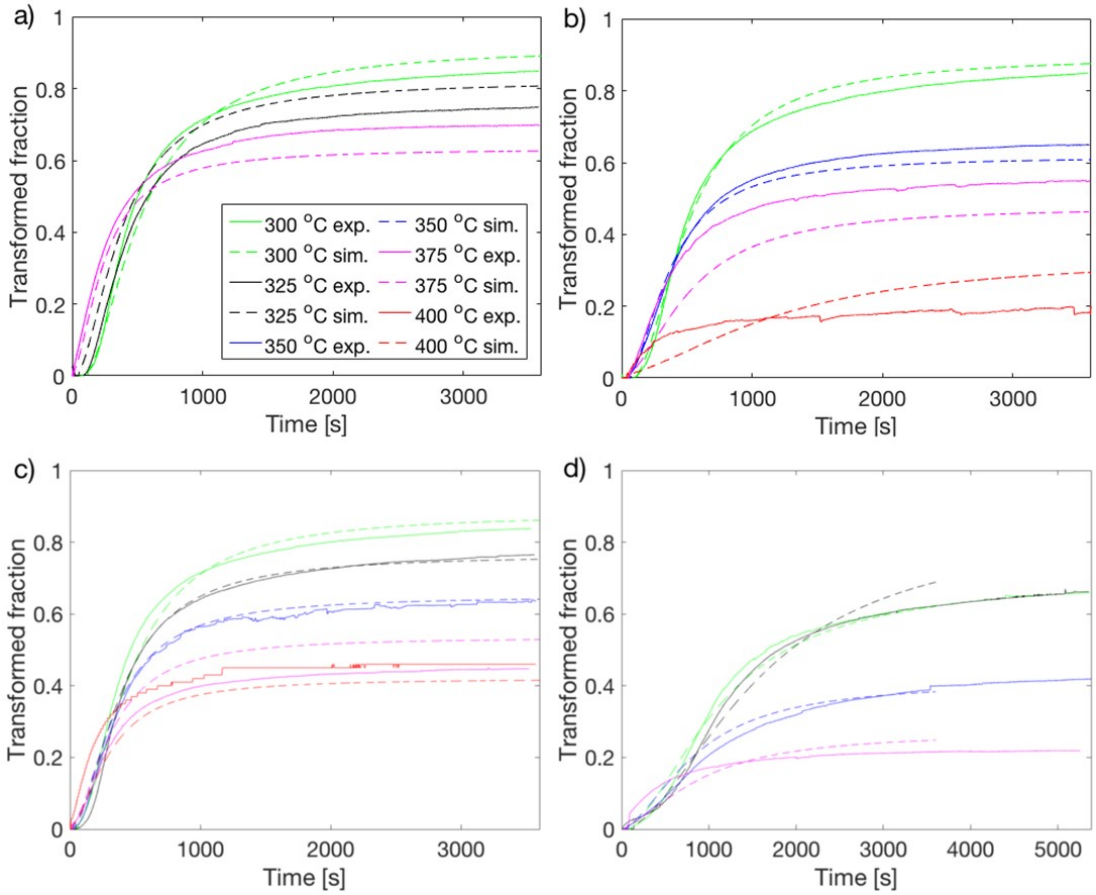

Figure 136. Comparison of the fitted phase transformation model to the experimental data for four different steels a) NR, b) NR+Mo+Nb, c) NR+Nb+V and d) NR+C+Nb+V for isothermal holding tests.

Figure 137. Image illustrating the width differences between calibration sample and actual sample used during the TMCP simulations.

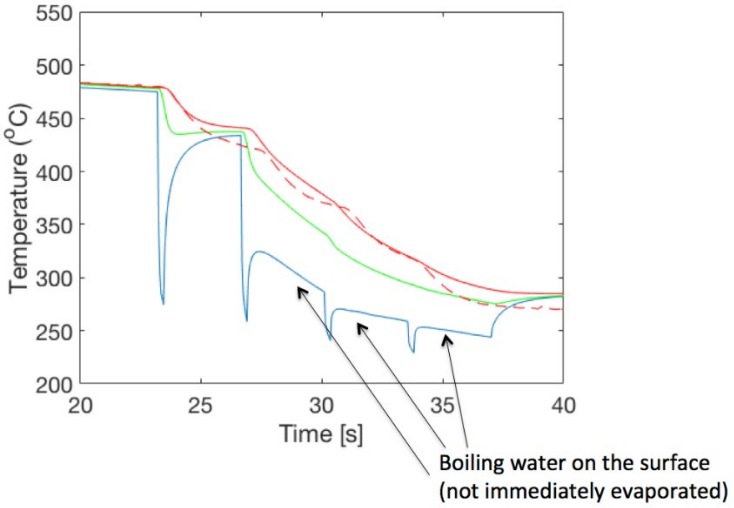

Figure 138. The simulated temperatures (solid lines) at surface (blue), quarter thickness from upper surface (green) and the center (red) compared to the measured temperature in the center (red solid line).

6.1.2 An improved bainite transformation model (tkSE)

An improved bainite transformation model was developed in the course of this project to enable estimations of industrially observed bainite transformation kinetics. The model is based on recent research on bainitic transformations [40] that takes into account the characteristic sluggish kinetics [2]. This part of the report deals with the modifications to the existing bainite transformation models.

6.1.2.i Model overview

A useful bainite transformation model needs to accurately predict the fraction of phase transformation that is taking place over time to adapt process parameters like temperature and cooling rate conditions to the expected extent of transformation. The formation of bainite often exhibits sluggish kinetics when measured for instance in dilatometer experiments. The sluggishness is reflected by reduced transformation rates at later stages of isothermal transformation experiments, typically when more than 50% of austenite is transformed into bainite. Conventional phase transformation approaches utilizing the Avrami (JMAK) equation return a sigmoidal phase fraction profile over time, but cannot reproduce the aforementioned sluggish transformation. One of the assumptions in the Avrami equation is a constant growth rate of nuclei independent of the previously transformed phase fraction. However, it has been established that a constant growth rate cannot be assumed for the bainitic transformation mainly due to two effects [2].

Firstly, even when assuming a pure displacive bainitic nucleation, the growth is accompanied by carbon diffusion from supersatured bainitic ferrite into the remaining austenite, which chemically stabilizes the austenite and therefore impedes further transformation. Secondly, the formation of bainite involves dislocation strengthening in the austenitic matrix. This dislocation strengthening has contrary effects on transformation kinetics. On the one hand, the higher dislocation density increases the nucleation site density for phase transformation. This potentially accelerates the transformation kinetics. On the other hand, plastic accommodation of deformation states generated by the displacive formation of bainite is hindered at higher dislocation densities, which affects the driving force for growth by increasing the elastic energy in austenite. The latter mechanical stabilization of austenite is included in the transformation model, that the work in this report is based on ref [40].

In contrast, the Azuma model and the modifications made in recent RFCS projects focus on the chemical stabilization by carbon diffusion [41–43]. Additionally, the Azuma approach incorporates cementite formation in both the austenite and bainitic ferrite phase to differentiate between upper and lower bainite. However, the model lacks a dimension to be able to consider the difference in carbon content between the austenitic bulk matrix and austenite surrounding bainite laths that is caused by the significantly lower diffusivity of carbon in austenite. The potential to distinguish these differently behaving domains of austenite would be required to reproduce physically meaningful formation of carbides in the high carbon austenite. Some efforts were made to extent the models in the described way, but the main focus of this work was on the aforementioned model of mechanical stabilization. In the following the model modifications and results will be demonstrated.

6.1.2.ii Introduction to transformation model.

6.1.2.ii.i Summary of transformation model.

The transformation rate in the original model is given by:

$$\frac{df_\alpha}{dt} = \kappa_0 * f_\gamma(1+\lambda f_\alpha)\frac{\Delta G^{\gamma\to\alpha} - G_e(f_\alpha, T_{hold})}{G_e(f_\alpha, T_{hold})}\exp\left(-\frac{Q}{RT}\right) \quad \text{Eq. 8}$$

where f_α and f_γ are the bainitic and austenitic phase fractions, respectively, λ is he autocatalysis factor, that takes into account the growth acceleration of bainite sheaves through autocatalysis, $\Delta G^{\gamma\to\alpha} = G^\gamma - G^\alpha$ is the driving force for diffusinless phase transformation from austenite to ferrite/bainite, $G_e(f_\alpha, T_{hold})$ is the elastic strain energy induced by the formation of bainite, which depends on the extent of transformed bainite and the formation temperature, Q is the activation energy of nucleation, R is the gas constant and κ_0 is a prefactor that depends on the austenite grain size, nucleation site density and critical bainite nucleus volume. The mentioned factors and equation is explained in more detail in the reference [40].

The decisive factor is the reduction of the driving force by the mechanical stabilization given by G_e. The growth factor reduces to

$$\frac{\Delta G^{\gamma\to\alpha} - G_e(f_\alpha, T_{hold})}{G_e(f_\alpha, T_{hold})} = \frac{\Gamma_B(B_{s*}(f_\alpha, T_{hold}) - T_{hold})}{G_{e0}(T_{hold}) + \Delta G_{e,b}(f_\alpha, T_{hold})} \quad \text{Eq. 9}$$

where $B_{s*}(f_\alpha, T_{hold})$ is the "bainite start temperature of mechanically stabilized austenite", -$\Gamma_B = 6.23$ J/(mol K) is the proportionality constant between the driving force $\Delta G^{\gamma\to\alpha}$ and the temperature in the temperature domain of bainite formation (400°C – 600°C), $G_{e0}(T_{hold})$ and $\Delta G_{e,b}(f_\alpha, T_{hold})$ are the terms in $G_e(f_\alpha, T_{hold})$ that are independent and dependent of the fraction of bainite, respectively.

Both $B_{s*}$and G_{e0} depend on a factor $\Delta G_{e0,\sigma}(T_{hold})$ in the following ways:

$$\Gamma_B B_{s*}(f_\alpha, T_{hold}) = \Gamma_B B_s - \Delta G_{e,b}(f_\alpha, T_{hold}) - \Delta G_{e0,\sigma}(T_{hold}) \quad \text{Eq. 10}$$

and

$$G_{e0}(T_{hold}) = G_{e0,Bs} + \Delta G_{e0,\sigma}(T_{hold}) \quad \text{Eq. 11}$$

where $\Delta G_{e0,\sigma}(T_{hold})$ is increasing the elastic strain energy of first formed bainite at temperature T_{hold} compared to the elastic strain energy at the bainite start temperature Bs $G_{0,Bs}$ due to an increases austenite strength at lower temperatures. Consequently, the increased strain energy $\Delta G_{e0,\sigma}(T_{hold})$ is given by:

$$\Delta G_{e0,\sigma}(T_{hold}) = 1.14\, \Gamma_B\left(\sigma_{y,T_{hold}} - \sigma_{y,Bs}\right) \quad \text{Eq. 12}$$

with the austenite strength at temperature T $\sigma_{y,T}$ and a proportionally factor 1.14 adopted from [40].

It is further assumed that $\Delta G_{e,b}(f_\alpha, T_{hold})$ is proportional to $\Delta G_{Ms,b}$ which is the shift in the required driving force to initiate martensite formation after mechanical stabilization of austenite through prior formation of bainite:

$$\Delta G_{e,b}(f_\alpha, T_{hold}) = p_2 \Delta G_{Ms,b}(f_\alpha, T_{hold}) \quad \text{Eq. 13}$$

This shift in the required driving force $\Delta G_{Ms,b}$ is demonstrated by and proportional by a factor Γ_M to the lowered martensite start temperatures after bainite formation. This difference in the martensite start temperature $\Delta M_s = M_s - M_{s*}$ caused by prior bainite formation is equal to the shift in the Koistinen-Marbuger temperature $\Delta M_s = \Delta T_{KM} = T_{KM} - T_{KM*}$ and the original model assumes the following equation for the dependency of this shift on the bainite fraction f_α:

$$\Delta T_{KM}(f_\alpha, T_{hold}) = -\frac{\log(1 - f_\alpha)}{\beta_{Ms,b}(T_{hold})} \quad \text{Eq. 14}$$

with

$$\beta_{Ms,b}(T_{hold}) = \alpha_m + \left|p_\beta (T_{hold} - T_{KM*})\right| \quad \text{Eq. 15}$$

and α_m being the Koistinen-Marbuger rate parameter. With $\beta_{Ms,b}(T_{KM*}) = \alpha_m$ Eq. 14 is similar to the Koistinen-Marbuger equation.

In summary the bainite fraction dependent term in the growth factor can be determined by:

$$\Delta G_{e,b}(f_\alpha, T_{hold}) = p_2 \Gamma_M \Delta T_{KM}(f_\alpha, T_{hold}) \quad \text{Eq. 16}$$

with $p_2 = 0.7$ and $\Gamma_M = 7.22$ J/(mol K) given in the original model.

In summary, the growth factor of Eq. 9 is given by:

$$\frac{\Gamma_B B_s - 0.7\Gamma_M \Delta T_{KM}(f_\alpha, T_{hold}) - 1.14\, \Gamma_B\left(\sigma_{y,T_{hold}} - \sigma_{y,Bs}\right) - \Gamma_B T_{hold}}{G_{e0,Bs} + 1.14\, \Gamma_B\left(\sigma_{y,T_{hold}} - \sigma_{y,Bs}\right) + 0.7\Gamma_M \Delta T_{KM}(f_\alpha, T_{hold})} \quad \text{Eq. 17}$$

6.1.2.ii.ii Modification to the model

It is well know that alloying silicon and aluminium has a crucial effect on bainite transformation kinetics. By decreasing the formation of carbides, a higher content of carbon is retained in the austenite matrix at higher Si/Al contents. The resulting chemical stabilization of austenite leads to slower bainite transformation and eventually to a halt of further phase transformation, i.e. an incomplete bainite transformation. This chemical effect is not taken into account in Eq. 14.To address this limitation the maximum possible transformed phase fraction at practically infinitely long hold times at holding temperature was added $f_\alpha^{max}(T_{hold})$:

$$\Delta T_{KM}(f_\alpha, T_{hold}) = -\frac{\log\left|1 - {f_\alpha}/{f_\alpha^{max}(T_{hold})}\right|}{\beta_{Ms,b}(T_{hold})} \qquad \text{Eq. 18}$$

6.1.2.iii Additional isothermal dilatometer experiments

To obtain data of the lowered martensite start temperatures of material with different fractions of bainite transformed at the same transformation temperatures, additional dilatometer experiments had to be carried out. The additional data is necessary to determine the extent of austenite stabilization to receive the parameters needed in the transformation rate function in Eq. 8. This section deals with these dilatometer experiments.

The targeted time-temperature profiles are shown in Figure 139. The cylindrical samples (9mm x ⌀4mm) of the three selected steels with different Si contents, i.e. Ref+Al-Si, Ref+Al, Ref+Al+Si, in Table 52, are austenized for three minutes at 1000°C. After the austenization the undeformed samples are cooled down at -50K/s to four different temperatures that are held isothermally for three varying transformation times. The isothermal transformation temperatures were chosen as 325°C, 350°C, 375°C and 400°C. The holding times are 600s, 900s and 1200s. These experimental parameters are selected to produce a range of different microstructures with different fractions of bainite. The transformation times are deliberately shorter than in the previous dilatometer tests in WP2. As explained above, the different levels of incomplete bainite transformation should result in different levels of austenite stabilization, which should be recognized by lowered martensite temperatures, when the samples are quenched after the isothermal bainite transformations.

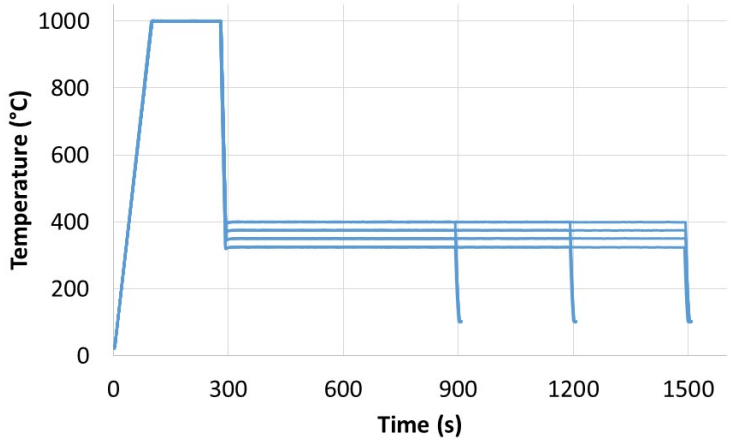

Figure 139: Targeted time-temperature profiles of additional dilatometer experiments: Four different isothermal bainite transformation (holding) temperatures (325°C, 350°C, 375°C, 400°C), each with three different bainite transformation (holding) times (600s, 900s, 1200s).

Table 52. Selection of chemical compositions from WP1 for tkSE modelling, all in wt.%.

	ID	C	Si	Mn	Mo	Cr	V	Al
REF+Al-Si	4	0.4	0.8	2	0	0.7	0	1
REF+Al	5	0.4	1.3	2	0	0.7	0	1
REF+Al+Si	6	0.4	1.5	2	0	0.7	0	1

In Figure 140 the measured dilatation signal for the whole temperature cycle is plotted for the Ref+Al-Si material at a transformation temperature of 325°C and three different holding times. Along with the measured dilatation data, the nonlinear lattice expansion functions for fcc and bcc lattices given in [44] are superimposed. An equal offset is added to both lattice expansion functions to align the data, such that the bcc expansion function tangentially touches the beginning of the dilatation data and the fcc expansion function overlaps the dilatation data during sample cooling after austenitization when a fully austenitic microstructure is assumed.

Evidently, the dilatation signal can be interpolated between the two lattice expansion functions to obtain the bainitic and martensitic phase fraction as described in [44]. The resulting phase fraction over time is shown in Figure 141. After 1200s at 325°C the bainite transformation has nearly reached a plateau at a phase fraction of approximately 75% and further kinetics are expected to slow down and eventually come to a halt. Ending the transformation at 600s yields a phase fraction of around 60%. The micrographs of both samples (325°C/600s and 325°C/1200s) in conjunction with the measured hardness results are included in Figure 142 and Figure 143, respectively. As expected, longer transformation times are reflected by a higher bainite fraction and a lower hardness of the microstructure.

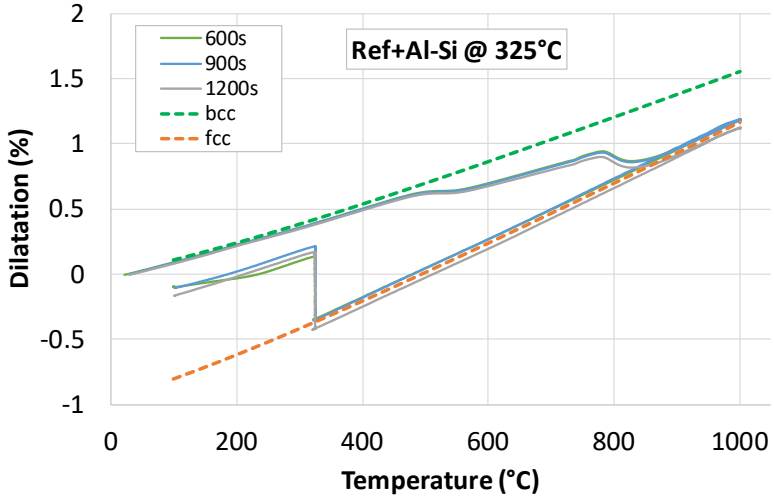

Figure 140: Longitudinal dilatation for the Ref+Al-Si material isothermally transformed at 325°C and three different holding times (solid).

Additionally, the retained austenite (RA) values measured by XRD are indicated by dashed bars in Figure 141, and together with the HV summarized in Table 53.

All phase transformation curves over time were compiled to generate the partial TTT diagram in Figure 144. Comparing the transformation kinetics of the low and high Si variants Ref+Al-Si and Ref+Al+Si are consistent with the hypothesis of slowed down kinetics by higher Si contents. The nose temperature for both steels is approximately between 350°C and 375°C. However, the transformation kinetics of the medium Si variant Ref+Al do not fall in line with the aforementioned trend. The transformation appears to be slower than the high Si variant for the lowest temperature 325°C which is unexpected and cannot be reasoned. For further analyses and model parameterizsation in the next section the results of steels Ref+Al-Si and Ref+Al+Si are compared.

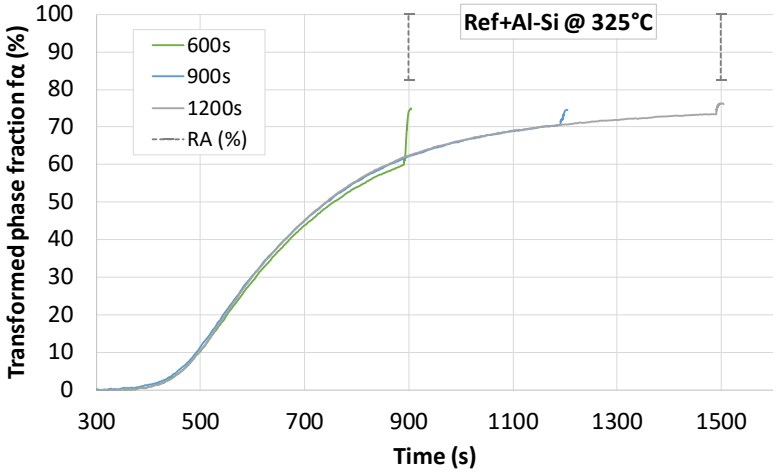

Figure 141: Transformed phase fraction during isothermal bainite transformation at 325°C and subequent quenching to 100°C for material Ref+Al-Si. Available XRD results of the fraction of retained austenite (RA) in the microstructure are shown as dashed bars.

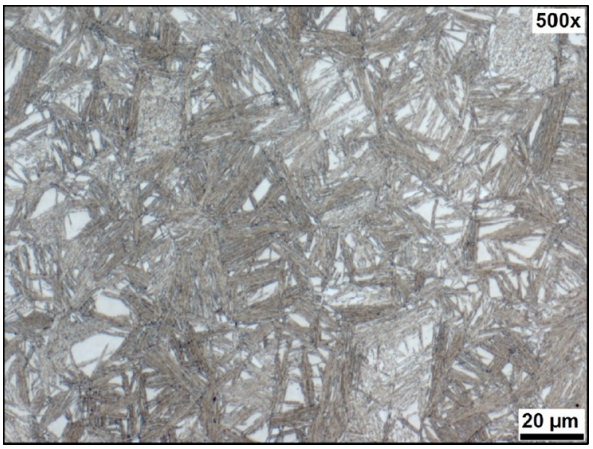

Figure 142: Micrograph of Ref+Al-Si @ 325°C for 600s: Hardness HV5 = 529.

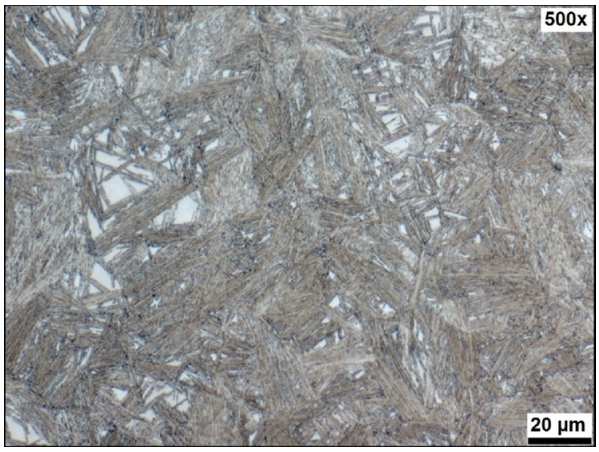

Figure 143: Micrograph of Ref+Al-Si @ 325°C for 1200s: Hardness HV5 = 488.

Table 53: RA (retained austenite by XRD) and hardness (HV5) of isothermal tests.

Material	Holding T (°C)	Holding t (s)	RA (%)	Hardness HV5
Ref+Al-Si	325	600	17.5	519
Ref+Al-Si	325	1200	17.5	488
Ref+Al-Si	400	600	22.0	467
Ref+Al-Si	400	1200	29.0	381
Ref+Al+Si	400	600	22.0	426
Ref+Al+Si	400	1200	29.0	400

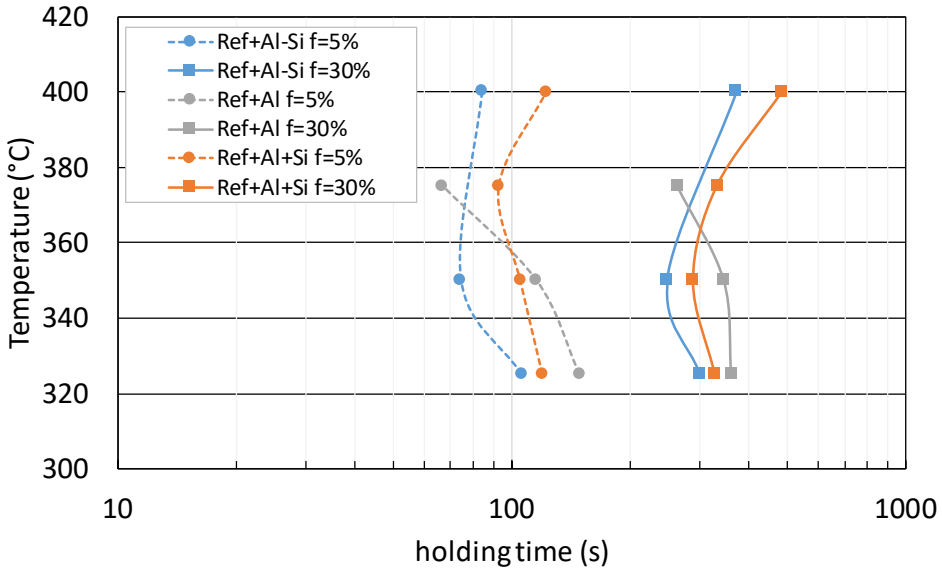

Figure 144: TTT diagram of the bainite region for steels Ref+Al-Si, Ref+Al and Ref+Al+Si.

6.1.2.iv Model parameterization

In order to parameterize Eq. 18 the lowered martensite start temperatures or better Koistinen-Marburger temperatures T_{KM*} have to be compared to the bainite fraction, which, as mentioned previously, stabilizes austenite and, thus lowers the martensite start temperature. As shown in Figure 141, martensite forms during quenching after the bainite transformation. When plotting the martensite fraction over the measured temperature, we should be able to fit the Koistinen-Marbuger equation:

$$f_{KM}(T) = 1 - \exp(-\alpha_m(T_{KM} - T)) \qquad \text{Eq. 19}$$

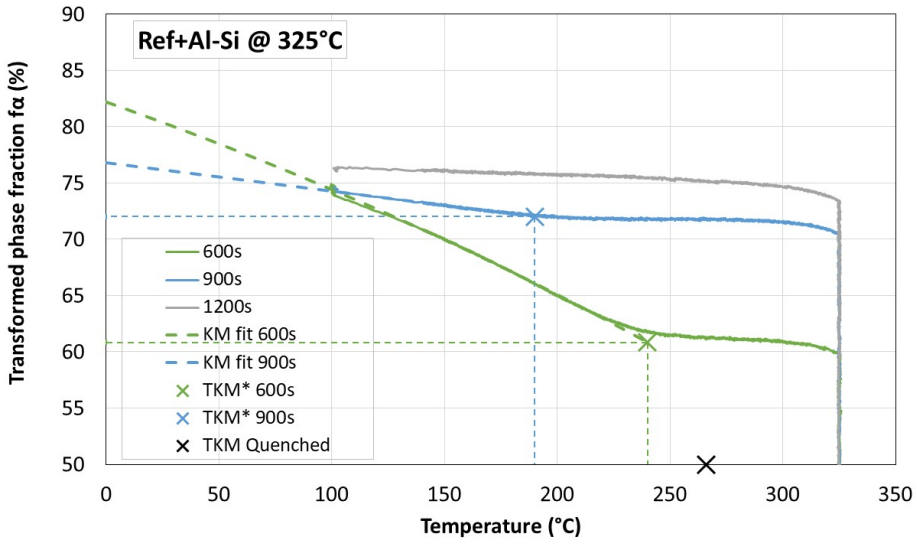

Figure 145: Transformed phase fraction over temperature after bainite transformation and during quenching. Fitted functions of Eq. 20 given by dashed lines. Koistinen-Marbuger temperatures TKM* (600s, 900s and no prior bainite formation: black) indicated by crosses.

However, as can be seen in Figure 145, Eq. 19 needs to be adjusted to cases where bainite is present before the material is quenched below the martensite start temperature. The following equation was used to fit the given phase fraction data:

$$f_{KM}^{*}(T) = f_{\alpha B} + f_{\alpha M} * \left(1 - \exp\left(-\beta_{Ms,b}(T_{KM*} - T)\right)\right) \quad \text{Eq. 20}$$

where $f_{\alpha B}$ is the previously accumulated fraction of bainite and $f_{\alpha M}$ is a limitation factor for decreased ultimate martensite fractions through increased RA fractions.

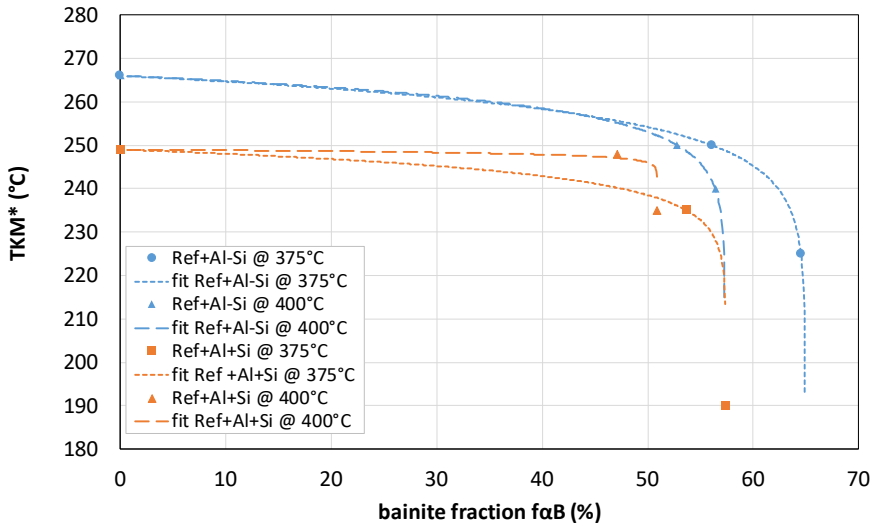

Figure 146: Data points: Fitting results T_{KM*} against $f_{\alpha B}$ of Eq. 20 for steels Ref+Al-Si and Ref+Al+Si at 375°C and 400°C. Dashed lines: Corresponding fitted functions Eq. 18.

Figure 146 shows the fit results (Koistinen-Marburger temperature T_{KM*} against prior bainite fraction $f_{\alpha B}$) for Eq. 20 to the obtained phase fraction curves at holding temperatures of 375°C and 400°C and the Ref+Al-Si and Ref+Al+Si steels. As discussed above, a higher Si-content yields decreased maximum bainite fractions.

The data points in Figure 146 were used to fit the parameters $f_{\alpha}^{max}(T_{hold})$ and $\beta_{Ms,b}(T_{hold})$ in Eq. 18. The fitted functions are indicated in Figure 146 by dashed lines. Clearly, more data points at different holding times between 60s and 900s would be necessary to validate the obtained fitted curves and $f_{\alpha}^{max}(T_{hold})$ and $\beta_{Ms,b}(T_{hold})$ values.

In Figure 147 the obtained maximum possible transformed phase fraction $f_{\alpha}^{max}(T_{hold})$ and the Martensite formation rate parameter $\beta_{Ms,b}(T_{hold})$ are plotted against the corresponding bainite transformation temperatures T_{hold} at 375°C and 400°C. For the samples that were quenched after austenitization with $f_{\alpha B} = 0$ and $\beta_{Ms,b}(T_{KM}) = \alpha_m$ Eq. 18 is equal to Eq. 20 with $f_{\alpha M} = f_{\alpha}^{max}$. Therefore, Figure 147 contains the data points $f_{\alpha}^{max}(T_{KM}) = f_{\alpha M}$ and $\beta_{Ms,b}(T_{KM}) = \alpha_m$ at the Koistine Marburger temperatures 249°C and 266°C for steels Ref+Al+Si and Ref+Al-Si, respectively. Based on these results, it is deemed possible to linearly parameterize both $f_{\alpha}^{max}(T_{hold})$ and $\beta_{Ms,b}(T_{hold})$ like Eq. 15 and

$$f_{\alpha}^{max}(T_{hold}) = f_{\alpha M} + |p_{\alpha max}(T_{hold} - T_{KM*})| \quad \text{Eq. 21}$$

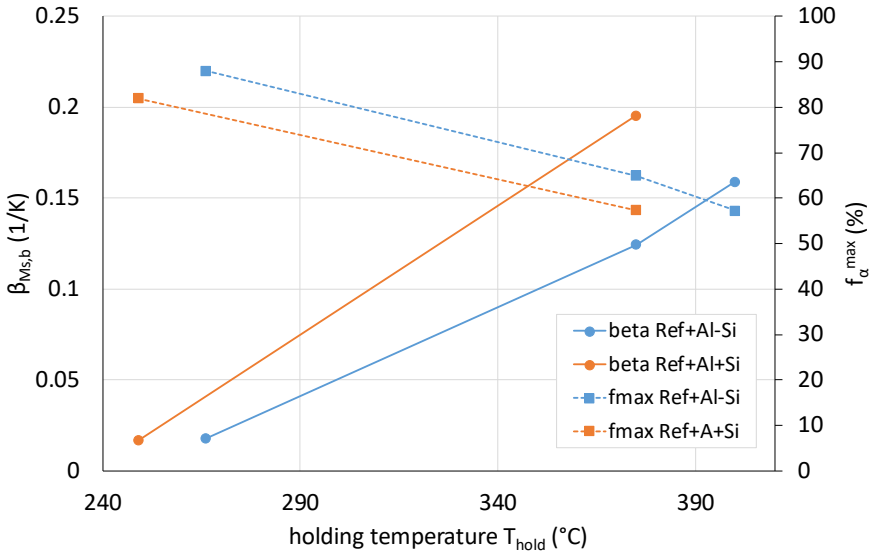

Figure 147: Fitting results of $f_\alpha^{max}(T_{hold})$ and $\beta_{Ms,b}(T_{hold})$. The data points at the lowest temperatures 249°C and 266°C (T_{KM} for Ref+Al+Si and for Ref+Al-Si, respectively) correspond to the values of $f_{\alpha M}$ and α_m in Eq. 20 of quenched sample with not prior bainite formation ($f_{\alpha B} = 0$).

In conjunction with the previously fitted parameters of Eq. 18 it is now possible to fit the rate function Eq. 8 with the growth factor in Eq. 17 to match the dilatometer data of bainitic phase fraction over time. The austenite yield strength $\sigma_{y,T}$ is calculated by model from [45]. The remaining fitting factors are the rate factor κ_0, the autocatalysis factor λ, the activation energy Q, the bainite start temperature B_s and the initial bainite strain energy for bainite formed at B_s $G_{e0,Bs}$.

Three different parameter sets were received by fitting (i) all of the phase fraction curves of material "Ref+Al-Si", (ii) all of the phase fraction curves of material "Ref+Al+Si" and (iii) all of the phase fraction curves of both "Ref+Al-Si" and "Ref+Al+Si". The results are compiled in Table 54. It should be noted, that these parameters are mere fitting parameters and the originally ascribed physical properties are likely lost during the fitting procedure which can be seen in the low values of the initial bainite strain energies $G_{e0,Bs}$. The calculated bainitic ferrite fraction at different T is plotted against that estimated from dilatometric curves in Figure 148 and Figure 149,

Table 54: Obtained fitting parameters for bainite rate model.

	DIL data	λ	$\kappa_0/10^{-3}$[s^{-1}]	Q[kJ/mol]	B_s[°C]	$G_{e0,Bs}$[J/mol]
1	Ref+Al-Si	40.5	0.11	4.9	419	0.26
2	Ref+Al+Si	32.2	1.00	14.8	412	9.54
3	Ref+Al-Si +Ref+Al+Si	33.5	0.37	10.1	417	7.44

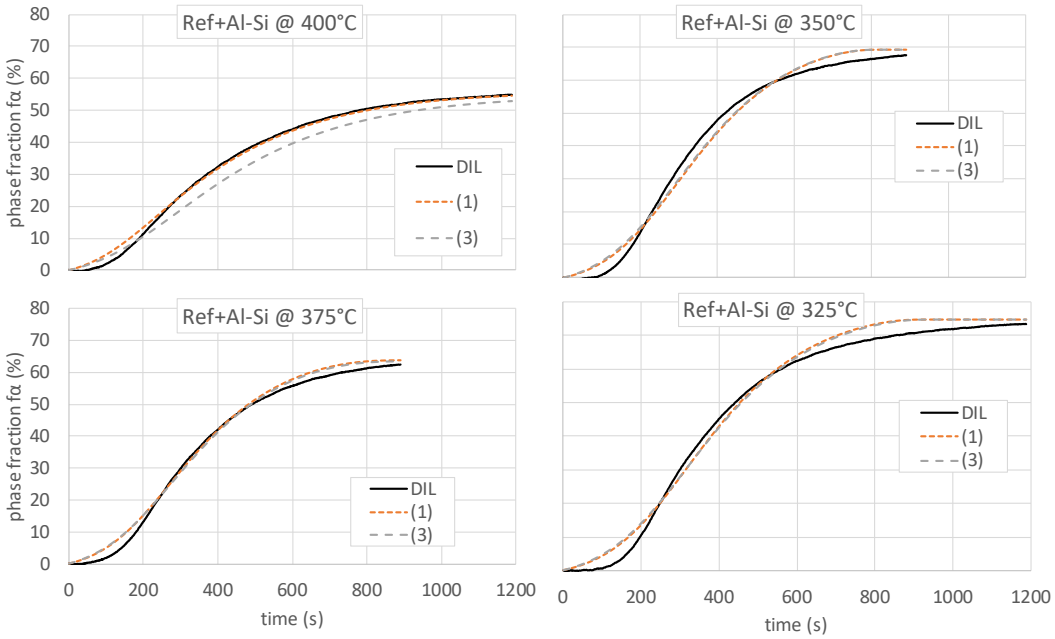

Figure 148. For R+AL-Si in Table 52, bainitic ferrite fraction at different isothermal T, calculated according to the indicated model and compared with obtained from the dilatometric curve.

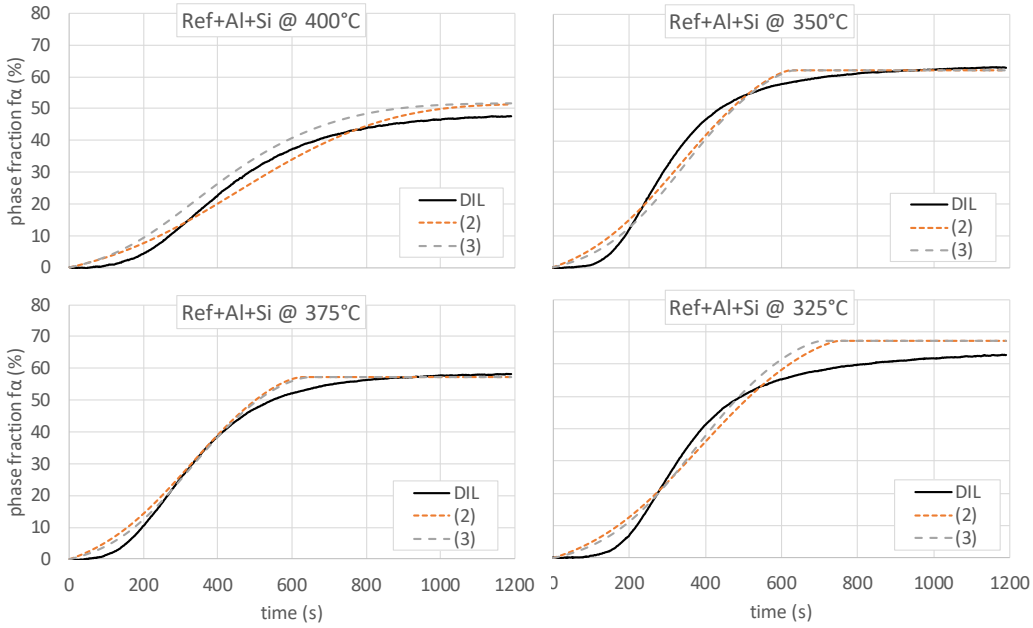

Figure 149. For R+AL+Si in Table 52, bainitic ferrite fraction at different isothermal T, calculated according to the indicated model and compared with obtained from the dilatometric curve.

6.1.2.v Final remarks

The approach outlined above determines the mechanical stabilization of austenite by Eq. 16 and Eq. 18 which is the crucial term in the bainite growth factor of Eq. 9. However, more dilatometer experiments are needed to parameterize the dependence of the lowered martensite start temperature T_{KM*} on the prior bainite fraction $f_{\alpha B}$ and subsequently the dependence of f_{α}^{max} and $\beta_{Ms,b}$ on the bainite transformation holding temperature T_{hold}.

A bainite transformation model was then parameterized to predict the bainitic phase transformation of two steels selected in this project with special consideration of the Si content. As can be seen by the transformation model predictions compared to the dilatometer results in Figure 148 and Figure 149, the models achieve an adequate level of accuracy. However, discrepancies arise at the transformation curves where the martensite stabilization parameters f_{α}^{max} and $\beta_{Ms,b}$ could not be determined with certainty, e.g. Ref+Al+Si@400°C or Ref+Al+Si@325°C, see Figure 147. This stresses the fact that more dilatometer experiments are needed to confirm the and validate the linear relationship between the holding temperature and f_{α}^{max} and $\beta_{Ms,b}$.

6.1.3 An integrated-model for austenite yield strength considering the influence of temperature and strain rate in lean steels (CENIM, tkSE)

Two other models have been developed in the frame of this project. As both models have been already published, and therefore a through description is already provided, only the abstract and full reference are provided in this document.

The model has been published, see Ref [45], therefore only the abstract is included.

Due to the necessity to exhaustively control the hot deformation of austenite, a strong effort has been made in the past to propose predictive models for the yield strength. Such models have shown accurate predictions within relatively narrow compositional range, closely related to the limitations of the database employed. Nevertheless, by testing those models with a large database, including a wider range of temperatures and compositions, the authors have observed that such narrow compositional ranges cause these models to be inaccurate. The strain rate is also an important parameter that has been ignored in previous works, and deeply affects mechanical behavior. In this work, we propose a more robust model, which includes the contribution of the strain rate and wider composition and temperature ranges by integrating different formulations, providing improvement at predicting yield strength with respect to previous models.

6.1.4 Stress or strain induced martensitic and bainitic transformations during ausforming processes (CENIM).

The model has been published, see Ref [34], therefore only the abstract is included.

The so-called ausforming treatment consists in plastically deforming a fully austenitized steel below the recrystallization stop temperature, prior to either a martensitic or a bainitic transformation. Although this procedure is envisioned as a way to improve the mechanical response of the attained microstructure, it is not without its drawbacks, as the possibility of phase transformations occurring during the deformation step. When such step is applied at relatively higher temperatures than those of the aimed microstructure, the presence of those softer phases could be rather detrimental for the final microstructure. The current study aims to further study those phase transformations to analyze whether they are induced via either stress or strain and to identify the temperature ranges in which they tend to occur, so that they can be avoided or used to improve the final microstructure properties in the future. A final evaluation on the impact of these induced transformations on the final microstructure when deformation is followed by either cooling or an isothermal treatment is also performed.

7 Stage 3. Recommendation for full scale TMCP (WP6, All)

A final set of recommendations are made for the development of an optimal bainitic microstructure by means of TMCP. In addition the industrial feasibility and limitations of current hot rolling lines, which could impede the industrial implementation of a nanostructured bainite are discussed. The focus will be on the steels NR+Nb+V and NR+C+Nb+V, which have shown the best combinations of strength and ductility (WP5).

Note that experimental data for some of the following sections could be found in Task 3.3 & 3.4 section.

7.1 Slab-reheating.

Coarse as-cast niobium carbide precipitates can take a long time to dissolve at reheating temperatures close to the equilibrium precipitate dissolution temperature. So, although the dissolution temperature for NbC precipitates is in the range of 1200°C for 0.02 wt % Nb in 0.4-0.5 wt% C steels (WP1), the reheating temperature is recommended to be around ~1250°C to ensure dissolving as much niobium as possible in the reheated austenite.

Due to the high contents of Mn, Si and Cr, the project steels are susceptible to segregation (WP4). The resulting chemical inhomogeneities influence e.g. the locally varying phase transformation kinetics and thus the local microstructure and mechanical properties. Therefore, measures to reduce segregation, e.g. soft reduction, should be applied.

7.2 TMCP for 3 mm product

7.2.1 LT- and MT-TMCP-3 mm

The implementation of the MT- and LT-TMCP-3 mm cycle already posed enormous challenges on the laboratory scale. Rolling experiments on the pilot plant hot rolling mill could not be carried out due to the required high deformation forces. The design of commercial hot rolling mills makes it practically impossible to perform the MT- or LT-TMCP cycle on them. Despite critical rolling loads, a sufficient and accurate cooling between the final rolling stands of the finishing mill is not possible to achieve the needed low deformation temperatures. Thus the remainder of this section will focus on the HT-TMCP-3 mm cycle.

7.2.2 HT-TMCP-3 mm

The rolling schedule for HT-TMCP needs to be designed so that the microstructure does not recrystallize in the last passes of the finishing mill and thus a considerable amount of residual strain (~0.4) occurs. Since both the time between the deformation passes and the deformation temperature decreases with each finishing pass, conditions for recrystallization become less favourable with each rolling pass.

Using steelytics® Hot Rolling [46] with the recrystallization models developed in WP3, recrystallization during finish rolling on a typical 7 stand finishing mill has been simulated for NR+Nb+V and NR+C+Nb+V. According to WP3 a finish rolling temperature of 820 °C was used. The entry temperature and thickness in the finishing mill were chosen as 1000 °C and 40 mm, respectively. The reduction is decreasing with each rolling pass. Starting with a reduction of 50 % and ending with a reduction of 7 %, a linear decrease of the reduction was assumed with each stand. This results in a final thickness of 5 mm after the fourth stand. Interpass times between the last rolling stands are shorter than 1 s.

The mean strip temperature and the estimated recrystallized fraction at the entry is shown in Figure 150 for each rolling pass. After the fifth pass the rolling temperature is low enough and the interpass times are short enough that strain accumulation occurs and desired residual strains of approximately 0.4 are possible.

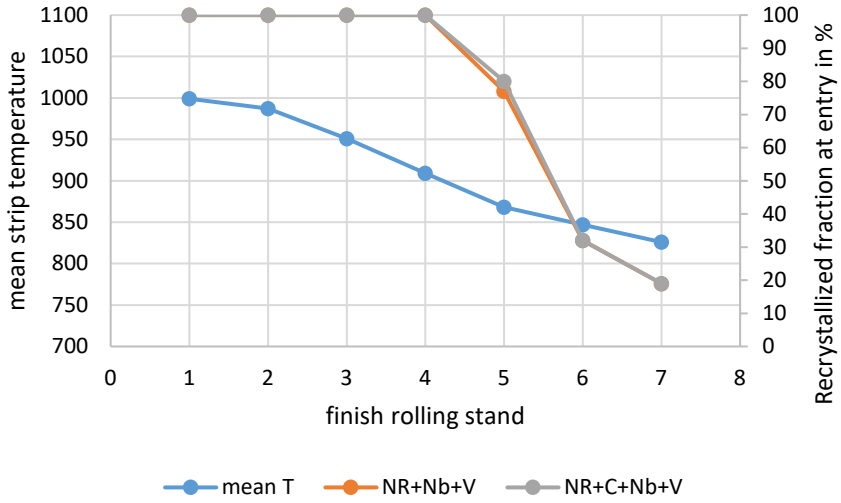

Figure 150: Mean strip temperature and recrystallized fraction at the stand entry for NR+Nb+V and NR+C+Nb+V calculated with steelytics® Hot Rolling using a realistic rolling schedule with a final strip thickness of 3 mm.

Since the needed deformation temperatures (below ~850 °C) are within the lower end of typical rolling temperatures at powerful commercial hot rolling mills and the deformation below the no recrystallization temperature can be realized using multiple rolling passes, no special care is required with regard to the rolling forces.

7.3 TMCP for 12 mm product

7.3.1 LT-MT-TMCP 12mm

As demonstrated during hot rolling with a 300ton capacity laboratory rolling mill, ausforming at temperatures as low as 350°C can be possible with limited plate dimensions. But full-scale industrial feasibility for such low-temperature ausforming even at finish rolling temperatures <800°C will be very challenging because of very high rolling loads during low-temperature deformations. Even during laboratory rolling, water cannot be used to cool down the plates before the last rolling pass at low temperatures because water forms a hard martensite layer on the plate surface risking damage to the rolls. Instead, forced air cooling is recommended. The critical cooling rate of > 1ºC/s to avoid the ferrite-pearlite bay for these compositions (WP2) can be achieved by forced air cooling. One disadvantage of forced air cooling would be heterogeneous cooling of the plates, but the homogeneity can be improved by a smart set-up of forced-air cooling.

7.3.2 HT-TMCP 12mm

Based on the successful HT-TMCP lab rolling trials during the course of the project, recommended finish rolling temperature can be 820-850°C to keep austenite non-recrystallised. Finish rolling at 820-850°C

should be possible with state-of-art industrial hot-rolling mills. Though sufficient risk-analysis should be undertaken in collaboration with respective mills before introducing new chemistries in the line.

Nevertheless, the necessary cooling rates and coiling temperatures for the HT-TMCP can be achieved. In a commercial heavy plate mill accelerated water cooling between rolling passes is in principle possible.

7.4 Rolling forces

With regard to the rolling forces needed for the final deformation step in the different TMCP, the process parameters obtained and measured in the Task 2.3, 3.3 and 3.4 have been analysed. The evaluation of the dilatometer results in WP 2 (see **Table 30**) has already shown that for the MT- and LT-TMCP very high deformation forces are needed. For the MT-TMCP maximum flow stresses of approximately 600-650 MPa were measured. For the LT-TMCP even higher flow stresses up to 1000 MPa at 300 °C were obtained for the hardest material R+C+Nb+V. The results of Task 3.3 and 3.4 are in line with this (see e.g. **Figure 47**(b)).

The two empirical approximations of Jedlicka [47,48] and Ford and Alexander [49,50] were used to estimate the needed rolling forces during industrial rolling in a finishing and heavy plate mill:

$$F_{\text{Jedlicka}} = 1.15\, k_{fm} w_m l_d \left(1 + \frac{\mu\, l_d}{h_0 + h_1}\right)$$

$$F_{\text{Ford\&Alexander}} = \frac{1}{2} k_{fm} w_m l_d \left(\frac{\pi}{2} + \frac{l_d}{h_0 + h_1}\right)$$

k_{fm} is the mean flow stress, w_m the mean plate width, l_d is the contact length, which was approximated as $\sqrt{R\,\Delta h}$, μ is the friction coefficient, which was kept constant (0.4) and h_0 and h_1 are the initial and final plate thicknesses. In addition, two-dimensional FEM simulations of the rolling process were executed using Simufact Forming 15.0.

For the finishing mill $h_0 = 4$ mm, $h_1 = 3$ mm, $w_m = 1$ m with a reasonable $R = 0.35$ m was chosen. The results are shown in Figure 151 (dashed lines and triangles, respectively). Considering the HT-TMCP-3 mm process with a deformation temperature of 820 °C and a $k_{fm} = 350$ MPa (Figure 47), a rolling force of approximately 15 MN can be found. This is in line with the rolling forces obtained in Task 3.3. With $h_0 = 5$ mm and $w_m = 0.2$ m rolling forces between 3.8 and 4.7 MN were measured, which is equivalent to k_{fm} between 340 and 400 MPa (Jedlicka model). Assuming a reasonable maximal possible rolling force of 40 MN, the HT-TMCP-3mm should be within the limits of a powerful commercial hot rolling mill.

For the heavy plate mill $h_0 = 16$ mm, $h_1 = 12$ mm and a rather low width of 1 m was chosen. The roll radius in a heavy plate mill is typically larger compared to a finishing mill. A reasonable value of $R = 0.55$ m was used. The results are also shown in Figure 151 (solid lines and squares, respectively). Assuming a maximal possible rolling force of 100 MN [51] and regarding the measured mean flow stresses in Figure 47, all 12 mm TMCP should be within the limits of 100 MN with a width of only 1 m. Considering a more common plate width of 2 m, already the necessary forces for the MT-TMCP-12 mm will be critical ($k_{fm} = 500$ MPa). Independend of the plate width, material imprints or damage on the rolls can occur due to the much higher mean flow stresses compared to typical rolling conditions (100 – 400 MPa).

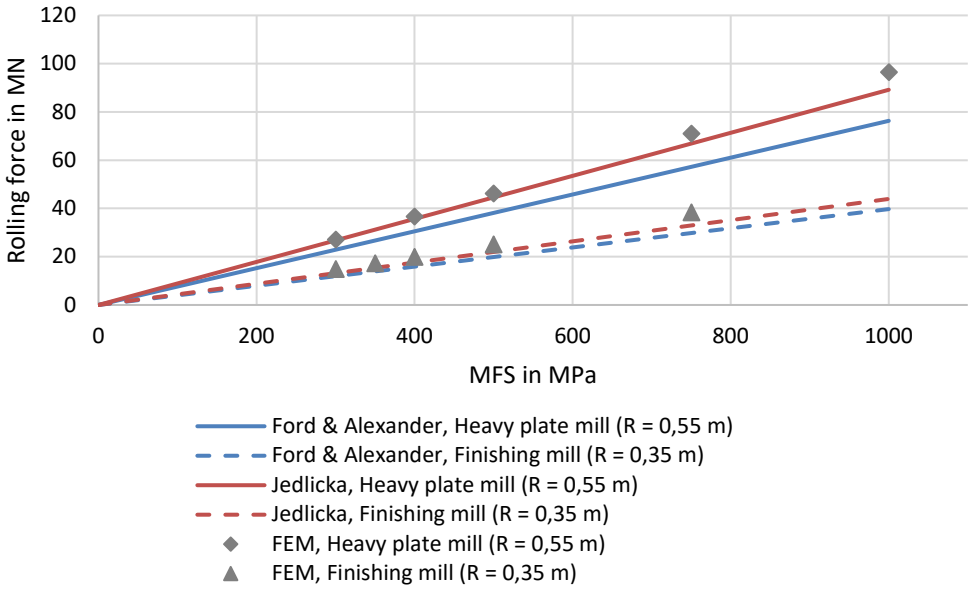

Figure 151. Approximation of the expected rolling force for a given mean flow stress in a finishing and heavy plate mill for a given rolling geometry, respectively.

7.5 Cooling

In order to cool the strip within the cooling section of a hot rolling mill to the required coiling temperatures (~ 350 °C), forced water cooling is required. The cooling rates required to avoid any ferritic or pearlitic phase transformation (>10 K/s) can be achieved easily by water cooling. Due to the breakage of the steam film (Leidenfrost effect) the cooling rate sharply increases at around 550-600 °C, which makes it more difficult, but not impossible, to hit the desired coiling temperature with state-of-the-art cooling section control software. Here it is an advantage that no transformation takes place in the cooling section and thus no heat of transformation is released counteracting the water cooling.

While the calibrated phase transformation model can be used to calculate the transformation start and subsequent kinetics for the fitted steels using the parameters [38], the heat transfer model needs to be calibrated for the specific water cooling system in order to simulate the water cooling with a good accuracy. Once the heat transfer model has been calibrated, the simulation method provides a way to virtually optimize the water cooling practice to cool down the steel so that lower bainitic microstructure is achieved. Therefore, experimental tests for calibration of the heat transfer model in industrial setting are recommended.

7.6 Coiling procedures

As demonstrated in Task 3.3 & 3.4 section, the coiling T must be carefully adjusted in order to maximize the amount of bainitic, and minimize that of martensite, through the different sections of the coil.

The recalescence due to the bainitic phase transformation causes an increase of the coil temperature. Due to the rather slow phase transformation, which can take minutes to hours, and the inhomogeneous cooling of the coil (the coil surface cools down much faster than the coil core), the time-temperature profile differs locally. As a result, the phase transformation takes place in different areas of the coil at different

temperatures. This in turn can lead to differences in the microstructure and ultimately in inhomogeneous material properties as shown in WP4 and 5. Therefore, measures to achieve a more homogeneous cooling, e.g. coil covering, should be considered.

Due to the phase transformation during coil cooling, attention should be paid to additional aspects during industrial testing. The coil could possibly collapse due to the locally varying evolution of the volume expansion during phase transformation and the consequent loss of stability. Due to the high strength and the phase transformation during coil cooling, the strip could be under high tension. Therefore, industrial testing of the optimum winding condition and maybe the use of two binding tapes is necessary. The high strength also requires the use of a strong decoiler.

It is important to note that we approximated the plastic deformation between the flat and coiled strip. The maximum strain will appear in the coil eye and should be ~0.5 %, thus a significant amount of RA transformation to martensite due to the strain is not expect.

8 Foreseeable future (All)

The steels used in the project are ordinary high-Si medium-carbon steels with various alloying elements including Mn, Cr, Mo, Nb, etc. The idea was to design and use compositions that may provide desired mechanical properties with special microstructures. The steels of the project should be considered as future products without special restrictions of today's plants. Generally speaking, steel plants and their future technology will develop into the direction that is viable not only economically, but will also be beneficial ecologically, as the property requirements and ecological considerations will be tightened all the time. However, it is true that the concept should also be refined as far as possible for better adaptability in the current set-up of infrastructure.

The microstructures developed in this project can be used as abrasive wear resistant steels in mining industry (yellow goods), farming machineries (green goods), construction and transportation industry (trucks, trailers), cement industry, machinery parts for excavation, bulk handling, crushing and screening equipment, earthmoving and heavy duty demolition equipment, waste and recycling machineries. State of art wear resistant steels are based on classical low alloy quenched and tempered martensitic (Q&T) metallurgy which provide excellent wear resistance due to high hardness but not known for ductility, toughness and bendability properties. The retained austenite in the fine bainitic microstructure developed in this project contribute towards better ductility, better tensile toughness (UTS x El%) and better bendability while maintaining abrasive wear resistance at par or, sometimes even better than the commercial quenched martensitic based wear resistant steels.

Other wear resistance applications like in rail steels, bearing steels where classical cementite-free bainitic microstructures are used occasionally, can also be potential application areas for the novel ausformed low C (0.4 wt% C) bainitic microstructures developed in this project.

Due to the high yield strength and high elongation and therefore high energy absorption capacity of the investigated steels, these could be suitable for safety critical components in the automotive industry like pillars, side-impact intrusion beams and bumper bars [52]. Based on that, Figure 152 and Figure 153 shows some potential niche of application, where nowadays, dual phase (DP) [53], complex phase (CP) [54] and press hardened martensitic based steels [55,56] are being used. The indicated element ranges are maximum

values for the steel groups. Still, some aspects, as weldability, toughness and high edge crack sensitivity of punched holes need further considerations.

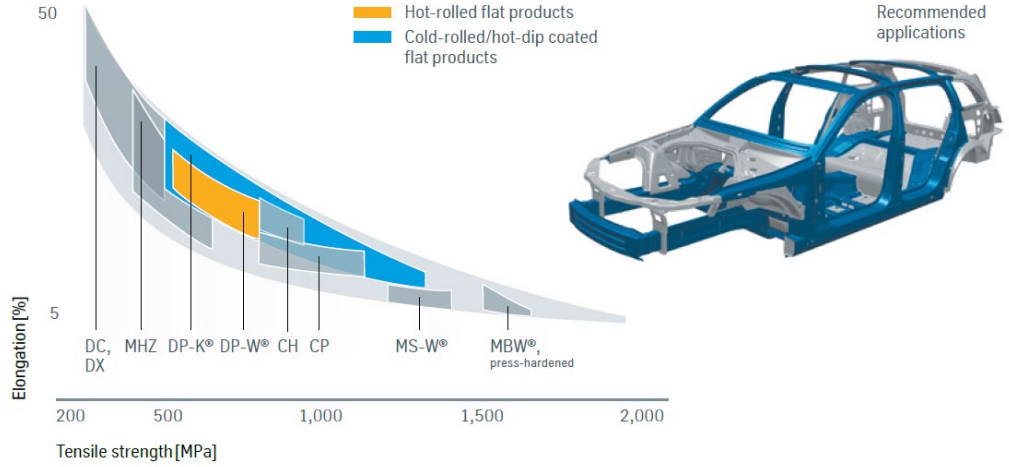

Multiphase steels
CP family (complex phase) steels
0.2 C+ 1 Si+ 2.2 Mn+ 0.25 Ti+Nb + 0.015-2 Al + 1.2-1.4 Cr+Mo+ 0.005B

DP family (dual phase) steels
0.2 C+ 0.8 Si+ 2.6 Mn+ 0.15 Ti+Nb + 0.015-1 Al + 1 Cr+Mo+ 0.25 V+ 0.005B

Figure 152. Elongation v.s UTS of typical CP and DP tkSE products [53,54].

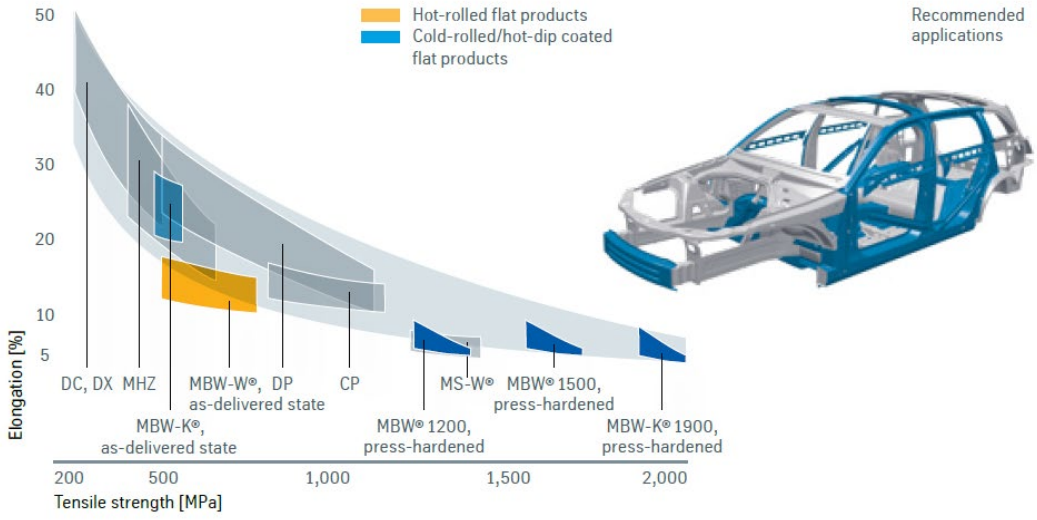

Martensitic based microstructures
MBW/MS - Mn+B family steels
0.25-0.4 C+ 0.4-0.8 Si+ 1.4-2.5 Mn+ 0.05-0.25 Ti+Nb+ 0.015-2 Al+ 0.5-1.2 Cr+Mo+ 0.005B

Figure 153. Elongation v.s UTS of typical Mn+B martensitic tkSE products [55,56].

These steels can also be envisioned to use in applications where original high C (0.9wt% C) nanostructured bainitic steels are used like in ballistic applications, though the ballistic properties of the novel ausformed low C (0.4 wt% C) bainitic microstructures still need to be evaluated. Compared to original high C (0.9wt% C) nanostructured bainitic microstructure, lower C contents in the steels investigated in the current project

improves the weldability and accelerates the bainitic transformation, making this concept feasible via classical thermo-mechanical controlled hot rolling processes.

Direct quenching and bainitic holding (DQ&B) following TMCP and austenite conditioning (ausforming) can be considered as an energy-efficient, cost-effective innovative process, viable for online industrial application and with the possibility of lean, inexpensive alloying. Unlike in the case of energy-intensive quenching and tempering (Q&T), the idea of the DQ&B processing is to develop tough, ductile, ultrahigh strength steel with high strain hardening capacity and good bendability characteristics. An appropriate process design facilitates the formation of extremely refined (nanostructured) bainite-austenite microstructures with the possibility of TRIP effect to impart capability of energy absorption, quintessential in the mentioned applications. Ausforming is less energy intensive compared to quench and tempered steels in the sense that the former eliminates the need for an extra reheating step followed by quenching and tempering.

Ausforming at high finish rolling temperatures of 800-850°C (HT-TMCP) is similar to state-of-art industrial practise of TMCP controlled high strength hot-rolled steels. Therefore, industrialisation of the HT-TMCP concept as proposed in the project should be possible. However, sufficient risk-analysis should be undertaken in collaboration with respective mills before introducing new chemistries in the line.

Ausforming at medium and low finish rolling temperatures of 550-400°C (MT and LT-TMCP) will be industrially quite challenging as these will need more powerful and stronger mills, but not impossible with current and near future technological prowess. In this project, it has been demonstrated that with a 300 ton capacity laboratory rolling mill, ausforming at temperatures as low as 350°C can be possible with limited plate dimensions.

Still, with hot strip mill type continuous production route, mass production is easier compared to batch type production route for original high carbon nanobainite concepts. Very few commercial grades at these such high strength levels has been commercialised e.g. martensitic steels, press-hardened steels, the high-carbon nanobainitic steels, see Figure 154.

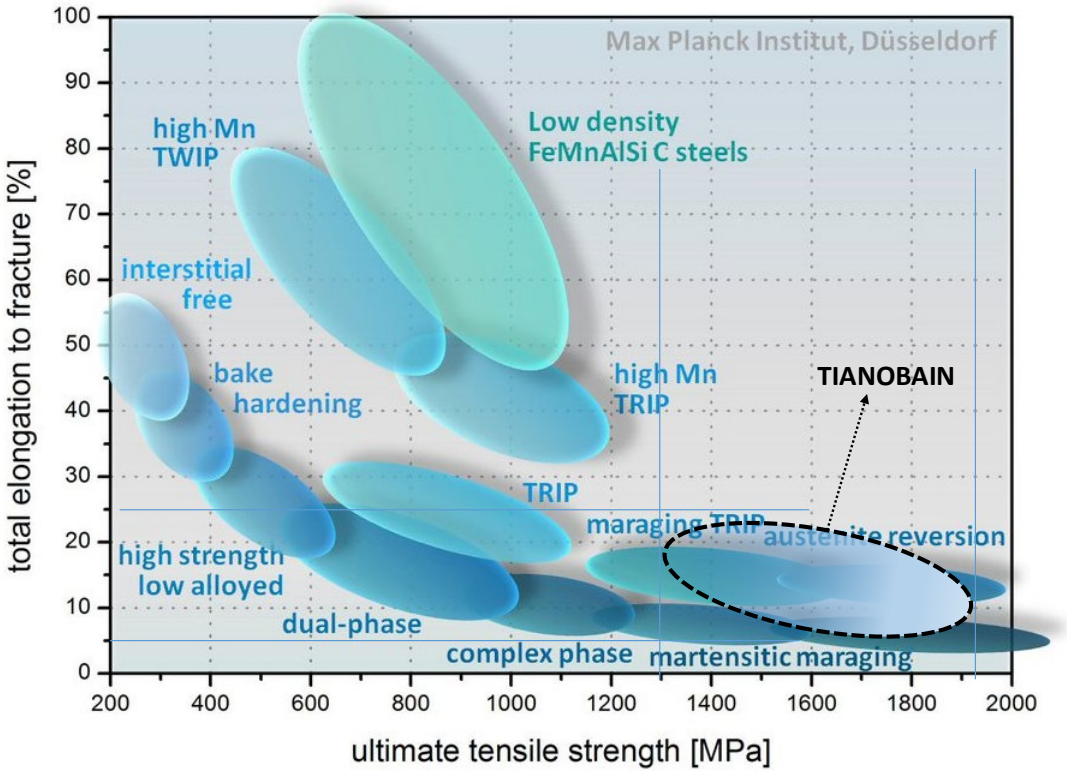

Figure 154. Position of TIANOBAIN results in the UTS-total elongation chart.

The present project has been a first step towards industrial implementation. Being based on laboratory experiments, it has not been possible to investigate for example effects related to on-line cooling and coiling. Variations in cooling rate and coiling temperature along the length of a hot-rolled strip followed by the homogenization of temperature in the coil are best addressed in full-scale rolling trials, which are now needed after this laboratory research. The small plastic strains involved in decoiling and levelling will also have a small effect on the tensile yield strength and uniform elongation. The magnitude of these effects will depend on the details of the equipment and parameters used and, again, need to be investigated with the aid of full-scale trials.

9 Dissemination of results

Dissemination of the results has been profuse, a list of the publications and presentation in international conferences is as follows:

Ref [1]. Garcia-Mateo, C.; Paul, G.; Somani, M.C.; Porter, D.A.; Bracke, L.; Latz, A.; de Andres, C.G.; Caballero, F.G. Transferring nanoscale bainite concept to lower C contents: A perspective. Metals (Basel). 2017, 7, doi:10.3390/met7050159.

Ref [57] .Garcia-Mateo, C. TIANOBAIN - Towards industrial applicability of (medium C) nanostructured bainitic steels - RFCS. *Impact* **2018**, *2018*, 94–96, doi:10.21820/23987073.2018.94.

EUROMAT 2017 (Thessaloniki, Greece, 17-22 September, 2017) "Ausforming: Challenges and Developments for Nanostructured Bainite" as a Highlight presentation.

THERMEC 2018 (Paris 8-13/07/2018) "Developing Nanostructured Bainite by means of Ausforming" as Invited presentation.

Material Science and Engineering MSE 2018, (Darmstadt, Germany) "Constitutive flow behavior of austenite at low temperatures and its influence on transformation characteristics of ausformed medium carbon bainitic steels" as oral presentation.

Ref [58] **CHS2** (The 7th International Conference on Hot Sheet Metal Forming of High-Performance Steel). (Lulea ,Sweden, 2-5 June 2019). "Effect of the Deformation Temperature in the Bainitic Transformation During Ausforming Treatments."

EUROMAT 2019. (Stockholm, Sweden, September 1-5, 2019)**. In EUROMAT 2019 a devoted Symposium (B1: Advanced Steels) was organised with the aim of presenting and sharing the most relevant results of the project. The presentations delivered by different partners were named as follows:.**

- Effect of ausforming temperature on the anisotropy of the bainitic transformation in medium carbon steels: a crystallographic study.
- On the kinetics of bainitic transformation at low temperatures in ausformed medium-carbon steels.
- On the control of the scale of nanobainitic microstructures by prior austenite strengthening
- Nanostructured bainitic steels with carbide precipitations – a new steel class
- TIANOBAIN. On the quest of ultrafine bainite by means of low temperature ausforming in medium carbon steels.

Ref [23] Eres-Castellanos, A.; Morales-Rivas, L.; Latz, A.; Caballero, F.G.; Garcia-Mateo, C. Effect of ausforming on the anisotropy of low temperature bainitic transformation. Mater. Charact. 2018, 145, 371–380, doi:10.1016/j.matchar.2018.08.062.

Ref [45] Eres-Castellanos, A.; Toda-Caraballo, I.; Latz, A.; Caballero, F.G.; Garcia-Mateo, C. An integrated-model for austenite yield strength considering the influence of temperature and strain rate in lean steels. Mater. Des. 2020, 188, 108435, doi:10.1016/j.matdes.2019.108435.

Ref [34] Eres-Castellanos, A.; Caballero, F.G.; Garcia-Mateo, C. Stress or strain induced martensitic and bainitic transformations during ausforming processes. Acta Mater. 2020, 189, 60–72, doi:10.1016/j.actamat.2020.03.002.

Ref [59] Kaikkonen, P.M.; Somani, M.C.; Miettunen, I.H.; Porter, D.A.; Pallaspuro, S.T.; Kömi, J.I. Constitutive flow behaviour of austenite at low temperatures and its influence on bainite transformation characteristics of ausformed medium-carbon steel. *Mater. Sci. Eng. A* **2020**, *775*, 9–11, doi:10.1016/j.msea.2020.138980.

Ref [60] Zorgani, M.; Garcia-Mateo, C.; Jahazi, M. The role of ausforming in the stability of retained austenite in a medium-C carbide-free bainitic steel. *J. Mater. Res. Technol.* **2020**, *9*, 7762–7776, doi:10.1016/j.jmrt.2020.05.062.

At least 5 other paper are in the process of review/ to be submitted at the time of preparation of this report.

10 List of Figures

11 List of Tables

Cγ the volume fraction and C content of austenite respectively measured by XRD, also reported the maximum stress measured during deformation.

Table 11. Summary of the main results obtained from the D-CCT diagrams. F/P stands for Ferrite/Perlite, B for bainite, M for martensite, Ms is the martensite start T at 25ºC/s, HV is the Vickers hardness, Vγ and Cγ the volume fraction and C content of austenite respectively measured by XRD, also reported the maximum stress measured during deformation.

Table 12 Summary of the main results obtained from the D-CCT diagrams. F/P stands for Ferrite/Perlite, B for bainite, M for martensite, Ms is the martensite start T at 25ºC/s, HV is the Vickers hardness, Vγ and Cγ the volume fraction and C content of austenite respectively measured by XRD, also reported the maximum stress measured during deformation.

Table 13. Summary of the main results obtained from the TTT diagrams. F/P stands for Ferrite/Perlite, B for bainite, M for martensite, Ms is the martensite start T measured on cooling after isothermal transformation, HV is the Vickers hardness, Vγ and Cγ the volume fraction and C content of austenite respectively measured by XRD. Time for the onset, maximum transformation rate and end of transformation are also provided when possible.

Table 14. Summary of the main results obtained from the TTT diagrams. F/P stands for Ferrite/Perlite, B for bainite, M for martensite, Ms is the martensite start T measured on cooling after isothermal transformation, HV is the Vickers hardness, Vγ and Cγ the volume fraction and C content of austenite respectively measured by XRD. Time for the onset, maximum transformation rate and end of transformation are also provided when possible.

Table 15. Summary of the main results obtained from the TTT diagrams. F/P stands for Ferrite/Perlite, B for bainite, M for martensite, Ms is the martensite start T measured on cooling after isothermal transformation, HV is the Vickers hardness, Vγ and Cγ the volume fraction and C content of austenite respectively measured by XRD. Time for the onset, maximum transformation rate and end of transformation are also provided when possible.

Table 16. Bainitic ferrite plate thickness measurements in some selected cases. The error corresponds to the standard deviation. Error denotes the 95% confidence error.

Table 17. Summary of the main results obtained from the LT-DTTT diagrams. F/P stands for Ferrite/Perlite, B for bainite M for martensite, Ms is the martensite start T, HV is the Vickers hardness, Vγ and Cγ the volume fraction and C content of austenite respectively measured by XRD.

Table 18. Summary of the main results obtained from the LT-DTTT diagrams. F/P stands for Ferrite/Perlite, B for bainite M for martensite, Ms is the martensite start T, HV is the Vickers hardness, Vγ and Cγ the volume fraction and C content of austenite respectively measured by XRD.

Table 19. Summary of the main results obtained from the LT-DTTT diagrams. F/P stands for Ferrite/Perlite, B for bainite M for martensite, Ms is the martensite start T, HV is the Vickers hardness, Vγ and Cγ the volume fraction and C content of austenite respectively measured by XRD.

Table 20. Summary of the main results obtained from the MT-DTTT diagrams. F/P stands for Ferrite/Perlite, B for bainite M for martensite, Ms is the martensite start T, HV is the Vickers hardness, Vγ and Cγ the volume fraction and C content of austenite respectively measured by XRD.

Table 21. Summary of the main results obtained from the MT-DTTT diagrams. F/P stands for Ferrite/Perlite, B for bainite M for martensite, Ms is the martensite start T, HV is the Vickers hardness, Vγ and Cγ the volume fraction and C content of austenite respectively measured by XRD.

12 List of symbols, indices, acronyms and abbreviations

B	Bainite
Bs	Bainite Start Temperature
CCT	Continuous Cooling Transformation
$C\gamma$	Carbon in retained austenite
CR	Cooling rate
D-CCT	Deformation-CCT
D-TTT	Deformation-TTT
F/P	Ferrite/Pearlite
HT-DTTT	High Temperature D-TTT
IDS	Inter-Dendritic-Segregation
LOM	Light Optical Microscopy
LT-DTTT	Low Temperature D-TTT
M	Martensite
MFS	Mean flow stress
Ms	Martensite Start Temperature
MT-DTTT	Medium Temperature D-TTT
RST	Recrystallization Stop Temperature
SEM	Scanning Electron Microscopy
TMCP	thermo-mechanically controlled processing
T_{NR}	Temperature No Recrystallization
TTT	Temperature Time Transformation
$V\gamma$	Volume fraction of austenite
XRD	X-Ray diffraction

13 List of References

1. Garcia-Mateo, C.; Paul, G.; Somani, M.; Porter, D.; Bracke, L.; Latz, A.; Garcia De Andres, C.; Caballero, F. Transferring Nanoscale Bainite Concept to Lower C Contents: A Perspective. *Metals (Basel).* **2017**, *7*, 159, doi:10.3390/met7050159.
2. Bhadeshia, H.K.D.H. *Bainite in Steels. Theory and Practice*; Third.; Maney Publishing: London, 2015; ISBN 978-1-909662-74-2.
3. Bhadeshia, H.K.D.H. Thermodynamic analysis of isothermal transformation diagrams. *Met. Sci.* **1982**, *16*, 159–166, doi:10.1179/030634582790427217.
4. Peet, M.; Bhadeshia, H.K.D.H. MAP_STEEL_MUCG83.
5. Saunders, N.; Guo, Z.; Li, X.; Miodownik, A.P.; Schillé, J.P. Using JMatPro to model materials properties and behavior. *Jom* **2003**, *55*, 60–65, doi:10.1007/s11837-003-0013-2.
6. Laboratory, N.P. MTDATA 2003.
7. Andersson, J.-O.; Helander, T.; Höglund, L.; Shi, P.; Sundman, B. Thermo-Calc & DICTRA, computational tools for materials science. *Calphad* **2002**, *26*, 273–312, doi:10.1016/S0364-5916(02)00037-8.
8. Andrews, K.W. Empirical formulae for the calculation of some transformation temperatures. *J. Iron Steel Inst.* **1965**, *203*, 721–727.
9. Bhadeshia, H.K.D.H.; Honeycombe, R.W.K. Steels: Microstructure and Properties (Fourth Edition). In *Steels: Microstructure and Properties (Fourth Edition)*; Bhadeshia, H.K.D.H., Honeycombe, R.W.K., Eds.; Butterworth-Heinemann, 2017; p. 488 ISBN 978-0-08-100270-4.
10. Maccagno, T.M.; Jonas, J.J.; Yue, S.; McCRADY, B.J.; Slobodian, R.; Deeks, D. Determination of Recrystallization Stop Temperature from Rolling Mill Logs and Comparison with Laboratory Simulation Results. *ISIJ Int.* **1994**, *34*, 917–922, doi:10.2355/isijinternational.34.917.
11. Miettinen, J.; Louhenkilpi, S.; Kytönen, H.; Laine, J. IDS: Thermodynamic-kinetic-empirical tool for modelling of solidification, microstructure and material properties. *Math. Comput. Simul.* **2010**, *80*, 1536–1550, doi:10.1016/j.matcom.2009.11.002.
12. Martin, D.C. Selected heat conduction problems in thermomechanical treatment of steel, Oulu University: Oulu University, 2011, Vol. PhD.
13. Guo, L.; Roelofs, H.; Lembke, M.I.; Bhadeshia, H.K.D.H. Modelling of transition from upper to lower bainite in multi-component system. *Mater. Sci. Technol. (United Kingdom)* **2017**, *33*, 430–437, doi:10.1080/02670836.2016.1221495.
14. Hollomon, J.H. Tensile deformation. *Trans. Am. Inst. Mech. Eng.* **1945**, *162*, 268–290.
15. Santajuana, M.A.; Eres-Castellanos, A.; Ruiz-Jimenez, V.; Allain, S.; Geandier, G.; Caballero, F.G.; Garcia-Mateo, C. Quantitative Assessment of the Time to End Bainitic Transformation. *Metals (Basel).* **2019**, *9*, 925, doi:10.3390/met9090925.
16. Garcia-Mateo, C.; Jimenez, J.A.J.A.; Lopez-Ezquerra, B.; Rementeria, R.; Morales-Rivas, L.; Kuntz, M.; Caballero, F.G. Analyzing the scale of the bainitic ferrite plates by XRD, SEM and TEM. *Mater. Charact.* **2016**, *122*, 83–89, doi:10.1016/j.matchar.2016.10.023.
17. Eres-Castellanos, A.; Morales-Rivas, L.; Latz, A.; Caballero, F.G.; Garcia-Mateo, C. Effect of ausforming on the anisotropy of low temperature bainitic transformation. *Mater. Charact.* **2018**, *145*, 371–380, doi:10.1016/j.matchar.2018.08.062.
18. Somani, M.; Karjalainen, L.P. *Modelling the Deformation and Annealing Processes: Physical and Regression Approaches*; 2007; Vol. 550;.
19. Somani, M.C.; Karjalainen, L.P.; porter, D.A.; Morgridge, A.R. Regression modelling of the recrystallization kinetics of austenite. *Int. Conf. Thermomechanical Process. Mech. Microstruct. Control* 2002, 411–436.
20. Nyyssönen, T.; Peura, P.; Kuokkala, V.-T. Crystallography, Morphology, and Martensite Transformation of Prior Austenite in Intercritically Annealed High-Aluminum Steel. *Metall. Mater.*

Trans. A **2018**, *49*, 6426–6441, doi:10.1007/s11661-018-4904-9.
21. Bachmann, F.; Hielscher, R.; Schaeben, H. Texture Analysis with MTEX – Free and Open Source Software Toolbox. *Solid State Phenom.* **2010**, *160*, 63–68, doi:10.4028/www.scientific.net/SSP.160.63.
22. Fan, H.L.; Zhao, A.M.; Li, Q.C.; Guo, H.; He, J.G. Effects of ausforming strain on bainite transformation in nanostructured bainite steel. *Int. J. Miner. Metall. Mater.* **2017**, *24*, 264–270, doi:10.1007/s12613-017-1404-7.
23. Eres-Castellanos, A.; Morales-Rivas, L.; Latz, A.; Caballero, F.G.; Garcia-Mateo, C. Effect of ausforming on the anisotropy of low temperature bainitic transformation. *Mater. Charact.* **2018**, *145*, 371–380, doi:10.1016/j.matchar.2018.08.062.
24. ISO ISO 2566-1:1984 Steel — Conversion of elongation values — Part 1: Carbon and low alloy steels 1984, *1984*, 1–28.
25. Ojala, N.; Valtonen, K.; Kivikytö-Reponen, P.; Vuorinen, P.; Kuokkala, V.-T. High speed slurry-pot erosion wear testing with large abrasive particles. *Finnish J. Tribol.* **2015**, *33*, 36–44.
26. Ojala, N.; Valtonen, K.; Antikainen, A.; Kemppainen, A.; Minkkinen, J.; Oja, O.; Kuokkala, V.-T. Wear performance of quenched wear resistant steels in abrasive slurry erosion. *Wear* **2016**, *354–355*, 21–31, doi:https://doi.org/10.1016/j.wear.2016.02.019.
27. ASTM International *ASTM G 65-16 Standard Test Method for Measuring Abrasion Using the Dry Sand/Rubber Wheel Apparatus*; ASTM International, West Conshohocken, PA, 2016;
28. Neuhaus, R.; Borsutzki, M. Plattchen-biegeversuch nach VDA 238-100. *Mater. Test.* **2013**, *55*, 654–659, doi:10.3139/120.110484.
29. SSAB STRENX, HARDOX AND DOCOL -BENDING OF HIGH STRENGTH STEEL.
30. Karelova, A.; Krempaszky, C.; Werner, E.; Tsipouridis, P.; Hebesberger, T.; Pichler, A. Hole expansion of dual-phase and complex-phase AHS steels - Effect of edge conditions. *Steel Res. Int.* **2009**, *80*, 71–77, doi:10.2374/SRI08SP110.
31. Leonhardt, A.; Kräusel, V.; Paar, U. Automated hole expansion test with pneumatic crack detection. *IOP Conf. Ser. Mater. Sci. Eng.* **2019**, *480*, 012026, doi:10.1088/1757-899X/480/1/012026.
32. Javaheri, V.; Nyyssönen, T.; Grande, B.; Porter, D. Computational Design of a Novel Medium-Carbon, Low-Alloy Steel Microalloyed with Niobium. *J. Mater. Eng. Perform.* **2018**, *27*, 2978–2992, doi:10.1007/s11665-018-3376-9.
33. Bernier, N.; Bracke, L.; Malet, L.; Godet, S. An alternative to the crystallographic reconstruction of austenite in steels. *Mater. Charact.* **2014**, *89*, 23–32, doi:10.1016/j.matchar.2013.12.014.
34. Eres-Castellanos, A.; Caballero, F.G.; Garcia-Mateo, C. Stress or strain induced martensitic and bainitic transformations during ausforming processes. *Acta Mater.* **2020**, *189*, 60–72, doi:10.1016/j.actamat.2020.03.002.
35. Pohjonen, A.; Paananen, J.; Mourujärvi, J.; Manninen, T.; Larkiola, J.; Porter, D. Computer simulations of austenite decomposition of microalloyed 700 MPa steel during cooling. In Proceedings of the AIP Conference Proceedings; 2018; Vol. 1960, p. 090010.
36. Pohjonen, A.; Kaijalainen, A.; Mourujärvi, J.; Larkiola, J. Computer simulations of austenite decomposition of hot formed steels during cooling. *Procedia Manuf.* **2018**, *15*, 1864–1871, doi:10.1016/j.promfg.2018.07.203.
37. Pohjonen, A.; Somani, M.; Porter, D. Modelling of austenite transformation along arbitrary cooling paths. *Comput. Mater. Sci.* **2018**, *150*, 244–251, doi:10.1016/j.commatsci.2018.03.052.
38. Pohjonen, A.; Kaikkonen, P.; Ilmola, J.; Seppälä, O.; Manninen, T.; Somani, M. Modelling of thermo-mechanical processing of medium-carbon steels at low temperatures for achieving fine-structured bainite. *Under Eval.* **2020**.
39. Uusikallio, S.; Koskenniska, S.; Ilmola, J.; Paavola, J.; Pohjonen, A.; Larkiola, J.; J., K. Determination of effective heat transfer coefficient for water spray cooling of steel. *Procedia Manuf.* **2020**.
40. van Bohemen, S.M.C. Bainite growth retardation due to mechanical stabilisation of austenite. *Materialia* **2019**, *7*, 100384, doi:10.1016/j.mtla.2019.100384.
41. Azuma, M.; Fujita, N.; Takahashi, M.; Senuma, T.; Quidort, D.; Lung, T. Modelling upper and lower

bainite trasformation in steels. *ISIJ Int.* **2005**, *45*, 221–228, doi:10.2355/isijinternational.45.221.
42. Paul, G.; Großterlinden, R.; Aldazabal, J.; Garcia, O.; Dickert, H.H.; Katsamas, A.I.; Kamoutsi, E.; Haidemenopoulos, G.N.; Hebesberger, T.; Satzinger, K. *Design of bainite in steels from homogeneous and inhomogeneous microstructures using physical approaches (Bainite Design). RFSR-CT-2007-00022*; EUROPEAN COMMISSION Directorate G - Industrial Technologies, Unit G.5 — Research Fund for Coal and Steel, D.-G. for R. and I., Ed.; European Commission, 2013; ISBN 978-92-79-28948-4.
43. Savran, V.; Zhu, V.; Gutierrez Sanz, I.; van Bohemen, S.; Hisker, F.; Sietsma, J. *Bainite and second-phase engineering for improved formability (BASEFORM). RFSR-CT-2014-00017*; EUROPEAN COMMISSION Directorate G - Industrial Technologies, Unit G.5 — Research Fund for Coal and Steel, D.-G. for R. and I., Ed.; European Commission: Luxembourg, 2018;
44. Van Bohemen, S.M.C.C. The nonlinear lattice expansion of iron alloys in the range 100–1600K. *Scr. Mater.* **2013**, *69*, 315–318, doi:10.1016/j.scriptamat.2013.05.009.
45. Eres-Castellanos, A.; Toda-Caraballo, I.; Latz, A.; Caballero, F.G.; Garcia-Mateo, C. An integrated-model for austenite yield strength considering the influence of temperature and strain rate in lean steels. *Mater. Des.* **2020**, *188*, 108435, doi:10.1016/j.matdes.2019.108435.
46. Baron, T.J.; Latz, A.; Schreiber, S.; Hülstrung, J.; Kern, A. *steelytics® Hot Rolling -calculation of steel properties over strip length*; 2019;
47. Jedlicka, J. *Neue Methoden der Berechnung der Walzkraft*; 1970; Vol. 15;.
48. Hinkfoth, R. *Bulk forming process*; Verlagshaus Mainz GmbH Aachen ; ISBN 9783861301844.
49. Ford, H.; Alexander, J.M. Simplified hot rolling calculations. *J. Inst. Met* **1963**, *92*, 397–404.
50. Popoff, A.A. Simplified hot rolling load calculations incorporating material strain rates. *Int. J. Mech. Sci.* **1976**, *18*, 529–532, doi:https://doi.org/10.1016/0020-7403(76)90078-3.
51. HEAVY-PLATE MILLS (SMS SIEMAG AG).
52. Keeler, S.; Kimchi, M.; Mooney, P.J. *Advanced High-Strength Steels Application Guidelines V.6*; 2017;
53. thyssenkrupp Dual-phase steels – tailored portfolio for modern lightweight construction | | thyssenkrupp Steel Available online: https://www.thyssenkrupp-steel.com/en/products/sheet-coated-products/multiphase-steel/dual-phase-steel/ (accessed on May 19, 2020).
54. thyssenkrupp Complex-phase steel: Product portfolio of thyssenkrupp Available online: https://www.thyssenkrupp-steel.com/en/products/sheet-coated-products/multiphase-steel/complex-phase-steel/ (accessed on May 19, 2020).
55. thyssenkrupp MBW® – manganese-boron steel for hot forming | thyssenkrupp Steel Available online: https://www.thyssenkrupp-steel.com/en/products/sheet-coated-products/manganese-boron-steel-for-hot-forming/mbw-manganese-boron-steel-for-hot-forming/ (accessed on May 19, 2020).
56. thyssenkrupp Hot-rolled martensite-phase steel | thyssenkrupp Steel Available online: https://www.thyssenkrupp-steel.com/en/products/hot-strip/multiphase-steel/martensite-phase-steel/martensite-phase-steel.html (accessed on May 19, 2020).
57. Garcia-Mateo, C. TIANOBAIN - Towards industrial applicability of (medium C) nanostructured bainitic steels - RFCS. *Impact* **2018**, *2018*, 94–96, doi:10.21820/23987073.2018.94.
58. Eres-Castellanos, A.; Caballero, F.G.; Garcia-Mateo, C. Effect of the deformation temperature in the bainitic transformation during ausforming treatments. In *Hot Sheet Metal Forming of High-Performance Steel, CHS2*; Oldenburg, M., Hardell, J., Casellas, D., Eds.; Lulea, 2019; p. 793 ISBN 978-3-95735-104-3.
59. Kaikkonen, P.M.; Somani, M.C.; Miettunen, I.H.; Porter, D.A.; Pallaspuro, S.T.; Kömi, J.I. Constitutive flow behaviour of austenite at low temperatures and its influence on bainite transformation characteristics of ausformed medium-carbon steel. *Mater. Sci. Eng. A* **2020**, *775*, 9–11, doi:10.1016/j.msea.2020.138980.
60. Zorgani, M.; Garcia-Mateo, C.; Jahazi, M. The role of ausforming in the stability of retained austenite in a medium-C carbide-free bainitic steel. *J. Mater. Res. Technol.* **2020**, *9*, 7762–7776, doi:10.1016/j.jmrt.2020.05.062.